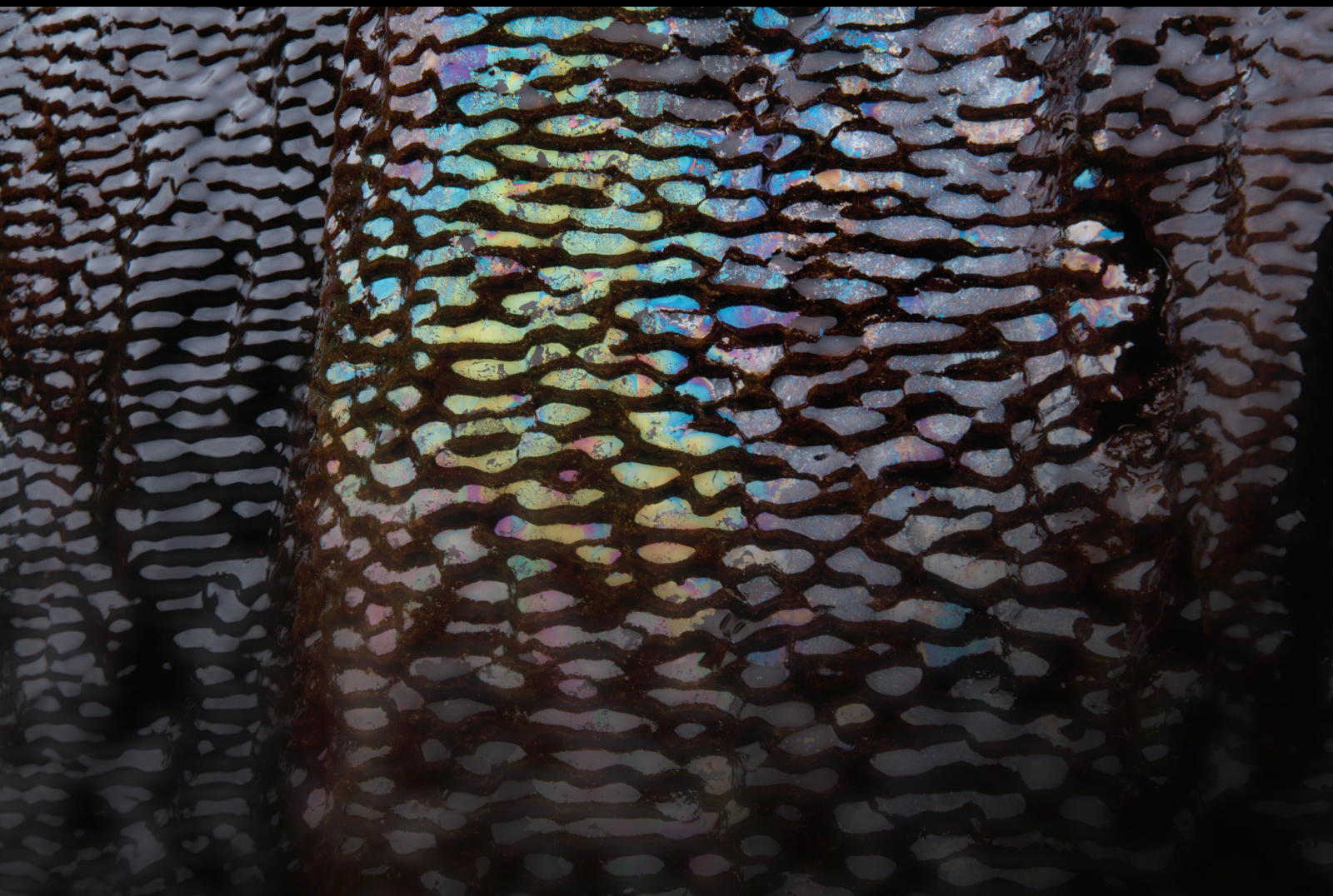


The Role of Water-Rock Interaction Processes in Soil Formation: Geochemical, Mineralogical, Geomorphological, and Engineering-Geological Aspects

Special Issue Editor in Chief: Carmine Apollaro

Guest Editors: Francesco Perri, Luigi Borrelli, and Tommaso Caloiero





**The Role of Water-Rock
Interaction Processes in Soil Formation:
Geochemical, Mineralogical, Geomorphological,
and Engineering-Geological Aspects**

**The Role of Water-Rock
Interaction Processes in Soil Formation:
Geochemical, Mineralogical, Geomorphological,
and Engineering-Geological Aspects**

Special Issue Editor in Chief: Carmine Apollaro
Guest Editors: Francesco Perri, Luigi Borrelli,
and Tommaso Caloiero



Copyright © 2019 Hindawi. All rights reserved.

This is a special issue published in "Geofluids." All articles are open access articles distributed under the Creative Commons Attribution License, which permits unrestricted use, distribution, and reproduction in any medium, provided the original work is properly cited.

Editorial Board

Carmine Apollaro, Italy
Baojun Bai, USA
Maurizio Barbieri, Italy
Julien Bourdet, Australia
Andrea Brogi, Italy
David A. Butterfield, USA
Mauro Cacace, Germany
I. Chambeftort, New Zealand
Sh. Nancy Chen, Canada
Paola Cianfarra, Italy
Daniele Cinti, Italy
Timothy S. Collett, USA
Nicoló Colombani, Italy
Mercè Corbella, Spain
Henrik Drake, Sweden
Lionel Esteban, Australia
Cinzia Federico, Italy
Paulo Fonseca, Portugal
Francesco Frondini, Italy
Paolo Fulignati, Italy
Paola Gattinoni, Italy
Mauro Giudici, Italy

Fausto Grassa, Italy
Salvatore Inguaggiato, Italy
Francesco Italiano, Italy
Jaewon Jang, Republic of Korea
Luchao Jin, USA
Shinsuke Kawagucci, Japan
Karsten Kroeger, New Zealand
Cornelius Langenbruch, USA
Huazhou Li, Canada
Liangping Li, USA
Marcello Liotta, Italy
Stefano Lo Russo, Italy
Constantinos Loupasakis, Greece
Lin Ma, USA
Paolo Madonia, Italy
Fabien Magri, Germany
Andrew H. Manning, USA
Micòl Mastrocicco, Italy
John A. Mavrogenes, Australia
Agnes Mazot, New Zealand
Yuan Mei, Australia
Jean-Luc Michelot, France


Ferenc Molnar, Finland
Julie K. Pearce, Australia
Daniele Pedretti, Italy
Marco Petitta, Italy
Christophe Renac, France
Reza Rezaee, Australia
Mohammad Sarmadivaleh, Australia
Christian Siebert, Germany
Ricardo L. Silva, Canada
Ondra Sracek, Czech Republic
Andri Stefansson, Iceland
Pietro Teatini, Italy
Svetlana G. Tessalina, Australia
Rene Therrien, Canada
Umberta Tinivella, Italy
Tivadar M. Tóth, Hungary
Zhenjiang You, Australia
Keni Zhang, China
Ye Zhang, USA
Ling-Li Zhou, Ireland

Contents


The Role of Water-Rock Interaction Processes in Soil Formation: Geochemical, Mineralogical, Geomorphological, and Engineering-Geological Aspects

Carmine Apollaro , Francesco Perri , Luigi Borrelli , and Tommaso Caloiero 
Editorial (4 pages), Article ID 8453136, Volume 2019 (2019)




Geothermal and Mineralogic Analysis of Hot Springs in the Puracé-La Mina Sector in Cauca, Colombia

Darwin Augusto Torres-Ceron , Carlos Daniel Acosta-Medina, and Elisabeth Restrepo-Parra
Research Article (20 pages), Article ID 3191454, Volume 2019 (2019)


Geochemical Characterization of Spring Waters in the Crati River Basin, Calabria (Southern Italy)

Simona Gaglioti, Ernesto Infusino, Tommaso Caloiero , Giovanni Callegari, and Ilaria Guagliardi
Research Article (16 pages), Article ID 3850148, Volume 2019 (2019)



Research on Stability of an Open-Pit Mine Dump with Fiber Optic Monitoring

Tao Zhigang , Zhu Chun , Wang Yong, Wang Jiamin , He Manchao, and Zhang Bo
Research Article (20 pages), Article ID 9631706, Volume 2018 (2019)

Feldspar Dissolution and Its Influence on Reservoirs: A Case Study of the Lower Triassic Baikouquan Formation in the Northwest Margin of the Junggar Basin, China

Meng Xiao , Xuanjun Yuan, Dawei Cheng, Songtao Wu, Zhenglin Cao, Yong Tang, and Zongrui Xie
Research Article (19 pages), Article ID 6536419, Volume 2018 (2019)


Effects of Initial Porosity and Water Pressure on Seepage-Erosion Properties of Water Inrush in Completely Weathered Granite

Jinquan Liu, Weizhong Chen, Taogen Liu, Jianxin Yu, Jingliang Dong , and Wen Nie 
Research Article (11 pages), Article ID 4103645, Volume 2018 (2019)

Study on the Law of Membrane Efficiency of Unsaturated Shale and Its Application

Long Chang , Hongkui Ge , Yinghao Shen , Zehui Huang, and Qian Zhang
Research Article (12 pages), Article ID 2854958, Volume 2018 (2019)

Study of the Corrosion Characteristics of Tunnel Fissures in a Karst Area in Southwest China

Yanjie Zhao, Fugang Wang , Cangsong Li, Yuqing Cao, and Hailong Tian
Research Article (19 pages), Article ID 6234932, Volume 2018 (2019)

Groundwater-Mixing Mechanism in a Multiaquifer System Based on Isotopic Tracing Theory: A Case Study in a Coal Mine District, China

Pinghua Huang  and Xinyi Wang 
Research Article (10 pages), Article ID 9549141, Volume 2018 (2019)

Editorial

The Role of Water-Rock Interaction Processes in Soil Formation: Geochemical, Mineralogical, Geomorphological, and Engineering-Geological Aspects

Carmine Apollaro ¹, **Francesco Perri** ¹, **Luigi Borrelli** ², and **Tommaso Caloiero** ³

¹Department of Biology, Ecology and Earth Sciences (DIBEST), University of Calabria, 87036 Rende CS, Italy

²National Research Council of Italy, Research Institute for Geo-Hydrological Protection (CNR-IRPI), 87036 Rende CS, Italy

³National Research Council of Italy, Institute for Agricultural and Forest Systems in the Mediterranean (CNR-ISAFOM), 87036 Rende CS, Italy

Correspondence should be addressed to Carmine Apollaro; apollaro@unical.it

Received 5 December 2018; Accepted 26 December 2018; Published 10 April 2019

Copyright © 2019 Carmine Apollaro et al. This is an open access article distributed under the Creative Commons Attribution License, which permits unrestricted use, distribution, and reproduction in any medium, provided the original work is properly cited.

The abundance and mobility of minor and trace elements and the thermodynamic considerations on water-rock interaction processes are important in order to characterize the weathering processes affecting the rock masses. The tectonic conditions play a key role for the water circulation in the ground. Thus, the combination of the tectonics of an area with its climatic conditions (in terms of rain amount and types) influences the chemical, mineralogical, and physical transformations of rock masses occurring during weathering processes [1–4]. These changes further affect the stability of rock masses with a considerable decay of their physical-mechanical properties and, thus, can result in the onset of adverse geomorphological consequences [5]. In particular, pedogenetic alteration processes weaken the rock producing thick sequences of weathered materials (residual soils such as saprolites) and a reduction of mechanical properties—due to cycles of wetting-drying, softening, and infiltration of different aqueous solutions—making slopes vulnerable to landslides [6–8]. An in-depth characterization of geotechnical properties and soil thickness may lead to correct decisions in land management, soil erosion estimation, shallow landslide susceptibility assessment, and the design of risk mitigation countermeasures [9, 10]. Moreover, when weathering affects rocks, some naturally occurring potentially harmful elements (e.g., Cr, Ni, Co, and V) become enriched in soils

[11, 12]. In turn, these elements may be extracted from soils and may be concentrated in plant tissues, leading to either their further dispersion in the environment or possible phytoremediation uses. The qualitative interpretation of these phenomena is often insufficient for understanding pedogenetic processes and other processes of interest. Consequently, it is advisable to simulate these processes by geochemical modeling [13, 14], thanks to the availability of both laboratory measurements of dissolution rates for several minerals including silicates, oxides, hydroxides, carbonates, sulphates, phosphates, and sulfides and sufficiently complete and accurate thermodynamic data for numerous minerals, aqueous species, and gases.

This special issue solicits methodological contributions and multidisciplinary case studies on all the aspects of water-rock interaction in soil formation and specifically on the analysis and modeling of pedogenetic alteration processes, also in relation to the chemical characteristics of percolating waters feeding groundwater reservoirs, authigenic solid phases, and the underlying bedrock.

Given the above scenario, the call for papers for publication in this special issue, which was launched in October 2017, is aimed at considering methodological contributions and multidisciplinary case studies on all the aspects of water-rock interaction in soil formation and specifically

on the analysis and modeling of pedogenetic alteration processes, also in relation to the chemical characteristics of percolating waters feeding groundwater reservoirs, authigenic solid phases, and the underlying bedrock.

Potential topics of this special issue included but were not limited to

- (i) geochemical modeling of soil processes
- (ii) groundwater and soil water geochemistry
- (iii) environmental geochemistry
- (iv) climatic variations
- (v) rock-forming minerals containing potentially harmful elements
- (vi) weathering formation processes and rates and landscape evolution
- (vii) soil erosion
- (viii) weathering profile characterization and mapping

From mid December 2017 to late June 2018, a total of 10 papers have been submitted to be considered for publication in the special issue. After rigorous editorial check and peer-review processes which involved external and independent experts in the field, 1 paper was rejected, 1 paper has been withdrawn, and 8 papers have been accepted, with an acceptance rate of 80%. 39 authors from 3 different continents (South America, Europe, and Asia) contributed to the special issue.

In the paper "Groundwater-Mixing Mechanism in a Multiaquifer System Based on Isotopic Tracing Theory: A Case Study in a Coal Mine District, China," P. Huang and X. Wang through a geochemical and isotopic study evaluate the mixing characteristics of various types of groundwater and determine the sources of groundwater and their mixing mechanism in the main aquifers in an environment where the degree of coal mining is becoming increasingly serious.

In the paper "Study of the Corrosion Characteristics of Tunnel Fissures in a Karst Area in Southwest China," Y. Zhao et al. establish the numerical model of the Wulong tunnel (study area) to quantitatively analyze the corrosion range, corrosion ratio, and changes in the permeability and porosity of the fissures in soluble rock of karst areas of the tunnel over the past 100 years. The obtained results, verified by field experiments, show that the main controlling factor of the fissure corrosion of the tunnel in the karst area is the flow rate. The opening of the dead-end pores greatly enhanced the permeability and slightly increased the porosity, which caused the differential corrosion of fissures in the karst area. The simulation model can be used to quantitatively predict the corrosion evolution of a fissure zone within the acceptable range of error.

In the paper "Study on the Law of Membrane Efficiency of Unsaturated Shale and Its Application," L. Chang et al. highlight that the microscopic interaction mechanism between working fluids and shale reservoirs

is the key basic issue for the efficient development of shale gas. In this paper, the characteristics of shale water saturation are considered. The model calculating membrane efficiency is obtained, and the shale membrane efficiency of the reservoir studied, based on the triple-layer model of clay mineral-water interface electrochemistry. Membrane efficiency of unsaturated shale depends on the excess charge density of the surface of the solid in different water saturations. The analysis of factors influencing shale membrane efficiency in unsaturated reservoirs shows that the shale membrane efficiency decreases with the increase of water saturation under unsaturated conditions. The partition coefficient of counterion in the Stern layer, cation exchange capacity, and solute concentration in pore fluid will affect the membrane efficiency of unsaturated shale. The membrane efficiency of the reservoir section shale in Fuling area is calculated and analyzed, and the water-absorbing capacity by chemical osmosis of the reservoir interval shale is evaluated based on the membrane efficiency model of unsaturated shale.

In the paper "Effects of Initial Porosity and Water Pressure on Seepage-Erosion Properties of Water Inrush in Completely Weathered Granite," L. Jinqian et al. used a self-designed large-scale triaxial testing system in order to investigate the effects of water pressure and initial porosity on the mass transfer and flow properties in completely weathered granite. The results indicate that the particle transfer could cause an increase in porosity, permeability, and water inflow, which is the essential reason for water inrush in completely weathered granite. Moreover, due to the effect of particle transfer, the flow properties may change from a Darcy to non-Darcy flow, which is a key signal for water inrush. Finally, with the increasing of water pressure, the transfer mass, permeability, and water inflow increased gradually, and a critical value that caused the water inrush was obtained. Furthermore, with the decreasing of initial porosity, the mass transfer and flow properties were suppressed rapidly, and a critical porosity to anti-inrush was observed.

In the paper "Feldspar Dissolution and Its Influence on Reservoirs: A Case Study of the Lower Triassic Baikouquan Formation in the Northwest Margin of the Junggar Basin, China," M. Xiao et al. investigated feldspar dissolution in the Baikouquan Formation in the northwestern margin of the Junggar Basin (China). Results show that the content of feldspar is high in the conglomerate reservoir of the Baikouquan Formation and that feldspar dissolution in the subaqueous distributary channel of a fan delta plain significantly improves the properties of the reservoir. The authors also evidenced that the strength of feldspar dissolution increases with depth but varies in different sedimentary environments and that in the subaqueous distributary channel, the content of rigid particles, such as quartz and feldspar, is high and has better sorting and higher original physical properties.

In the paper "Geochemical Characterization of Spring Waters in the Crati River Basin, Calabria (Southern Italy)," S. Gaglioti et al. showed the results of a qualitative analysis on about 200 samples of spring waters collected in

the largest catchment of the Calabria region (southern Italy). In particular, several physical and chemical parameters were analyzed and the Langelier-Ludwig diagram was built to evaluate the hydrochemical facies of the sampled waters. Results showed a good quality status of the spring waters in the Crati basin, with a predominant Ca-Mg type hydrochemical facies. Moreover, some peculiarities have been highlighted, in particular, in the Pollino Massif and Mt. Cocuzzo areas which showed high concentrations of almost all the investigated parameters. Finally, through the application of a geostatistic approach, the sampled data were spatially distributed, thus allowing a global overview of the hydrochemical state of natural water springs in the basin.

In the paper “Geothermal and Mineralogic Analysis of Hot Springs in the Puracé-La Mina Sector in Cauca, Colombia,” D. A. Torres-Ceron et al. through a geochemical study of several thermal sources at the Puracé-La Mina sector (Cauca, Colombia) strengthen and determine the potential applications of those thermal waters also in order to contribute to enhance the continental tourism in Colombia. In this work, the authors develop a broad study of several characteristics that allows classifying a great quantity of thermal sources in the Puracé-La Mina sector (Cauca, Colombia) in order to find more suitable applications. The physicochemical analyses show that most of the sources have a sulfated-acid nature which makes them heated vapor waters and volcanic waters, whereas the mineralogical analyses of the rocks exposed to water interaction are mainly characterized by high content of silica isomorphous minerals. This work further shows that these thermal sources are immature waters and still do not reach chemical equilibrium, indicating that the sources have not sufficiently interacted with the rocks.

In the paper “Research on Stability of an Open-Pit Mine Dump with Fiber Optic Monitoring,” T. Zhigang et al. propose monitoring the stability of Dump II within the Nanfen Open-Pit Iron Mine, located in Northeast China, using the fiber optic sensing technology. To pursue this aim, the authors firstly propose a physical model similarity ratio according to the on-site engineering geological survey data. The governing principles of deformation in the shallow dump layers in terms of different heaped loads and rainfall were then determined using fiber optic sensing to conduct an experimental study on the monitoring of the dump stability with an indoor physical mode. Finally, the FLAC3D method was used to simulate the deformation features in the shallow part of Dump II under different heaped load conditions and verify the experimental results of the indoor physical model. The obtained results provide the scientific basis for stability monitoring of similar dumps by detecting the early warning signs of instability phenomena.

Conflicts of Interest

The guest editors declare that they have no conflicts of interest or private agreements with companies.

Acknowledgments

The guest editor thanks all the authors and reviewers for their great contributions and commitment to this special issue.

Carmine Apollaro
Francesco Perri
Luigi Borrelli
Tommaso Caloiero

References

- [1] F. Perri, “Reconstructing chemical weathering during the Lower Mesozoic in the Western-Central Mediterranean area: a review of geochemical proxies,” *Geological Magazine*, vol. 155, no. 4, pp. 944–954, 2018.
- [2] F. Perri, L. Borrelli, S. Critelli, and G. Gullà, “Investigation of weathering rates and processes affecting plutonic and metamorphic rocks in Sila Massif (Calabria, southern Italy),” *Rendiconti Online Societa Geologica Italiana*, vol. 21, pp. 557–559, 2012.
- [3] I. Guagliardi, N. Rovella, C. Apollaro et al., “Effects of source rocks, soil features and climate on natural gamma radioactivity in the Crati valley (Calabria, Southern Italy),” *Chemosphere*, vol. 150, pp. 97–108, 2016.
- [4] F. Perri, F. Ietto, E. Le Pera, and C. Apollaro, “Weathering processes affecting granitoid profiles of Capo Vaticano (Calabria, southern Italy) based on petrographic, mineralogic and reaction path modelling approaches,” *Geological Journal*, vol. 51, no. 3, pp. 368–386, 2016.
- [5] L. Borrelli and G. Gullà, “Tectonic constraints on a deep-seated rock slide in weathered crystalline rocks,” *Geomorphology*, vol. 290, pp. 288–316, 2017.
- [6] F. Ietto, F. Perri, and G. Fortunato, “Lateral spreading phenomena and weathering processes from the Tropea area (Calabria, southern Italy),” *Environmental Earth Sciences*, vol. 73, no. 8, pp. 4595–4608, 2015.
- [7] L. Borrelli, S. Coniglio, S. Critelli, A. La Barbera, and G. Gullà, “Weathering grade in granitoid rocks: the San Giovanni in Fiore area (Calabria, Italy),” *Journal of Maps*, vol. 12, no. 2, pp. 260–275, 2016.
- [8] L. Borrelli, M. Ciurleo, and G. Gullà, “Shallow landslide susceptibility assessment in granitic rocks using GIS-based statistical methods: the contribution of the weathering grade map,” *Landslides*, vol. 15, no. 6, pp. 1127–1142, 2018.
- [9] L. Cascini, M. Ciurleo, and S. Di Nocera, “Soil depth reconstruction for the assessment of the susceptibility to shallow landslides in fine-grained slopes,” *Landslides*, vol. 14, no. 2, pp. 459–471, 2017.
- [10] M. Ciurleo, M. C. Mandaglio, and N. Moraci, “Landslide susceptibility assessment by TRIGRS in a frequently affected shallow instability area,” *Landslides*, vol. 16, no. 1, pp. 175–188, 2019.
- [11] A. Bloise, E. Barrese, C. Apollaro, and D. Miriello, “Flux growth and characterization of Ti- and Ni-doped forsterite single crystals,” *Crystal Research and Technology*, vol. 44, no. 5, pp. 463–468, 2009.
- [12] C. Apollaro, I. Fuoco, G. Brozzo, and R. De Rosa, “Release and fate of Cr(VI) in the ophiolitic aquifers of Italy: the role of Fe(III) as a potential oxidant of Cr(III) supported by reaction

- path modelling,” *Science of The Total Environment*, vol. 660, pp. 1459–1471, 2019.
- [13] C. Apollaro, E. Dotsika, L. Marini et al., “Chemical and isotopic characterization of the thermomineral water of Terme Sibarite springs (Northern Calabria, Italy),” *Geochemical Journal*, vol. 46, no. 2, pp. 117–129, 2012.
- [14] G. Vespasiano, C. Apollaro, F. Muto, E. Dotsika, R. de Rosa, and L. Marini, “Chemical and isotopic characteristics of the warm and cold waters of the Luigiane Spa near Guardia Piemontese (Calabria, Italy) in a complex faulted geological framework,” *Applied Geochemistry*, vol. 41, pp. 73–88, 2014.

Research Article

Geothermal and Mineralogic Analysis of Hot Springs in the Puracé-La Mina Sector in Cauca, Colombia

Darwin Augusto Torres-Ceron ¹, Carlos Daniel Acosta-Medina,²
and Elisabeth Restrepo-Parra¹

¹Laboratorio de Física del Plasma, Universidad Nacional de Colombia, Manizales, Colombia

²Departamento de Matemáticas y Estadística, Universidad Nacional de Colombia, Manizales, Colombia

Correspondence should be addressed to Darwin Augusto Torres-Ceron; dtorresce@unal.edu.co

Received 15 June 2018; Revised 13 September 2018; Accepted 8 November 2018; Published 27 February 2019

Guest Editor: Francesco Perri

Copyright © 2019 Darwin Augusto Torres-Ceron et al. This is an open access article distributed under the Creative Commons Attribution License, which permits unrestricted use, distribution, and reproduction in any medium, provided the original work is properly cited.

Thermal waters are natural resources of great value to geothermal sciences, the tourism industry, and health. In this work, geochemical classification of physicochemical results of 17 sources at the Puracé-La Mina (Cauca, Colombia) sector was implemented in order to strengthen and determine their potential applications and enhance the continental tourism in Colombia. The analyzed parameters were developed following the *Standard Methods* 22nd edition, at Universidad Nacional de Colombia-Manizales. According to the results obtained by means of a geochemical classification, it was found that most of the sources have a sulfated-acid nature which makes them heated vapor waters and volcanic waters. Likewise, it was observed that all the sources are immature waters and still do not reach chemical equilibrium. On the other hand, mineralogical and chemical characterization by means of XRD and XRF showed a high content of silica isomorphous minerals with a low concentration. In addition, the presence of Fe_2O_3 was observed, which is insoluble at $\text{pH} > 5$ and remains in the rock. Nevertheless, considering that mine sources possess $\text{pH} \pm 2$ and temperatures of 40°C , leaching is possible for iron justifying its presence in the water. Instead, elements like Na^+ , K^+ , Mg^{2+} , and Ca^{2+} have high mobility at the conditions of mine sources (low pH) as a consequence of hydrolysis processes, which produce variations in water composition.

1. Introduction

Geothermal processes are directly related to the composition of hot springs giving useful information about the components that affect these hot springs and allowing the evaluation of their applications [1], such as heating, medicinal applications, and bathing [2]. Hot springs can be located around the world in different countries and regions. These different locations make hot springs exhibit a great diversity of geophysical, geochemical, and biological properties depending on the region and the origin of the waters. In this way, rock and mineral chemistry is important in hot spring studies taking into account that information about water-rock interactions can be obtained [3].

These differences make hot springs an interesting area of research for specific biotechnological or ecological applications [4]. For this reason, several studies of hot springs placed

in different countries have been reported in the literature as it is the case of Chabaane et al. [5] who developed a work that attempted to enhance and optimize the potential exploitation of the Hammam Sayala thermal spring in NW Tunisia. Using several electrical techniques, new information of the hydrothermal system in this region was obtained helping to create a therapeutic center for encouraging the regional thermal tourism development [5]. Kikawada et al. [6] performed a geothermometric study of hot spring waters in the Manza area near the Kusatsu-Shirane volcano. These studies might be meaningful for geochemical monitoring of active volcanoes through the changes in the calculated equilibrium temperatures of appropriate minerals for volcanic hot springs.

Apollaro et al. [7] carried out chemical and mineralogical characterization studies in Calabria, south Italy, which were aimed at evaluating the risks posed by pure amianthus (asbestos) tremolite rocks found in Unidad Gimigliano-Monte

Reventino to human health. Results showed high contents of Mn, V, and Cr and a minimal presence of Fe. Traces of Sr, Cu, As, Pb, and Ba were also found in low concentrations. These element contents are in accordance with reports in literature, and some trace metals present in tremolite samples are highly harmful for the human health.

Marini et al. [8] carried out a route model of a reaction focused on simulating exchanges in the water-rock interaction between rain water sediments and local currents during the generation of Ca-HCO₃ waters. This model was made by Marini and Ottonello [9] from data obtained in springs located in Bisagno valley (Italy) in 1996. From these results, the role that calcite plays can be highlighted, which absorbs trace elements of Mn, Zn, Cd, and Co. This is due to the precipitation of calcite which is faster compared to the oxides and hydroxides of clays. Al adsorption of these elements from calcite can present a damper in the long term, which can disturb other processes.

Several reports on hot spring studies in Latin America have been found in Argentina, Brazil, and Mexico. Guido and Campbell [10] developed a study of Jurassic hot spring deposits of the Deseado Massif (Patagonia, Argentina), where they conducted a detailed geological mapping and sample analyses in five different sites that represented the variety of hot spring deposits in the region. With the purpose of observing the possibility of harvesting minerals from Rio Grande (Brazil) volcanic rocks, Ramos et al. [11] carried out studies in chemical and mineralogical characterization. They found that the availability of P, K, and macronutrients like Zn, Cu, Fe, and Mg, was evaluated by means of XRD, XRF, and ICP-MS. On the other hand, a low concentration of Al in aqueous media was evidenced, which is favorable for plants due to the toxicity of this element at high concentrations. Prieto-Barajas et al. [4] explored the diversity of bacterial culture communities residing in hot springs from Araró, México. They also analyzed the effect of seasonality and related changes in physicochemical parameters of spring waters. Physicochemical parameters, measured every season, showed slight variations except for the temperature and arsenic concentration. Then, taking into account that each hot spring has its own characteristics, there is a great interest in performing studies of hot springs in Puracé-La Mina (Cauca, Colombia) to identify their peculiarities.

With this objective in mind, Megyesi [12] reported studies regarding sulfur deposits in the Puracé sector in order to corroborate that mineralization occurs in the porous rocks of andesite and dacite tuffs through fractures impregnated and filled with cold sulfur. On the other hand, in the INGEOMINAS (for its acronym in Spanish: Instituto Colombiano de Geología y Minería) report, Garzón [13] reported studies of geochemical analysis in the Puracé sector, including sources in several sites like Piscina Tabio, La Mina, and Pilimbalá, among others and registered the type of water according to the cations and anions. This study was performed around 20 years ago and, since then, the studied sources could have been affected by several causes such as changes in the weather and the influence of the inhabitants of this region, among others. Consequently, it is necessary to update these studies and add other sources.

It is also of great importance to classify hot springs. Thermal fluids, for instance, can be classified as primary and secondary types. The primary thermal fluids are deep deposits originating from magmatic waters that can undergo changes during their rise to the surface. The secondary thermal fluids are shallow fluids that generally come from the primary fluids. Such fluids can be of several types, including chlorinated, sulfated acid or carbonated fluids [14–18]. Mineral waters emerge to the surface in a natural way [19]. During the rise of the water to the surface, it undergoes compositional changes [17] due to cationic exchange processes, hydrolysis [20], boiling, cooling, and leaching with rocks [16, 21]. The elemental and chemical compositions have been studied by analyzing the mineralogy, finding the water alteration, and observing rocks such as pyrite, elemental sulfur, zeolites, and clays. Chlorite, among others, produces changes in the fluids [16]. Although a classification was carried out to some of these waters and sources, it is necessary to develop a broad study of several characteristics that allows classifying a great quantity of sources in this area in order to find more suitable applications.

It is well known that territories like Puracé-La Mina can have huge potential applications in tourism and sulfur and other mineral harvesting. As a consequence, it is important to consider all the variables in order to evaluate the possibilities of industrial applications in this sector. One of these variables is the quality of water and the presence of minerals in rocks from a physicochemical analysis and mineralogical characterization. The study was divided into three parts, according to the location in the region of Cauca. In this work, geochemical classifications of physicochemical results are carried out in order to strengthen the mineralogical characterization of thermal water in 17 sources of Puracé-La Mina (Cauca, Colombia, South America) to acquire information that contributes to enhancing the continental tourism in Colombia.

2. General Geological Setting

Colombia is located in South America, between the Pacific and Atlantic oceans. Colombia has a wide diversity of geothermal systems (approximately 300) located in the zones of Paipa, Azufral, Ruiz, Chiles, Cumbal, Galeras, Sotará, Doña Juana, Huila, and Puracé UPME (for its acronym in Spanish: Unidad de Planeación Minero Energética) [22, 23]. Puracé is located in the Andean Region of Colombia, southeast of the city of Popayán, Department of Cauca, in the Cordillera Central mountain range (Figure 1). According to Simkin and Institution, the study area is close to the Puracé volcano, which has presented volcanic activity in the last century [24]. According to the reports by Sturchio et al. [25], a detailed geological map of the area has not been made. However, Oppenheim [26] mentions that this volcanic area is a dacitic shield and rises on a metamorphic basement from 2600 to 3800 meters above sea level, covered by a pyroclastic lava andesitic cone [27].

The 17 sources included in this study are shown in Figure 2. In this figure, the studied sites are described according to the reports developed by INGEOMINAS as

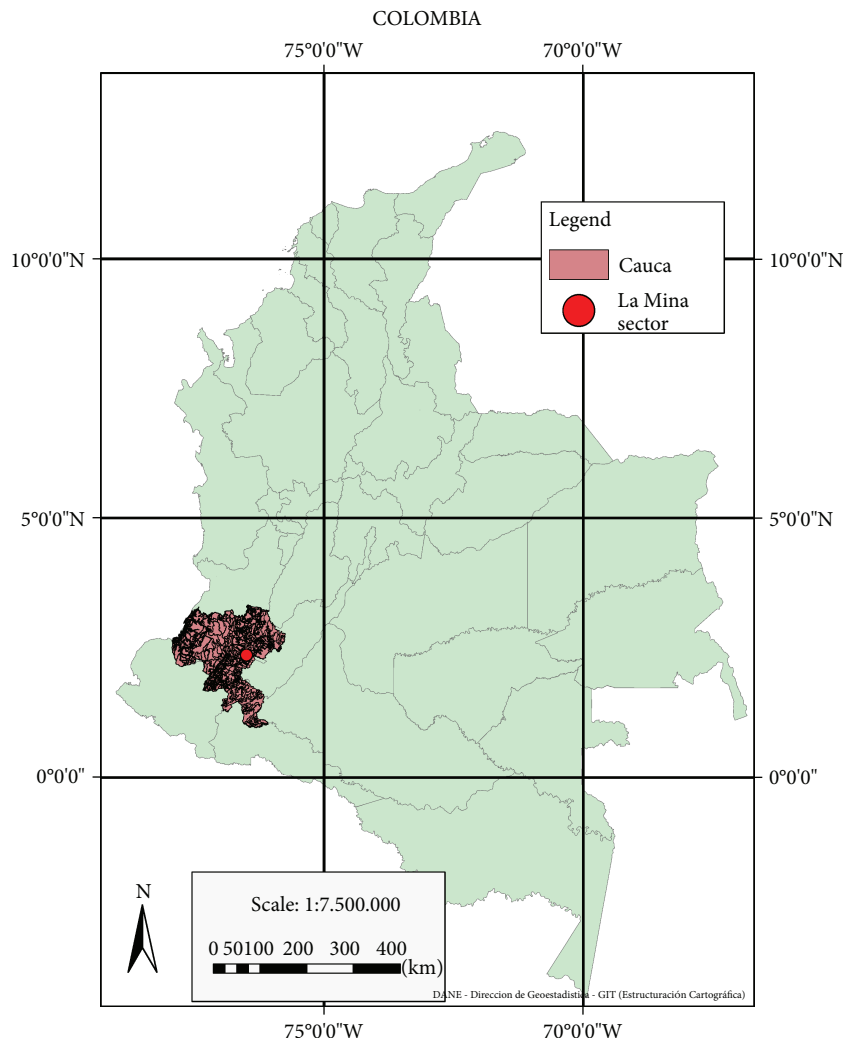


FIGURE 1: Colombian map and location of La Mina sector. Map of the Agustín Codazzi Geographic Institute [54].

follows: COMI (upwellings in La Mina) (Figure 3(a)), COPU (Pululó sector upwellings), COCI (natural waterfall of Ichiago) (Figure 3(b)), COPT (natural upwelling of Puente Tierra (Pilimbala), COTA (upwelling of Piscina Tabio), COPV (water birth of Plan del Vinagre), COSA (waterfall of San Antonio) (Figure 3(c)), and COGU (upwellings of Guarquelló) [13]. Their respective classifications, georeferences, and codifications are listed in Table 1.

3. Sampling and Analysis Methodology

3.1. Sampling. Twelve representative samples of surface manifestations were collected on May 2017 from the geothermal systems of the Puracé-La Mina sector (Table 1) for the analysis of the physicochemical properties of interest. The type of sampling performed was simple or timely. The sampling was carried out in 10-liter containers, with 1-liter graduations. The vessel was purged two or three times, and it was then placed in the flow, measuring the time with a timer. In this way, the parameter $Q = V/t$ was obtained. The flow, Q is given in L/s , where V and t represent the volume and time, respectively. During the sampling, HNO_3 was

added until $pH < 2$ for hardness and metal analyses; pH , temperature, and conductivity parameters were measured for all samples. Titanium and ORP analysis was not carried out in this study.

The seven representative solid samples of the sector were taken on November 2017 in the sources P1-A, P1-B, P2-A, P2-B, P3-A, P3-B, and P10-A for the XRD and XRF analyses.

3.2. Analysis Methodology

3.2.1. Physicochemical Characterization of the Sources. Physicochemical characterization of the sources was carried out in the Water Laboratory at Universidad Nacional de Colombia-Manizales, based on *Standard Methods* 22nd edition [28], and the laboratory is accredited by IDEAM (for its acronym in Spanish: Instituto de Hidrología, Meteorología y Estudios Ambientales) through the ISO standard 17025. Some of the methods of analysis are described as follows: The total hardness was determined by means of the 2340-C EDTA method, with an aliquot of 15 mL at a concentration of 0.01 M of EDTA. Then, 2 mL of ammoniacal buffer solution and 2 drops of eriochrome black indicator were added

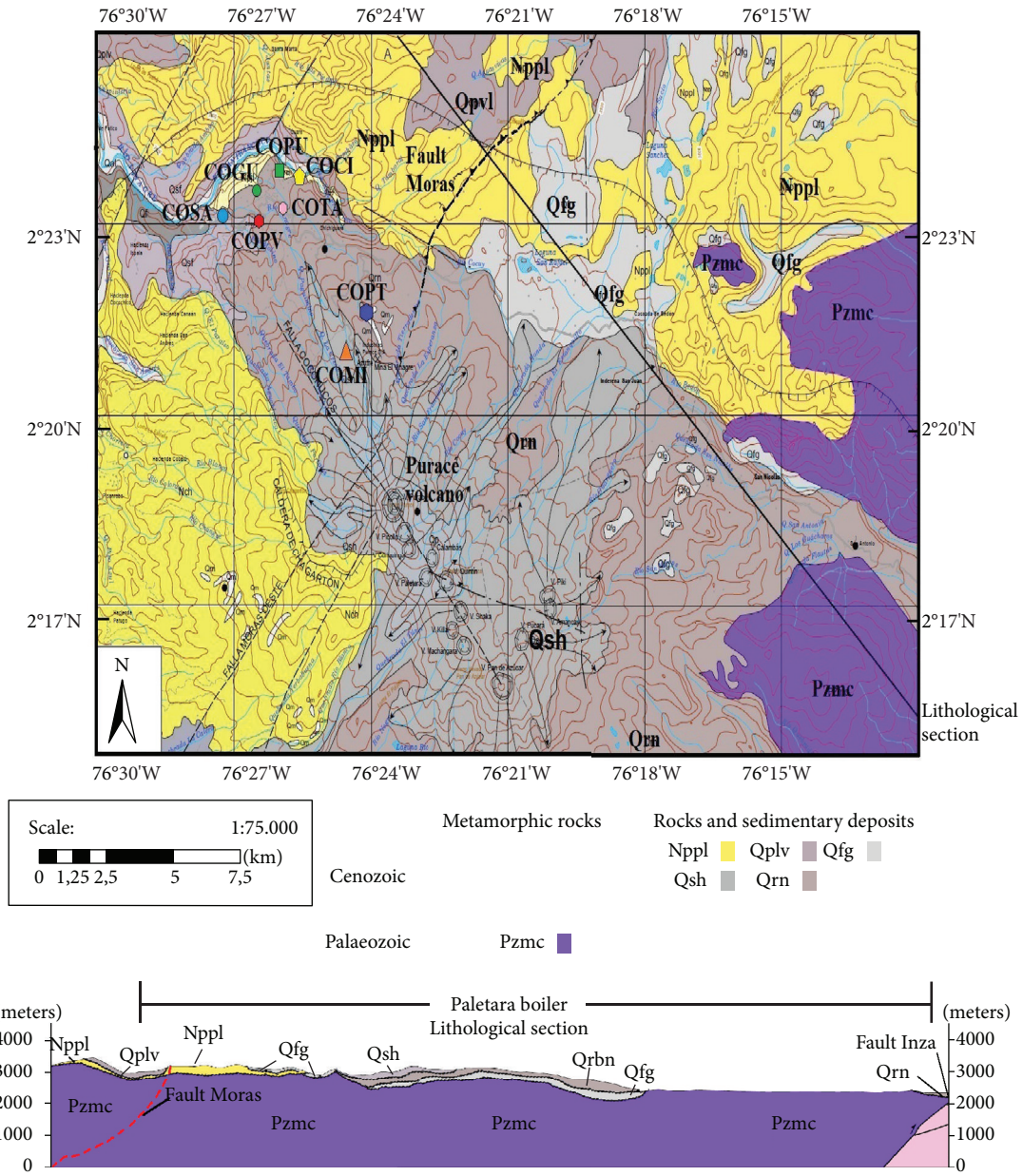


FIGURE 2: Location of the monitoring sites of the Puracé-La Mina sector and lithological section. Map of the Servicio Geológico Colombiano [55]. Nppl (lavas of andesitic compositions), Qplv (ash flow reservoirs), Qfg (fluvioglacial deposits), Qsh (andesitic lava), Qrn (andesitic lava) (Batolito Ibagué), and Pzmc (green and black shales).

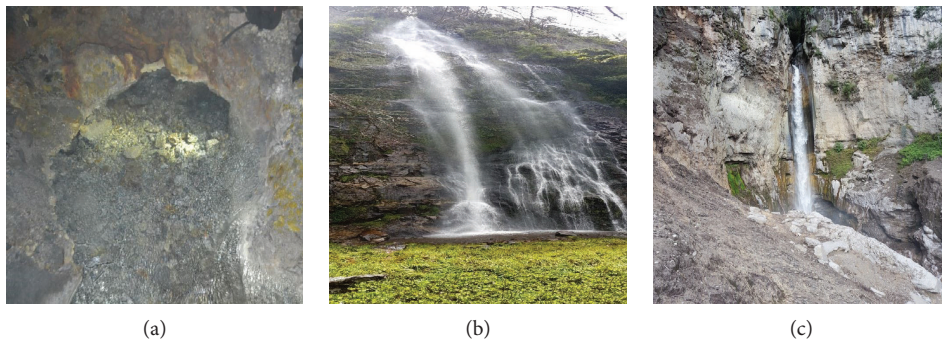


FIGURE 3: (a) Upwelling of the mine placed at approximately 1700 m inside the sulfur mine, (b) waterfall of Ichiago, and (c) waterfall of San Antonio.

TABLE 1: Points of the Puracé-La Mina sector.

Code	Cod.	Source	N	W
COMI	P1	The mine upwelling	2°21'2.2"*	76°24'32.7"*
	P2	Water jet of rock 2 mine		
	P3	Outside of carpentry	2°21'06.8"	076°24'36.1"
	P4	Water jet of soda mine	2°21'2.2"*	76°24'32.7"*
	P5	Water jet of rock 1 mine		
COPU	P6	Upwelling of soda water	2°21'2.2"	76°24'32.7"
	P7	Waterfall of Pululó village	2°23'42.5"	076°25'54.0"
COCI	P8	Waterfall of Ichiago	2°23'38.5"	076°25'23.7"
COPT	P9	Intake tank of natural water of Puente Tierra	2°21'36.9"	076°24'4.9"
	P10	Pool of Puente Tierra	2°21'46.6"	076°24'12.0"
COTA	P11	Tabío, lateral upwelling of pool	2°23'7.1"	076°25'49.5"
	P12	Tabío, behind the pool	2°23'6.8"	076°25'49.7"
COPV	P13	Before the bridge of Rio Vinagre	2°22'55.4"	76°26'17.5"
COSA	P14	Waterfall of San Antonio	2°23'0.6"	76°27'2"
COGU	P15	Upwelling of rock 1 in Guarqueyó	2°23'26.3"	76°26'21.0"
	P16	Upwelling of rock 2 in Guarqueyó	2°23'26.8"	76°26'24.6"
	P17	Upwelling of rock 3 in Guarqueyó	2°23'26.8"	76°26'25.0"

*It is located inside the sulfur extraction mine about 1800 m from the entrance. In the interior, no coordinates were taken; then, the coordinates of the entrance are recorded at a height of 3607 MAMSL (meters above mean sea level). Code, codification (Cod.), source, coordinates refer to 17 sources.

and, finally, it was labeled. The nitrates were determined by means of the 4500-NO₃-B method. The sample was filtered and acidified with 1 mL of HCl, at a concentration of 1.0 M. Afterwards, a calibration curve was obtained plotting the absorbance as a function of the concentration with standards prepared from a certificated NO₃ nitrate standard in a range between 0 and 7 mg-N/L. Finally, the measurement was made using a UV spectrophotometer (Perkin Elmer UV-Vis Spectrometer Lambda 20) with a lambda = 220 nm. The (SO₄)²⁻ ions were determined by means of the 4500 (SO₄)²⁻-E method with 20 mL of buffer solution to a sample of 100 mL. Later, the sample was agitated, and afterwards, BaCl₂ was added and the measurement was made using a turbidimeter. For the Cl⁻ ions, the 4500-Cl-B method was used, where a sample of 100 mL was taken. For those which were too colored, 3 mL of Al(OH)₃ was added. Then, it was filtered, the pH was fixed between 7 and 10, and finally, it was labeled with AgNO₃, using K₂CrO₄ as an indicator. Atomic absorption by flame was employed for metal detection using the iCE 3000 (Thermo Fisher Scientific) equipment; the limits of detection are shown in Table 2. Turbidity was determined by means of the 2130-B. A Metrohm Swiss-made device was used for the pH-L measurements, pH = 4. A Merck buffer solution (citric acid/sodium hydroxide/hydrogen chloride) and Merck pH = 7 buffer solution (disodium hydrogen phosphate/potassium dihydrogen phosphate) were used. Metrohm Swiss-quality titration equipment was used for the multiprobe analysis, and the charge imbalance is carried out using PHREEQC software.

TABLE 2: Atomic absorption by flame.

Metal	Detection limit (ppm)
Fe	0.0043
Al	0.0280
Zn	0.0037
Na	0.0037
K	0.0009
Ca	0.0037
Mg	0.0022
Mn	0.0016

3.2.2. *Mineralogical Characterization.* The mineralogical characterization was carried out in the GMAS⁺ Laboratory, Bogotá, Colombia. For the XRD and XRF analyses, the samples were pulverized and sieved with 63 μm nets at an approximate weight of 2 g.

The mineralogical composition and structural parameters of the rocks were evaluated by XRD with an X-ray diffractometer (Bruker D8 Advance-series I) that was operated at 20 kV and 30 mA, with an X-ray source emitting CoK (1.7890 Å) radiation. The measuring range was from 5 to 70 with a scan speed of 0.3 s/step and a step size of 0.015; a nickel filter was used. The analysis was carried out using the EVA [29] and TOPAS software [30].

For the XRF measurements, the samples were dried at 105°C for 12 hours. Then, spectrometry wax (Merck) was

TABLE 3: Major element concentrations of the geothermal waters from the Puracé-La Mina sector, Cauca, Colombia. Units are in ppm, total hardness (CaCO₃), less than detection limit (<DL), not detectable (ND), and charge imbalance (CI).

Sample	SO ₄	Cl ⁻	Na	K	Ca	Mg	Fe	Mn	Al	HCO ₃ ⁻	CO ₃ ²⁻	CaCO ₃	F ⁻	CI
P1	3242	949	405	72.5	367	286	64.6	8.3	79.4	0.0	0.0	1653	0.1	5:8
P2	3356	1056	348	132	178	240	76.4	11.0	113	0.0	0.0	1890	0.1	16:3
P3	3162	903	260	79.6	283	270	80.4	4.8	119	0.0	0.0	1593	0.1	9:5
P4	3633	1129	375	103	543	377	75.5	12.4	188	0.0	0.0	1930	0.1	5:8
P5	3809	1153	268	87.8	457	316	75.9	13.2	171	0.0	0.0	1930	0.1	8:3
P6	950	218	69.4	16.4	56.3	82.5	5.1	3.0	35.7	0.0	0.0	485	0.1	4:3
P7	969	362	81.1	21.5	62.2	97.6	12.2	3.6	38.8	0.0	0.0	544	0.1	18:2
P8	36.4	1.3	2.3	1.8	3.6	1.9	<IDL	<IDL	IDL	15.2	0.0	19.8	0.0	39:8
P9	7.8	1.3	1.3	1.1	0.9	0.6	0.6	<IDL	IDL	14.0	0.0	10.9	0.0	70:9
P10	156	36.4	18.9	4.8	34.5	13.3	<IDL	0.4	3.1	0.0	0.0	128	0.1	0:3
P11	964	355	110	25.7	74.0	85.2	22.0	3.4	37.4	0.0	0.0	702	0.1	13:6
P12	131	56.5	6.0	5.7	38.6	15.4	3.2	0.7	5.6	0.0	0.0	150	0.1	6:3
P13	117	76.5	23.3	8.1	14.0	26.1	1.8	1.3	15.7	0.0	0.0	178	0.1	16:9
P14	2058	462	128	36.1	104	90.5	92.1	4.6	51.6	0.0	0.0	830	0.1	29:2
P15	934	274	76.2	17.4	61.3	67.9	7.3	3.3	41.2	0.0	0.0	530	0.1	20:4
P16	907	266	70.8	18.8	62.3	81.2	6.7	3.2	40.0	0.0	0.0	470	0.1	16:4
P17	911	256	67.0	18.6	96.4	87.3	8.2	3.2	27.8	0.0	0.0	475	0.1	13:8

added in 10:1 ratio and the samples were homogenized by means of a hydraulic press at 120 kN for one minute until pills of 337 mm diameter were obtained. The XRF semiquantitative analysis was done with the SemiQ 5 software, scanning 11 times with the purpose of detecting all the elements present in the sample excluding H, C, Li, Be, B, N, and O, and the transuranic elements.

4. Results

4.1. Physicochemical Analyses. The physicochemical composition of the 17 sources of the Puracé-La Mina sector are shown in Tables 3 and 4. The sources present mostly acidic pH, but ions of sulfates (up to 3809 ppm) and chlorides (up to 1153 ppm) and a total hardness of up to 1930 ppm are the most predominant. The concentrations of some metals such as Zn and Cr are low or very low and were below the limit of quantification. The sources exhibited maximum and minimum temperatures of 48°C and 9.7°C, respectively.

Table 4 shows that pH values measured in the laboratory were lower than those measured on the site, finding decrements of 2.1 pH units for P8 and P9 sources and ±0.3 pH units for the other sources. This change is attributed to the temperature variations due to transport from the sampling site to the laboratory. As a consequence of this decrease of temperature, a dissociation of (HSO₄)²⁻ ions [31] and secondary ion precipitation were produced [32].

The chemical classification of the 17 sources of the Puracé-La Mina sector, based on the majority of the ions, was represented by Piper (Figure 4) and Stiff diagrams (Figure 5).

Table 5 shows that most of the waters are partially equilibrated with 13 sources (76%), while 3 sources (18%) of

waters were magnesium type, and only one source (6%) was calcium type. Likewise, in the classification of the anions (Table 5), it was observed that 16 sources (94% of waters) were of sulfated type and one source (6%) of partially bicarbonated type, corresponding to the natural water source.

The classification of the 17 sources analyzed in this work was developed according to water type with the following percentages: 4 sources (24%) of sodium chloride and potassium, and sulfate magnesium; 6 sources (35%) of sodium chloride and potassium sulfated magnesium; 2 sources (12%) of sodium chloride and magnesium; 2 sources (12%) of chloride and sulfated calcium, and one source (12%) of mildly sulfated bicarbonate, chloride-type calcium, and sulfated magnesium, respectively.

Taking into account the previous classification, it was observed that the majority of the waters in the Puracé-La Mina sector are of sulfated nature. The sulfated water has an acidic nature with a pH lower than 4. In the studied cases, it was observed that most sources have a pH between 2.15 and 3.93, discarding the sources of COCI and COPT. These waters would correspond to acidic waters heated with vapor, which occurs after the boiling of the thermal waters.

Cl⁻/(SO₄)²⁻ correlation showed R² = 0.98. This ratio of salinity of the COMI source is relatively high in comparison to other sources. Sources with lower salinity are Guarquelló sources (P15, P16, and P17) that possess similar features and moderate salinity. Finally, P8 and P9 are sources with low salinity [33] as is shown in Figure 6(a). Likewise, ratios of Cl⁻/(SO₄)²⁻ under 0.65 indicate that La Mina sector waters are not developing during a long period of time and at a depth enough to react with rock [34]. On the other hand, considering the total ionic salinity [35, 36] (Figure 6(c)), the following observations were made:

TABLE 4: Major element concentrations of the geothermal waters from the Puracé-La Mina sector, Cauca, Colombia. Units are in ppm; laboratory (pH-L), on site (pH-S), suspended solid totals (SST), conductivity (C) (in $\mu\text{S}/\text{cm}$), flow (F) (in L/s), dissolved oxygen (DO), not detectable (ND), less than detection limit (<IDL).

Sample	t ($^{\circ}\text{C}$)	pH-S	pH-L	F	C	SST	Cr	NO_3	NO_2	DO	Si	Zn
P1	47.0	2.21	1.99	22.4	9790	0.5	<IDL	0.3	ND	0.0	45.4	1.0
P2	48.0	2.14	1.89	22.3	11,230	5.0	<IDL	0.3	ND	0.0	48.9	1.2
P3	40.6	2.17	1.93	—	9780	4.0	<IDL	0.3	0.5	0.0	60.6	1.0
P4	40.0	2.27	1.92	0.15	11,650	22.0	<IDL	0.3	ND	0.0	53.7	1.2
P5	36.0	2.15	1.86	10.7	11,710	19.0	<IDL	0.5	0.1	0.0	50.4	1.2
P6	24.4	2.88	2.52	1.8	2660	5.5	<IDL	0.8	0.2	0.0	34.5	0.3
P7	21.3	2.72	2.36	13.7	3160	4.5	<IDL	1.8	0.1	0.0	38.7	0.4
P8	15.3	8.08	5.98	98.3	50.3	1.5	<IDL	0.2	0.5	7.5	7.7	<IDL
P9	9.7	7.81	5.68	11.9	26.2	3.0	<IDL	0.1	1.2	5.5	IDL	<IDL
P10	16.7	3.93	4.16	3.4	391	4.0	<IDL	0.1	ND	1.2	21.5	<IDL
P11	26.6	2.72	2.35	12.1	3900	2.0	<IDL	2.2	2.1	3.0	41.4	<IDL
P12	14.2	3.39	3.15	40.3	604	6.5	<IDL	0.3	ND	6.7	10.8	0.0
P13	16.7	3.70	3.40	3.3	755	2.5	<IDL	0.6	ND	0.0	27.5	0.1
P14	16.9	2.37	2.05	69.3	6490	8.5	<IDL	12.0	2.9	4.6	35.4	0.5
P15	21.7	2.77	2.54	0.1	3010	6.5	<IDL	1.0	0.3	0.0	38.0	0.3
P16	22.3	2.81	2.59	0.9	2710	1.5	<IDL	0.9	1.6	0.0	38.1	0.3
P17	22.0	2.81	2.57	0.7	2830	2.0	<IDL	0.9	ND	0.0	39.3	0.3

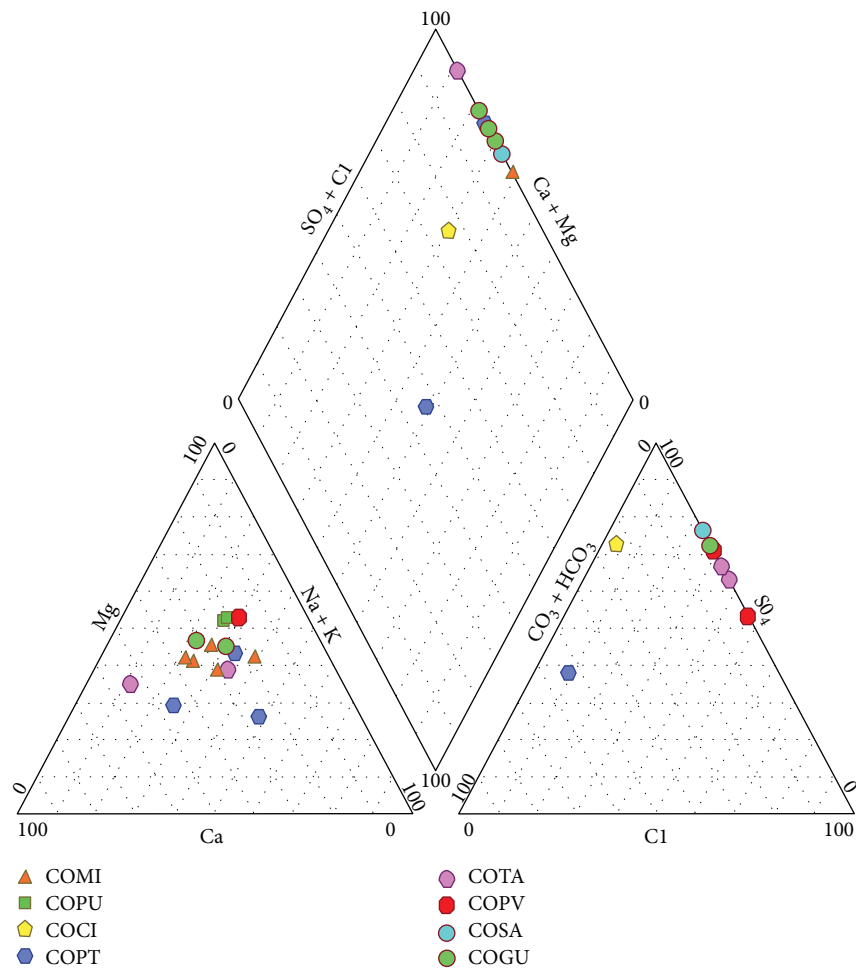


FIGURE 4: Piper diagram showing the hydrochemical compositions of some hot springs in the Puracé-La Mina sector.

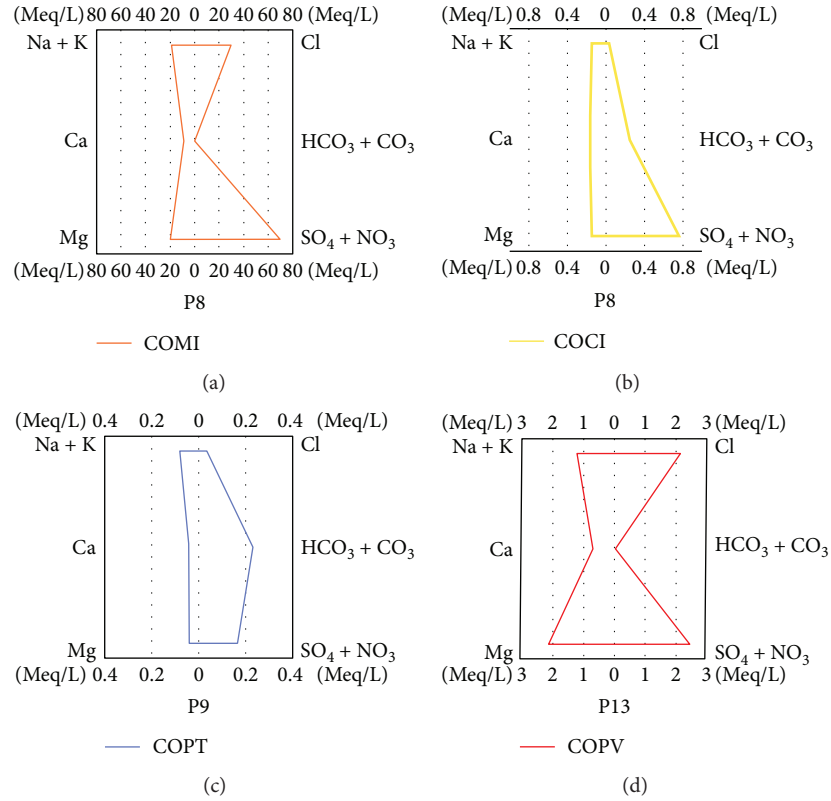


FIGURE 5: Representative Stiff diagrams of the sources of the Puracé-La Mina sector.

- (1) For COMI sources, a TIS between 200 and 250 meq/L is observed, which supposes that chemical features were acquired to depth levels by means of water-rock interaction with smooth rocks and dolomite, although Na/K ratios do not exceed 10 equivalent units
- (2) For the case of other sources, their majority present a TIS between 0 and 100 meq/L, and Na/K ratios are below the COMI ones and do not exceed 7 equivalent units. This low salinity indicates that waters from these sources come from low-depth wells and can be a product of a mixture of cold and warm waters

The high correlation value $R^2 = 0.83$ between $\text{Cl}^-/\text{Ca}^{2+}$ ions confirms the strong presence of chloride-calcium waters. Similarly, high correlations were obtained for Cl^-/Na , Cl^-/K^+ , and $\text{Cl}^-/\text{Mg}^{2+}$ with $R^2 = 0.919$, $R^2 = 0.917$, and $R^2 = 0.954$, respectively, as shown in Figure 6(b). These relationships indicate that soluble salts prevail in most of the sources of the area and that Ca^{2+} and Mg^{2+} are causing hardness in the samples [34, 37].

For the classification of hardness, the following parameters were established by the World Health Organization (WHO): soft type, 0–60; moderately hard, 61–120; hard, 121–180; and very hard, >180 ppm of CaCO_3 , respectively. Based on the results of Table 3, sources in the Puracé-La Mina sector contain two soft-type sources, three hard-type sources and, twelve very-hard-type sources. From this

classification, COMI sources stand out, which have values between 1653.3 and 1930 ppm of CaCO_3 . According to the literature, the mobile elements such as Na, K, Mg, and Ca are the product of the lixiviation of clay minerals such as rhyolites [16, 38], which may be responsible for the high presence of these ions, in the sources in the Puracé-La Mina sector.

4.2. Cl^- , $(\text{SO}_4)^{2-}$, and $(\text{HCO}_3)^-$ Giggensbach Diagram. In Figure 7, all the samples were classified according to the ternary diagram $\text{Cl}^- - (\text{SO}_4)^{2-} - (\text{HCO}_3)^-$ described by Giggensbach in 1988 [39]. In this type of sources, HCl is assumed to be derived from HCl of magmatic origin, $(\text{SO}_4)^{2-}$ from the oxidation of magmatic SO_2 , and HCO_3^- from CO_2 . This anions are generally associated with the acid immature waters of fluids originally magmatic [32, 40].

Most of the sources are sulfated-acid type as it is observed in Figure 4 and Table 5. In Figure 7, the sources are grouped in the volcanic origin sections, which are typical of volcanic geothermal systems associated to volcanos. These sources have low pH value, caused by the Cl^- and $(\text{SO}_4)^{2-}$ ions which, in turn, form a $\text{HSO}_4^-/(\text{SOP})^{2-}$ buffer. During the water-rock interaction process, this system produces higher rock dissolution, generating higher conductivity [14, 41]. In the case of the COMI sources (Figure 5(a)), higher metal concentrations were observed, such as Fe and Si, which in turn produce oxides such as SiO_2 (from minerals like cristobalite, quartz, tridimite, among others) and Fe_2O_3 (pyrite). Those minerals have covalent bonds which are very difficult to break;

TABLE 5: Chemical classification of waters of the Puracé-La Mina sector, according to cations, anions, and water type.

Sample	Cations	Anions	Water type
P1	Partially equilibrated	Sulfated type	Chlorinated sodium and calcium Sulfated sodium and potassium
P2	Partially equilibrated	Sulfated type	Chlorinated sodium and calcium Sulfated sodium and potassium
P3	Partially equilibrated	Sulfated type	Chlorinated sodium and calcium Sulfated sodium and potassium
P4	Partially equilibrated	Sulfated type	Chlorinated sodium and calcium Sulfated sodium and potassium
P5	Partially equilibrated	Sulfated type	Sodium chloride and potassium Sulfated magnesium
P6	Magnesium type	Sulfated type	Sodium chloride and magnesium
P7	Magnesium type	Sulfated type	Sodium chloride and magnesium
P8	Partially equilibrated	Slightly sulfated	Mildly sulfated
P9	Partially equilibrated	Slightly bicarbonated	Mildly bicarbonate
P10	Partially equilibrated	Sulfated type	Chloride and sulfated calcium
P11	Partially equilibrated	Sulfated type	Sodium chloride and potassium Sulfated magnesium
P12	Calcium type	Sulfated type	Chloride and sulfated calcium
P13	Magnesium type	Sulfated type	Sodium chloride and potassium Sulfated magnesium
P14	Partially equilibrated	Sulfated type	Sodium chloride and potassium Sulfated magnesium
P15	Partially equilibrated	Sulfated type	Sodium chloride and potassium Sulfated magnesium
P16	Partially equilibrated	Sulfated type	Sodium chloride and potassium Sulfated magnesium
P17	Partially equilibrated	Sulfated type	Chloride-type calcium and sulfated magnesium

however, since they are sulfated acid with $\text{pH} < 2$, they would favor this dissolution and their high presence, as it is observed in Tables 3 and 4.

On the other hand, the vapors of geothermal systems, which flow through the fractures, heat the underground waters. In this case, it is observed that the P8 (COCI) source is located in heated vapor waters and, as a consequence, it has low concentrations of $(\text{SO}_4)^{2-}$ as it is observed in Figure 5(b). Finally, the P9 (COPT) source belongs to the peripheral waters which are characterized for being waters that, although they have interacted with the rocks, have not reached the equilibrium with these rocks, and they are characterized for having a low contribution of HCO_3^- and a neutral pH, as it is observed in Figure 5(c).

The HCO_3^- and other ionic species originated from the mixture between CO_2 and H_2O . Based on the above, values of 15.2 ppm and 14.0 ppm of HCO_3^- for the P8 and P9 fountains are observed in Table 3. This is because this species is stable at pH between 5.5 and 8.0, and this is the reason why only these two fountains present values of HCO_3^- . In the other fountains, values of 0.0 ppm of HCO_3^- are observed, due to the high temperatures and to the fact that at pH between 3 and 1, the formation of HCO_3^- is inhibited [32]. However, some fountains like P10, P12, P13, and P14 present temperatures below 20°C (Table 4).

4.3. $\text{Na}^+ - \text{K}^+ - \text{Mg}^{2+}$ Diagram. This diagram allows establishing a physicochemical equilibrium between the water-rock interaction and temperatures of the geothermal reservoirs [42], thus allowing the study of the maturity of the waters by means of the principal cations $\text{Na}^+ - \text{K}^+ - \text{Mg}^{2+}$ [39].

Figure 8 shows that all the sources tend to be close to Mg^{2+} , which indicates that the upwellings of the Puracé-La Mina sector are immature waters and that they have not reached the chemical equilibrium. Likewise, Giggenbach mentions that this type of waters is not suitable for evaluating the temperature by means of the Na/K relationship [39]. This indicates that these waters do not interact with the rocks for a sufficient amount of time.

According to the K/Mg geothermometer [39] (equation (1)), it is indicated that, for the sector of COMI and P14, the temperature oscillates between 71.61 and 91.61°C .

$$t = \frac{4410}{13.95 - \log(K^2/\text{Mg})} - 273.15. \quad (1)$$

For subsequent studies, it is recommended to measure the geothermal gradient in order to establish the depth of the reservoir in such a way that more information can be found about the recharge area and the main structures that control the ascent to the surface, since some sources have

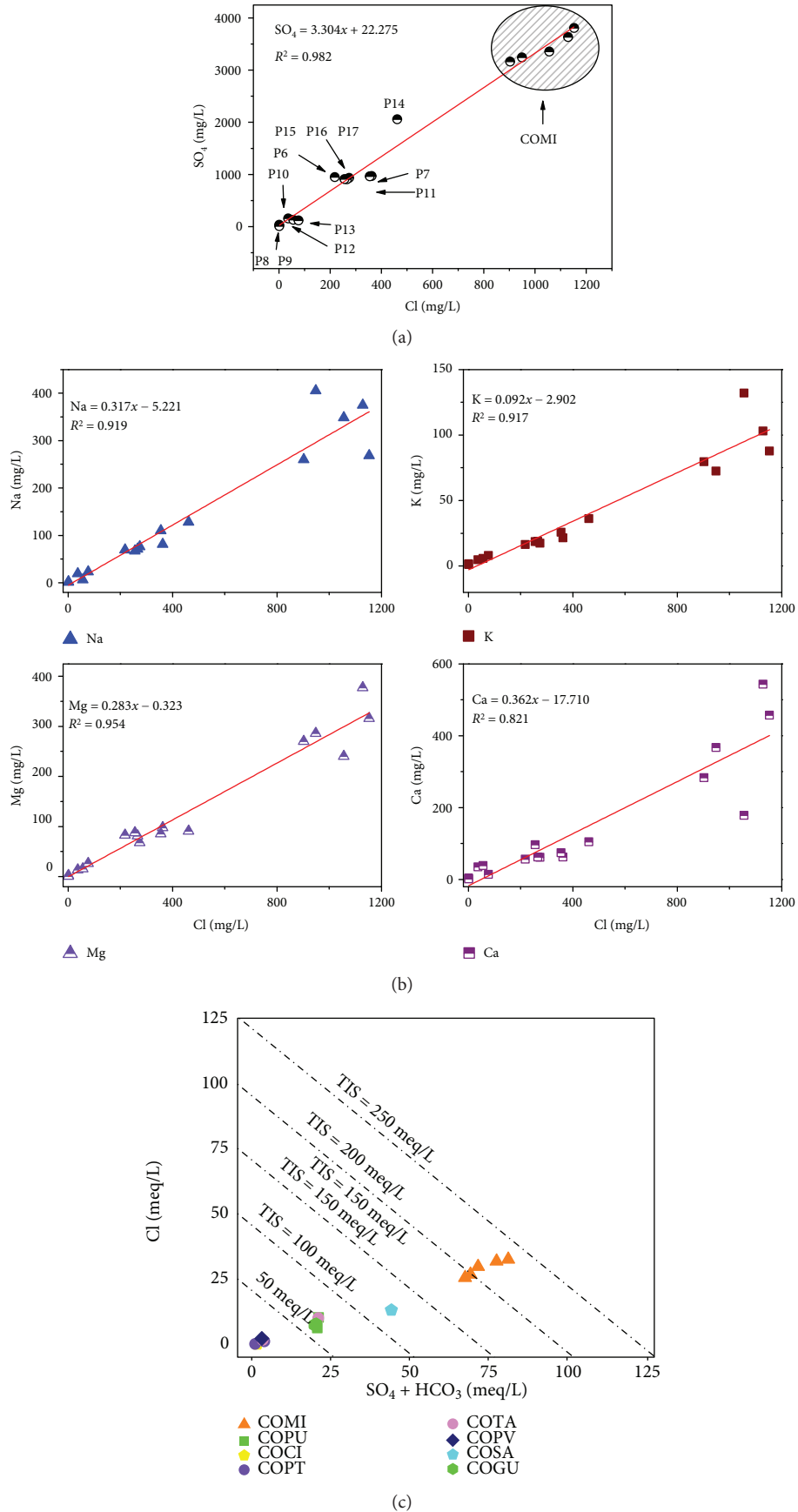


FIGURE 6: Correlation plots: (a) Cl vs SO_4 , (b) Cl vs Na, K, and Mg, and (c) total ionic salinity (TIS) lines.

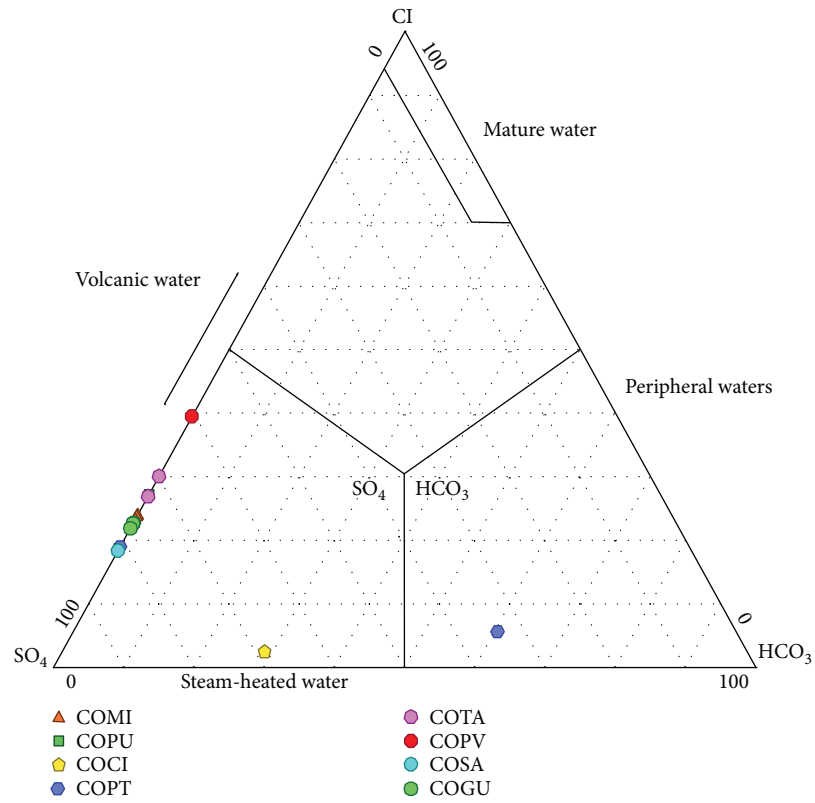


FIGURE 7: Ternary diagram of anions for the sources in Puracé-La Mina [39].

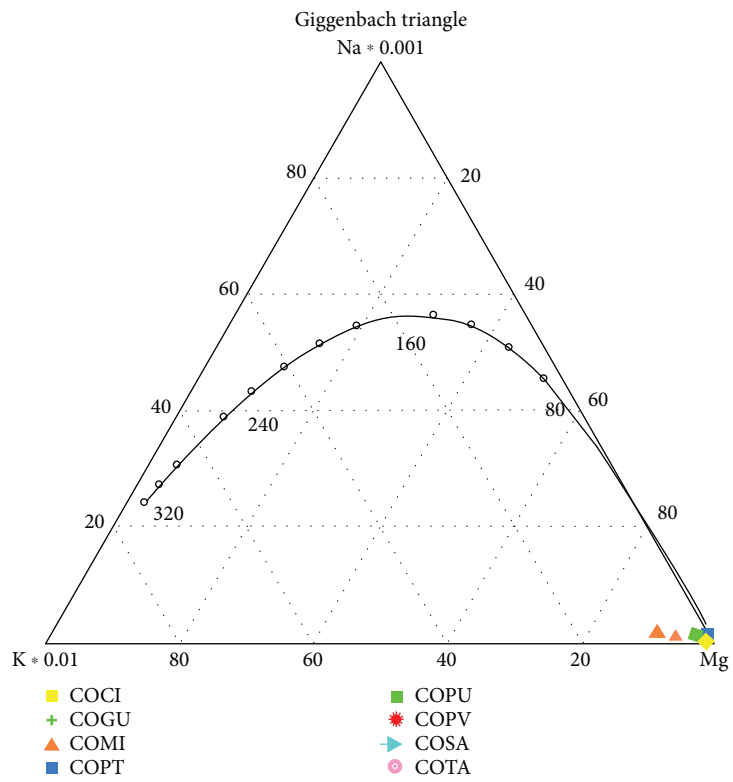


FIGURE 8: Ternary diagram of cations for the sources in Puracé-La Mina [39].

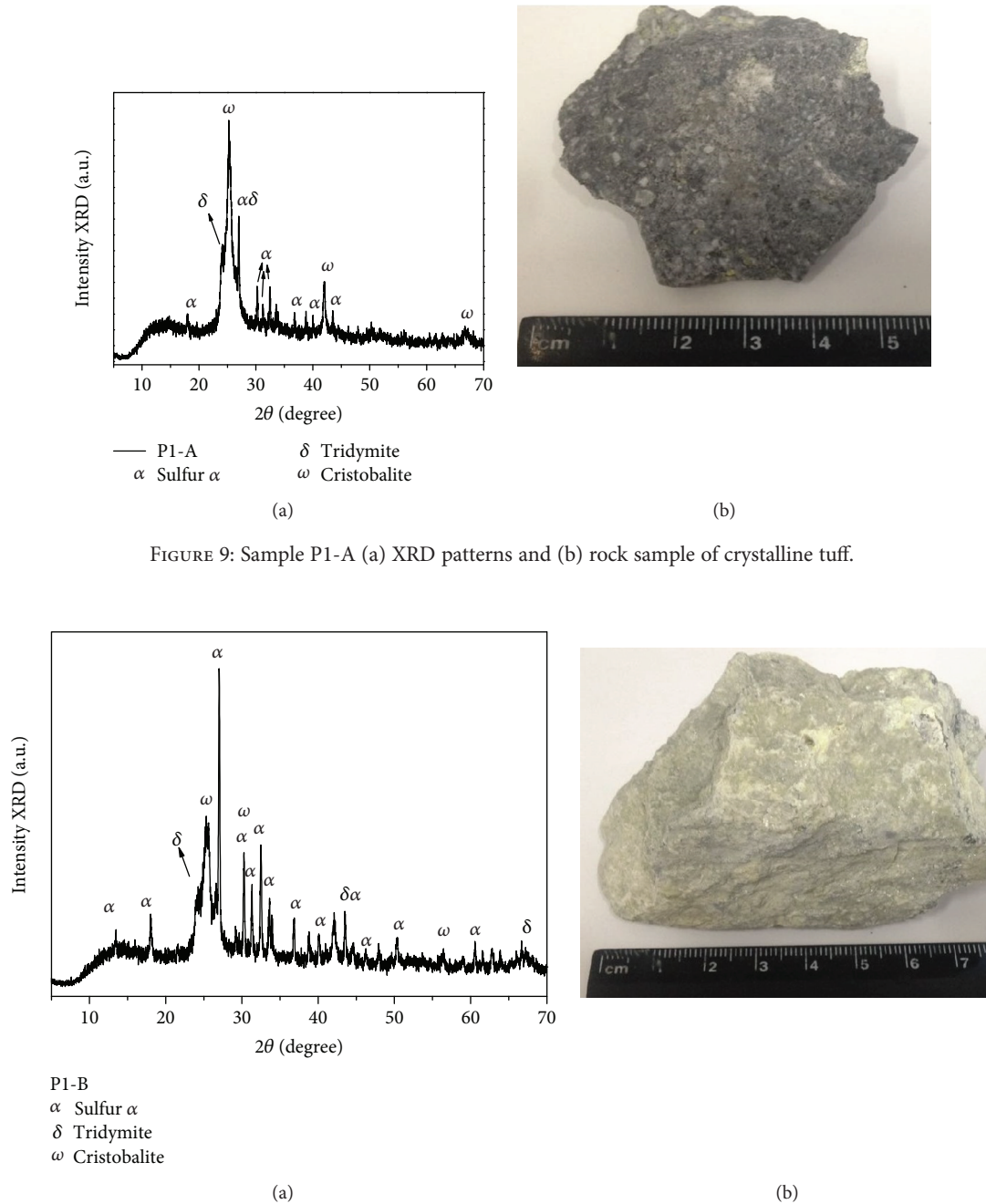


FIGURE 9: Sample P1-A (a) XRD patterns and (b) rock sample of crystalline tuff.

FIGURE 10: Sample P1-B (a) XRD patterns and (b) rock sample of crystalline tuff.

been little studied and this type of studies have not been reported in the literature.

4.4. Mineralogical characterization. XRD results and the analysis of the macroscopic description of the samples show that the P1-A sample (Figures 9(a) and 9(b)) is a dark-gray-colored rock with inlays of white minerals, white subtranslucent, somewhat tabular, light yellow crystals, and lithic black volcanic rock type (crystalline tuff). The P1-B sample (Figures 10(a) and 10(b)) is volcanic ash composed of silica with high sulfur mineralization of volcanic rock type (crystalline tuff). The P2-A sample (Figures 11(a) and 11(b))

is a medium gray to dark-gray-colored rock with silica isomorphs such as cristobalite, tridymite, and sulfur of volcanic rock type (crystalline tuff). The P2-B sample (Figures 12(a) and 12(b)) is a volcanic rock (crystalline tuff) with white and yellow crystals. The P3-A sample (Figures 13(a) and 13(b)) is a volcanic rock (crystalline tuff) with titanium mineralization (black). The P3-B sample (Figures 14(a) and 14(b)) is a volcanic rock (breccia). The P10-A sample (Figures 15(a) and 15(b)) presents a variety of minerals such as cristobalite, tridymite, and albite; the latter being the one present at the highest proportion, and the rock type is a crystalline weathered tu with iron oxides.

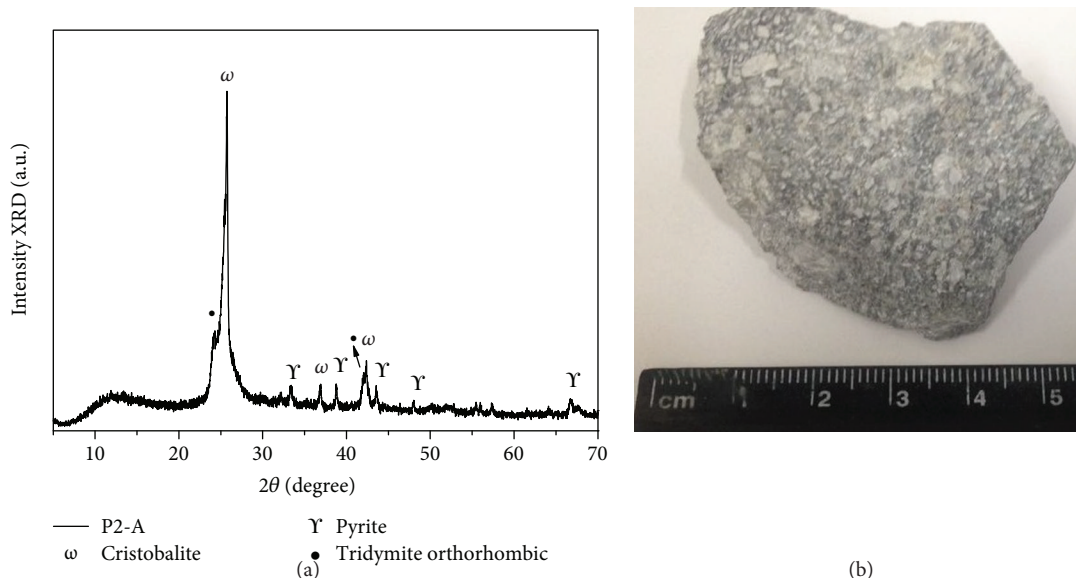


FIGURE 11: Sample P2-A (a) XRD patterns and (b) rock sample of crystalline tuff.

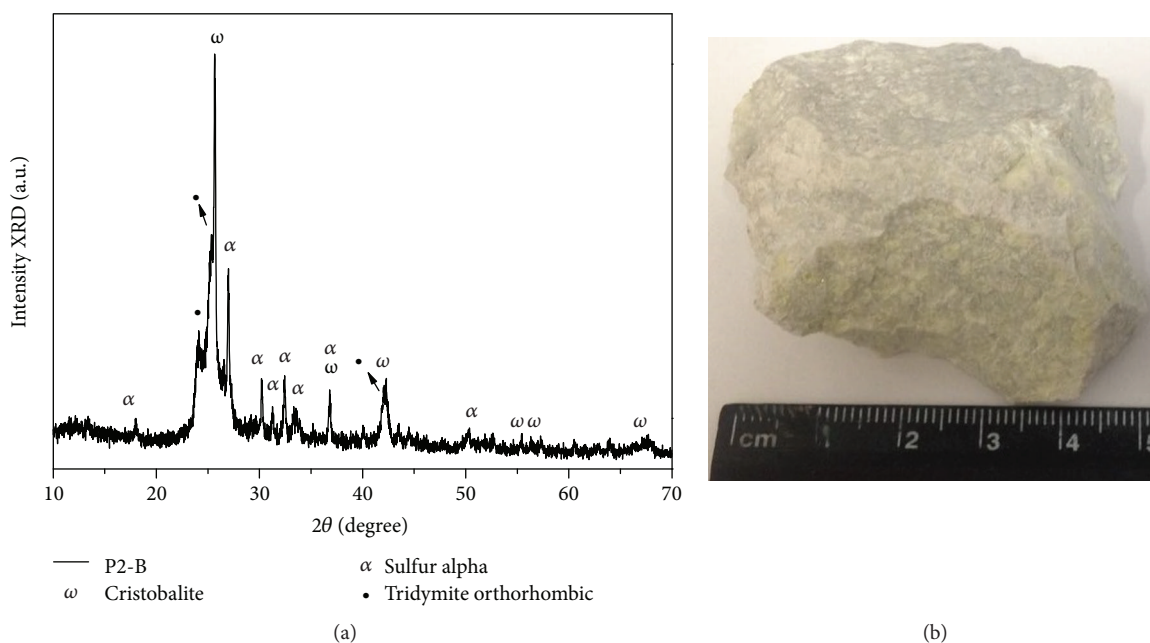


FIGURE 12: Sample P2-B (a) XRD patterns and (b) rock sample of crystalline tuff.

In samples P1, P2, and P3, the presence of a TiO₂ anatase phase is observed. Ramos et al. [43] relate Ti- and Fe-based compounds with the titanomagnetite mineral whose Fe leaching is not favored at pH above 5. However, in sources P1, P2, and P3, with pH values under 2:21 and temperatures of 40°C (Table 4), iron leaching is favored as a consequence of water-rock interaction, generating an increase in the TiO₂ phase in the form of anatase and rutile.

Tables 8 and 7 show that the samples are mostly composed of SiO₂, Al₂O₃, and SO₃. On the other hand, Ti and Fe oxides are observed with concentrations lower

than 81 ppm in the P1, P2, and P3 fountains, and lower than <IDL in P10. As mentioned earlier, Fe solubility is subjected to temperature and mainly to the pH [43]. Titanium analysis was not carried out in this study.

5. Discussion

5.1. Changes in pH and Error Charge Imbalance. Taking into account that the zone of study considered in this work (Puracé-La Mina) presents sources with pH between 2 and 4 for the majority of sources and (SO₄)²⁻ ion as the

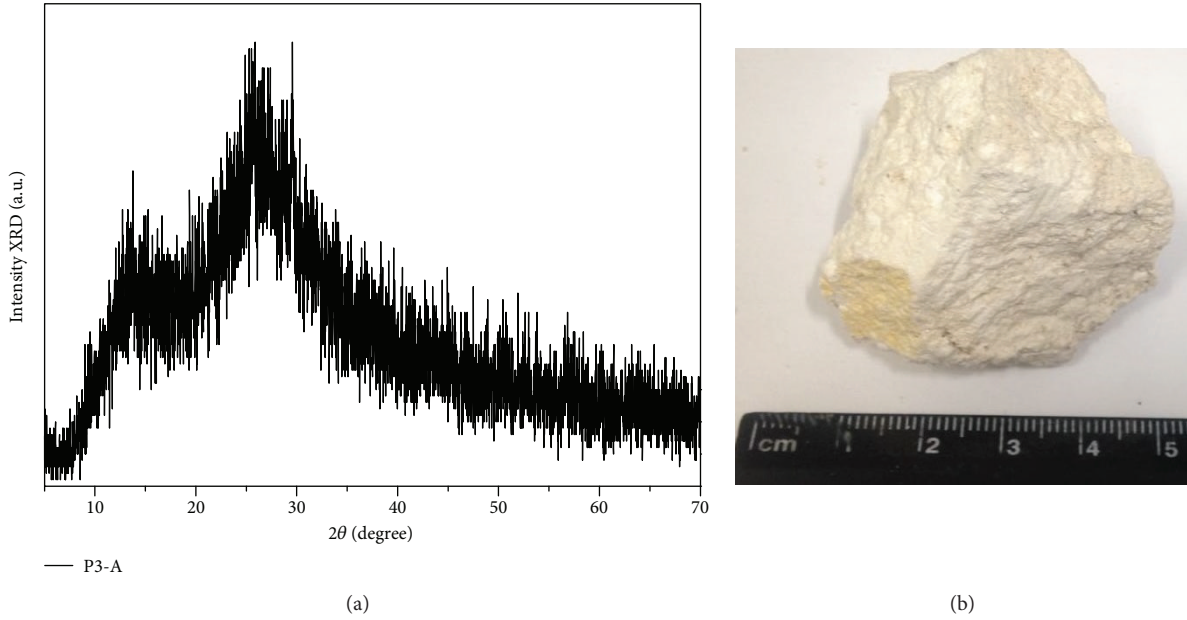


FIGURE 13: Sample P3-A (a) XRD patterns and (b) sample of breccia.

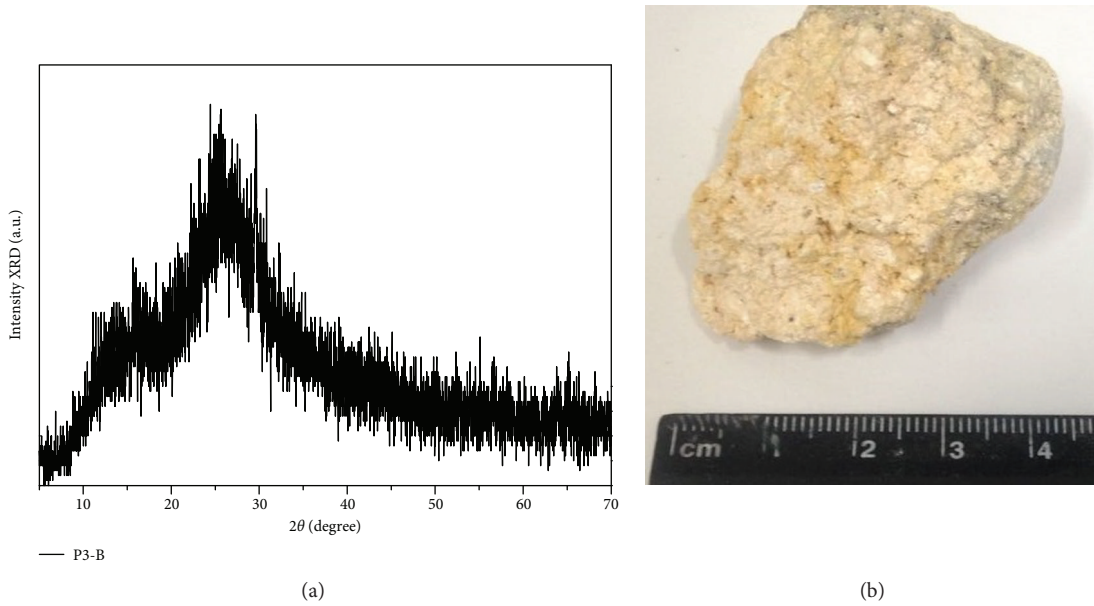
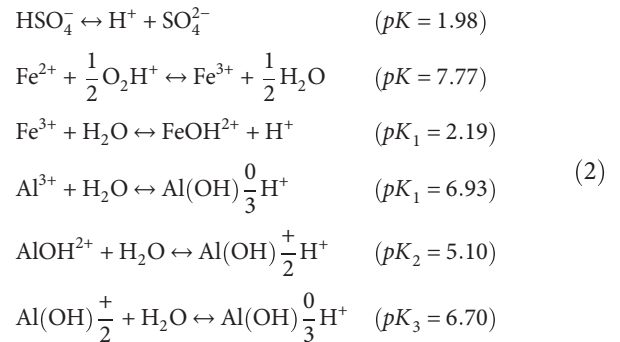


FIGURE 14: Sample P3-B (a) XRD patterns and (b) rock sample of crystalline tuff.

major component, error in charge imbalance can be attributed to the oxidation of compounds and elements as Fe, H_2S , and S_2O_3 , and the degassing of CO_2 and the decrement of temperature. In this case, it is important to consider that during hydrolysis and oxidation reactions processes, free H^+ ion can be considered as a main cation with $\text{pH} < 2.5$. In order to verify the abovementioned results, Nordstrom carried out a test related to how $(\text{S}_2\text{O}_3)^{2-}$ oxidation affected the water chemistry [44]. During this process, it was also observed how the oxidation of thiosulfate would produce considerable amounts of $(\text{SO}_4)^{2-}$ ion, which can result in an important imbalance in ion balance. On the other hand, the increment in temperature can cause a major difference in pH. Additional

to this, it is important to consider the next chemical reactions [44, 45]:



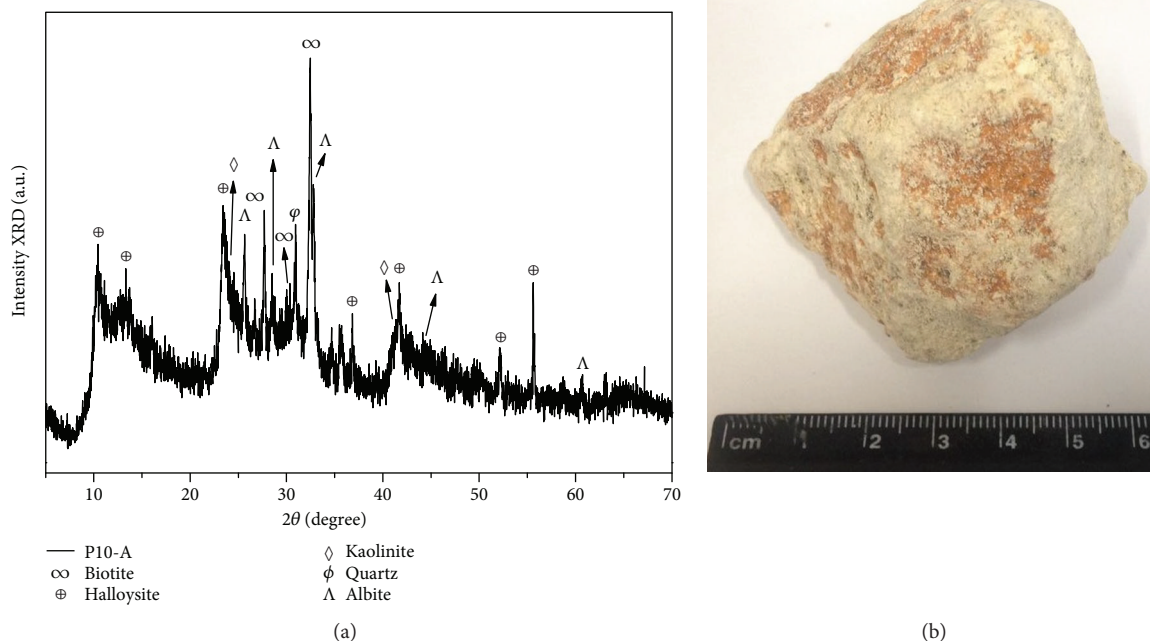


FIGURE 15: Sample P10-A (a) XRD patterns and (b) rock sample of kaolinite (arcillocite).

TABLE 6: Minerals in samples from the Puracé-La Mina sector.

Minerals	Chemical formula	P1-A	P1-B	P2-A	P2-B	P3-A	P3-B	P1O-A
Cristobalite	SiO ₂	48	45	69	43	58	62	—
Tridymite	SiO ₂	32	16	27	32	—	—	—
Sulfur	S	20	39	—	25	—	—	—
Pyrite	Fe ₂ O ₃	—	—	4	—	—	—	—
Gypsum	CaSO ₄ *2H ₂ O	—	—	—	—	24	25	—
Anatase	TiO ₂	—	—	—	—	18	13	—
Quartz	SiO ₂	—	—	—	—	—	—	4
Halloysite	Al ₂ Si ₂ O ₅ (OH) ₄ *2H ₂ O	—	—	—	—	—	—	10
Koalinite	Al ₂ Si ₂ O ₅ (OH) ₄	—	—	—	—	—	—	27
Biotite	K(Mg, Fe) ₃ AlSi ₃ O ₁₀ (OH,F) ₂	—	—	—	—	—	—	8
Albite	NaAlSi ₃ O	—	—	—	—	—	—	51

Finally, when pH < 3, ion H⁺ percentage in meq increases in a such a way that at pH < 2.2, it can represent the 50% in moles of the total ions. In addition, this can lead to an increment in (SO₄)²⁻ concentration approaching the pure H₂SO₄ line and Fe and Al ions are dominant.

Some sources were compared with more recent records reported by INGEOMINAS in the case of the *La Mina 1* source, and similar values are observed in pH (difference of ±0.2), concentration of (SO₄)²⁻, Cl⁻ with sources P1 and P2, with a difference of ±140 ppm, and similarity in the Piper and Stiff diagrams. The Guarquelló source presents similarity (Pipper and Stif diagrams) with the sources P15, P16, and P17. However, an increase in the (SO₄)²⁻ ions is observed, which indicates that during the time elapsed from the taking of the sample and the measurement in the laboratory, there was an increase in the concentration of

(SO₄)²⁻, thus generating an imbalance in the ion charge. Finally, the sources P8 and P9 showed a charge imbalance > 20%, which was due to the addition among ions that was less than 1.5 meq/L.

5.2. Thermal Water. The absorption of magmatic volatile products that prevails in groundwater leads to the formation of reactive substances. In the magmatic vapor phase, SO₂ is one the main components that, when interacting with H₂O, is transformed into H₂S and (SO₄)²⁻ (equation (3)). Then, the oxidation of H₂O to (SO₄)²⁻ by atmospheric CO₂ and gas vapors present in the surface waters lead to the formation of sulfated-acid waters with high concentrations of (SO₄)²⁻ (equation (4)) [32] and Cl⁻ ions [16, 46]. Another issue to take into account, concerning the high concentration of (SO₄)²⁻ ions in the Puracé-La Mina sector, is the closeness

TABLE 7: XRF analysis of La Mina samples (a) P1-A, (b) P1-B, and (c) P2-A.

(a)	
Element compound	P1-A (%) wt
SiO ₂	56.15
SO ₃	41.30
Fe ₂ O ₃	1.74
TiO ₂	0.42
Ba	0.11
Al ₂ O ₃	0.07
Cl	0.06
Ce	0.03
Na ₂ O	0.02
MgO	0.02
CaO	0.02
Cr	0.02
Zr	82 ppm
K ₂ O	81 ppm
MnO	70 ppm
P ₂ O ₅	51 ppm
Nb	48 ppm
Cu	40 ppm
Se	18 ppm

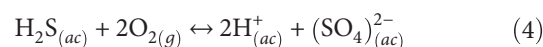
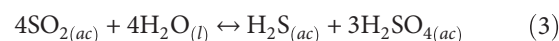
(b)	
Element compound	P1-B (%) wt
SO ₃	72.14
SiO ₂	26.47
Fe ₂ O ₃	0.91
TiO ₂	0.33
Ba	0.07
Al ₂ O ₃	0.03
Cl	0.02
Ce	98 ppm
CaO	77 ppm
W	69 ppm
Zr	46 ppm
Bi	43 ppm
Pb	35 ppm
Cu	22 ppm
Se	20 ppm
Sr	15 ppm
Nb	10 ppm

(c)	
Element compound	P2-A (%) wt
SiO ₂	85.56
SO ₃	9.27
Fe ₂ O ₃	3.50

TABLE 7: Continued.

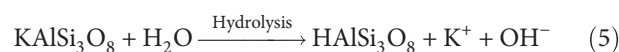
Element compound	P2-A (%) wt
TiO ₂	0.86
Ba	0.25
Al ₂ O ₃	0.22
Cl	0.08
MgO	0.05
Na ₂ O	0.04
CaO	0.03
Cr	0.02
Zr	0.02
Nb	0.02
MnO	0.01
P ₂ O ₅	0.01
K ₂ O	0.01
Pb	80 ppm
Cu	51 ppm
Sr	29 ppm

of the thermal sources to the Puracé volcano, which has been the source of S exploitation.



Taking into account the high solubility of magmatic gases like HCl and HF [47], it can be inferred, based on Table 3, that there is a higher presence of magmatic gases of the HCl type, since the amount of Cl⁻ ions are high.

5.3. *Minerals*. Considering the results shown in Table 6, a great variety of minerals composed of mainly Si, Fe, Ti, Al, and S are observed. In this way, rocks exposed to water can react under several agents being involved with physical and chemical alterations due to water absorption and resulting in the rupture of ionic bonds and hence in rock expansion. Similarly, hydrolysis processes lead to transformations in rocks giving special characteristics to the water. This is the reason why elements like Na, K, Mg, and Ca exhibit high mobility and high concentration due to the leaching of minerals as igneous rhyolite [16, 38]. An example of water-rock interactions is expressed in the following chemical reaction [48]:



Some metals which can be considered as health hazards are found in very low concentrations in both water and rocks including Cr, Zn, Rb, Sr, Ba, Ce, and Se. Some metals are not found in elementary form such as Cr. This element is generally found in the form of chromite (FeCr₂O₄), in the oxidation state Cr⁶⁺ (most toxic form), and in crocoite (PbCrO₄). At pH < 4, its dominant form

TABLE 8: XRF analysis of La Mina samples (a) P2-B, (b) P3-B, and (c) P10-A.

(a)	
Element compound	P2-B (%) wt
SiO ₂	62.34
SO ₃	36.38
TiO ₂	0.63
Al ₂ O ₃	0.19
Fe ₂ O ₃	0.16
Ba	0.09
Na ₂ O	0.06
Cl	0.03
MgO	0.03
CaO	0.02
K ₂ O	0.02
Ce	0.02
Cr	0.01
Zr	0.01
MnO	0.01
P ₂ O ₅	86 ppm
Nb	83 ppm
Sr	22 ppm
Se	13 ppm

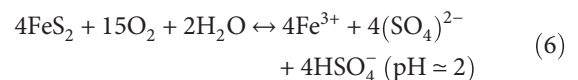
(b)	
Element compound	P3-B (%) wt
SiO ₂	93.44
TiO ₂	3.05
Al ₂ O ₃	1.25
SO ₃	0.97
Fe ₂ O ₃	0.66
Ba	0.23
CaO	0.08
K ₂ O	0.07
MgO	0.06
P ₂ O ₅	0.06
Na ₂ O	0.03
Zr	0.03
Ce	0.02
W	0.02
Cl	0.02
Cr	93 ppm
Pb	64 ppm
Sr	60 ppm
Nb	39 ppm
Cu	38 ppm

(c)	
Element compound	P10-A (%) wt
SiO ₂	53.26
Al ₂ O ₃	35.34
Fe ₂ O ₃	3.42
TiO ₂	2.21
Na ₂ O	1.98
CaO	1.92
K ₂ O	0.66
SO ₃	0.36
Ba	0.33
P ₂ O ₅	0.21
MgO	0.10
Sr	0.06
V	0.05
Zr	0.04
MnO	0.02
Cl	0.02
Cu	0.02
Zn	52 ppm
Nb	37 ppm
Rb	23 ppm

is Cr³⁺ (its less contaminating form). This element generally forms complexes with Cl⁻, OH⁻, F⁻, and (SO₄)²⁻. However, the Cr concentration in waters was below IDL (Table 4) [49].

For the sample P10-A, XRD results showed a high concentration of albite (Table 6). This mineral is mainly composed of Na, Al, Si, O, and traces of Ca. According to the report of Apollaro et al. [50], albite presents high concentrations of metal traces as Sr, Fe, Ba, and Rb, among others; meanwhile, other elements are present in concentrations lower than 10 ppm. In this manner, for the analyzed samples, these metal traces measured by XRF are present in concentrations lower than those reported by Apollaro (Table 8), except Fe, which is present in the form of oxide (3.42%).

Only for a sample corresponding to the P2-A source (Table 6) can the presence of pyrite (Fe₂O₃) be observed as determined by XRD analysis, corresponding to the results obtained from XRF analysis (Tables 7 and 8). On the other hand, in other sources, there is a low percentage of the (Fe₂O₃) phase, as shown in the XRF analysis. Nevertheless, there is no evidence in the results of the XRD analysis of this compound, being an indication that it can be in a low concentration or in an amorphous phase. Pyrite generally reacts with water and oxygen allowing the formation of sulfates [51] as evidenced in the following equation [52, 53]:



The alteration of the minerals, considering the mobility when reacting with the reported water, would be described as follows: $\text{Cl} > \text{SO}_4 > \text{Ca} > \text{Na} > \text{Mg} > \text{K} > \text{SiO}_2 > \text{Fe}_2\text{O}_3 > \text{Al}_2\text{O}_3$. This would explain the high presence of Cl^- and $(\text{SO}_4)^{2-}$ ions in the fountains of the mine (P1, P2, and P3). For example Cl^- , which is in low concentrations according to the XRF analysis, would have higher values in the water analyses [49].

6. Conclusions

The physicochemical characteristics of 17 sources of the Puracé-La Mina sector were analyzed by means of ternary diagrams allowing their classification based on the most representative ions. In this way, it was possible to classify the sources, observing that most of the water analyzed is of sulfated chloride type. These results are consistent with the interpretations of the Piper and Stiff diagrams since most of the sources have an acidic pH due to the high concentrations of $(\text{SO}_4)^{2-}$ and Cl^- ions.

The sources of the Puracé-La Mina are immature waters, and they have not reached the chemical equilibrium yet. This indicates that the sources have not interacted for a sufficient time with the rocks, and the sources have a volcanic origin, which is typical of volcanic geothermal systems associated with volcanoes. The P8 source is placed in heated vapor water with low thermal contributions, and the P9 source belongs to peripheral waters with low thermal contribution.

The correlations of Cl vs Na, K, Mg, and Ca present values of $R^2 > 0.82$, indicating that the soluble salts prevail in the sector and that chloride-calcium type waters also prevail. The correlation of Cl vs SO_4 contains values of $R^2 > 0.98$, and the ratio of Cl/SO_4 is less than 0.65, indicating that the waters of this sector do not interact with sufficiently deep regions to react with the rocks, which is consistent with the diagram of cations that show the immaturity of the waters.

Taking into account the characteristics such as low pH, temperatures $\sim 30^\circ\text{C}$, high concentration of $(\text{SO}_4)^{2-}$, and the geographical location near the Puracé volcano, in the La Mina sector, the error in the charge balance of the sources exceeding 10% is a product of the oxidation of compounds such as Fe, H_2S , and S_2O_3 , the degassing of CO_2 , and the decrease in temperature that generates an increase in H^+ ions, which must be included as the main cation because, according to [44], H^+ ions can represent up to 50% by mole of total ions.

Chemical and mineralogical characterization showed the presence of TiO_2 and Fe_2O_3 that can be associated to the titanomagnetite phase which has no solubility at $\text{pH} > 5$. Nevertheless, some sources of the analyzed territory have pH values in the order of 2 and temperatures of 40°C , which favor iron leaching, justifying the presence of this metal in water for these sources. In this way, the hydrolysis processes are favored at low pH and high temperatures ($>30^\circ\text{C}$), producing transformations in rocks, and hence, elements like Na, K, Mg, and Ca have high mobility and are present in high concentrations in water.

The composition of minerals and lytic oxides of volcanic type rock, crystalline tuff, and breccia are represented by the presence of several isomorphous minerals of silica SiO_2 with accessories like Ti, Zr, and Cr, which are at low concentrations and are not that important to determine the name of the rock.

Data Availability

The data used to support the findings of this study are included within the article. However, any additional information that is required may be acquired from the corresponding author upon request.

Conflicts of Interest

The authors declare that they have no conflicts of interest.

Acknowledgments

The authors gratefully acknowledge the financial support of the Dirección de Investigaciones Manizales (DIMA) Universidad Nacional de Colombia, in the framework of the project for the development of a technological environment “Termacolores in the Puracé Indigenous Reservation” (RIP) for research and innovation in the use of hot springs, mineral waters, and use of natural sulfur aimed at promoting tourism and well-being in the Department of Cauca “Desarrollo de un entorno tecnológico Termacolores en el resguardo indígena Puracé para la investigación e innovación en el uso de aguas termales, aguas minerales y aprovechamiento del azufre natural orientados a potenciar el turismo y bienestar en el Departamento del Cauca.” (in English, “Development of a technological environment Termacolores in the Puracé indigenous reservation for research and innovation in the use of thermal waters, mineral waters, and natural sulfur utilization aimed at promoting tourism and well-being in the Department of Cauca”).

References

- [1] Q. Guo, Z. Pang, Y. Wang, and J. Tian, “Fluid geochemistry and geothermometry applications of the Kangding high-temperature geothermal system in eastern Himalayas,” *Applied Geochemistry*, vol. 81, pp. 63–75, 2017.
- [2] M. Yamada, J. Shoji, S. Ohsawa et al., “Hot spring drainage impact on fish communities around temperate estuaries in southwestern Japan,” *Journal of Hydrology: Regional Studies*, vol. 11, pp. 69–83, 2017.
- [3] F. Perri, L. Borrelli, G. Gullà, and S. Critelli, “Chemical and mineralogical features of plio-pleistocene fine-grained sediments in Calabria, southern Italy,” *Italian Journal of Geosciences*, vol. 133, no. 1, pp. 101–115, 2014.
- [4] C. M. Prieto-Barajas, R. Alfaro-Cuevas, E. Valencia-Cantero, and G. Santoyo, “Effect of seasonality and physicochemical parameters on bacterial communities in two hot spring microbial mats from Araró, Mexico,” *Revista Mexicana de Biodiversidad*, vol. 88, no. 3, pp. 616–624, 2017.
- [5] A. Chabaane, B. Redhaounia, and H. Gabtni, “Combined application of vertical electrical sounding and 2D electrical

- resistivity imaging for geothermal groundwater characterization: Hammam Sayala hot spring case study (NW Tunisia),” *Journal of African Earth Sciences*, vol. 134, pp. 292–298, 2017.
- [6] Y. Kikawada, T. Ono, K. Ogawa, M. Fukai, and T. Oi, “Chemical geothermometry studies on a geothermal system in Manza Hot Springs near Kusatsu-Shirane volcano, Japan,” *Proceedia Earth and Planetary Science*, vol. 17, pp. 253–256, 2017.
- [7] C. Apollaro, I. Fuoco, G. Vespasiano et al., “Geochemical and mineralogical characterization of tremolite asbestos contained in the Gimigliano Mount Reventino Unit (Calabria, South Italy),” *Journal of Mediterranean Earth Sciences*, vol. 10, pp. 5–15, 2018.
- [8] L. Marini, G. Ottonello, M. Canepa, and F. Cipolli, “Water-rock interaction in the Bisagno valley (Genoa, Italy): application of an inverse approach to model spring water chemistry,” *Geochimica et Cosmochimica Acta*, vol. 64, no. 15, pp. 2617–2635, 2000.
- [9] L. Marini and G. Ottonello, *Atlante degli Acquiferi del Comune di Genova*, I Alta Val Bisagno ed Alta Val Polcevera, Pacini, Pisa, 1997.
- [10] D. M. Guido and K. A. Campbell, “Jurassic hot spring deposits of the Deseado Massif (Patagonia, Argentina): characteristics and controls on regional distribution,” *Journal of Volcanology and Geothermal Research*, vol. 203, no. 1–2, pp. 35–47, 2011.
- [11] C. G. Ramos, A. G. De Mello, and R. M. Kautzmann, “A preliminary study of acid volcanic rocks for stonemeal application,” *Environmental Nanotechnology, Monitoring & Management*, vol. 1–2, pp. 30–35, 2014.
- [12] I. Megyesi, “Estudios sobre los depósitos de azufre en la mina de El Vinagre,” *Servicio Geológico Nacional-Ingeominas*, vol. 10, pp. 109–160, 1962.
- [13] G. Garzón, *Catálogo De Fuentes Termales Del Suroccidente Colombiano*, Ingeominas, 1997.
- [14] S. Arnorsson, A. Stefánsson, and J. O. Bjarnason, “Fluid-fluid interactions in geothermal systems,” *Reviews in Mineralogy and Geochemistry*, vol. 65, no. 1, pp. 259–312, 2007.
- [15] H. Ármannsson, “The fluid geochemistry of Icelandic high temperature geothermal areas,” *Applied Geochemistry*, vol. 66, pp. 14–64, 2016.
- [16] J. K. Björke, A. Stefánsson, and S. Arnórsson, “Surface water chemistry at Torfajökull, Iceland—quantification of boiling, mixing, oxidation and water-rock interaction and reconstruction of reservoir fluid composition,” *Geothermics*, vol. 58, pp. 75–86, 2015.
- [17] H. Kaasalainen and A. Stefánsson, “The chemistry of trace elements in surface geothermal waters and steam, Iceland,” *Chemical Geology*, vol. 330–331, pp. 60–85, 2012.
- [18] J. Gunnarsson-Robin, A. Stefánsson, S. Ono, and P. Torssander, “Sulfur isotopes in Icelandic thermal fluids,” *Journal of Volcanology and Geothermal Research*, vol. 346, pp. 161–179, 2017.
- [19] F. Armijo, D. Michele, and M. Giacomino, “Análisis de las aguas minerales de la provincia de Entre Ríos, Argentina,” *El termalismo Argentino*, vol. 4, pp. 55–84, 2008.
- [20] M. Corral, J. López, I. Muñoz, and G. Luis, *Estudio de la Relación entre los Componentes Físico-Químicos de las Aguas Minerales y las Características Geológicas de Galicia*, Instituto Geológico y Minero de España, 2006.
- [21] D. Chandrasekharam and J. Bundschuh, *Low-Enthalpy Geothermal Resources for Power Generation*, CRC Press, Leiden, 2008.
- [22] Unidad de Planeación Minero Energética, “Utilización de la Energía Geotérmica Documento Descriptivo,” *Formulación de un programa básico de normalización para aplicaciones de energías alternativas y difusión*, p. 49, 2003.
- [23] E. Lozano, “Hot springs and geothermal energy in Colombia,” *Geothermics*, vol. 17, no. 2–3, pp. 377–379, 1988.
- [24] T. Simkin and S. Institution, *Volcanoes of the World: A Regional Directory, Gazetteer, and Chronology of Volcanism During the Last 10000 Years*, Hutchison Ross Publishing Company, 1981, https://books.google.com.co/books?id=G8_BU6H-RpUC.
- [25] N. C. Sturchio, S. N. Williams, and Y. Sano, “The hydrothermal system of Volcan Purace, Colombia,” *Bulletin of Volcanology*, vol. 55, no. 4, pp. 289–296, 1993.
- [26] V. Oppenheim, “The Volcano Purace,” *American Journal of Science*, vol. 248, no. 3, pp. 171–179, 1950.
- [27] J. J. Monsalve, Z. I. Galarza, M. Zuluaga, and C. A. Laverde, “Mapa de amenaza volcánica del volcán puracé actual (Cauca Colombia) segunda versión (2014). Memoria Bogotá, Octubre de 2014 proyecto investigación y monitoreo de la amenaza volcánica dirección de geoamenazas mapa de amenaza volcánica del volcán puracé,” Tech. Rep. Servicio Geológico Colombiano, Bogotá, 2014, https://www2.sgc.gov.co/sgc/volcanes/VolcanPurace/Documents/Memoria_MapaAmenaza_Purace.pdf.
- [28] APHA, “Standard methods for examination of water and wastewater,” pp. 5–16, 1998, <https://store.awwa.org/store/productdetail.aspx?productid=28493774>.
- [29] A. X. S. Bruker, *EVA*, Software, Karlsruhe, Germany, 2001.
- [30] A. C. Coelho, *TOPAS Academic*, Software, Brisbane Australia, 2007.
- [31] C. H. Gammons, S. A. Wood, F. Pedrozo et al., “Hydrogeochemistry and rare earth element behavior in a volcanically acidified watershed in Patagonia, Argentina,” *Chemical Geology*, vol. 222, no. 3–4, pp. 249–267, 2005.
- [32] M. A. Gaviria Reyes, M. R. Agosto, M. A. Trinelli, A. T. Caselli, M. dos Santos Afonso, and S. Calabrese, “Estudio hidrogeoquímico de las áreas termales del complejo volcánico Copahue Cavihue,” *Revista de la Asociación Geológica Argentina*, vol. 73, no. 2, pp. 256–269, 2016.
- [33] B. Ladouche and P. Weng, “Hydrochemical assessment of the Rochefort marsh. Role of surface and groundwater in the hydrological functioning of the wetland,” *Journal of Hydrology*, vol. 314, no. 1–4, pp. 22–42, 2005.
- [34] F. Bahri, H. Saibi, and M.-E.-H. Cherchali, “Characterization, classification, and determination of drinkability of some Algerian thermal waters,” *Arabian Journal of Geosciences*, vol. 4, no. 1–2, pp. 207–219, 2011.
- [35] C. Apollaro, G. Vespasiano, F. Muto, R. de Rosa, D. Barca, and L. Marini, “Use of mean residence time of water, flow rate, and equilibrium temperature indicated by water geothermometers to rank geothermal resources. Application to the thermal water circuits of Northern Calabria,” *Journal of Volcanology and Geothermal Research*, vol. 328, pp. 147–158, 2016.
- [36] G. Vespasiano, C. Apollaro, F. Muto, E. Dotsika, R. de Rosa, and L. Marini, “Chemical and isotopic characteristics of the warm and cold waters of the Luigiane Spa near Guardia Piemontese (Calabria, Italy) in a complex faulted geological framework,” *Applied Geochemistry*, vol. 41, pp. 73–88, 2014.

- [37] M. E. Soltan, "Characterisation, classification, and evaluation of some ground water samples in upper Egypt," *Chemosphere*, vol. 37, no. 4, pp. 735–745, 1998.
- [38] E. P. Joseph, N. Fournier, J. M. Lindsay, and T. P. Fischer, "Gas and water geochemistry of geothermal systems in Dominica, Lesser Antilles island arc," *Journal of Volcanology and Geothermal Research*, vol. 206, no. 1-2, pp. 1–14, 2011.
- [39] W. F. Giggenbach, "Geothermal solute equilibria. Derivation of Na-K-Mg-Ca geothermometers," *Geochimica et Cosmochimica Acta*, vol. 52, no. 12, pp. 2749–2765, 1988.
- [40] W. F. Giggenbach, "Relative importance of thermodynamic and kinetic processes in governing the chemical and isotopic composition of carbon gases in high-heatflow sedimentary basins," *Geochimica et Cosmochimica Acta*, vol. 61, no. 17, pp. 3763–3785, 1997.
- [41] H. Ármannsson, "Application of geochemical methods," in *Short Course VII on Exploration for Geothermal Resources*, pp. 1–8, Elsevier B.V., 2007.
- [42] X. Wang, G. L. Wang, H. N. Gan, Z. Liu, and D. W. Nan, "Hydrochemical characteristics and evolution of geothermal fluids in the Chabu high-temperature geothermal system, Southern Tibet," *Geofluids*, vol. 2018, Article ID 8532840, 15 pages, 2018.
- [43] C. G. Ramos, X. Querol, M. L. S. Oliveira, K. Pires, R. M. Kautzmann, and L. F. S. Oliveira, "A preliminary evaluation of volcanic rock powder for application in agriculture as soil a remineralizer," *Science of the Total Environment*, vol. 512-513, pp. 371–380, 2015.
- [44] D. Kirk Nordstrom, R. Blaine McCleskey, and J. W. Ball, "Sulfur geochemistry of hydrothermal waters in Yellowstone National Park IV acid sulfate waters," *Applied Geochemistry*, vol. 24, no. 2, pp. 191–207, 2009.
- [45] D. K. Nordstrom and D. G. Archer, "Arsenic thermodynamic data and environmental geochemistry," in *Arsenic in Ground Water* pp. 1–25, Kluwer Academic Publishers, Boston.
- [46] J. Wrage, D. Tardani, M. Reich et al., "Geochemistry of thermal waters in the Southern Volcanic Zone, Chile—implications for structural controls on geothermal fluid composition," *Chemical Geology*, vol. 466, pp. 545–561, 2017.
- [47] M. Agosto, F. Tassi, A. T. Caselli et al., "Gas geochemistry of the magmatic hydrothermal fluid reservoir in the Copahue Cavihue Volcanic Complex (Argentina)," *Journal of Volcanology and Geothermal Research*, vol. 257, pp. 44–56, 2013.
- [48] N. C. Brady and R. R. Weil, "Organisms and Ecology of the Soil," *The nature and properties of soil*, vol. 11, pp. 328–360, 1996.
- [49] V. T. Sepulveda, D. A. d. I. R. Pérez, and J. A. Velasco Trejo, "Summary for policymakers," *Climate Change 2013—The Physical Science Basis: Working Group I Contribution to the Fifth Assessment Report of the Intergovernmental Panel on Climate Change*, Intergovernmental Panel on Climate Change, Ed., Cambridge University Press, Cambridge, 2005.
- [50] C. Apollaro, L. Marini, T. Critelli et al., "Investigation of rock-to-water release and fate of major, minor, and trace elements in the metabasalt–serpentine shallow aquifer of Mt. Reventino (CZ, Italy) by reaction path modelling," *Applied Geochemistry*, vol. 26, no. 9-10, pp. 1722–1740, 2011.
- [51] L. F. O. Silva, M. Izquierdo, X. Querol et al., "Leaching of potential hazardous elements of coal cleaning rejects," *Environmental Monitoring and Assessment*, vol. 175, no. 1–4, pp. 109–126, 2011.
- [52] J. D. Rimstidt and D. J. Vaughan, "Pyrite oxidation: a state-of-the-art assessment of the reaction mechanism," *Geochimica et Cosmochimica Acta*, vol. 67, no. 5, pp. 873–880, 2003.
- [53] K. Sasaki, "Raman study of the microbially mediated dissolution of pyrite by *Thiobacillus ferrooxidans*," *The Canadian Mineralogist*, vol. 35, no. 4, pp. 999–1008, 1997.
- [54] G. de Colombia, "IGAC Geoportal," <http://ssiglwps.igac.gov.co/ssigl2.0/visor/galeria.req?mapaId=57>.
- [55] Servicio Geológico Colombiano, "Mapa Geológico de Colombia PLANCHA 365 Coconuco," <https://www2.sgc.gov.co/ProgramasDeInvestigacion/Geociencias/Paginas/MapaGeologico.aspx>.

Research Article

Geochemical Characterization of Spring Waters in the Crati River Basin, Calabria (Southern Italy)

Simona Gaglioti,¹ Ernesto Infusino,¹ Tommaso Caloiero ,² Giovanni Callegari,² and Iaria Guagliardi²

¹University of Calabria-Department of Environmental and Chemical Engineering (DIATIC), 87036 Rende (CS), Italy

²National Research Council of Italy-Institute for Agricultural and Forest Systems in the Mediterranean (CNR-ISAFOM), 87036 Rende (CS), Italy

Correspondence should be addressed to Tommaso Caloiero; tommaso.caloiero@isafom.cnr.it

Received 16 May 2018; Revised 19 September 2018; Accepted 18 November 2018; Published 3 February 2019

Academic Editor: Paulo Fonseca

Copyright © 2019 Simona Gaglioti et al. This is an open access article distributed under the Creative Commons Attribution License, which permits unrestricted use, distribution, and reproduction in any medium, provided the original work is properly cited.

The characterization of the spatial variation of geochemical parameters in spring waters, especially the ones used for drinking purpose, is essential to identify potential risks to humans. In this work, results of a qualitative analysis on 190 samples of spring waters collected in the largest catchment of the Calabria region (southern Italy) are shown. Several physical and chemical parameters were analysed and the Langelier-Ludwig diagram was built to evaluate the hydrochemical facies of the sampled waters. Additionally, the relationships between water temperature and altitude and electric conductivity (EC) and altitude were assessed. Geostatistical methods were used to map the physical and chemical parameters. Results showed a good quality status of the spring waters in the Crati basin, with a predominant Ca-Mg-type hydrochemical facies. Then, a connection between EC and temperature with elevation has been detected in some area of the basin. Finally, the spatial analysis allowed identifying the distribution of the concentration of the several parameters.

1. Introduction

Water is the most essential element for the existence of life on Earth, which is becoming increasingly precious during the last decades. In fact, water quality issues are one of the major challenges that humanity is facing in the twenty-first century considering safe drinking water the basic need for every citizen. About 80% of the diseases in the world and one-third of the deaths in the developing countries are caused by contaminated water [1]. In particular, the groundwater is the main source for drinking purposes, sanitary uses, irrigation, and industrial processes. A good management of this resource is very important especially in some areas such as the Mediterranean basin, which is located in a transition zone between North Africa (arid climate) and central Europe (temperate and rainy climate), which is affected by the interaction between midlatitude and tropical processes and which can be considered as potentially vulnerable to climatic changes [2]. In fact, groundwater quality is getting deteriorated also

due to climate changes which cause low rainfall and high evapotranspiration [3]. Groundwater quality in a region largely depends on natural processes, like dissolution and precipitation of minerals, groundwater velocity, quality of recharge waters and interaction with other types of water aquifers, and weathering and catchment erosion [4, 5], and on anthropogenic inputs including urbanization, agricultural, and industrial activities. Among the natural factors, geology of the catchment area, degree of chemical weathering of the various rock types, and inputs from sources other than water-rock interaction play a significant role in controlling the chemistry of the water [6–9]. In the last decades, numerous studies have been published about major ions, trace elements, and potentially harmful elements in the water [10–12], giving information about the possible geological and anthropogenic influences on aquifers [13–20]. In fact, by analysing different physical and chemical parameters it is possible to understand the behaviour of groundwater in relation with the lithologies present in each area. High pH and

EC values characterize waters coming from carbonate aquifer where the long-time contact with limestones, dolostones, gypsum, and anhydrite make them alkaline as well as for those from the siliciclastic rocks (in particular calcium-, magnesium-, or iron-rich reservoirs) which present high capacity of CO₂ mineral trapping [21]. Erosion of rocks (e.g., limestone and dolomite) and minerals (e.g., calcite and magnesite) is the most common source of calcium and magnesium [21]. More precisely, calcium is a widespread refractory lithophile element forming several common minerals including calcite CaCO₃, gypsum CaSO₄·2H₂O, dolomite CaMg(CO₃)₂, anhydrite CaSO₄, and fluorite CaF₂. Calcium is also widely distributed in other minerals such as feldspar, amphibole, and pyroxene and is often associated with clay minerals such as illite, chlorite, and Ca-montmorillonite. In igneous rocks, calcium is enriched in anorthosite, which is composed predominantly of calcium-rich plagioclase feldspar, and in mafic rocks. However, rocks such as granite and sandstone, and their metamorphic equivalents, have relatively low total CaO contents. Magnesium is a lithophile metallic element and a major constituent of many mineral groups, including silicates, carbonates, sulphates, phosphates, and borates. It forms several important minerals, including magnesite MgCO₃, dolomite CaMg(CO₃)₂, pyrope garnet Mg₂Al₂(SiO₄)₃, and kieserit MgSO₄·H₂O. It is a major component of many mafic rock-forming minerals, such as olivine, e.g., forsterite Mg₂SiO₄, pyroxene, amphibole, spinel MgAl₂O₄, biotite mica, chlorite, serpentine, and talc, and clay minerals, such as montmorillonite, as well as less common mineral groups, such as arsenates, halides, nitrates, and oxalates. In magmatic systems, Mg is concentrated in high-temperature minerals like olivine and pyroxene.

Sodium and potassium generally come from main silicates of magmatic and clay rocks [21]. Minerals containing Na are numerous, the most common being the silicates, i.e., feldspar and Na-mica. However, Na forms a major and/or minor component of many phosphate, halide, carbonate, nitrate, borate, and sulphate minerals.

Potassium is a major constituent of many rock-forming minerals, including important silicate minerals such as alkali feldspar, leucite, biotite, muscovite, phlogopite, and some amphiboles. It is also a component of many phosphate, halide, and sulphate minerals.

Chlorides constitute approximately 0.05% of the Earth's crust and, usually, they come from rock salt dissolution or, in coastal areas, from saltwater aquifer, sea spray, and coastal flooding [21]. The main factors affecting sulphate concentration are decomposition and oxidation of substances containing sulphur (fossil fuels and dissolution of sulphur-bearing minerals such as pyrite, anhydrite, and gypsum) and human activities [15, 22]. Finally, nitrate concentration in spring water deserves particular attention because it can be a clear marker of anthropic activities affecting the aquifer (agriculture, farming, and landfilling) above all for those aquifers lying below soils without vegetation covering. Indeed, nitrate content in water bodies is the result of the balance between its input and consumption by vegetation, which plays an important role in controlling the release of nutrients [23].

The analysis of water quality finds its roots in understanding and quantifying spatially water patterns related to geological and human setting. There is thus a need to connect the information from each spring water to better understand the complex geochemical processes at a regional scale. For this reason, geostatistical methods [24] are now an essential part of the toolbox of most water scientists, who, through the spatial autocorrelation of data that creates calculated representations of spatial correlation structures, are able to study the spatial structure of spring water parameters and map their spatial distribution. Among various geostatistical methods, kriging has been defined the "BLUE," i.e., the "Best Linear Unbiased Estimator" to regionalize a variable in an unsampled location [25, 26]. Past applications of the geostatistical techniques have provided good results in investigating the relationship between the lithological nature of the aquifer and chemical composition of spring waters at a relatively small scale [27] or detecting groundwater contamination [28]. Furthermore, other studies are trying to extend the spatial groundwater analysis at a large scale [29, 30] collecting considerable amount of data and giving a precious contribution in making decision processes about water management.

The present work is the first attempt to analyse groundwater quality at a relatively large scale in the main catchment of the Calabria region (southern Italy), i.e., the Crati river basin. This area is characterized by many spring waters, and groundwater is largely used for drinking purpose, thus representing a natural and socio-economic important resource. However, few analyses on few samples have been carried out in the past years to assess the quality and the degradation processes affecting the aquifers of the Calabria region [27, 31].

The objectives of the present study were to (i) analyse the physicochemical parameters of spring water samples collected in the Crati river basin in Calabria, (ii) determine their spatial distribution, and (iii) define potential spatial anomalies. The study provides baseline information about water quality for the welfare of the society that may help in future water resource planning for the area.

2. Materials and Methods

2.1. Description of the Sampling Site. The Crati, located in the NW sector of the Calabria region, is the main basin in the region both for its extension and for its artificial lakes [32]. It has a perimeter of about 320 km and an area of 2447.7 km² within which a wide hydrographical network flows, including waters coming from different geological environments. The main river length is 95 km; it rises upon the Sila Massif and flows into the Ionian Sea. The average and maximum altitudes of the basin are 597 m a.s.l. and 2258 m a.s.l., respectively (Figure 1). The basin is L-shaped and can be divided into a N-S-oriented Crati and an E-W-oriented Sibari subbasins [33].

The Crati basin presents a high climatic variability owing to its position in the Mediterranean area and the mountainous nature, denoting a subtropical Mediterranean climate [34]. Specifically, on the eastern sector, high temperatures and short and heavy rainfall are observed due to the warm

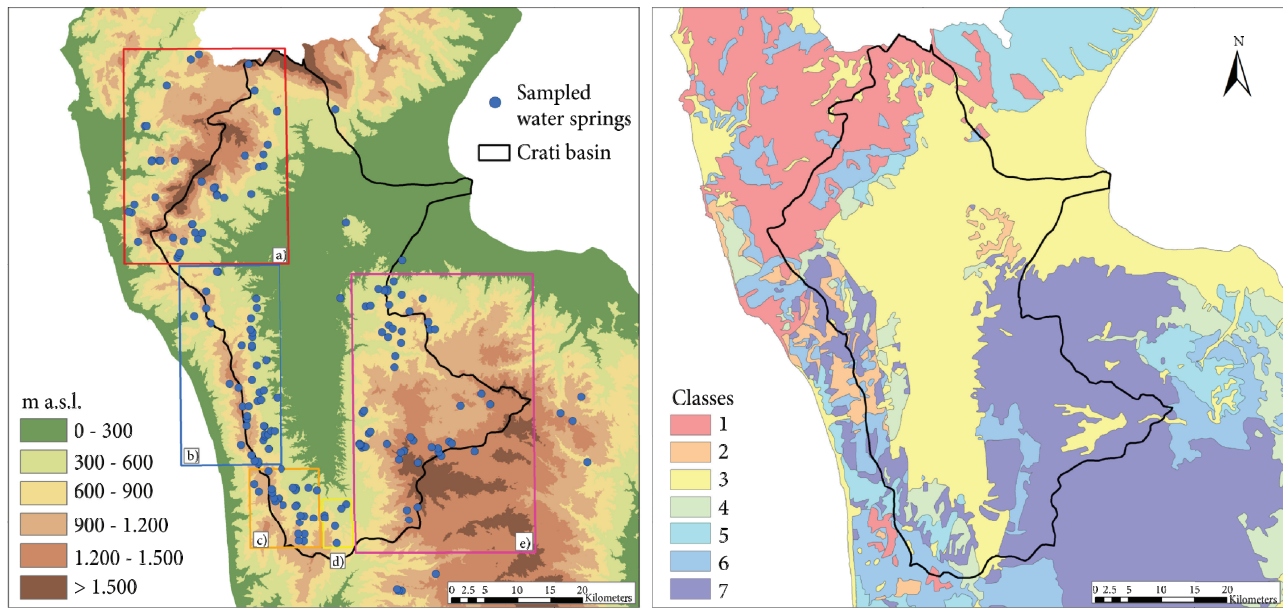


FIGURE 1: (a) Crati river basin with spring location and subzones delimited in this study: (A) Pollino Massif, (B) Coastal Chain, (C) Mt. Cocuzzo, (D) Serre Area, and (E) Sila Massif. (b) Lithological map of the basin. Lithological units are grouped into seven classes: (1) limestones and dolostones, (2) metamorphic rocks with ophiolites, (3) sand, clay and gravel, (4) clayey and marly terranes, (5) flysch, (6) sandstones, conglomerates and limestone banks, and (7) intrusive metamorphic complex.

African air currents, while the western air current affects the western side causing milder temperatures and orographic precipitation. The annual maximum and minimum precipitation are, respectively, 2106 mm (registered on the western side of the basin) and 596 mm (on the eastern side) with an average of 1212 mm. The inner areas present colder, sometimes snowy, winters and fresher, with some precipitation, summers [35, 36].

Geologically, the Crati basin is an intra-arc tectonic depression located in the north-western part of the Calabrian Arc, which is an arc-shaped continental fragment interposed between the Sicilian Maghrebide belts, to the south, and the Apennine edifice, to the north [37–39]. In particular, the Crati basin is a graben bounded by three morpho-structural highs: the plutonic and metamorphic crystalline rocks of the Sila Massif to the east, the crystalline and sedimentary rocks of the Coastal Chain to the west and south, and the carbonate and siliciclastic sedimentary rocks of the Pollino group to the north [40]. The study area is characterized by a sequence of pliocenic sediments among which are light brown and red sands and gravels, blue grey silty clays with silt interlayers, Pleistocene to Holocene alluvial sands and gravels, and very small outcrops of Miocene carbonate rocks [41, 42]. Sedimentary covering overlapped on a Palaeozoic intrusive-metamorphic complex formed by paragneiss, biotite schists, and grey phyllitic schists (with dominant quartz, chlorite, and muscovite), which are often affected by weathering processes [43]. Due to the particular tectonic setting of the basin controlled by NS, SW-NE, and NW-SE-trending faults [44], a great number of natural spring waters are located above the 300 m a.s.l. Most of them have a remarkable discharge and are currently used for drinking purposes.

In particular, the Sila Massif consists of three different Variscan metamorphic complexes (Gariglione, Mandatoriccio, and Bocchigliero complexes), respectively, representing high-, medium-, and low-grade metamorphic facies and of late-Variscan plutonites intruding them and forming the Sila batholith. The batholith consists of multiple intersecting, syn- and posttectonic intrusions, ranging in length from several kilometers to less than 1 km. They have heterogeneous texture and composition from gabbro to leucomonzogranite, with prevailing tonalite and granodiorite.

The Coastal Chain consists mainly of Paleozoic rocks with the presence of crystalline schists and ophiolites overlapped by layers of Triassic limestones as those found in Mt. Cocuzzo (1541 m a.s.l.), the highest peak of the Coastal Chain. In the tectonic window, the dolomites and the Triassic limestones appear in this area. These are stratified sedimentary deposits and occasionally massifs of an ancient carbonatic platform.

From the lithological point of view, the mountains of the Pollino are formed of Triassic, Jurassic, and Liassic limestone with frequent karst phenomena (caves, shelters, and sink-holes). Moreover, some areas near the coast have sandstone, clays, and Eocene marls. During the Mesozoic era, there is the formation in the marine environment of carbonate rocks, light grey and blackish dolomites and limestone. Starting from the Miocene Inferiore, during the formation of the Apennines, it is recorded, in the ophiolite unit and in the Oligo-Miocene terrigenous coverings, a compressive tectonics testified by folds and overlaps, which lead to the accumulation of Flysch.

In this site of the study, there is a spring of sulphur water known as “acqua fetente” (foul-smelling water). It is a condition where the running water contains a high amount of

hydrogen sulphide gas that escapes into the air. The $\delta^{34}\text{S}$ values of dissolved sulphate are constrained by the mixing of thermomineral waters with cold waters, both interacting with Upper Triassic carbonate-evaporite rocks, as well as occurrence of bacterial sulphate reduction. In the light of the geological and hydrogeological framework of the study area, this chemical and isotopic evidence suggests that the thermal circuit develops entirely into the Upper Triassic sedimentary sequence. The area is characterized also by the presence of the Rock Salt Mine of Lungro, where the Sibariti and the Romans even extracted salt and traded the rock salt. In the early 1900s, the business began to decline and the government decided the closure of the mine on November 3, 1976. Since 2015, the site is subjected to recovery and restoration.

2.2. Physical-Chemical Analyses. The discharge system of the analysed spring waters has a seasonal behaviour. The aquifers' recharge occurs generally in the period September-December, when rainfall reaches its maximum intensity and the discharge value of the spring increases with a lag time of about two months [31]. For this reason, the sampling procedure was carried out in the period from February 2016 to May 2016, when generally the maximum discharges have been recorded. In particular, 190 spring water samples were collected within the study area. In order to give a global overview of the physicochemical status, for each spring point one sample was collected by using high-density polyethylene (PE-HD) clean bottles with screw caps. In situ portable apparatus including a pH meter and a conductivity meter were used to determine the physical parameters (i.e., temperature, pH, and specific EC compensated at 20°C), while approved laboratory standard methods were applied to determine the chemical parameters, such as major cations (Ca^{2+} , Mg^{2+} , Na^+ , and K^+) and major anions (SO_4^{2-} , Cl^- , and HCO_3^-) [45]. Specifically, the major cations were evaluated by using AAS (Atomic-Absorption-Spectroscopy) method; sulphate, chloride, and nitrate by UV Spectrophotometry; alkalinity by acidimetric titration; and hardness by using complexometric EDTA titration. A complete analytical quality control scheme was implemented with sampling and analytical duplicates. Analytical precision was calculated by the 20% analysis (in duplicate) of randomly chosen samples and was found to be within accepted the international standards (<5%).

2.3. Langelier-Ludwig Squared Diagram. Various diagrams have been developed over the years for visualization of water chemistry and they have been widely used by the researchers and practitioners. The first graphical technique has been proposed by [46] but, actually, the most popular diagrams are the Piper [47] and the Langelier-Ludwig square diagrams [48] which have been largely applied [49–52]. In particular, Langelier and Ludwig proposed a diagram in which rectangular coordinates are used representing patterns and correlations between major cations and anions for multiple samples, thus allowing to separate between Ca from Mg facies and Cl from SO_4 facies. More precisely, the so-called Langelier-Ludwig (LL) squared diagram allows the determination of what in geochemical practice is indicated

as hydrochemical facies, reflecting the effects of chemical interaction with the lithotypes. The water classification is so ensured by positioning the water sample in one of the four sectors of which the LL diagram is composed:

- (I) Chloride-sulphate Ca-Mg waters
- (II) Chloride-sulphate alkaline waters
- (III) Bicarbonate-alkaline waters
- (IV) Bicarbonate Ca-Mg waters

The ion concentrations are expressed in meq/l. The alignment of the sample points into the different sectors allows the identification of possible phenomena such as mixing or evolutionary processes of water [31, 53].

2.4. Geostatistical Analysis. Spatial continuous data play a significant role in planning, risk assessment, and decision-making in environmental management [54]. Consequently, the mapping and spatial analysis requires converting the field measurements into continuous space. Thus, the values of an attribute at unsampled points need to be estimated, meaning that spatial interpolation from point data to spatial continuous data is necessary. The main application of geostatistics [55] to environmental sciences is the estimation and mapping of environmental matrix attributes in unsampled areas [56]. Geostatistics includes several methods that use kriging algorithms for estimating continuous attributes. For a detailed presentation of the theory of random functions, interested readers should refer to textbooks such as [25, 57–60], among others.

Before mapping and spatially interpreting the water physicochemical parameter concentration analysed, a log transformation was applied on the data, according to the assumption of decreasing data variability and allowing the data to conform more closely to normal distribution. In this way, the validity of the associated statistical analyses increases and the best data interpolation is provided. The log transformation is the most popular among the different types of transformations used to transform skewed data into approximately normal distributed data.

The level of spatial correlation is defined by the construction of the variogram and by the evaluation of the committed error. Experimental variogram is a plot showing how half of the squared differences between the sampled values (semivariance) changes with the distance between the point-pairs. It is typically expected to see smaller semivariances at shorter distances and then a stable semivariance (equal to global variance) at longer distances. It can be expressed as

$$\gamma(h) = \frac{1}{2N(h)} \sum_{i=1}^{N(h)} [Z(x_i) - Z(x_i + h)]^2, \quad (1)$$

where $\gamma(h)$ is the semivariance at a given distance h , $Z(x_i)$ is the value of variable Z at x_i location, and $N(h)$ is the number of pairs of sample points separated by the lag distance h .

TABLE 1: Maximum, minimum and mean concentration values of the water parameters in the 5 subzones.

	Pollino Massif			Coastal Chain			Mt. Cocuzzo			Serre Area			Sila Massif		
	Max	Min	Mean	Max	Min	Mean	Max	Min	Mean	Max	Min	Mean	Max	Min	Mean
pH	8.1	6.8	7.6	7.8	5.5	6.8	8.1	6.5	7.4	8.0	6.7	7.5	8.6	5.5	6.9
Cond ($\mu\text{S}/\text{cm}$)	936.0	195.0	414.3	636.0	65.7	206.0	1185.0	87.0	396.2	439.0	132.0	243.7	710.6	45.0	172.5
Hardness ($^{\circ}\text{f}$)	49.5	10.7	23.7	34.4	1.6	9.1	46.1	2.7	19.0	21.8	5.0	12.1	33.6	1.0	7.3
Ca^{2+} (mg/l)	116.8	28.0	55.6	102.2	4.0	26.7	166.1	7.2	61.1	54.1	12.0	31.7	110.0	1.6	15.7
Mg^{2+} (mg/l)	50.5	2.4	23.4	21.7	1.2	6.0	27.9	1.3	9.1	20.2	4.9	10.1	20.5	1.0	7.7
K^{+} (mg/l)	2.4	0.0	1.2	15.3	0.0	1.7	19.5	0.0	1.9	2.4	0.8	1.6	2.9	0.0	1.4
Na^{+} (mg/l)	149.2	2.8	18.4	19.1	3.4	8.1	22.0	4.2	8.8	11.3	5.1	7.3	59.0	4.5	10.9
HCO_3^{-} (mg/l)	452.8	12.0	163.3	346.9	4.0	99.1	429.4	28.0	198.2	232.3	90.6	153.2	209.8	8.0	59.7
Cl^{-} (mg/l)	101.6	8.6	18.8	28.1	1.7	15.6	40.8	10.1	19.3	19.0	13.1	16.3	85.1	7.8	18.0
SO_4^{-} (mg/l)	140.0	0.0	7.7	32.9	0.0	3.8	48.5	0.0	6.4	15.0	1.9	7.1	25.0	0.1	2.0
NO_3^{-} (mg/l)	17.8	0.2	4.1	14.5	0.0	1.4	8.8	0.0	2.5	5.2	0.0	1.2	24.0	0.0	4.4

Kriging is an optimal interpolator offering a minimum error variance. To estimate the variogram value analytically for any distance h , a theoretical function is fitted to the experimental variogram. The fitted variogram model allows building a model that captures the major spatial features of the attribute under study (water physicochemical parameter concentration in this study). The optimal model fitting will be chosen based on cross-validation, which checks the compatibility between the data and the structural model considering each data point in turn, removing it temporarily from the data set and using its neighbouring information to predict the value of the variable at its location [61]. The goodness of fit was evaluated by the mean error (ME) and the Mean Squared Deviation Ratio (MSDR). The difference between the measured and estimated values, represented by ME, proves the unbiasedness of estimate if its value should be close to 0, while the ratio between the squared errors and the kriging variance [26], represented by MSDR, should be 1 if the model for the variogram is accurate. In the present application for each subarea and for each analysed chemical parameter, four different semivariogram models (spherical, circular, exponential, and Gaussian) were applied and the one which provided the minor mean error (ME) was chosen as the best model. The fitted variogram was used to estimate water physicochemical parameters at unsampled locations using ordinary kriging. It aims to estimate a value of the random variable $Z(x)$ at a point of a region x_0 for which a variogram is known, using data in the neighbourhood $Z(x_\alpha)$ of the estimation location as

$$Z_{\text{OK}}^*(x_0) = \sum_{\alpha=1}^{n(x_0)} \lambda_{\alpha}^{\text{OK}} z(x_{\alpha}), \quad (2)$$

where λ_{α} is the ordinary kriging weights and $n(x_0)$ is the number of data closest to the location x_0 to be estimated. In particular, λ_{α} values must be evaluated in order to obtain an unbiased estimation and to minimize the variance.

Simulations are then run on normally distributed data, and the results are back-transformed. Back-transformation

of each (co)kriging result was carried out by exponentiation to reverse

$$y(x_0) = \log Z(x_0), \quad (3)$$

where $Z(x_0)$ is the measured value at location x_0 . This back-transformation provides a prediction for water physicochemical parameters expressed in original units.

All statistical and geostatistical analyses were performed by using the software package using cc.

3. Results and Discussion

Due to its extension, as well as to its geomorphological and hydrogeological properties, the investigated area was split into 5 subareas (Figure 1): (a) Pollino Massif, (b) Coastal Chain, (c) Mt. Cocuzzo, (d) Serre Area, and (e) Sila Massif, whose sampled waters showed different hydrochemical behaviour. In particular, the Mt. Cocuzzo area has been considered because of its calcareous nature, clearly different from the surroundings. The Serre Area has been also identified as an independent unit much more similar to a merging point between the organogenic limestones of the Mt. Cocuzzo unit, the sands and conglomerates of the graben of the Crati valley, and the granitic acid units of the Sila Massif. Basic statistics for physicochemical parameters of spring waters sampled are reported in Table 1.

Some of the following analyses have been previously presented in Gaglioti et al. [62] but for a smaller number of sampled points.

3.1. Langelier-Ludwig Squared Diagram. As a result of the physical and chemical analysis of the 190 sampled points, the Langelier-Ludwig diagram, shown in Figure 2, was obtained. The majority of the sampled spring waters falls within the first sector and the fourth sector of the diagram, corresponding to bicarbonate alkaline-earth waters and chloride-sulphate alkaline-earth waters, respectively. This result reflects very well the global lithological environment of the study area, which is mainly constituted of

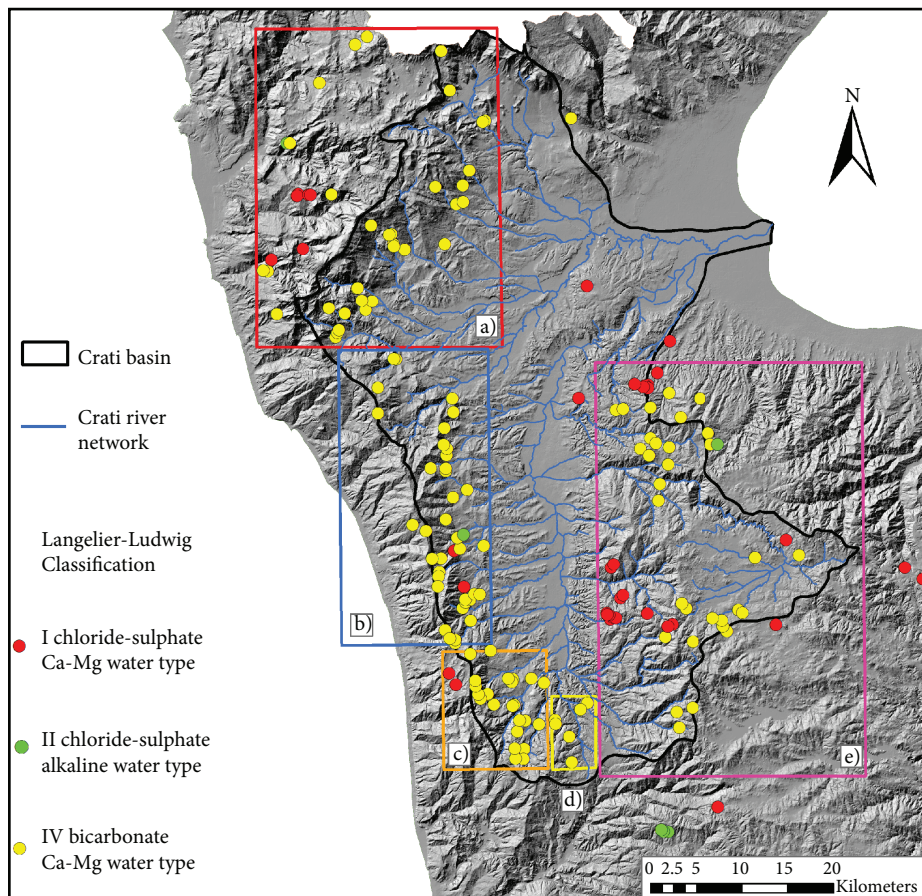
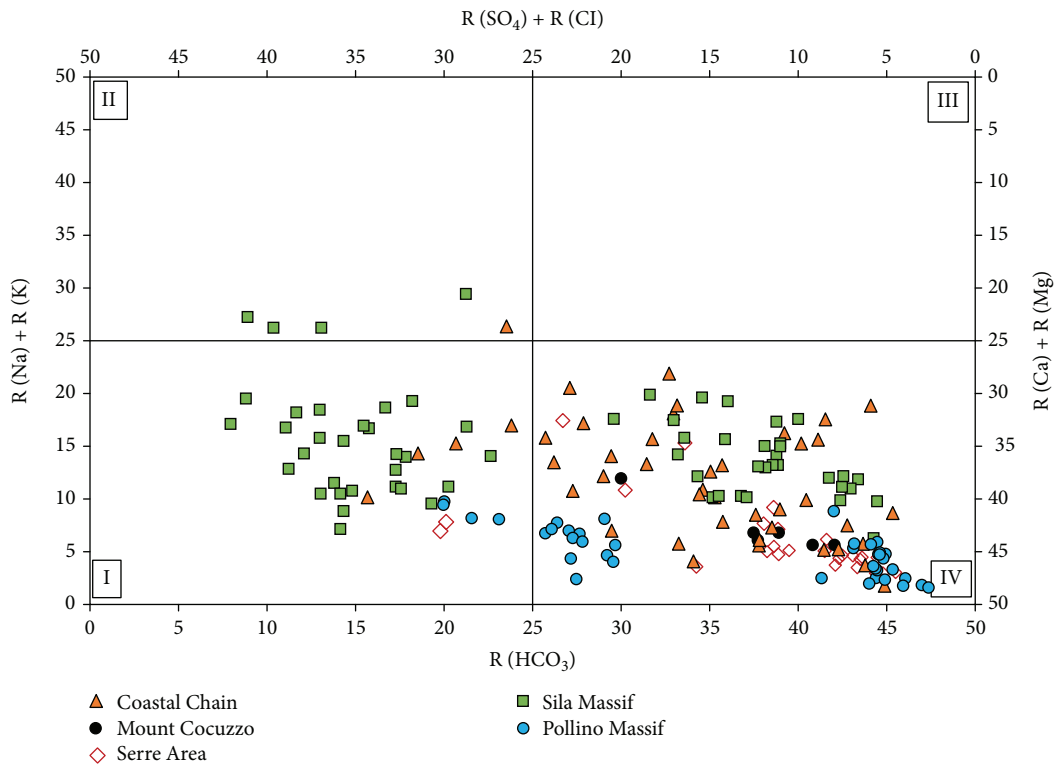


FIGURE 2: Langelier-Ludwig squared diagram for each area and spatial distribution of the spring water geochemical facies.

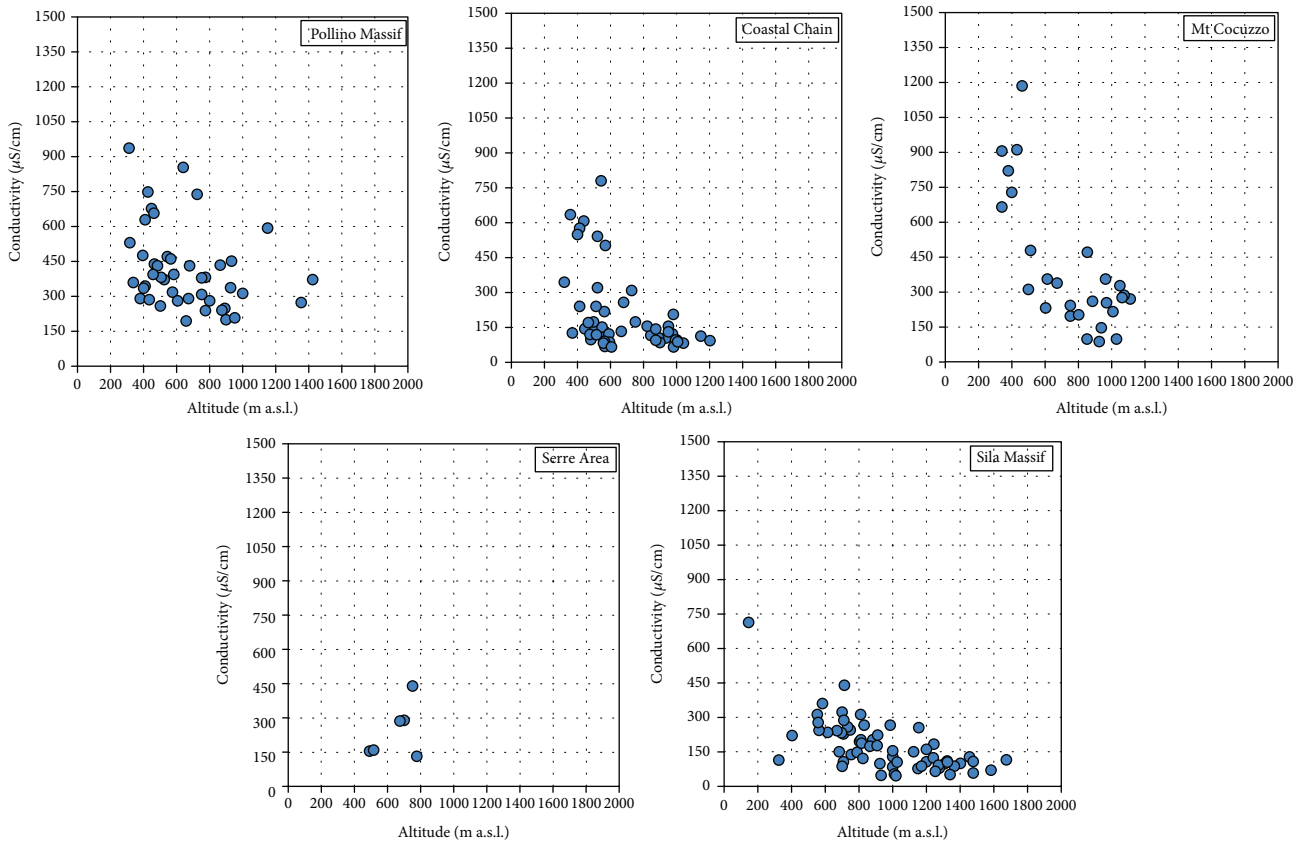


FIGURE 3: Relationship between spring water EC and elevation.

calcareous and carbonatic rocks (providing high Ca^{2+} , Mg^{2+} , and HCO_3^- ion concentration in water) and intrusive magmatic or metamorphic rocks (providing high SO_4^{2-} , Cl^- ion concentration in water). In particular, considering the Pollino Massif, the highest number of the samples has been identified in the fourth sector, due to hard waters particularly rich in bicarbonates, calcium, and magnesium. Moreover, these samples can be divided in two different groups, the first one very close to the lower right vertex representative of springs having low elevation, while the second group, bordering on the first sector, represents springs less conductive and thus with low mineralisation, with much more high elevation. The Coastal Chain sampled waters fall also within the fourth sector. Their position within the diagram is a little higher than those of the Pollino Massif and shows a casual distribution representative of the chemical and physical characteristic variability imputable to a mixing effect between different water types [31]. Usually, the groundwater flowing in strongly faulted areas has this behaviour [63]. In the Mt. Cocuzzo area, the results showed homogeneously grouped samples localized in the fourth sector. The lithology of this area, defined as a tectonic window, is very similar to those of the Pollino Massif, with the same calcareous origin and similar hydrochemistry. In fact, results of the analysed samples evidenced waters coming from deep aquifer, with high levels of calcium and magnesium and high alkalinity and pH values. These values are typical in carbonate aquifers. Only few spring waters differ from the others showing high

sulphate content, evidencing a good correspondence with the chalky bedrock, which can be found in a very restricted area of Mt. Cocuzzo. As regards the Serre Area, the physical and chemical parameters of the sampled spring waters showed a peculiar behaviour, which differs from the neighbouring basic water of Mt. Cocuzzo and the acid ones found in the Sila Massif. Unfortunately, few numbers of sampled points did not allow getting further conclusions. Finally, from the analysis of points of the Sila Massif the water samples are located in the first sector and the fourth sector of the LL diagram, where water rich in sodium and potassium and, at the same time, poor in calcium, magnesium, and alkalinity is represented. Flowing into acid intrusive magmatic or plutonic rocks, this aquifer provides to make the water particularly acid.

3.2. Relationship between Spring Water Conductivity and Elevation. Figure 3 shows the results of the comparison between EC and altitude. This analysis allows putting in evidence some aquifer behaviour and to detect their interaction with some external factors.

For the Pollino Massif area, an almost homogeneous behaviour was identified, thus evidencing no significant trends in the diagram. In fact, limestones and dolostones make water more conductive but the depth of the aquifers, flowing in a system through rocks affected by karst phenomena, does not allow a remarkable interaction with external precipitation.

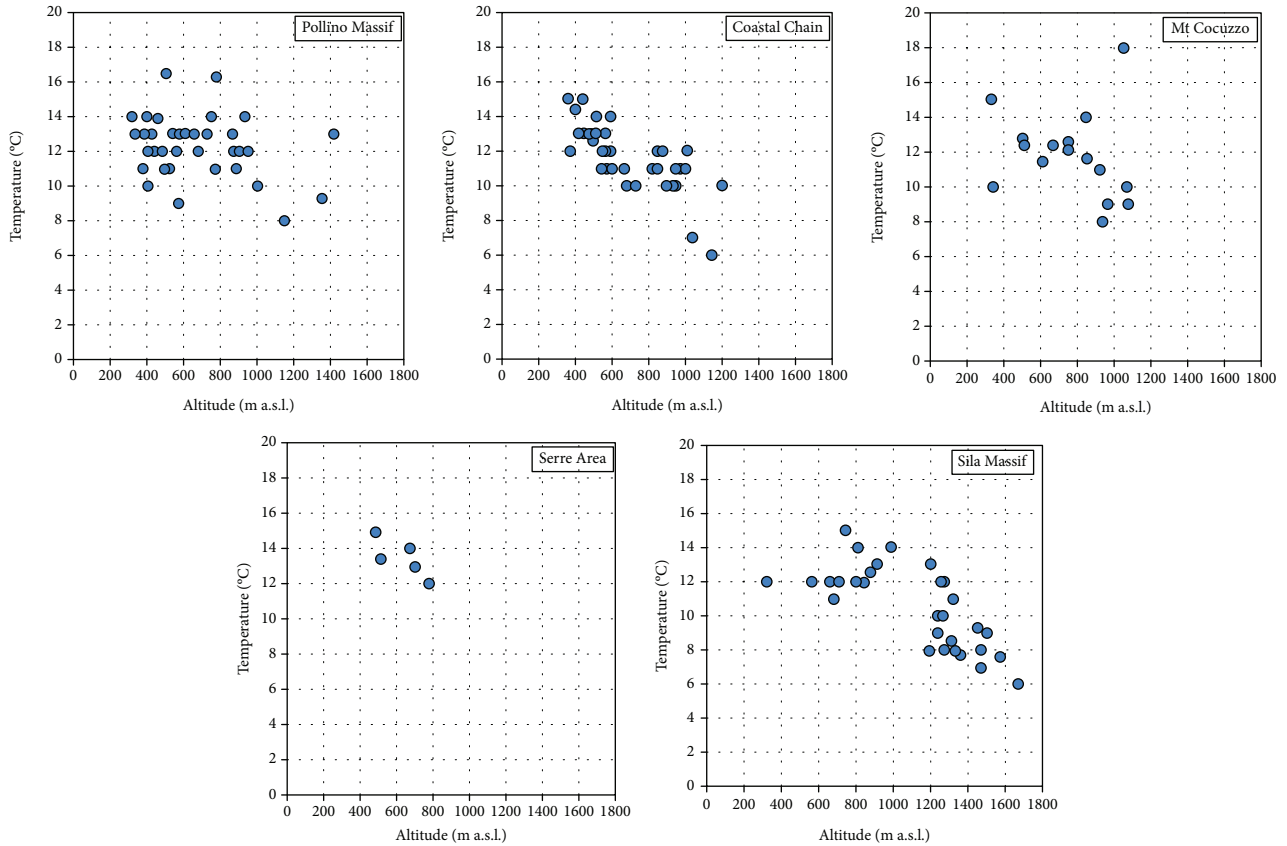


FIGURE 4: Relationship between spring water temperature and elevation.

In the Coastal Chain, a slight downward behaviour of the conductivity with the elevation was detected. Moreover, three different spring water groups, which should be individually studied, were identified, probably due to the presence of several aquifers at different depths.

The maximum conductivity value in all the study area (1185 $\mu\text{S}/\text{cm}$) has been detected in the Mt. Cocuzzo area, which evidenced a high variability of the conductivity with the elevation. Moreover, in this area, given the different conductivity values, two distinct spring water groups can be clearly identified. In particular, the group with high conductivity values is located on a sulphurous-chalk lithological bedrock.

In the Serre Area, no relation between spring water conductivity and elevation was evidenced.

The most interesting results have been detected in the Sila Massif, which is the area with the highest spring water altitude (1674 m a.s.l.). In fact, in this area, the lowest conductivity value (45 $\mu\text{S}/\text{cm}$) was found, thus revealing the possible presence of shallow aquifers usually influenced by rainfall [64] and infiltration into the soil. Moreover, the increase of water mineralization with altitude is strongly dependent on water-rock interaction and over time the contact. In fact, waters that infiltrate in altitude have a long route inside the aquifer (emerging at lower levels) with a consequent increase of the amount of dissolved salts transported in solution which leads to high conductive values in the spring waters at the lowest altitude. These results suggest

that high-elevation springs have low solute concentration similar to those of precipitation. By contrast, due to a long time contact, lower-elevation springs are geochemically more evolved than the high-elevation springs [65].

3.3. Relationship between Spring Water Temperature and Elevation. By a visual inspection of diagrams, comparing temperature and elevation of the spring waters (Figure 4), further information can be derived. In fact, temperature can be used as a tracer of hydrologic and flowing processes for natural spring waters. Moreover, measuring the temperature accurately in field is easy, quick, and inexpensive and it also provides an insight of the subsurface geological processes. Many factors influence the spring water temperature, such as the period of the survey, the latitude, and the elevation, although the influence of the elevation is strictly dependent from the depth of the aquifer. Air temperature, solar radiation, and geothermal gradient can be considered other influencing factors on spring water temperature [66].

In the Pollino Massif and Mt. Cocuzzo areas, the sampled spring waters showed a certain homogeneity of temperature variation with the altitude, with a thermal gradient of -0.0018 and $-0.0020^\circ\text{C}/\text{m}$, respectively. These features are clear sign of aquifers, which are slightly affected by the outside temperature and which, in function of their depth, maintain a certain temperature regularity evident at the spring.

Conversely, the other areas evidenced a marked reduction of the spring water temperature with elevation, thus

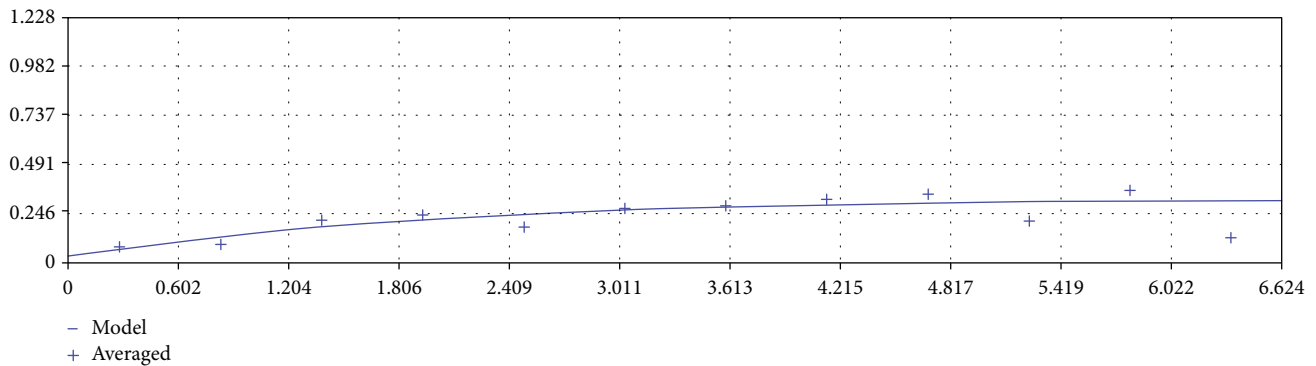


FIGURE 5: Experimental variogram (plotted points) and fitted model (solid line) of the calcium values in the spring waters of Mt. Cocuzzo.

denoting superficial aquifers in which water temperature is affected by air temperature. In these areas three different spring water thermal gradients with the altitude were detected, -0.0056 , -0.0067 , and $-0.0052^{\circ}\text{C}/\text{m}$, respectively, which are quite similar to the annual average atmospheric gradient of the Crati valley of about $-0.0068^{\circ}\text{C}/\text{m}$ [67].

3.4. Maps of Physicochemical Parameter Spatial Distribution. To fit the shape of the experimental variogram, for each analysed parameter, four basic structures were tested including a Circular model (Cir), a Spherical model (Sph), an Exponential model (Exp), and a Gaussian model (Gau). Figure 5 shows (as an example) the variogram for calcium values in the spring waters of Mt. Cocuzzo.

The goodness of fit was checked by cross-validation and the results were quite satisfactory because the statistics used, i.e., mean of the raw estimation errors, were close to 0, while the variance of the standardized error was close to 1 (Table 2). Consequently, the best model, obtained comparing the results of ME and MSDR, was chosen to map the distribution of physicochemical parameters.

In order to obtain an instant evaluation of the main hydrogeochemical characteristics of the Crati river basin, ten thematic maps were produced, each representing the spatial distribution of the different chemical and physical parameters, making easy the identification of maximum and minimum values within the five subareas (Figures 6–8).

The maps were obtained using the ordinary kriging technique. Considering the particular distribution of the spring points, placed on average above a certain altitude, it was chosen to represent the spatial distribution maps by setting the computation process above 300 m a.s.l. The results were represented using the digital terrain model in background.

The Ca^{2+} ion is one of the most important constituents of groundwater (Figure 6). In the distribution map, the higher calcium concentrations are indicated with the most intense colours while lighter colours show areas with less concentration. By a first observation, it can be noticed that the major concentrations were found on the Pollino Massif and Mt. Cocuzzo area (in this latter case in a strictly circumscribed area); in both cases, the results agree well with the lithologic formations present, mostly of calcareous-dolomite type. On the Coastal Chain, a progressive calcium enrichment is

observed, descending along the east side of the mountains, while the concentrations remain very low on the Sila Massif, both in agreement with the local geology.

The distribution map of the magnesium shows high concentrations in the northern area of the basin, where from a geological point of view, there are dolomites or rocks particularly rich in magnesium salts. On the other areas, concentrations are kept lower, ranging from 5 to 20 mg/l (Figure 6).

Observing the distribution of sodium is possible to find a particular enrichment in the Sila Massif, moving northward, whereas more restricted areas have been located in the Mt. Cocuzzo area and on the Pollino Massif where some salt mine were historically present (Figure 6).

The distribution of potassium remains fairly homogeneous throughout the basin except for the Coastal Chain where a general enrichment was recorded, descending along the slope. This behaviour is attributable to the lithological variation of the area where an important very active fault system persists that causes a “mixing” effect between waters in contact with lithologies of different nature. Also in the Serre Area, where an ancient lake basin laid, high potassium concentration was found (Figure 6).

The map of the chlorides shows the smallest concentrations on the highest altitudes of the investigated areas and gradually enriching downstream into the basin, most likely due to the different atmospheric depositions that insist on the study area. The highest concentrations were found in the Coastal Chain most likely for the residual contributions resulting from the orographic rainfall, which transport some sea aerosols, and from water-rock interaction along groundwater path (Figure 7).

Sulphate ion can be instead attributed to different origins. An exogenous nature attributable, for example, to the transport by atmospheric deposition and marine aerosols (obviously in areas near the sea) can be considered as well as in most of the cases in the present study, endogenous one. Moreover, sulphate ion can come from the dissolution of gypsum and anhydrite as in the case of the Pollino Massif, or anthropogenic input when it is together with NO_3 , or due to the presence of ancient sulphur spring waters as found in the Mt. Cocuzzo area (Figure 7).

The nitrate distribution aroused a particular interest: this parameter is often indicative of the presence of intense

TABLE 2: Results of the cross-validation for the different subzones and the different variables.

Subzones	Variable	Model	ME	MSDR
Pollino Massif	Calcium	Circular	-0.025	0.940
	Magnesium	Exponential	-0.020	0.963
	Sodium	Spherical	-0.013	1.092
	Potassium	Gaussian	0.001	0.786
	Chloride	Exponential	-0.017	1.078
	Sulphate	Exponential	-0.065	1.009
	Nitrate	Exponential	0.015	0.945
	Alkalinity	Gaussian	-0.016	1.249
	Hardness	Exponential	0.018	0.866
	Conductivity	Spherical	-0.017	0.947
Coastal Chain	Calcium	Gaussian	-0.049	1.214
	Magnesium	Gaussian	-0.106	1.440
	Sodium	Gaussian	-0.048	0.920
	Potassium	Gaussian	-0.033	1.224
	Chloride	Gaussian	0.000	0.812
	Sulphate	Exponential	-0.060	1.583
	Nitrate	Spherical	-0.117	1.381
	Alkalinity	Exponential	-0.083	1.062
	Hardness	Circular	-0.068	1.327
	Conductivity	Exponential	-0.109	1.266
Mt. Cocuzzo	Calcium	Exponential	0.021	0.784
	Magnesium	Exponential	-0.002	1.100
	Sodium	Circular	0.024	0.941
	Potassium	Exponential	0.017	0.984
	Chloride	Gaussian	0.009	0.857
	Sulphate	Gaussian	0.052	0.875
	Nitrate	Exponential	0.008	0.959
	Alkalinity	Gaussian	-0.011	1.015
	Hardness	Circular	0.007	0.775
	Conductivity	Gaussian	0.000	1.044
Serre Area	Calcium	Gaussian	-0.016	0.505
	Magnesium	Gaussian	-0.022	0.222
	Sodium	Exponential	-0.006	1.221
	Potassium	Gaussian	-0.017	0.385
	Chloride	Gaussian	-0.035	0.536
	Sulphate	Gaussian	-0.023	0.201
	Nitrate	Gaussian	0.036	0.484
	Alkalinity	Gaussian	-0.022	0.152
	Hardness	Circular	0.076	0.977
	Conductivity	Gaussian	-0.023	0.150
Sila Massif	Calcium	Exponential	-0.041	1.045
	Magnesium	Exponential	-0.027	1.082
	Sodium	Exponential	-0.013	1.079
	Potassium	Gaussian	0.022	1.050
	Chloride	Circular	0.001	1.071
	Sulphate	Gaussian	0.008	1.019
	Nitrate	Gaussian	0.033	0.891

TABLE 2: Continued.

Subzones	Variable	Model	ME	MSDR
	Alkalinity	Exponential	-0.035	0.996
	Hardness	Exponential	-0.019	1.222
	Conductivity	Gaussian	0.017	1.086

anthropic activities, in particular farming and breeding activity, which are widespread on the Pollino Massif and Sila Massif areas. In that latter case, it has to be underlined the subsequent reforestations since the postwar period and the related cleaning and maintenance activities of the woods that have deprived the subsoil of that organic substrate necessary for denitrifying bacterial colonies (Figure 7).

Alkalinity shows high concentrations in those areas where carbonatic rocks occur, such as Pollino Massif with a quite homogeneous distribution and Mt. Cocuzzo area, where high alkalinity levels were detected in a certain localized area. The very low interaction was confirmed, in terms of carbonates and bicarbonates dissolved, for crystalline and siliceous rocks localized on the Sila Massif (Figure 7).

The map of hardness distribution, here expressed in French degrees ($1^\circ F = 10 \text{ mg/l} = 10 \text{ mg kg}^{-1}$), that is the sum of the calcium and magnesium hardness, still highlights the presence of very hard waters between the Pollino Massif and the Mt. Cocuzzo area with maximum values of $50^\circ F$ for waters flowing into limestone, dolostone, and evaporitic rocks. While on the Coastal Chain and the Sila Massif the results showed the presence of soft water, mostly coming from igneous and siliceous rocks (Figure 8).

The last map (Figure 8) represents the distribution of EC, the physical parameter that synthesizes the sum of all ionic species dissolved in the water. Specifically, it is currently used in geochemistry as an indicator of the level of the so-called “maturity” of groundwaters and their flow direction. The samples with higher conductivity were found on the Pollino Massif and Mt. Cocuzzo area ($849 \mu\text{S/cm}$ and $1185 \mu\text{S/cm}$, respectively) demonstrating the presence of deep aquifers with a long-time contact with carbonatic rocks. In the Coastal Chain, a progressive enrichment was detected descending along the slope towards the east side of the basin. Relatively less conductive waters were found in the remaining areas where shallow aquifers are assumed to be present with a lower interaction with the rock substrate.

4. Conclusions

The present study is an attempt in the Crati river basin for the evaluation of the water quality of some spring waters, largely used for drinking purposes by the population. The investigation was carried out by analysing 190 spring waters all localized above 300 m a.s.l., allowing a first classification of the hydrochemical facies of the aquifers from which the same springs rise. In particular, following a preliminary analysis based on the geological characteristics of the Crati basin, the entire study area was divided into five subareas (Pollino Massif, Coastal Chain, Mt. Cocuzzo, Serre Area, and Sila Massif).

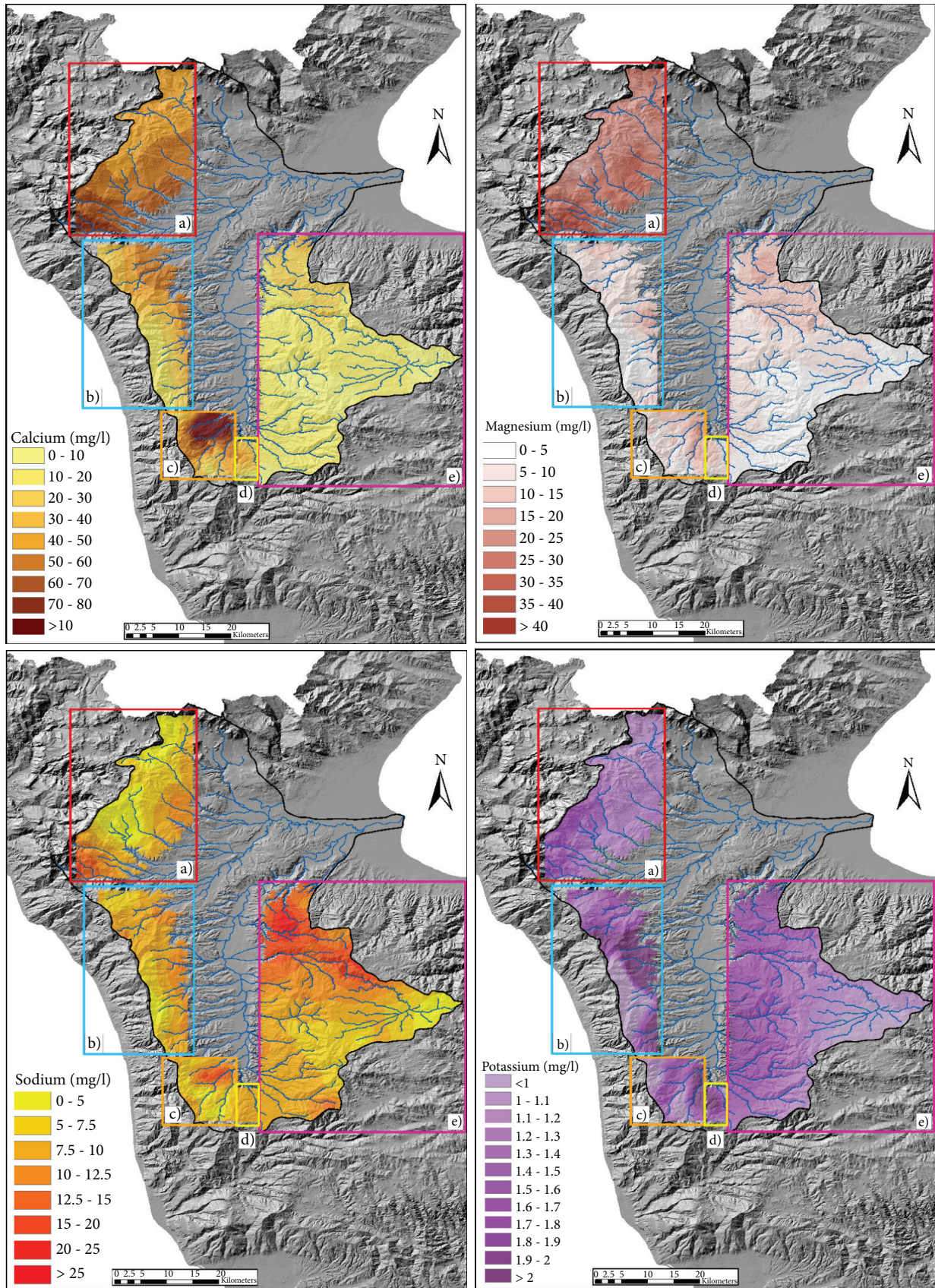


FIGURE 6: Spatial distribution of concentration of calcium, magnesium, sodium and potassium in waters from the 5 subareas of the Crati river basin.

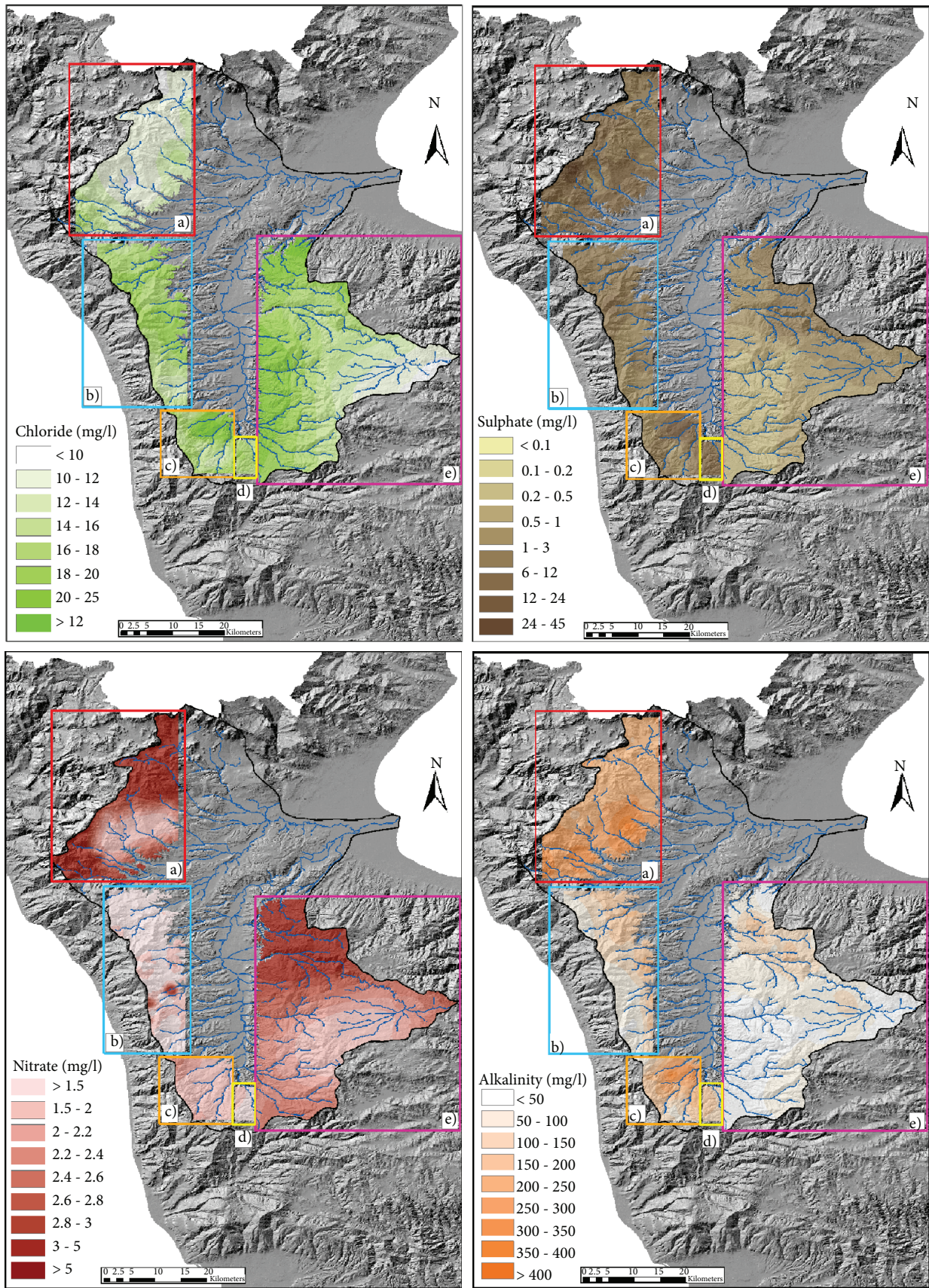


FIGURE 7: Spatial distribution of chloride, sulphate, nitrate and alkalinity in waters from the 5 subareas of the Crati river basin.

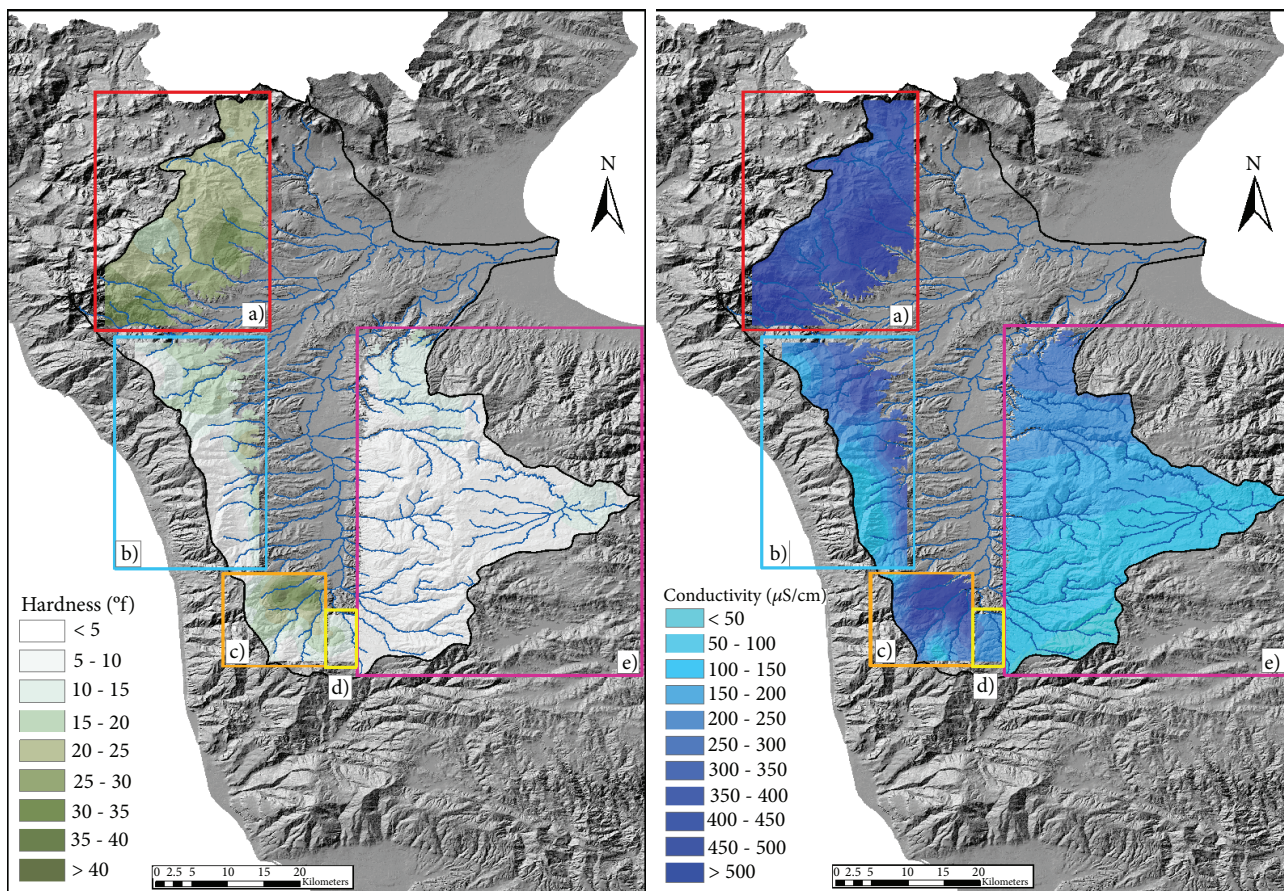


FIGURE 8: Spatial distribution of hardness and conductivity in waters from the 5 subareas of the Crati river basin.

As a result, the most representative water types are the bicarbonate alkaline-earth and the chloride-sulphate alkaline-earth, and only in few cases, chloride-sulphate alkaline type occur. Furthermore, the occurrence of the bicarbonate alkaline-earth water types is recorded at the highest elevations, very close to the basin borders. In particular, on the Pollino Massif and in the Mt. Cocuzzo area, very hard and alkaline waters with high conductivity and low acidity have been found. Moreover, low floating temperature values have been detected, thus evidencing waters circulating into deep calcareous aquifers having long-time contact with limestone, dolostone, and evaporitic rocks. In the Coastal Chain, a much variable behaviour in terms of dissolved salt content, conductivity, and pH levels was detected. This is probably due to the lithologic heterogeneity of the area and the presence of an important active fault system, which allows contact between lithological units with different chemical-physical characteristics. In the Sila Massif, a more homogeneous behaviour was observed, with softer water, low pH values, and low conductivity and temperature values that show a substantial downward trend as the altitude increases. These characteristics are typical of relatively shallow waters, coming from intrusive aquifers such as the granitoids and siliceous formations typical of the area.

From the observation of the distribution maps, some issues have been highlighted:

- (i) In the Mt. Cocuzzo area, there is a group of spring waters showing high concentrations for almost all the investigated parameters, probably due to the process of dissolution occurring in the presence of a sulphurous-chalk lithological bedrock
- (ii) In the Sila Massif, a general enrichment of the dissolved salts moving towards the north-eastern areas has been identified. An exception has been represented by nitrates, which showed high concentrations. These results are mainly due to the agriculture and the breeding activities in the area and secondly to the massive reforestation made after the Second World War and the subsequent seasonal maintenance which did not allow the natural supplying of organic substrate necessary for denitrifying bacterial colonies
- (iii) Despite the little number of sampled spring waters, the Serre Area has been identified as a merging point with its intermediate lithological characteristics between the organogenic limestones of the Mt. Cocuzzo unit, the Crati graben sands and conglomerates, and Sila Massif granitic units
- (iv) As concerns the Coastal Chain area, the maps confirm the presence of different lithological units that

give a noticeable water enrichment for almost all the investigated parameters descending along the east side slope of the basin

- (v) The Pollino Massif area shows the highest values, homogenous distributed, in term of dissolved salts and EC

Data Availability

The data used to support the findings of this study are available from the corresponding author upon request.

Conflicts of Interest

The authors declare that they have no conflicts of interest.

References

- [1] WHO, "Guidelines for drinking water quality," in *Health Criteria and other supporting information*, vol. 2, World Health Organization, Geneva, 2004.
- [2] G. Pellicone, T. Caloiero, G. Modica, and I. Guagliardi, "Application of several spatial interpolation techniques to monthly rainfall data in the Calabria region (southern Italy)," *International Journal of Climatology*, vol. 38, no. 9, pp. 3651–3666, 2018.
- [3] S. Dixit, S. K. Gupta, and S. Tiwari, "Nutrients overloading of a freshwater lake in Bhopal, India," *Electronic Green Journal*, vol. 21, pp. 2–6, 2005.
- [4] S. K. Nag and S. Das, "Quality assessment of groundwater with special emphasis on irrigation and domestic suitability in Suri I & II Blocks, Birbhum District, West Bengal, India," *American Journal of Water Resources*, vol. 2, no. 4, pp. 81–98, 2014.
- [5] D. A. Shigut, G. Liknew, D. D. Irge, and T. Ahmad, "Assessment of physico-chemical quality of borehole and spring water sources supplied to Robe Town, Oromia region, Ethiopia," *Applied Water Science*, vol. 7, no. 1, pp. 155–164, 2017.
- [6] P. A. Domenico, *Concepts and Models in Groundwater Hydrology*, McGraw-Hill, New York, NY, USA, 1972.
- [7] W. M. Schuh, D. L. Klinekebiel, J. C. Gardner, and R. F. Meyer, "Tracer and nitrate movement to groundwater in the Northern Great Plains," *Journal of Environmental Quality*, vol. 26, no. 5, pp. 1335–1347, 1997.
- [8] S. K. Singh, M. M. Sarin, and C. France-Lanord, "Chemical erosion in the eastern Himalaya: major ion composition of the Brahmaputra and $\delta^{13}\text{C}$ of dissolved inorganic carbon," *Geochimica et Cosmochimica Acta*, vol. 69, pp. 3573–3588, 2000.
- [9] S. Krishna Kumar, N. Chandrasekar, P. Seralathan, S. Prince, and N. S. M. Godson, "Hydrogeochemical study of shallow carbonate aquifers, Rameswaram Island, India," *Environmental Monitoring and Assessment*, vol. 184, no. 7, pp. 4127–4138, 2012.
- [10] P. E. Potter, "Petrology and chemistry of modern big river sands," *The Journal of Geology*, vol. 86, no. 4, pp. 423–449, 1978.
- [11] A. Karim and J. Veizer, "Weathering processes in the Indus River Basin: implications from riverine carbon, sulfur, oxygen, and strontium isotopes," *Chemical Geology*, vol. 170, no. 1–4, pp. 153–177, 2000.
- [12] J. Quade, N. English, and P. G. Decelles, "Silicate versus carbonate weathering in the Himalaya: a comparison of the Arun and Seti River watersheds," *Chemical Geology*, vol. 202, no. 3–4, pp. 275–296, 2003.
- [13] P. S. Datta and S. K. Tyagi, "Major ion chemistry of groundwater in Delhi area: chemical weathering processes and groundwater flow regime," *Journal of the Geological Society of India*, vol. 47, pp. 179–188, 1996.
- [14] W. J. Deutsch, *Groundwater Geochemistry: Fundamentals and Application to Contamination*, CRC, Boca Raton, FL, USA, 1997.
- [15] C. A. J. Appelo and D. Postma, *Geochemistry, Groundwater and Pollution*, Balkema Publishers, Rotterdam, 2005.
- [16] W. Y. Fantong, H. Satake, S. N. Ayonghe, F. T. Aka, and K. Asai, "Hydrogeochemical controls and usability of groundwater in the semi-arid Mayo Tsanaga River Basin: Far North Province, Cameroon," *Environmental Geology*, vol. 58, no. 6, pp. 1281–1293, 2009.
- [17] T. Subramani, N. Rajmohan, and L. Elango, "Groundwater geochemistry and identification of hydrogeochemical processes in a hard rock region, Southern India," *Environmental Monitoring and Assessment*, vol. 162, no. 1–4, pp. 123–137, 2010.
- [18] G. Jeelani, N. A. Bhat, K. Shivanna, and M. Y. Bhat, "Geochemical characterization of surface water and spring water in SE Kashmir Valley, western Himalaya: implications to water–rock interaction," *Journal of Earth System Science*, vol. 120, no. 5, pp. 921–932, 2011.
- [19] A. A. Ako, J. Shimada, T. Hosono et al., "Spring water quality and usability in the Mount Cameroon area revealed by hydrogeochemistry," *Environmental Geochemistry and Health*, vol. 34, no. 5, pp. 615–639, 2012.
- [20] B. T. Kamtchueng, W. Y. Fantong, A. Ueda et al., "Assessment of shallow groundwater in Lake Nyos catchment (Cameroon, Central-Africa): implications for hydrogeochemical controls and uses," *Environment and Earth Science*, vol. 72, no. 9, pp. 3663–3678, 2014.
- [21] E. Merian, M. Anke, M. Ihnat, and M. Stoepler, *Elements and Their Compounds in the Environment*, vol. 1, Wiley, Weinheim, 2004.
- [22] A. M. Nikanorov and L. V. Brazhnikova, "Water chemical composition of rivers lakes, and wetlands," in *Types and Properties of Water*, Encyclopedia of Life Support System, Vol II, EOLSS-UNESCO, 2009.
- [23] E. Infusino, G. Callegari, and N. Cantasano, "Release of nutrients into a forested catchment of southern Italy," *Rendiconti Lincei*, vol. 27, pp. 127–134, 2015.
- [24] G. Matheron, "The theory of regionalised variables and its applications," in *Les Cahiers du Centre de Morphologie Mathématique de Fontainebleau*, Chateau Fontainebleau, Paris, 1971.
- [25] J. P. Chilès and P. Delfiner, *Geostatistics: Modelling Spatial Uncertainty*, Wiley, New York, NY, USA, 2nd edition, 2012.
- [26] R. Webster and M. A. Oliver, *Geostatistics for Environmental Scientists, Second Edition*, Wiley, Chichester, 2007.
- [27] C. Apollaro, C. Artusa, C. Franco, R. de Rosa, M. Polemio, and R. Virga, "Geochemical studies of spring water belonging to the Vaccuta and Abatemarco river basins (north-western Calabria, Italy)," *Italian Journal of Engineering Geology and Environment*, vol. 2, pp. 59–75, 2006.
- [28] V. Elumalai, K. Brindha, B. Sithole, and E. Lakshmanan, "Spatial interpolation methods and geostatistics for mapping

- groundwater contamination in a coastal area," *Environmental Science and Pollution Research*, vol. 24, no. 12, pp. 11601–11617, 2017.
- [29] B. Raco, A. Bucciante, M. Corongiu et al., "GEOBASI: the geochemical Database of Tuscany Region (Italy)," *Acque Sotterranee Italian Journal of Groundwater*, vol. 4, no. 1, pp. 7–18, 2015.
- [30] W. De Vos, T. Tarvainen, R. Salminen et al., *Geochemical Atlas of Europe. Part 2. Interpretation of Geochemical Maps, Additional Tables, Figures, Maps, and Related Publications*, Geological Survey of Finland, Otamedia Oy, Espoo, 2006.
- [31] N. Cantasano, F. Ietto, G. Callegari, R. Froio, and E. Infusino, "Assessment of the spring water quality in the municipal area of Chiaravalle Centrale (CZ, Italy)," *L'Acqua*, vol. 3, pp. 69–76, 2013.
- [32] I. Guagliardi, N. Rovella, C. Apollaro et al., "Modelling seasonal variations of natural radioactivity in soils: a case study in southern Italy," *Journal of Earth System Science*, vol. 125, no. 8, pp. 1569–1578, 2016.
- [33] A. Colella, P. L. De Boer, and S. D. Nio, "Sedimentology of a marine intermontane Pleistocene Gilbert-type fan-delta complex in the Crati Basin, Calabria, southern Italy," *Sedimentology*, vol. 34, no. 4, pp. 721–736, 1987.
- [34] R. Coscarelli, R. Gaudio, and T. Caloiero, "Climatic trends: an investigation for a Calabrian basin (southern Italy)," in *Proceedings of the International Symposium the Basis of Civilization of Water Science?*, pp. 255–266, Wallingford, 2004IAHS Publications No. 286.
- [35] T. Caloiero, B. Sirangelo, R. Coscarelli, and E. Ferrari, "An analysis of the occurrence probabilities of wet and dry periods through a stochastic monthly rainfall model," *Water*, vol. 8, no. 2, p. 39, 2016.
- [36] G. Buttafuoco, T. Caloiero, N. Ricca, and I. Guagliardi, "Assessment of drought and its uncertainty in a southern Italy area (Calabria region)," *Measurement*, vol. 113, pp. 205–210, 2018.
- [37] L. Amodio Morelli, G. Bonardi, V. Colonna et al., "L'Arco Calabro Peloritano nell'orogene appenninico-maghrebide," *Memorie della Società Geologica Italiana*, vol. 17, pp. 1–60, 1976.
- [38] G. Bonardi, W. Cavazza, V. Perrone, and R. Rossi, "Calabria--Peloritani terrane and northern Ionian Sea," in *Anatomy of an Orogen: The Apennines and Adjacent Mediterranean Basins*, G. Bonardi, W. Cavazza, V. Perrone, and S. Rossi, Eds., pp. 287–306, Springer, Dordrecht, 2001.
- [39] G. Robustelli and F. Muto, "The Crati River Basin: geomorphological and stratigraphical data for the Plio-Quaternary evolution of northern Calabria, South Apennines, Italy," *Geologica Carpathica*, vol. 68, no. 1, pp. 68–79, 2017.
- [40] I. Guagliardi, N. Rovella, C. Apollaro et al., "Effects of source rocks, soil features and climate on natural gamma radioactivity in the Crati valley (Calabria, Southern Italy)," *Chemosphere*, vol. 150, pp. 97–108, 2016.
- [41] D. Fabbriatore, G. Robustelli, and F. Muto, "Facies analysis and depositional architecture of shelf-type deltas in the Crati Basin (Calabrian Arc, south Italy)," *Italian Journal of Geosciences*, vol. 133, no. 1, pp. 131–148, 2014.
- [42] I. Guagliardi, N. Ricca, and D. Cicchella, "From rock to soil: geochemical pathway of elements in Cosenza and Rende area (Calabria, southern Italy)," *Rendiconti Online della Società Geologica Italiana*, vol. 38, pp. 55–58, 2016.
- [43] E. Le Pera, J. Arribas, S. Critelli, and A. Tortosa, "The effects of source rocks and chemical weathering on the petrogenesis of siliciclastic sand from the Neto River (Calabria, Italy)," *Sedimentology*, vol. 48, no. 2, pp. 357–378, 2001.
- [44] C. Tansi, F. Muto, S. Critelli, and G. Iovine, "Neogene-Quaternary strike-slip tectonics in the central Calabrian Arc (Southern Italy)," *Journal of Geodynamics*, vol. 43, no. 3, pp. 393–414, 2007.
- [45] APHA, *Standard Methods for the Examination of Water and Wastewater*, American Public Health Association, Washington, 2002.
- [46] W. D. Collins, "Graphic representation of water analyses," *Industrial and Engineering Chemistry*, vol. 15, no. 4, pp. 394–394, 1923.
- [47] A. M. Piper, "A graphic procedure in the geochemical interpretation of water-analyses," *Transactions, American Geophysical Union*, vol. 25, no. 6, pp. 914–923, 1944.
- [48] W. F. Langelier and H. F. Ludwig, "Graphical methods for indicating the mineral character of natural waters," *Journal American Water Works Association*, vol. 34, no. 3, pp. 335–352, 1942.
- [49] P. Ravikumar, K. L. Prakash, and R. K. Somashekar, "Evaluation of water quality using geochemical modeling in the Bellary Nala Command area, Belgaum district, Karnataka State, India," *Carbonates and Evaporites*, vol. 28, no. 3, pp. 365–381, 2013.
- [50] N. Subba Rao, A. Subrahmanyam, S. Ravi Kumar et al., "Geochemistry and quality of groundwater of Gummanampadu sub-basin, Guntur District, Andhra Pradesh, India," *Environmental Earth Sciences*, vol. 67, no. 5, pp. 1451–1471, 2012.
- [51] W. Cao, H. Yang, C. Liu, Y. Li, and H. Bai, "Hydrogeochemical characteristics and evolution of the aquifer systems of Gonghe Basin, Northern China," *Geoscience Frontiers*, vol. 9, no. 3, pp. 907–916, 2017.
- [52] N. Subba Rao, G. Vidyasagar, P. Surya Rao, and P. Bhanumurthy, "Chemistry and quality of groundwater in a coastal region of Andhra Pradesh, India," *Applied Water Science*, vol. 7, no. 1, pp. 285–294, 2017.
- [53] C. Apollaro, A. Bloise, R. De Rosa et al., "Caratterizzazione idrogeochimica e qualità delle acque di un acquifero ospitato entro rocce metamorfiche nella Calabria nord occidentale," *Engineering Hydro Environmental Geology*, vol. 12, pp. 95–102, 2009.
- [54] J. Li and A. Heap, "A review of spatial interpolation methods for environmental scientists," *Geoscience Australia*, Canberra, 2008.
- [55] G. Matheron, "Principles of geostatistics," *Economic Geology*, vol. 58, no. 8, pp. 1246–1266, 1963.
- [56] P. Goovaerts, "Geostatistics in soil science: state-of-the-art and perspectives," *Geoderma*, vol. 89, no. 1–2, pp. 1–45, 1999.
- [57] P. Goovaerts, *Geostatistics for Natural Resources Evaluation*, Oxford University Press, New York, NY, USA, 1997.
- [58] A. G. Journel and C. J. Huijbregts, *Mining Geostatistics*, Academic, San Diego, CA, USA, 1978.
- [59] H. Wackernagel, *Multivariate Geostatistics: An Introduction with Applications*, Springer-Verlag, Berlin, 2003.
- [60] E. H. Isaaks and R. M. Srivastava, *Applied Geostatistics*, Oxford University Press, New York, NY, USA, 1989.
- [61] G. Buttafuoco, A. Tallarico, G. Falcone, and I. Guagliardi, "A geostatistical approach for mapping and uncertainty assessment of geogenic radon gas in soil in an area of southern Italy,"

- Environmental Earth Sciences*, vol. 61, no. 3, pp. 491–505, 2010.
- [62] S. Gaglioti, E. Infusino, T. Caloiero, and G. Callegari, “Hydrochemical and qualitative assessment of natural water spring in southern Italy,” *European Water*, vol. 57, pp. 399–405, 2017.
- [63] L. Tortorici, “Lineamenti geologico-strutturali dell’Arco Calabro-Peloritano,” *Rendiconti, Società Italiana di Mineralogia e Petrologia*, vol. 38, pp. 927–940, 1982.
- [64] E. Infusino, G. Callegari, and G. Frega, “Deposizioni atmosferiche nell’area urbana di Cosenza in Calabria,” in *Proceedings XXIII of the Giornata dell’ambiente 2005 “Qualità dell’aria nelle città Italiane”*, vol. 227, pp. 145–154, Accademia dei Lincei, Bardi editore, Rome, 2006.
- [65] J. C. Wilcox, W. D. Holland, and J. M. McDougald, “Relation of elevation of a mountain stream to reaction and salt content of water and soil,” *Canadian Journal of Soil Science*, vol. 37, no. 1, pp. 11–20, 1956.
- [66] P. Celico, “Prospezioni geochimiche,” in *Prospezioni idrogeologiche*, pp. 307–357, Liguori Editore, Napoli, 1986.
- [67] G. Callegari, G. Frega, and E. Infusino, “Problemi di stabilità atmosferica. Loro influenza sulle precipitazioni - un caso di studio nella valle del F. Crati,” in *Proceedings (in CD) of the International Symposium di Ingegneria Sanitaria Ambientale*, pp. 1–16, Taormina, 2004.

Research Article

Research on Stability of an Open-Pit Mine Dump with Fiber Optic Monitoring

Tao Zhigang ^{1,2} Zhu Chun ^{1,2,3} Wang Yong^{1,2} Wang Jiamin ^{1,2} He Manchao,^{1,2}
and Zhang Bo^{1,2}

¹State Key Laboratory for Geomechanics & Deep Underground Engineering, Beijing 100083, China

²School of Mechanics and Civil Engineering, China University of Mining & Technology (Beijing), Beijing 100083, China

³College of Construction Engineering, Jilin University, Changchun 130026, China

Correspondence should be addressed to Zhu Chun; zhuchuncumtb@163.com

Received 16 June 2018; Revised 17 August 2018; Accepted 26 August 2018; Published 30 October 2018

Academic Editor: Luigi Borrelli

Copyright © 2018 Tao Zhigang et al. This is an open access article distributed under the Creative Commons Attribution License, which permits unrestricted use, distribution, and reproduction in any medium, provided the original work is properly cited.

China has over 1500 open-pit mines and 5000 dumps consisting of waste rock from the mining process. Due to dump instability in an open-pit mine and its diverse foundations, landslides and mudslides frequently occur. Heaped loose waste rock and concentrated heavy rainfalls are the two important factors affecting slope stability of a dump. Using the high Dump II within the Nanfen Open-Pit Iron Mine with a slope height of 300 m as a case study, this paper first proposes a physical model similarity ratio according to the on-site engineering geological survey data. The governing principles of deformation in the shallow dump layers in terms of different heaped loads and rainfall were then determined using fiber optic sensing to conduct an experimental study on the monitoring of the dump stability with an indoor physical model. Experimental results confirm that the amount of rainfall and heaped load has a great impact on the landslide in a dump. With an increase in the amount of material heaped onto the pile, the place between two heaped load points is squeezed and slowly deformed. As rainfall begins, the deformation of the rock-soil mass is significant, and constantly increasing rainfall intensity is accompanied by a dangerous sliding surface. Finally, the FLAC3D method was used to simulate the deformation features in the shallow part of Dump II under different heaped load conditions and verify the experimental results of the indoor physical model. By comparing the physical model experiments and numerical simulation results, we propose monitoring the stability of Dump II using this fiber optic sensing technology and provide the scientific basis for stability monitoring of similar dumps to detect the early warning signs of mudslides or landslides.

1. Introduction

Open-pit mines are prolific throughout China, generating enormous amounts of stripped, exploited, and discarded rocks. Stripped rock-soil mass materials are stacked in a dedicated place, which is called the dump [1]. Typically, 30% to 50% of the total land used by open-pit mines is occupied by dumps, so constant improvement of the dumping capacity and safety is important to improve productivity of the mine. Landslides and mudslides constantly occur and significantly affect the safety of dumping operations. As the mining process continues to advance, safety production operations in open-pit mines will always be affected by the slope stability of quarries and dumps [2]. Research on the slope stability

of dumps is of important significance for the safety and economic benefits of mines [3].

A dump is a special engineered rock-soil mass consisting of discarded mixed soil and rock from quarries and created through stacking the materials. The spatial distribution of the dump, slope of the surface, height of slope sediments, strength of mixed materials, depth of slope water, and other factors all affect the stability of the dump slope [4–11]. The main disaster that affects dumps is landslides, and the key for preventing landslides is to control the slope stability of the dump. The main factors affecting dump slope stability are mechanical strength of loose rock-soil in the dump (friction strength parameter c and φ) and characteristic parameters of drainage and seepage of granular particles,

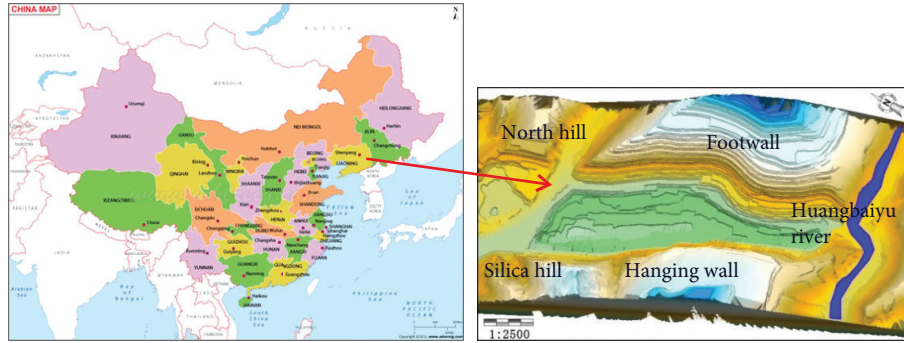


FIGURE 1: Location and satellite maps of the Nanfen Open-Pit Iron Mine.

topography, base lithology, discharge of surface water, groundwater flow, form of the dump slope, process and parameters of dump stacking, and shock caused by construction and earthquakes. In general, these factors can be divided into four categories: external force, physical and mechanical properties of the base, physical and mechanical properties of dumping materials, and the impact caused by water. Disasters affecting dumps can be effectively prevented if influence from these four aspects can be well controlled.

Compared to rock slope problems, research on the stability of dumps started just recently in the 1980s with the development of open-pit mine dump engineering, including methods and theoretical technology for ensuring slope stability. Research on dumps has determined the granular structure, landslide mechanisms, and other aspects based on features and methods of slope stability research, thus forming a complete basis for research on and analysis methods for dump stability.

Dump stability has been extensively analyzed [12–18]. Combined with geological features of the dump, the effects of blasting shock caused by mine production on the slope stability of the dump have been determined [19]. Field measurement units and a recording system were constructed and installed in a waste-dump slope at the Imgi mine to analyze the variation of conditions in unsaturated soil [20]. To investigate the effects of vegetation on runoff and erosion, a field experiment involving eight erosion plots was conducted on a dump at the Antaibao opencast coal mine in Shanxi Province [21]. In order to estimate the failure mode of sliding, numerical simulations on the failure mechanics of dumps were performed using FLAC3D, and a physical model test on the failure processes of dumps was performed using a floor friction model [22]. In order to maintain long-term protection of the environment, one study explored the possibilities of using local species for the mechanical stability of the waste dump in a surface iron ore mine [23]. For waste-dump slopes that form basements, landslides can be prevented by determining the stability evolution principles of dynamic development, and the relationship between the mechanical structure and stability of waste dumps with basements has previously been studied [24].

As the amount of deformation of the dump slope is much larger than that of an ordinary rock slope, it is difficult for conventional slope stability monitoring techniques and methods to be effectively applied to dump slope monitoring

[25, 26]. In terms of dump slope stability monitoring techniques and methods, surface cracks, collapses, land subsidence, and other anomalies are observed in the early period before the actual landslide through manual inspection. After the first observed surface anomalies, new methods, such as theodolite for surface displacement monitoring, total station, levels, and GPS monitoring, can be used. However, these methods are based on point monitoring, which cannot achieve long-distance and large-area monitoring, and have blind zones. Although the reliability can be improved by increasing monitoring points, monitoring costs will also greatly increase, and the increase in monitoring points will affect the integrity and structural safety of monitored rock-soil mass. Also, dumping of the material is a dynamic working process, and surface displacement will constantly change throughout, which will lead to frequent early warnings and cannot accurately provide an early warning of landslides or mudslides.

To address some of these issues, this paper uses Dump II located in the Nanfen Open-Pit Iron Mine in Northeast China as a case study. Fiber optic sensing technology was adopted to perform comparative analysis on the evolution features of dumps under different working conditions. Through the combination of the fiber optic monitoring of indoor physical model experiments and numerical simulations of the stability of the dump, a theoretical and practical foundation is laid for fiber optic monitoring solutions of a mine dump.

2. Regional Geological Survey of Dump II

2.1. Topography. The Nanfen Open-Pit Iron Mine is located in Benxi City, Liaoning Province, of Northeast China [27]. The Eastern boundary spans longitude $123^{\circ}50'$, and the northern boundary traverses latitude $41^{\circ}07'$. The mine is a monocline structure mainly composed of metamorphic rock strata, alpine glaciation landforms forming the surface, with an east-west strike (Figure 1). Gullies crisscross the landscape with relatively less vegetation coverage and steep hilltop slopes. The elevation of the general mountains near the mine reaches 500 m to 600 m, with the highest peak at 963 m and the lowest at 296 m, a relative height difference of 667 m. In the southwestern area of the mine, the relative height is 300 m to 400 m with surface vegetation currently being developed.

TABLE 1: Strength parameters of Dump II.

Lithology	State	Density ($\text{kg}\cdot\text{m}^{-3}$)	Parameter Cohesion (C/kPa)	Internal friction angle ($^{\circ}$)
Flint limestone	Natural	2650	670.0	40.0
Green-purple sandy shale	Natural	2600	620.0	32.0
Dark-purple mica shale	Natural	2580	490.0	27.8
Gray fine quartz sandstone	Natural	2680	760.0	40.2
Crystalline limestone	Natural	2650	670.0	40.0
Egg-green marl	Natural	2580	490.0	27.8
Quaternary residual slope deposit	Natural	1800	8.0	30.0
	Saturated	1920	10.0	28.0
Dumping materials (slag discharged from the hanging side of the mine)	Natural	2100	20.0	35.0
	Saturated	2250	45.0	30.0
Upper dumping materials (slag discharged from the heading side of the mine)	Natural	2100	40.0	33.0
	Saturated	2250	45.0	30.0
Middle dumping materials (slag discharged from the heading side of the mine)	Natural	2100	25.0	34.0
	Saturated	2250	50.0	31.0
Lower dumping materials (slag discharged from the heading side of the mine)	Natural	2100	10.0	35.0
	Saturated	2250	20.0	32.0
Debris accumulation	Natural	2100	80.0	20.0
	Saturated	2250	100.0	18.0

TABLE 2: Key deformation parameters of granular waste rock.

Lithology	Initial void ratio (n)	n	Parameter Compression modulus (MPa)	Poisson's ratio
Upper dumping materials of the dump	0.6	37.4%	26.05	0.37
Middle dumping materials of the dump	0.57	36.4%	26.4	0.35

The five original historical dumps have been combined into the three current dumps in the southwest, southeast, and northeast of the quarry, namely, Dumps II, IV, and V. The current Dump II, created by the merger of the original Dumps II and III, is located in the hanging side southwest of the quarry, which mainly uses an autocrushing-belt conveyor-dumping machine combined with the transportation and dump process to discard waste rock in the hanging side through an east-to-west “U”-shaped valley consisting of the Dadonggou and Fengjiadonggou gullies (Figure 2). Overall, the bottom of the Dadonggou and Fengjiadonggou gullies is high in the east and low in the west, and the elevation of the current valley below the slope foot of the dump changes from 330 m to 420 m.

2.2. Strata Lithology and Strength Parameters of Accumulation.

The main lithology of Dump II within the Dadonggou and Fengjiadonggou gullies consists of the Archean Anshan Group, Proterozoic Liaohe Group, Cambrian and Sinian strata, and Cenozoic Quaternary strata. Specifically, the strata consist of egg-green marl of the Nanfen Formation in the Sinian system, gray fine quartz sandstone from the Qiaotou Formation in the Sinian system, flint limestone of the Jianchang Formation in the Cambrian system, dark-purple mica shale of the Maozhuang Formation in the Cambrian

system, crystal limestone of the Zhangxia Formation in the Cambrian system, and green-purple sandy shale of Xuzhuang Formation in the Cambrian system. Among them, the basic section of the internal foundation of the dump is mainly made of marl, and a few quartz sandstones appear in the southeast corner of the dump. The upper part of the dump is covered with a Quaternary slope diluvium layer varying in thickness from 0.0 m to 6.0 m. The bearing capacity of the bed rock is mainly affected by the compressive strength of the bed rock and is related to the development of jointed fissures.

Based on the Code for Investigation of Geotechnical Engineering of China (GB50021-2001) and Specification of Soil Test of China (SL237-99), a large number of in situ direct shear field tests, indoor triaxial tests, indoor direct shear tests, and on-site push shear tests on Dump II in the Nanfen Open-Pit Iron Mine were performed in April 2014 by the Institute of Rock and Soil Mechanics, Chinese Academy of Sciences. According to the particle size distribution law of various granular waste rock measured at the site, the sample was made in the laboratory. The indoor triaxial compression test and the direct shear test of the granular waste rock were carried out according to the bulk gradation scheme and the stress state, the physical and mechanical parameters of the bulk material in Dump II are comprehensively obtained, and their results are shown in Tables 1 and 2.

TABLE 3: Statistics of precipitation in the Benxi area.

Indicator	Precipitation (mm)	Indicator	Precipitation (mm)
Average annual precipitation	848–856	Annual maximum precipitation	1212.7
Monthly maximum precipitation	487	Annual minimum precipitation	518.5
Daily maximum precipitation	83	Average annual evaporation	1628.4
Annual maximum evaporation	1843.4	Annual minimum evaporation	1374.1



FIGURE 2: Mining area diagram.

2.3. Hydrogeological Features. The mine is located at midlatitude within a monsoon and continental climate. The precipitation in the flood season accounts for about 70% in the entire year, of which the precipitation in July and August accounts for about 50% of the annual precipitation with a relatively high temperature difference all year round (Table 3). The Miao'ergou River to the north and Huangbaiyu River to the south cross the area from east to west and are parallel to Zones 1 (Dadonggou; east) and 2 (Fengjiadonggou; west) of Dump II and located outside the region. There are no rivers feeding into the dump site. Water in the region is not currently under development.

Dump II is classified as a gully dump, and atmospheric precipitation is a major source of surface water and groundwater, with strong seasonal variations (April–August). Currently, the dump, in Zone 1 (Dadonggou), has a convergence area of $86 \times 10^4 \text{ m}^2$ with a circumference of 3.7 km; in Zone 2 (Fengjiadonggou), the convergence area is $97.5 \times 10^4 \text{ m}^2$ with a circumference of 3.98 km. According to the survey carried out by the Institute of Rock and Soil Mechanics, Chinese Academy of Sciences, the extent of the water distribution on the platform surface area of Dump II in the Nanfen Open-Pit Iron Mine is mainly from atmospheric precipitation. In addition, there is a layer of phreatic groundwater, and there is a layer of bed rock fissure water within the site. The groundwater burial depth is about 12.0 to 15.0 m.

The waste rock in the dumping site is mainly composed of gravel, block stone, sand, and clay. The permeability coefficient is difficult to measure in an indoor test and is generally determined according to field testing. According to the site conditions, the test method for the permeability coefficient of the dumping site was performed using the preburied steel pipe method. According to local rainfall conditions, the on-site single-ring water injection tests were completed

in the investigation area of Zone 1 (Dadonggou) and Zone 2 (Fengjiadonggou), according to the requirements of the Water Injection Test Procedure (YS5014-2000). The permeability coefficient of each zone can be calculated as

$$\begin{aligned} \text{Zone 1 : } K_1 &= 1.92 \times 10^{-2} \text{ cm/s,} \\ \text{Zone 2 : } K_2 &= 1.65 \times 10^{-2} \text{ cm/s.} \end{aligned} \quad (1)$$

3. Fiber Optic Monitoring Indoor Physical Model Experiment of Dump II

Currently, real-time monitoring and early warnings of landslides and mudslides in the dump are enormous problems. In terms of the regional geological survey of Dump II of the open-pit mine, it is urgent to adopt new technologies and new methods to monitor the deformation of Dump II in order to maintain a safe work environment and continue to develop the iron belt at this location. Based on the principle of distributed optical fiber monitoring and the occurrence mechanism of mudslide in the dump, the experimental study on Dump II with the fiber optic monitoring indoor physical model was performed.

3.1. Working Principle of the Distributed Optical Fiber Monitoring System. The basic measurement principle of the Brillouin optical fiber time domain analysis (BOTDA) is shown in Figure 3. BOTDA uses the Brillouin frequency shift caused by the Brillouin scattering light through stimulation. The shift is caused by changes in axial temperature and strain of optical fibers. Lasers need to be placed at both sides of the optical fiber, and continuous and pulsed light are injected into the optical fiber to create loop monitoring [28–33]. BOTDA demodulation equipment used in the indoor physical model experiment was the NBX-6050A fiber optic strain demodulator produced by Neubrex (Japan). This instrument can obtain a relatively strong signal from a highly scattered source, and its spatial resolution can reach up to 5 cm with an accuracy $7 \mu\epsilon$ (0.3°C) with a monitoring distance of up to 20 km. The instrument was set up to continuously collect data for real-time monitoring.

3.2. Indoor Physical Model Test

3.2.1. Similarity Ratio Determination

(1) Model and Particle Size Determination. This experiment used Dump II within the Nanfen Open-Pit Iron Mine as the example with the physical simulation method. The

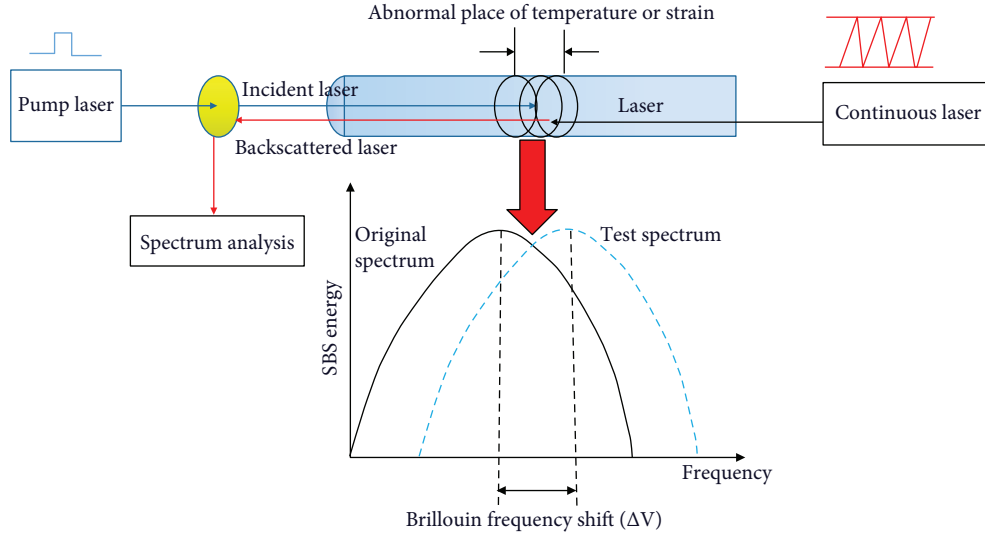


FIGURE 3: Basic principle diagram of BOTDA.

TABLE 4: Content of each grade of dispersion in the dump (Fengjiadonggou).

Particle group collectively	Particle group classification		Particle size range (d/mm)	Content (%)
Giant particle group	Boulder (rock)		$d > 200$	5.50
	Pebble (gravel)		$200 > d > 60$	17.72
Coarse grain group	Gravel (breccia)	Coarse gravel	$60 > d > 20$	27.15
		Medium gravel	$20 > d > 5$	27.55
		Fine gravel	$5 > d > 2$	10.91
Fine grain group	Grit, powder		$2 > d > 0.005$	10.38
	Clay particle		$0.005 > d$	0.80

simulated similarity ratio was calculated according to the following formula:

$$\frac{\text{Actual height of the dump slope } H_1}{\text{The maximum particle size } D_1 \text{ of the dump}} = \frac{\text{Simulated slope height } H_2}{\text{The maximum particle size } D_2 \text{ of the material used by the model}} \quad (2)$$

The following parameters were determined by summarizing and analyzing the current materials of Dump II:

- (i) $H_1 = 250$ m (Fengjiadonggou), $D_1 = 1000$ mm, and $H_2 = 1$ m; the largest volume of Dump II: $3800 \times 10^4 \text{ m}^3$
- (ii) According to local rainfall statistics, annual precipitation is typically 847 mm, the maximum annual precipitation is typically 1212 mm, and the minimum annual precipitation is typically 518 mm; the maximum flow of the basin in the rainy season is typically 110.5 L/S

In summary, D_2 can be obtained from formula (2):

$$D_2 = \frac{H_2 \times D_1}{H_1} = 4 \text{ mm}. \quad (3)$$

Therefore, the similarity ratio of the indoor physical model was set to 1:250, and the maximum particle size of the material used in the simulation was 4 mm. According to the principle of similarity ratio, the content of each grade of on-site sieved dispersion (Table 4), and the similarity ratio, indoor experiment materials were matched to meet outdoor conditions of the dump, as shown in Table 5.

(2) *Determining Daily Maximum Precipitation.* According to local rainfall statistics acquired by the local meteorological center, the daily maximum precipitation of the local area was set to 83 mm, the rainfall area s of the experimental model was 4 m^2 , and the hourly precipitation v was 60 L, and according to the experimental requirements, the rainfall time t needed to be calculated when the indoor

TABLE 5: Content of each grade of the indoor test.

S/N	Particle size range (d/mm)	Sieved quality (g)	Content (%)
1	$d > 2$	98	6.7
2	$2 > d > 1$	238	16.46
3	$1 > d > 0.75$	437	30.15
4	$0.75 > d > 0.5$	379	26.18
5	$0.5 > d > 0.25$	123	8.52
6	$0.25 > d > 0.075$	163	11.26
7	$0.075 > d$	10	0.73

test reached the maximum daily precipitation was calculated as follows:

$$t = \frac{ps}{v}, \quad (4)$$

where t is the rainfall time/h, p is the daily maximum precipitation of 83 mm, s is the precipitation area of 4 m^2 , and v is the hourly precipitation of 60 L.

The time needed to reach the maximum daily precipitation was calculated to be 5.5 h. During the experiment, according to local rainfall conditions, rainfall occurred for 5.5 h for the first day, 5.5 h for the second day, and 5.5 h for the third day. The amount of strain endured by a single fiber optic due to rainfall was then compared across these three days.

3.2.2. Physical Model Construction. According to the similarity principle of the indoor physical model experiment compared to outdoor conditions, this experiment design was based on the physical similarity simulation. According to the similarity ratio of 1:250, the experimental model was set up to be $2 \text{ m} * 2 \text{ m} * 1 \text{ m}$ with the slope top of $2 \text{ m} * 0.5 \text{ m}$ and the slope angle of 34° . Filling of experimental materials was executed in strict accordance with Table 5.

The main goal of this experiment was to simulate the analysis of deformation of rock-soil mass in different directions during dump heaped load and rainfall in the dump of the open-pit mine. Therefore, the laying of optical fibers becomes increasingly more important during the experiment. The three-dimensional schematic diagram of the laying of optical fibers is in Figure 4 (X direction is the slope's inclination direction, Y direction is the slope direction, and Z direction is the slope settlement direction). There were two layers in the X direction with six sensing optical fibers in each layer. Upper layers (Layer X1) were numbered as X11, X12, X13, X14, X15, and X16 with the linear length of the monitoring optical fiber of 67 cm, and lower layers (Layer X2) were numbered as X21, X22, X23, X24, X25, and X26 with the linear length of the monitoring optical fiber of 108 cm. There were two layers in the Y direction with two sensing optical fibers in each layer. Upper layers were numbered as Y11 and Y12, and lower layers were numbered as Y21 and Y22 with the linear length of the monitoring optical fiber of 200 cm. Four sensing optical fibers were arranged in the Z direction and were numbered as Z1, Z2,

Z3, and Z4 with the linear length of the monitoring optical fiber of 170 cm.

The spacing of each sensing optical fiber is shown in Figure 5. The spacing between optical fibers at the same level in the X layer was 360 mm, and the spacing between the optical fibers near the model boundary and the model boundary was 10 mm. The vertical distance between optical fibers in the X1 layer and the X2 layer was 220 mm. The horizontal distance between the Y11, Y12, and Y21 layers and the Y22 layer was 110 mm. The vertical distance between the Y1 layer and the Y2 layer was 220 mm. Z1 and Z2 were located 670 mm from the bottom of the slope and located at the point of trisection of the model in the Y direction. Z3 and Z4 and Z1 and Z2 were symmetrically distributed, and the horizontal distance between two sets of optical fibers was 426 mm. Parameters of the optical fiber strain analyzer are shown in Table 6.

Among many factors affecting the stability of the dump in the open-pit mine, heaped load and rainfall are the two most important factors. This experiment was divided into two sections to simulate the impact of different heaped loads and rainfall amounts on the deformation of the slope. Dumping in Dump II of Nanfen Open-Pit Iron Mine is divided into two ways—autodumping and dumping with a crawler-type rock-dumping machine. The heaped load process during the model experiment was mainly divided into two subsections according to the dumping features of the dump. The first subsection of the heaped load process mainly simulated the impact of autodumping on the deformation of the slope, and two passageways of rock dumping were set up at the point of trisection at the top of the slope to loads 20 kg, 50 kg, and 70 kg. When the rock-soil mass stabilized, the amount of deformation of each sensing optical fiber was calculated.

The second subsection of the heaped load process simulated the impact of dumping by the crawler-type rock-dumping machine on the deformation of the slope, and four passageways of rock dumping were set up at the point of quinquesection at the top of the slope to calculate the amount of deformation of each sensing optical fiber under the conditions of 100 kg and 140 kg. The impact of different rainfall conditions on the slope deformation was simulated when the heaped load stabilized. The rainfall time required to reach the local daily maximum precipitation was calculated as 5.5 h (Formula 4) according to hydrogeological conditions in the Nanfen Open-Pit Iron Mine. This experiment used 5.5 h of rainfall for three consecutive days and compared and analyzed the amount of deformation of each sensing optical fiber so as to obtain the impact of different amounts of rainfall on the slope deformation of the dump.

According to the schematic diagram of the indoor physical model test, a $2 \text{ m} * 2 \text{ m} * 1 \text{ m}$ single-stage dump experimental model was created on-site and reinforced by various materials. The layout line of the fiber optics was designed according to the model size and characteristics of the optical fibers. As the experiment mainly performed deformation of the dump under different loading and rainfall conditions through fiber optic monitoring, the optical fibers were arranged horizontally, longitudinally, and vertically to compare and capture

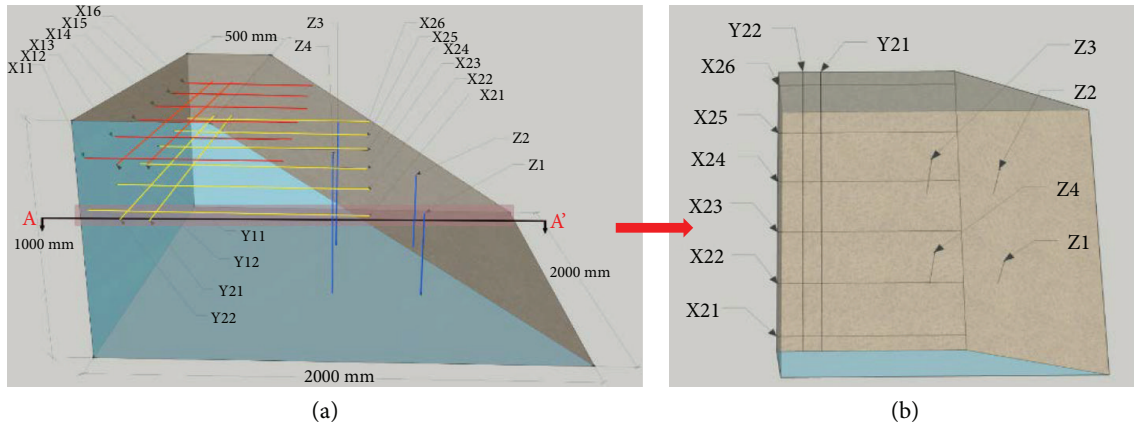


FIGURE 4: Three-dimensional plan for the laying of sensing optical fibers. (a) Three-dimensional schematic diagram. (b) A-A' cross-section drawing.

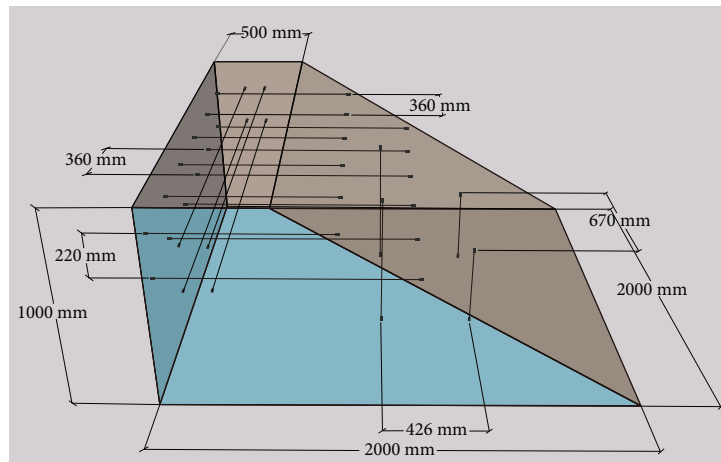


FIGURE 5: Three-dimensional plan of the distribution spacing of optical fibers.

TABLE 6: Parameter settings of the optical fiber strain analyzer.

Measurement range (m)	Sampling interval (m)	Pulse width (ns)	Average time	Starting frequency (GHz)	Scan interval (MHz)	Stop frequency (GHz)
100	0.05	10	2 ¹⁶	10.700	5	12.195

the location and size of deformation throughout the dump. The location of each optical fiber was indicated in the model in advance for the analysis of experimental data at a later period. Performing indoor matching according to the calculated content of each grade in the indoor experiment, experimental materials were blended according to set matching, optical fibers and fill material were laid layer by layer, and then laid optical fibers were welded to form the distributed monitoring network, as shown in Figure 6.

3.2.3. Analysis of Fiber Optic Strain under Different Loading Conditions. To survey the deformation of each optical fiber under loading conditions of 20 kg, 50 kg, 70 kg, 100 kg, and

140 kg, the amount of deformation of optical fibers was first surveyed before surcharging to obtain a background load. Then, each load of 20 kg, 50 kg, and 70 kg was individually and in sequence applied at the point of trisection at the edge of the slope top of the dump model, and the deformation of optical fibers was surveyed when the surcharge stabilized. Next, a load of 100 kg and 140 kg was applied at the point of quinquesection of the dump, and the deformation of each optical fiber was surveyed when the surcharge stabilized. The experimental process is shown in Figure 7. As the rock-soil mass materials were homogeneous, the symmetrical nature of the system indicates that the strain of the X11 optical fiber would be the same as the X16 optical fiber, the strain of the

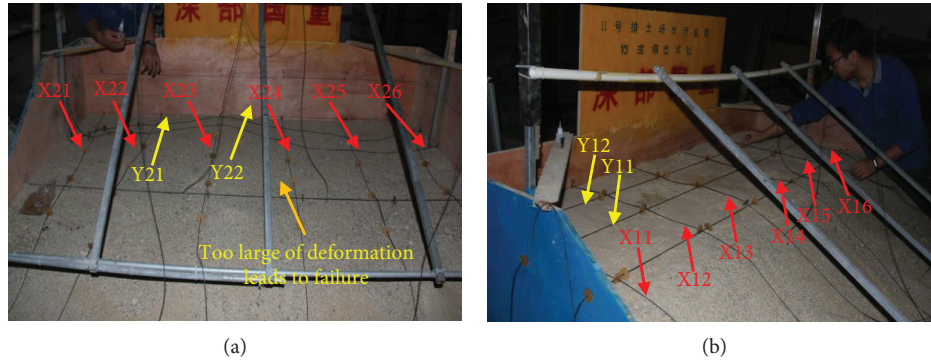


FIGURE 6: Laying and welding of optical fibers. (a) Laying of optical fibers in the lower layer. (b) Laying of optical fibers in the upper layer.

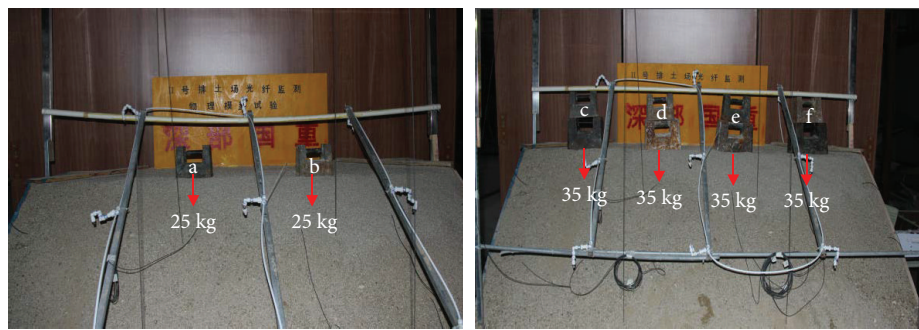


FIGURE 7: Fiber optic strain experiment under different loading conditions.

X12 optical fiber would be the same as the X15 optical fiber, the strain of the X13 optical fiber would be the same as the X14 optical fiber, the strain of the X17 optical fiber would be the same as the X22 optical fiber, the strain of the X18 optical fiber would be the same as the X21 optical fiber, the strain of the X19 optical fiber would be the same as the X20 optical fiber, the strain of the Z1 optical fiber would be the same as the Z2 optical fiber, and the strain of the Z3 optical fiber would be the same as the Z4 optical fiber. In actuality, the measured strain trend was consistent with the theoretical value, although differences did exist.

(1) *Analysis of Optical Fiber Strain in the X Direction.* Using the applied loads and the optical fibers to measure deformation within the rock-soil mass, positive values of the two indicate tension while negative values indicate pressure. Settings of various parameters of BOTDA in the experiment are shown in Table 6. Fiber optic data of each experiment was synthesized: the measured value was subtracted from the initial value to obtain the corresponding strain value and corresponding location data of each optical fiber to the fiber optic sensing network was intercepted to draw the strain network planning, which are shown in Figure 8.

With a constant increase in the load, the overall tensile strain of the optical fibers also gradually increased, and the amount of settlement and slippage in different locations of the dump also correspondingly increased (Figure 8). Deformation of optical fibers in the X1 layer was more obvious (Figure 8(a)) and located just below the location of the

applied load. The strain in the center of the optical fibers was more prominent, and the strain of the X12, X13, and X14 optical fibers extended about $3000 \mu\epsilon$ from the sensor, which was gradually reduced and tended to stabilize from the maximum strain along the direction of laying of the optical fibers. Compared to Figure 8(b), the overall change in the optical fibers in the X2 layer was quite obvious. Optical fiber strain in different positions increased as load increased; however, as the distance of the position of the optical fibers in the X2 layer from the slope top increased from the top relative to the optical fibers in the X1 layer, they were less affected by the load application position. Therefore, no obvious sudden change in the strain occurred.

(2) *Analysis of Optical Fiber Strain in the Y Direction.* Loads were applied at the points of trisection and quinquesection near the slope edge at the top of the slope of the indoor dump model. The loads applied at the trisection point were 20 kg, 50 kg, and 70 kg and 100 kg and 140 kg at the point of quinquesection. Because the impact of the trisection load on the optical fiber strain was quite different from that of the quinquesection loading in the direction of Y, the strain of optical fibers in the Y direction loaded at the point of trisection and the point of quinquesection is shown separately in Figure 9.

Figure 9 shows that the strain of optical fibers synchronously occurred with the deformation of the rock-soil mass of the dump, and the uneven settlement of the rock-soil mass occurred where the load was applied. When the optical fiber

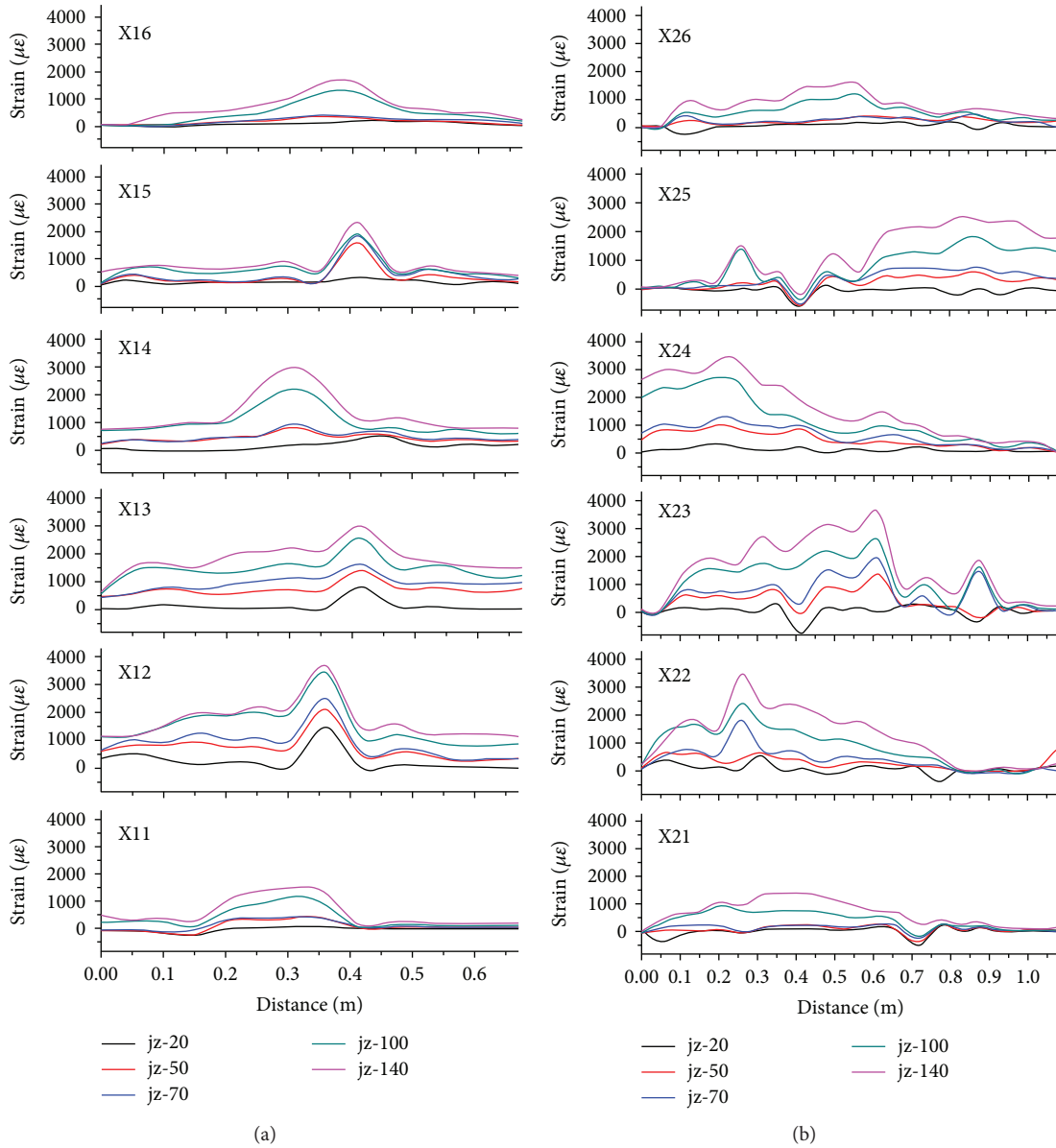


FIGURE 8: Strain diagram of optical fibers in the X direction under different loading conditions. (a, b) Strain diagram of upper and bottom optical fibers, respectively, in the X direction under different loading conditions.

is in a state of tension, the strain is positive. As the rock-soil mass in the entire dump can be regarded as a plastic body, the rock-soil mass will be squeezed in between the two applied loads. When the optical fiber is under pressure, the strain is negative. By comparing Figures 9(a) and 9(b), when three-level loads were applied to the dump, the maximum strains of the Y11, Y12, Y21, and Y22 optical fibers were $2060 \mu\epsilon$, $279 \mu\epsilon$, $615 \mu\epsilon$, and $229 \mu\epsilon$, respectively. When two-level loads were applied to the dump, the maximum strains of the Y11, Y12, Y21 and Y22 optical fibers were $2223 \mu\epsilon$, $409 \mu\epsilon$, $689 \mu\epsilon$, and $287 \mu\epsilon$, respectively. Experimental results show that a greater amount of deformation leads to the rock-soil mass being closer to the load application position in different directions. As the distance increased, the load had less influence on the deformation of the rock-soil mass.

(3) *Optical Fiber Strain Analysis in the Z Direction.* Z1, Z2, Z3, and Z4 optical fibers were laid from the bottom to the top of the slope vertically, where Z1 and Z2 were arranged symmetrically in the Y direction at the point of trisection, 67 cm from the slope foot, and Z3 and Z4 were arranged symmetrically in the Y direction at the point of trisection, 134 m from the slope foot. After applying loads of 20 kg, 50 kg, 70 kg, 100 kg, and 140 kg to the model, the strain on the optical fibers was tested in the Z direction to further determine settling of the dump more intuitively. Optical fiber strain in the Z direction is shown in Figure 10.

As the heaped load increased, the tensile strain of the optical fibers also correspondingly increased, indicating that settling of the dump model gradually increased with the increase in load. When the heaped load increased from

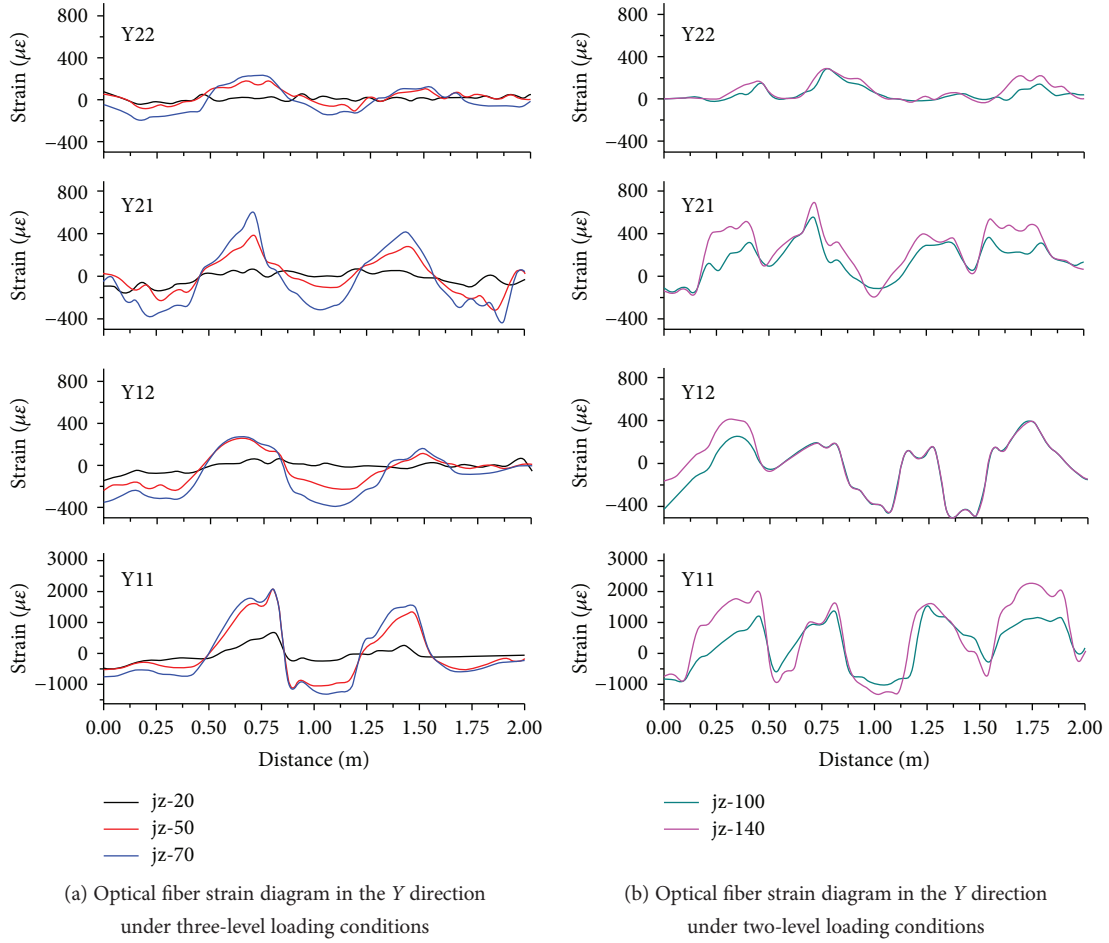


FIGURE 9: Strain diagram of optical fibers in the Y direction under different loading conditions.

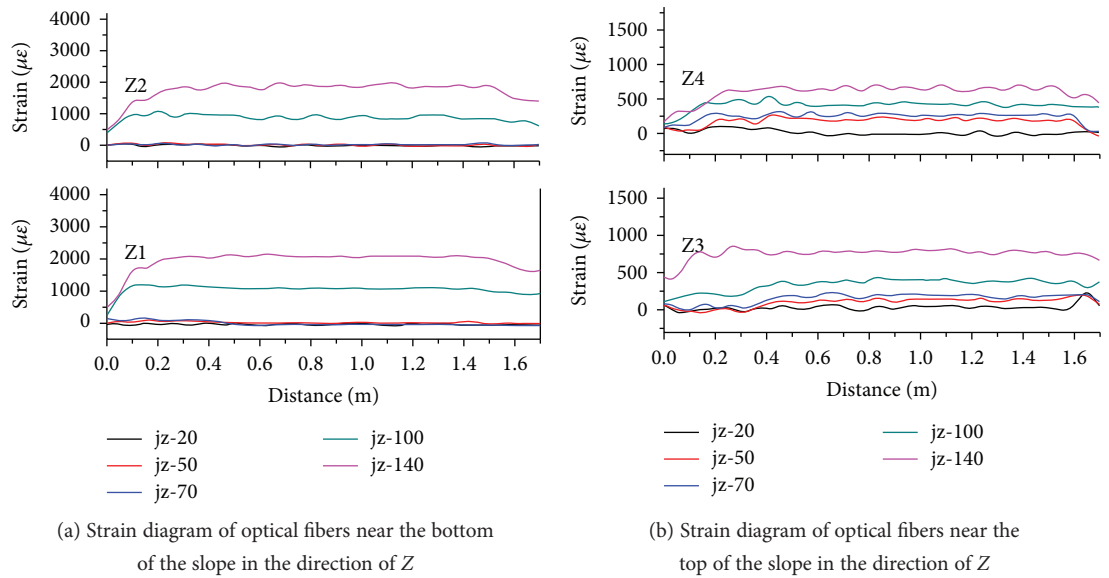


FIGURE 10: Strain diagram of optical fibers in the Z direction under different loading conditions.

20 kg to 70 kg, the relative strain increment of each optical fiber in the Z direction was not very obvious. As the heaped load continued to increase, the relative strain increment of

optical fibers gradually increased, and when the heaped load reached 140 kg, the relative settlement increment of the dump model reached its maximum value.



FIGURE 11: Fiber optic strain experiment under different rainfall conditions.

3.2.4. Analysis of Fiber Optic Strain under Different Rainfall Conditions. To determine the effects of rainfall on the stability of a dump, it “rained” for 5, 10, and 15 hours with a rainfall device. The strain of each optical fiber under different rainfall conditions was then determined. The experimental process is shown in Figure 11.

(1) *Analysis of Optical Fiber Strain in the X Direction under Different Rainfall Conditions.* Comparative analysis was performed for the six optical fibers’ strains in layers X1 and X2 on days one through three (Figure 12).

The strain of the sensing optical fibers was greatest with the rainfall on the first day, decreasing on the second day, and was least on the third day. On the first day of rainfall, a sudden change in the strain of each optical fiber occurred at various positions throughout the model (Table 7). The overall strain trend and positions of sudden change of the X11 optical fiber was essentially consistent with that of the X16 optical fiber, along with X12 and X15 and X13 and X14. This is consistent with the symmetrical arrangement of sensing optical fibers in the experimental model.

It can be seen from six optical fibers in the X2 layer that the sensing optical fiber strain shows the same variation trend as that in the X1 layer. Also same as X1, X2 had a sudden change in strain at various positions throughout the model with the first day of rainfall (Table 7). As the plane distance from the X2 layer to the load application position was large, the overall strain of the sensing optical fibers was much smaller than that of the optical fibers in the X1 layer.

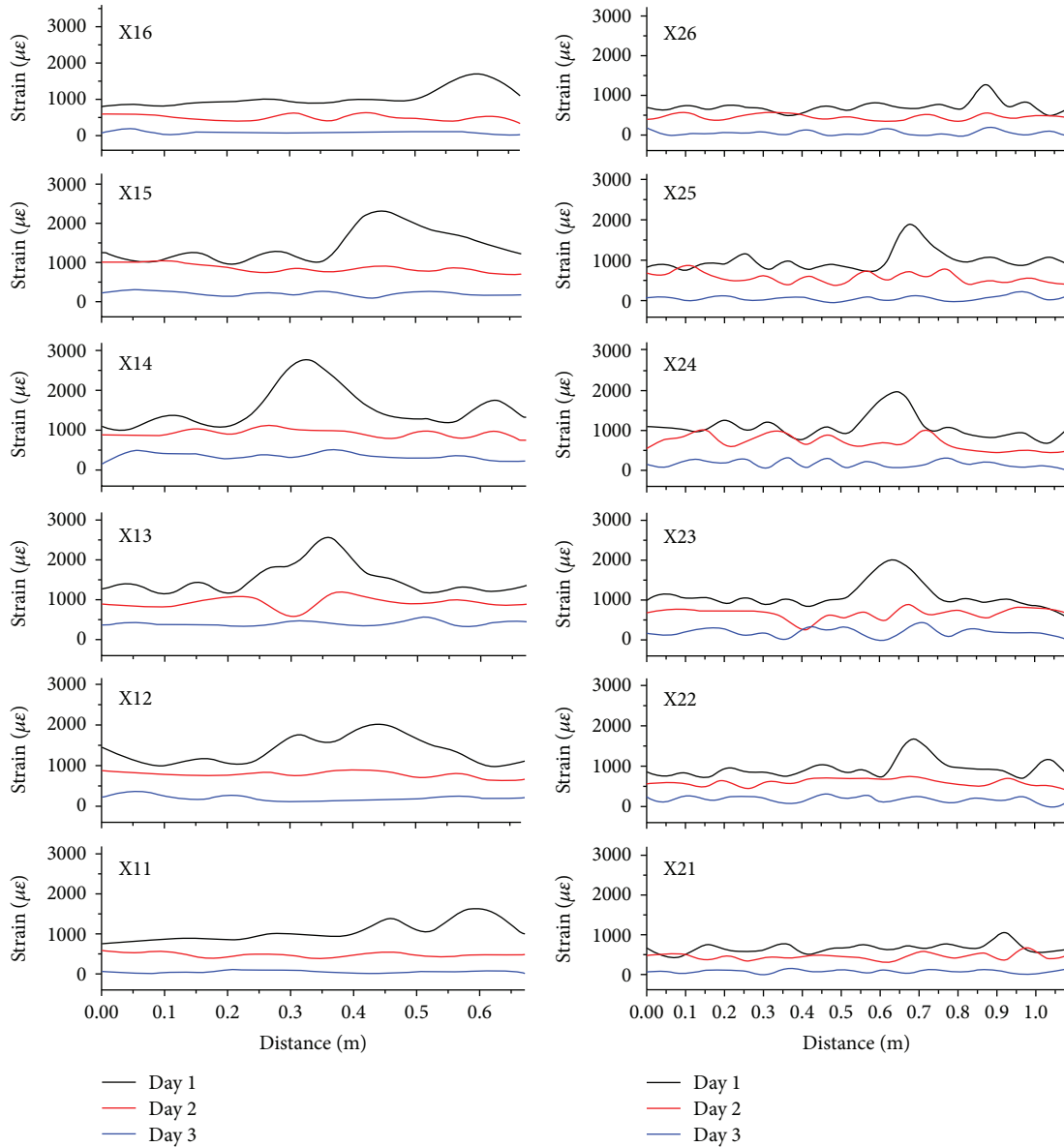
Using X13 and X23 sensing optical fibers for comparative analysis of strain during each day of rainfall, there was a very obvious trend of the strain endured by the optical fibers over the course of the three days of rainfall. On the first day of rainfall, the strain was relatively large, reaching $2560 \mu\epsilon$. On the second and third days of rainfall, the strain decreased and tended to stabilize along the direction of the length of the optical fiber. This occurred because loose particles of the rock-soil mass before rainfall have high porosity, are filled mostly with air rather than liquids, and are able to be highly compressed. With the rainfall on the first day, the rock-soil mass is washed out by rainwater, and the flow of pore water drives the deformation of the rock-soil mass; it also becomes gradually saturated. The strain in the positions 0.36 m from the X13 optical fiber and 0.63 m from the X23 optical fiber suddenly increased on the first day because the amount of

deformation of the rock-soil mass suddenly increased in this position due to movement of particles caused by the increased water in the dump. More attention is provided to the generation of a potential sliding surface in the follow-up analysis. At the end of the rainfall on the first day, the rock-soil mass started to consolidate and settle, becoming denser and less compressible. The impact of rainfall on the second and third days on the amount of deformation of optical fibers becomes increasingly smaller with the passage of time, indicating that the overall rock-soil mass was in a relatively stable state with relatively small amount of deformation.

(2) *Analysis of Optical Fiber Strain in the Y Direction under Different Rainfall Conditions.* As shown in Figure 13, optical fibers in the Y direction had a similar trend as those in the X direction. As the layout of optical fibers in the Y direction was parallel to the slope, the two positions of sudden change in the strain appeared along the length of the optical fibers. Positions with sudden change in strain were distributed symmetrically along the midpoint of the optical fibers; however, the overall trend of the Y22 optical fiber was relatively stable, without obvious strain with a sudden change. This is mostly due to the locations of the Y22 optical fiber. The Y22 optical fiber was far from the sliding direction of the rock-soil mass and close to the back of the model; the model had a great resistance to deformation in this place. The overall strain at this location was relatively small, and the strain along the direction of optical fibers was relatively stable. Optical fibers in both the upper and lower layers in the directions of X and Y were all in this same plane. Comparing Figures 12 and 13, the strain trends of the strain diagrams of optical fibers in each layer in the directions of X and Y were the same.

(3) *Analysis of Optical Fiber Strain in the Z Direction under Different Rainfall Conditions.* It can be seen from the strain diagram of the four optical fibers in the Z direction that the strain of Z1 was similar to that of Z2, as was Z3 and Z4 (Figure 14). All positions of optical fibers with a sudden change in strain appeared at the boundary of optical fibers and slope, which is shown in Figure 15. However, the overall strain was relatively small, and positions with sudden change and strain are shown in Table 7.

3.3. Potential Sliding Surface Judgments. Table 7 summarizes the sudden change in the strain of each optical fiber during



(a) Comprehensive strain diagram of upper optical fibers in the X direction with three days of rainfall

(b) Comprehensive strain diagram of bottom optical fibers in the X direction with three days of rainfall

FIGURE 12: Comprehensive strain diagram of optical fibers in the X direction with three days of rainfall.

rainfall on the first day. Strain increments at varying degrees appeared in each optical fiber during rainfall on the first day, and due to the symmetrical distribution of sensing optical fibers, strain of each optical fiber had symmetrical growth. These sudden changes in strain indicate new deformation at these locations, and the location of the most dangerous sliding surface was obtained from a comprehensive analysis of the strain of each optical fiber.

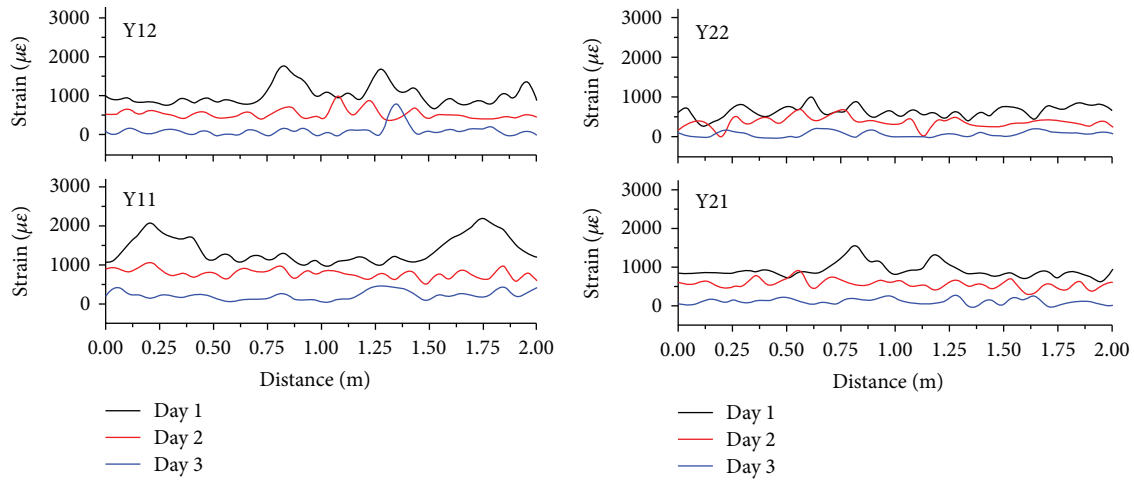
Based on the slope failure mechanisms and the geometrical characteristics of a sliding surface, the most common types of landslides that occurred during testing are classified as four types: plane slide failure, circular slide failure, wedge slide shape failure, and compound slide failure. The sudden change in the strain of each optical fiber shows that slow

trace deformation had already begun inside the dump, accompanied by shear failure due to partial tension and continuously decreased strength of the slope. However, no actual landslide had yet occurred. The sudden change in the strain of each sensing optical fiber during rainfall on the second and third days indicates that with the increase of rainfall time, the sliding surface gradually extended deeper into the slope, and finally, the sliding surface was completely linked. The process creating the sliding surface is shown in Figure 16. However, as rainfall stopped, the rock-soil mass of the dump consolidated and settled, and the entire dump stabilized.

Coordinates of positions with sudden change in the strain in the three-dimensional schematic diagram of the indoor

TABLE 7: Corresponding data of the strain of each optical fiber.

Fiber no.	Fiber length (m)	Position with sudden change in the strain (m)	Strain in the place with sudden change ($\mu\epsilon$)	Strain increment ($\mu\epsilon$)
X11	0.667	0.59	1624	571
X12	0.667	0.43	2028	917
X13	0.667	0.36	2558	1236
X14	0.667	0.32	2777	1497
X15	0.667	0.44	2323	1170
X16	0.667	0.61	1708	731
X21	1.078	0.92	1042	346
X22	1.078	0.69	1675	721
X23	1.078	0.63	1991	971
X24	1.078	0.64	1969	912
X25	1.078	0.67	1910	952
X26	1.078	0.87	1292	552
Y11	2.0	0.21/1.75	2066/2195	892/994
Y12	2.0	0.82/1.27	1772/1698	892/690
Y21	2.0	0.81/1.20	1541/1321	661/424
Y21	2.0	—	—	—
Z1	1.694	0.46	695	309
Z2	1.694	0.43	709	314
Z3	1.694	0.85	885	338
Z4	1.694	0.87	896	357



(a) Comprehensive strain diagram of upper optical fibers in the Y direction with three days of rainfall

(b) Comprehensive strain diagram of lower optical fibers in the Y direction with three days of rainfall

FIGURE 13: Comprehensive strain diagram of optical fibers in the Y direction with three days of rainfall.

physical model experiment were connected (Figure 17). The slope was in an extremely unstable state during rainfall on the first day, and a dangerous circular sliding surface formed (blue).

Figure 18 shows the porosity within the particles of rock-soil materials used by the experiment observed through 50x magnification by SEM before and after rainfall. The porosity before rainfall was significantly less than that after rainfall because the materials that comprised the

rock-soil mass were mainly fine sandstone composed of argillaceous cementation. Affected by rainfall, the argillaceous cements were eroded, so that cementation of sandstone particles diminished. During the rainfall, fine particles slid into the pores among the coarse particles and gradually formed small cracks as particles moved. These cracks gradually increased and linked into the dangerous sliding surface. Due to the limited precipitation in the experiment, no actual landslide occurred.

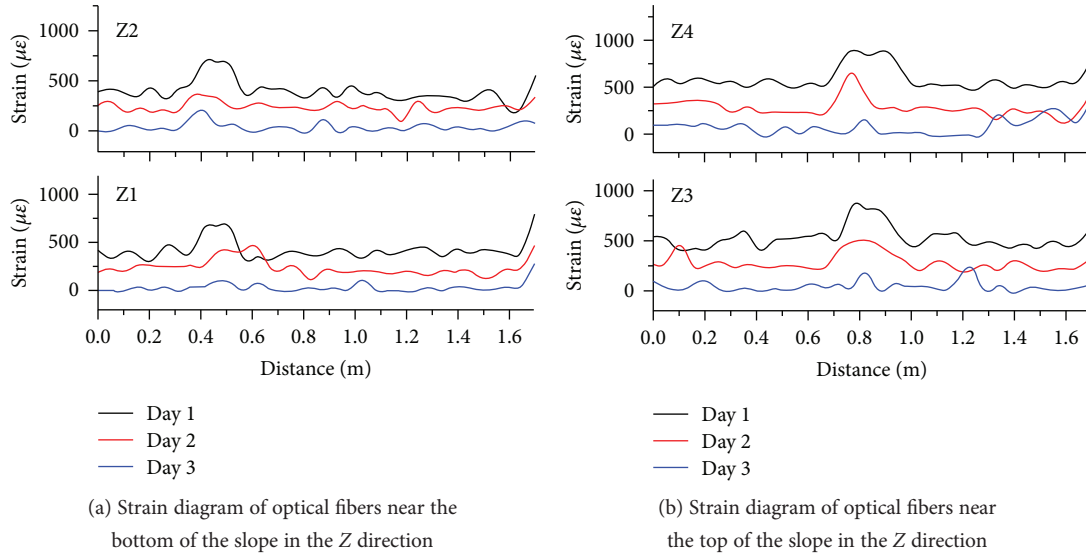


FIGURE 14: Comprehensive strain diagram of optical fibers in the Z direction with three days of rainfall.



FIGURE 15: Locations of sudden change in the strain of optical fibers in the Z direction.

4. Numerical Simulation Calculation of the Stability of Dump II

Combined with physical simulation test parameters, the numerical simulation used FLAC3D software to establish a Mohr-Coulomb constitutive model. The size of the model was the same as that of the indoor physical model (2 m * 2 m * 2 m), so that monitoring data of further numerical simulation could be consistent with those of the indoor test. This simulation was mainly performed to create a similar simulation based on the loading process in the contents of the experiment. The loading process was divided into two stages and five working conditions. In the first stage, loads of 20 kg, 50 kg, and 70 kg placed at the trisection at the top of the model were simulated, a total of two points. Simulation used vertical surface stress loading, and according to the contact area of the actual load weight of 240 m², the vertical compressive stress applied to each working point was 4.46e3 Pa, 4.46e3 Pa, and 1.458e4 Pa. In the second stage, loads of 100 kg and 140 kg were loaded onto the quinquesection at the top of the model, a total of four points. Simulation also used vertical surface stress loading, and the vertical

compressive stress applied to each working point was 1e4 Pa and 1.458e4 Pa, respectively.

4.1. Parameter Selection and Model Establishment. Numerical parameters were set according to the relevant parameters of the indoor physical simulation test model, which are shown in Table 8.

According to the relevant parameters and loading process, the detailed calculation process was divided into two parts. First, the elastic model was calculated and the stress conditions were generated consistent with the test site. Finally, the elastic-plastic calculation was performed. Figure 19 is the generated elastic stress field.

4.2. Analysis of Numerical Simulation Results under Different Conditions of Heaped Loads. The corresponding calculation results were obtained after numerical simulation of the dump model:

- (1) Calculation results of 20 kg of load: as shown in Figure 20, the maximum value of the vertical displacement was calculated as 0.09 mm after the model stabilized. In the model, there was a clear difference between the middle and lower stable zone and the upper strain zone. The model was free of damage after the calculation of model stability. However, after the model was loaded, a potential shear strain belt that was linked in its shear stress field was obvious, and the belt passed through a point of loading which was distributed in the shape of an arc
- (2) Calculation results of 50 kg of load: as shown in Figure 21, the maximum value of vertical displacement was calculated as 0.62 mm after the model stabilized. In the model, there was a clear difference between the middle and lower stable zone and the upper strain zone. The model was free of damage after the calculation of model stability. However, after

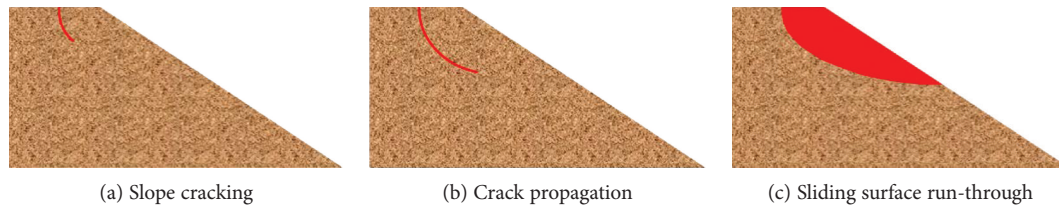


FIGURE 16: Slope instability process.

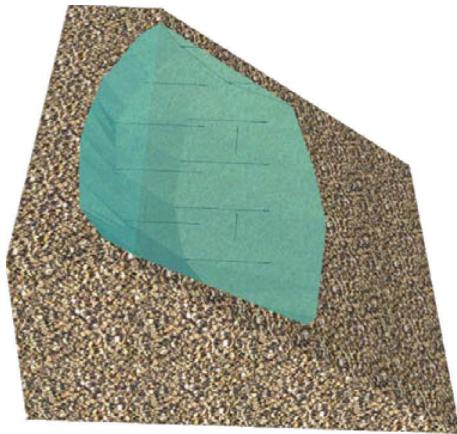


FIGURE 17: Three-dimensional schematic diagram of the sliding surface.

the model was loaded, the potential shear strain belt that was linked in its shear stress field was obvious, and the belt passed through the point of loading with an arc-shaped distribution

- (3) Calculation results of 70 kg of load: as shown in Figure 22, vertical deformation of the slope was calculated to be 1.2 mm after the model stabilized (the settlement of the loading point was not included in the maximum value). In the model, there was a clear difference between the middle and lower stable zone and the upper strain zone. The model was free of damage after model stabilization. However, after the model was loaded, model appearance did not show the obvious shear belt in its shear stress field. However, it can be seen from the perspective view that shear strain started at the top point of loading, and wedge deformation occurred around the loading area in this position. In the two points of loading, the arc-shaped surface that was linked in the lower part of the loading point on the right formed, indicating that during the loading process with these working conditions, the damage arc formed from the inside and from the top to bottom
- (4) Calculation results of 100 kg of load: as shown in Figure 23, in the working conditions of calculation, there were four loading points. Similar to the above calculation, the relatively large settlement and shear strain appeared first right at the location of the loading point, and the vertical deformation of the slope

was 1.2 mm after model stabilization, indicating that although the total load was relatively large, due to dispersed positions of loading points, the load too was dispersed. This helped protect slope stability. Similarly, in the shear perspective view of the model, the shear belt that was linked appeared preferentially in the two middle loading points, and an enlarged shear zone occurred in the loading position at the top

- (5) Calculation results of 140 kg of load: as shown in Figure 24, with these working conditions, there were four loading points. Similar to the above calculation, the relatively large settlement and shear strain first appeared right at the location of the loading points, and the vertical deformation of the slope was 4 mm after model stabilization. Although the locations of the loading points were dispersed, loads were also dispersed to some extent, maintaining slope stability. However, the deformation of the slope was relatively large after this loading and damage appeared, indicating that a large enough load can create an unstable slope after the loading point is arranged. Similarly, in the shear perspective view of the model, the shear belt that was linked appeared preferentially in the two middle loading points, and the enlarged shear zone occurred in the loading position at the top but did not extend to the outside of the model.

In general, numerical analysis results were similar to those of the indoor physical model. As the loading intensity continued to increase, vertical displacement of the slope gradually increased, and the shear stress field in the loading process of two points had an obvious potential shear strain belt that was linked. The damage arc formed from the inside and from the top to bottom. The way of loading changed in the loading process of four points, although the deformation of the slope increased as the load increased, and the slope was eventually damaged when the load reached 140 kg. The linked shear belt preferentially appeared in the two middle loading points, and an enlarged shear zone occurred in the loading position at the top but did not extend to the outside of the model.

5. Discussion

The location of the dangerous potential sliding surface was determined through the size of deformation in locations where optical fibers deformed within the indoor physical model. Rainfall and heaped load had a relatively extensive

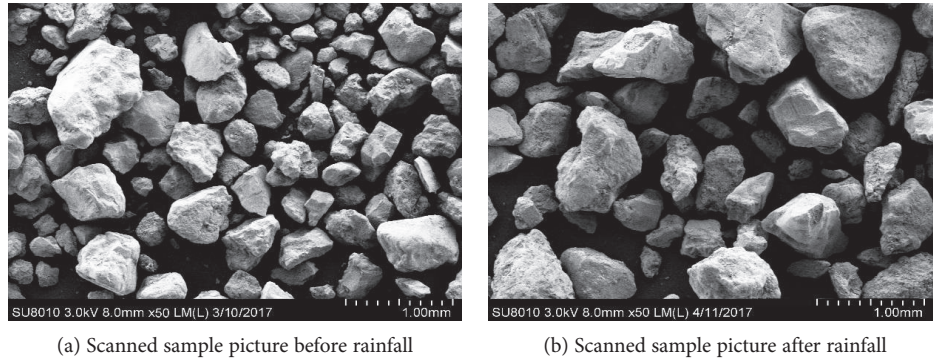


FIGURE 18: Sample SEM pictures before and after rainfall.

TABLE 8: Model of physical and mechanical parameters.

Names of rocks	Weight (kg/m ³)	Modulus of volume (MPa)	Shear modulus (MPa)	Cohesion (Pa)	Friction angle (°)	Tensile strength (Pa)
Chlorite amphibolite	2560	70	41	900	21	0

FLAC3D 5.00
 ©2012 Itasca Consulting Group Inc.
 Step 500
 2017/4/21 18:08:43
 Contour of ZZ-stress
 Calculated by volumetric averaging

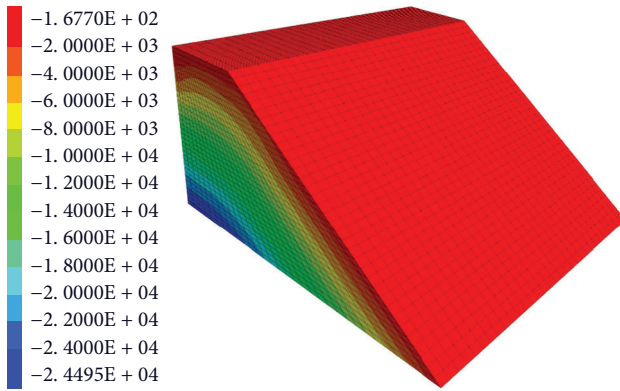


FIGURE 19: Results of the of elastic stress field calculation.

impact on landslides in a dump. With the increase of heaped load, the place between the two heaped load points was squeezed and deformation slowly increased; deformation of the rock-soil mass was obvious at the beginning of rainfall. As the rainfall intensity continued to increase, a dangerous sliding surface was generated. Because the rainfall intensity in the experiments failed to meet the requirements of landslide and mudslide (not enough total amount), no actual landslide ever occurred in these experiments. However, as rainfall stopped, the rock-soil mass of the dump consolidated and settled, and the entire dump tended to stabilize. Compared with other monitoring methods in dumps, fiber optic monitoring can be implemented over long distances and large areas, although it still does have blind spots in its

monitoring. This method does not affect the integrity and structural safety of the monitored rock-soil mass and can provide an early warning of landslides and deformation under a dynamic working process of a site, as proven by Naruse et al. [34] and Kogure and Okuda [35]. However, the workload needed for arranging optical fibers is relatively large, and fiber optics are fragile and easily damaged; thus, the fiber optics need to have installed the protective sleeve, which increases monitoring cost.

FLAC3D was adopted to analyze the vertical displacement and shear strain of the dump under different heaped load conditions, which provided the basis for the determination of the position of the sliding surface in the slope. As the loading intensity continued to increase, vertical displacement of the slope gradually increased, and the shear stress field in the two-point loading process showed an obvious linked potential shear strain belt. A damage arc formed from the inside and from top to bottom. The way of loading changed in the four-point loading process, although the deformation of the slope increased as the load increased, and the slope became damaged under a load of 140 kg. There was still the linked shear belt that preferentially appears in the two middle loading points, and an enlarged shear zone occurred at the location of loading at the top that did not extend to the outside of the model. In general, the results of numerical analysis were similar to results of the indoor physical model experiment and provided a theoretical basis for field experiments.

6. On-Site Experimental Scheme of Fiber Optic Monitoring of Dump II

Based on the fiber optic monitoring indoor physical model experiments and numerical simulation results of the stability of Dump II, a large deformation on-site monitoring design was implemented according to the status quo of dumping

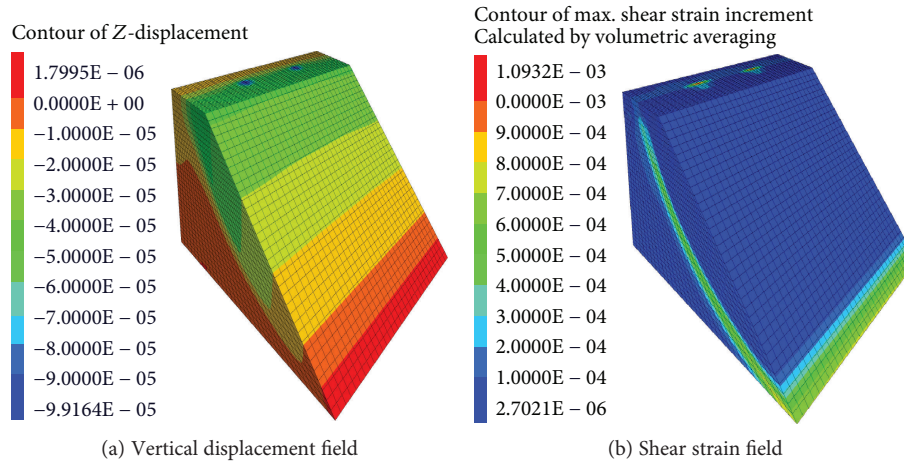


FIGURE 20: Vertical displacement field and shear strain field after loading of 20 kg.

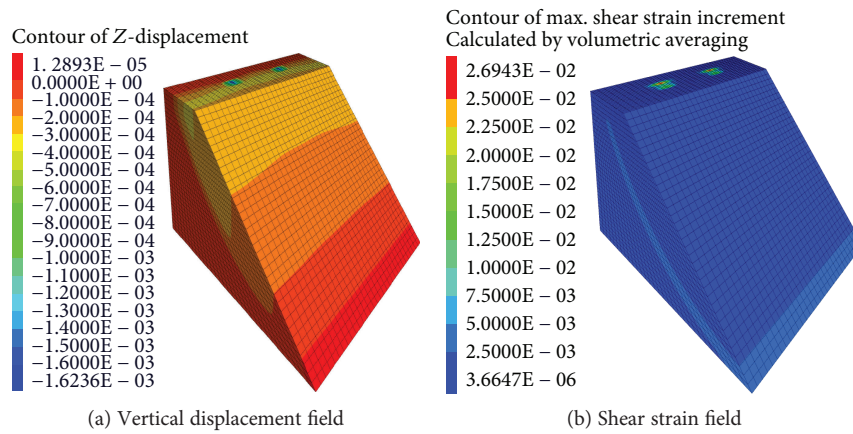


FIGURE 21: Vertical displacement field and shear strain field after loading of 50 kg.

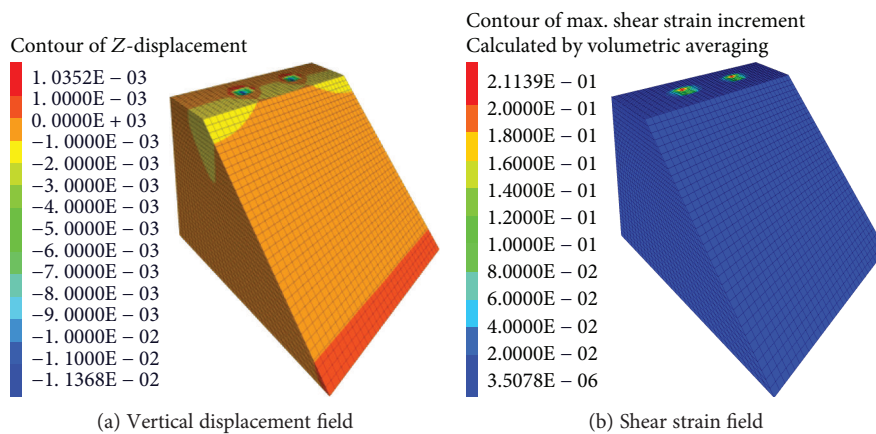


FIGURE 22: Vertical displacement field and shear strain field after loading of 70 kg.

within the dump. Different optical cables were selected and laid in different locations throughout the dump. Cables were selected by comparing which were suitable for soil deformation monitoring during the excavation of the slope in the open-pit mine. The lengths of A and B lines were 200 m each,

and each cable was redundant with 20 m at both ends. The length of each cable was 220 m (Figure 25). The trench was excavated at the top of the slope where the platform was located, and the distributed sensing cables and fiber optic monitoring pipes were buried into the slope. Soil of the slope

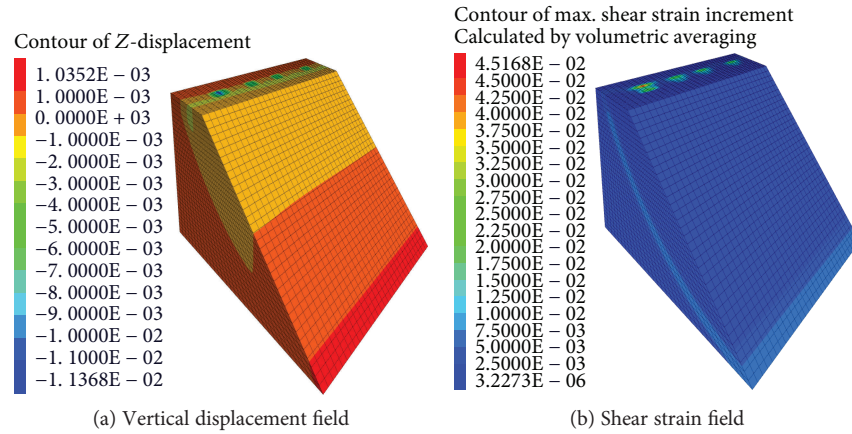


FIGURE 23: Vertical displacement field and shear strain field after loading 100 kg.

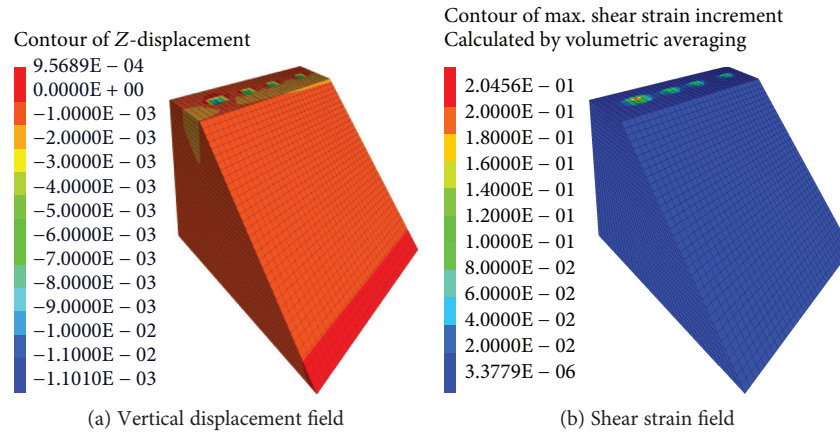


FIGURE 24: Vertical displacement field and shear strain field after loading of 140 kg.

slides downward as it is affected by slope dumping and excavation. In the area with soil deformation of the slope, cables deform with the soil, thus causing tensile deformation. A distributed optical fiber strain tester was used to test the amount of optical cable deformation and determine the area of deformation of the slope.

The trench was excavated according to the designed optical fiber monitoring line. The optical fiber sensor was installed in the trench and buried in the backfill soil. Wiring ports at the beginning and end of the monitoring line were reserved in order to be able to measure deformation and strain. The specific layout on site is shown in Figure 26.

Through the excavation test of the dump slope, a scheme for laying optical fibers suitable for the monitoring of Dump II was finally selected, which will also provide a field test for large-scale application of fiber optic monitoring in a dump that will be reported on at a later period. Monitoring and reporting of the fiber optic network will occur at a later date.

7. Conclusions

The Dump II (Fengjiadonggou) within the Nanfen Open-Pit Iron Mine was the prototype for determining strain and

deformation through experimental study and numerical simulation calculation on fiber optic monitoring with the indoor physical model combined with on-site engineering survey data and landslide analysis methods of the dump. The following conclusions are obtained:

- (1) The indoor physical model experiment of fiber optic monitoring of the dump determined the deformation in different positions of the dump under different heaped loads and rainfall amounts. The location of the dangerous potential sliding surface was determined using the size of deformation in locations where optical fibers were deformed. The reasoning for the sliding face was analyzed through theory, although the pore size among particles of the rock-soil mass before and after the experiment was measured using SEM. Rainfall and the heaped loading method have a relatively extensive impact on the occurrence of landslides in a dump
- (2) FLAC3D was used to analyze the vertical displacement and shear strain of the dump under different heaped load conditions, which provided the basis for the determination of the position of the sliding

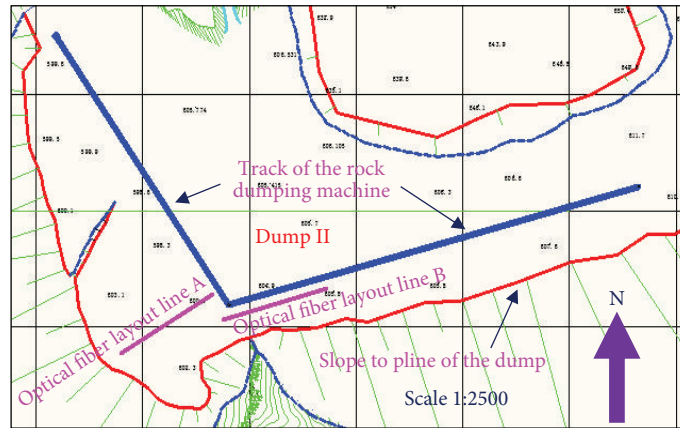


FIGURE 25: Optical fiber layout map of dump deformation monitoring.

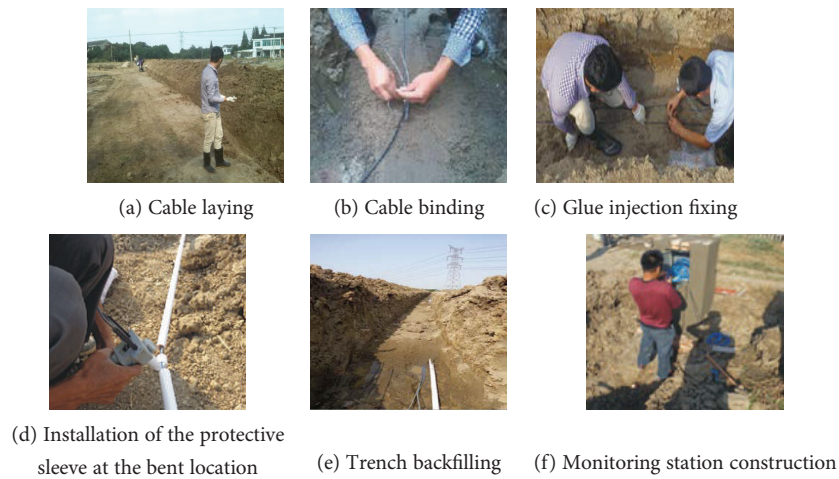


FIGURE 26: On-site laying of optical fiber monitoring of the dump.

surface of the slope. In general, the results of numerical analysis are similar to results of the indoor physical model experiment and provide a theoretical basis for field experiments

- (3) Through the indoor physical model experiment and numerical simulation results, evolution features of the dump under different working conditions were compared and analyzed in order to lay a theoretical and practical foundation for solutions using fiber optic monitoring of a dump site. Based on this, a fiber optic monitoring design suitable for the site of Dump II was proposed and installed. Monitoring and reporting of the fiber optic network will occur at a later date.

Data Availability

The data used to support the findings of this study are available from the corresponding author upon request.

Conflicts of Interest

The authors declare that they have no conflicts of interest.

Acknowledgments

This work is supported by the National Natural Science Foundation Item of China (No. 41502323) and Beijing Natural Science Foundation of China (8142032).


References

- [1] J. C. Wang and S. W. Sun, *Open-Pit Mine Slope Engineering [M]*, Science Press Ltd, Beijing, 2016.
- [2] R. F. Dawson, N. R. Morgenstern, and A. W. Stokes, "Liquefaction flowslides in rocky mountain coal mine waste dumps," *Canadian Geotechnical Journal*, vol. 35, no. 2, pp. 328–343, 2011.
- [3] S. K. Chaulya, R. S. Singh, M. K. Chakraborty, and B. K. Shrivastva, "Quantification of stability improvement of a dump through biological reclamation," *Geotechnical & Geological Engineering*, vol. 18, no. 3, pp. 193–207, 2000.
- [4] G. Nyamadzawo, F. Mapanda, P. Nyamugafata, M. Wuta, and J. Nyamangara, "Short-term impact of sulphate mine dump rehabilitation on the quality of surrounding groundwater and river water in Mazowe District, Zimbabwe," *Physics and Chemistry of the Earth*, vol. 32, no. 15-18, pp. 1376–1383, 2007.

- [5] W. P. Huang, C. Li, L. W. Zhang, Q. Yuan, Y. S. Zheng, and Y. Liu, "In situ identification of water-permeable fractured zone in overlying composite strata," *International Journal of Rock Mechanics and Mining Sciences*, vol. 105, pp. 85–97, 2018.
- [6] Y. W. Xu, "Slope protection with vegetation for waste dump at Guangyue road in Shanghai," *Advanced Materials Research*, vol. 594-597, pp. 465–471, 2012.
- [7] D. Verma, A. Kainthola, S. S. Gupte, and T. N. Singh, "A finite element approach of stability analysis of internal dump slope in Wardha valley coal field, India, Maharashtra," *American Journal of Mining and Metallurgy*, vol. 1, no. 1, pp. 1–6, 2013.
- [8] X. S. Liu and M. Xu, "The unsaturated hydromechanical coupling model of rock slope considering rainfall infiltration using DDA," *Geofluids*, vol. 2017, Article ID 1513421, 15 pages, 2017.
- [9] Y. Li, S. Zhang, and X. Zhang, "Classification and fractal characteristics of coal rock fragments under uniaxial cyclic loading conditions," *Arabian Journal of Geosciences*, vol. 11, no. 9, p. 201, 2018.
- [10] Z. Tao, M. Li, C. Zhu, M. He, X. Zheng, and S. Yu, "Analysis of the critical safety thickness for pretreatment of mined-out areas underlying the final slopes of open-pit mines and the effects of treatment," *Shock and Vibration*, vol. 2018, Article ID 1306535, 8 pages, 2018.
- [11] G. H. Sun, S. Lin, W. Jiang, and Y. Yang, "A simplified solution for calculating the phreatic line and slope stability during a sudden drawdown of the reservoir water level," *Geofluids*, vol. 2018, Article ID 1859285, 4 pages, 2018.
- [12] M. Khandelwal and T. N. Singh, "Reclamation of waste dump and its management," in *Nat Symp Sustainable Mining Technology*, vol. 2002, pp. 313–321, Present & Future, Chennai, 2002.
- [13] F. Arikian, F. Yoleri, S. Sezer, D. Caglan, and B. Biliyul, "Geotechnical assessments of the stability of slopes at the Cakmak-kaya and Damar open pit mines (Turkey): a case study," *Environmental Earth Sciences*, vol. 61, no. 4, pp. 741–755, 2010.
- [14] A. Kainthola, D. Verma, S. S. Gupte, and T. N. Singh, "A coal mine dump stability analysis—a case study," *Geomaterials*, vol. 1, no. 1, pp. 1–13, 2011.
- [15] N. Tripathi, R. S. Singh, and S. K. Chaulya, "Dump stability and soil fertility of a coal mine spoil in Indian dry tropical environment: a long-term study," *Environmental Management*, vol. 50, no. 4, pp. 695–706, 2012.
- [16] N. Adibee, M. Osanloo, and M. Rahmanpour, "Adverse effects of coal mine waste dumps on the environment and their management," *Environmental Earth Sciences*, vol. 70, no. 4, pp. 1581–1592, 2013.
- [17] S. P. Pradhan, V. Vishal, T. N. Singh, and V. K. Singh, "Optimisation of dump slope geometry vis-à-vis fly ash utilisation using numerical simulation," *American Journal of Mining & Metallurgy*, vol. 2, no. 1, pp. 1–7, 2014.
- [18] B. Poulsen, M. Khanal, A. M. Rao, D. Adhikary, and R. Balusu, "Mine overburden dump failure: a case study," *Geotechnical & Geological Engineering*, vol. 32, no. 2, pp. 297–309, 2014.
- [19] G. W. Ma, "Stability analysis of Jinduicheng open-pit mine's dump," *Metal Mine*, vol. 8, pp. 32–34, 2004.
- [20] Y. S. Song, Y. C. Cho, and S. Hong, "Analyses on variations in the unsaturated characteristics of a mine waste-dump slope during rainfall," *Environmental Earth Sciences*, vol. 75, no. 14, 2016.
- [21] L. Zhang, J. M. Wang, Z. K. Bai, and C. Lv, "Effects of vegetation on runoff and soil erosion on reclaimed land in an opencast coal-mine dump in a loess area," *Catena*, vol. 128, pp. 44–53, 2015.
- [22] J. C. Wang and C. Chen, "Stability analysis of slope at a disused waste dump by two-wedge model," *International Journal of Mining, Reclamation and Environment*, vol. 31, no. 8, pp. 575–588, 2016.
- [23] V. Ranjan, P. Sen, D. Kumar, and A. Saraswat, "Enhancement of mechanical stability of waste dump slope through establishing vegetation in a surface iron ore mine," *Environmental Earth Sciences*, vol. 76, no. 1, p. 35, 2017.
- [24] L. Han, J. Shu, Q. Cai, H. Jing, and H. Tian, "Mechanical characteristics of dip basement effects on dump stability in the Shengli open pit mine in Inner Mongolia, China," *Arabian Journal of Geosciences*, vol. 9, no. 20, p. 750, 2016.
- [25] Y. C. Cho and Y. S. Song, "Deformation measurements and a stability analysis of the slope at a coal mine waste dump," *Ecological Engineering*, vol. 68, no. 7, pp. 189–199, 2014.
- [26] Y. Sun, H. Xu, P. Gu, and W. Hu, "Application of FBG sensing technology in stability analysis of geogrid-reinforced slope," *Sensors*, vol. 17, no. 3, p. 597, 2017.
- [27] Z. Chun, T. Zhigang, Y. Sen, and Z. Shuai, "V shaped gully method for controlling rockfall on high-steep slopes in China," *Bulletin of Engineering Geology and the Environment*, 2018.
- [28] M. Schallert, W. R. Habel, and D. Hofmann, "Analysis of concrete foundation piles using structure-integrated fibre-optic sensors," *Technisches Messen*, vol. 75, no. 9, pp. 485–500, 2008.
- [29] C. D. Piao, B. Shi, and Y. Zhu, "Experimental study on BOTDR temperature compensation in bored pile detection," *Journal of Disaster Prevention & Mitigation Engineering*, vol. 29, no. 2, pp. 161–164, 2009.
- [30] A. Klar and R. Linker, "Feasibility study of automated detection of tunnel excavation by Brillouin optical time domain reflectometry," *Tunnelling and Underground Space Technology*, vol. 25, no. 5, pp. 575–586, 2010.
- [31] W. R. Habel and K. Krebber, "Fiber-optic sensor applications in civil and geotechnical engineering," *Photonic Sensors*, vol. 1, no. 3, pp. 268–280, 2011.
- [32] H. Zhang and Z. S. Wu, "Performance evaluation of PPP-BOTDA-based distributed optical fiber sensors," *International Journal of Distributed Sensor Networks*, vol. 8, no. 12, Article ID 414692, 2012.
- [33] H. Xiao and J. Huang, "Experimental study of the applications of fiber optic distributed temperature sensors in detecting seepage in soils," *Geotechnical Testing Journal*, vol. 36, no. 3, article 20120096, 2013.
- [34] H. Naruse, H. Uehara, T. Deguchi et al., "Application of a distributed fibre optic strain sensing system to monitoring changes in the state of an underground mine," *Measurement Science and Technology*, vol. 18, no. 10, pp. 3202–3210, 2007.
- [35] T. Kogure and Y. Okuda, "Monitoring the vertical distribution of rainfall-induced strain changes in a landslide measured by distributed fiber optic sensing with Rayleigh backscattering," *Geophysical Research Letters*, vol. 45, no. 9, pp. 4033–4040, 2018.

Research Article

Feldspar Dissolution and Its Influence on Reservoirs: A Case Study of the Lower Triassic Baikouquan Formation in the Northwest Margin of the Junggar Basin, China

Meng Xiao ¹, Xuanjun Yuan,¹ Dawei Cheng,¹ Songtao Wu,¹ Zhenglin Cao,¹ Yong Tang,² and Zongrui Xie²

¹PetroChina Research Institute of Petroleum Exploration & Development, Beijing 100083, China

²Research Institute of Exploration and Development, Xinjiang Oilfield Company, PetroChina, Karamay, 834000 Xinjiang, China

Correspondence should be addressed to Meng Xiao; xiaomeng422@126.com

Received 3 May 2018; Accepted 8 July 2018; Published 24 September 2018

Academic Editor: Tommaso Caloiero

Copyright © 2018 Meng Xiao et al. This is an open access article distributed under the Creative Commons Attribution License, which permits unrestricted use, distribution, and reproduction in any medium, provided the original work is properly cited.

Feldspar dissolution is a common feature in clastic rock reservoirs of petroliferous basins and has an important influence on reservoir quality. However, the effect of feldspar dissolution on reservoir quality varies under different depositional environments and diagenetic systems. The study area in this paper is located in the Baikouquan Formation in the northwestern margin of the Junggar Basin, which is significantly influenced by feldspar dissolution. Based on the analyses of core and thin section observations, QEMSEM, XRD, SEM, CL, fluorescence, and image analysis software combined with logging and physical property data, this study shows that feldspar dissolution in the subaqueous distributary channel of a fan delta plain, which has good original physical properties and low mud contents, significantly improves the properties of the reservoir. The main reasons for this are as follows: (1) the sedimentary facies with good original properties and low mud content is a relatively open system in the burial stage. The acidic fluids needed for feldspar dissolution are mostly derived from organic acids associated with the source rocks and migrate to the good-permeability area of the reservoir; (2) the by-products of feldspar dissolution, such as authigenic clay minerals and authigenic quartz, are transported by pore water in a relatively open diagenetic system and then precipitated in a relatively closed diagenetic system; and (3) the clay minerals produced by feldspar dissolution in different diagenetic environments and diagenetic stages have different effects on the reservoir. When the kaolinite content is less than 3%, the illite content is less than 4%, and the chlorite content is less than 12%, the clay minerals have a positive effect on the porosity. These clay minerals can reduce porosity and block pore throats when their contents are larger than these values.

1. Introduction

Approximately one-third of clastic rock oil and gas storage space is secondary porosity formed by mineral dissolution [1]. The migration process and precipitation of the by-products of mineral dissolution are important to the evolution of a reservoir [2–4]. Since the 1970s, there has been a large amount of research on the dissolution of single minerals by scholars. The organic acid dissolution theory was proposed, which covered topics such as organic acids produced by the thermal evolution of organic matter [5–7] and the dissolution mechanism of carbon dioxide from organic thermal evolution decarboxylation [8]. In addition, there is an

atmospheric water dissolution mechanism [9, 10] and an alkaline fluid dissolution mechanism [11, 12].

Feldspar dissolution in clastic reservoirs is a common geological phenomenon that results in dissolution pores, which improve the physical properties of the reservoir [13–15], and also a popular research topic in oil and gas reservoir geology [2, 6, 16]. Temperature has significant effects on feldspar dissolution because as temperature increases, feldspar dissolution increases. However, the effect of pressure on feldspar dissolution is relatively weak [17]. When the environment changes from an acidic environment with low pH to an alkaline environment with high pH, the feldspar dissolution rate changes in the shape of a U. The dissolution

rate is slowest under neutral conditions [18]. The by-products of feldspar dissolution are mainly clay minerals and authigenic quartz [9]. Authigenic quartz is a common diagenetic mineral in the process of clastic rock diagenesis, with a formation temperature of 90°C [19] which is responsible for significant porosity and permeability reduction [20]. The formation of authigenic clay minerals, which is influenced by the geothermal and diagenetic fluid properties of the reservoir, affects the physical properties of the reservoir by introducing considerable micropores that impact the rugosity, saturation, and wetting characteristics [21, 22]. Smectite, illite, and chlorite mainly form under alkaline conditions, and kaolinite mainly forms under acidic conditions [23]. The conversion of smectite and kaolinite to illite mainly occurs between 70°C and 140°C. When the local temperature increases to 100°C–140°C, the illite-smectite mixed-layer clays convert to illite. If the concentrations of the iron and magnesium ions in the pore water are high, kaolinite can convert to chlorite under weak alkali conditions. As the pore flow velocity gradually increases, smectite converts to illite and chlorite [24].

Different scholars have different views on the influence of feldspar dissolution on a reservoir. Some scholars [25, 26] believe that grain particle dissolution, especially feldspar dissolution, can effectively improve the physical properties of the reservoir. However, other scholars [21, 27, 28] believe that with continuous feldspar dissolution, the ion concentrations in the pore water continuously increase. Precipitation occurs when the pore water reaches saturation and forms authigenic minerals, such as kaolinite, chlorite, illite, and authigenic quartz, which can occupy pore space, block throats, and thus reduce the quality of the reservoir properties. This saturation of the solution is related to temperature, pressure, flow velocity, and ionic species. The factors that control the effectiveness of reservoir dissolution in improving the physical properties of the reservoir are whether the diagenesis environment is open, the character of the fluid, the solubility of the minerals, and the geotemperature during diagenesis [15, 29].

The Baikouquan Formation in the Mahu Sag of the northwestern margin of the Junggar Basin is a typical conglomerate reservoir. Recently, continuous discoveries have been made and the proven reserves of the basin have reached 1.83 million tons, which indicates that the Baikouquan Formation is a good exploration prospect. In the study area, because of the high mud content and the poor original reservoir properties, feldspar dissolution is one of the key factors that determine the formation of high-quality reservoirs [30]. Therefore, this paper carries out a large number of core observations, intensive and representative sample collection, advanced research methods, and experimental means to analyse the influence of feldspar dissolution, its by-products on the reservoir, and provide a reliable basis for the future exploration of favourable reservoirs.

2. Geological Setting

The Junggar Basin is a large superimposed oil-gas basin in northwestern China with Late Carboniferous to Quaternary

strata [31]. It can be further subdivided into six first-class tectonic zones [32]. It has characteristics of oil accumulation from multiple oil sources and multiple periods of hydrocarbon generation, accumulation, and adjustment in the oil-gas system [33]. Previous studies indicated that the Junggar Basin had a high geothermal gradient from the Carboniferous to Permian (the geothermal gradient has been estimated at 0.05°C/m–0.07°C/m), decreasing to 0.02°C/m–0.023°C/m in the Cenozoic [34]. The Mahu Sag, which is located in the northwestern Junggar Basin, is the most important hydrocarbon-generating sag in the basin [35]. The Mahu Sag is bounded to the northwest by the Wuxia and Kebai Fault Belts, to the east by the Shiyingtian Uplift, the Yingxi Sag, and the Sangequan and Xiayan Uplifts and to the south by the Dabasong and Zhongguai Uplifts [31] (Figure 1(a)). The Mahu Sag is a large depression lacustrine basin with an area approximately $6 \times 10^4 \text{ km}^2$ [36], and it mainly consists of a fan delta plain and fan delta front subfacies [37]. In the Late Permian, the Hercynian orogeny uplifted the northwestern basin and formed a series of high-angle thrust faults (Figure 1(b)). By the Triassic, the entire basin had evolved into an intracratonic basin, with sedimentation occurring on a stable basement. In the Late Triassic, the margins of the basin were still compressed [30]. The Baikouquan Formation is a gentle monocline structure that tilts to the southeast [38]. The strata in the slope area of the Mahu Sag are well developed, and the sediments that fill the basin comprise Carboniferous, Permian (Jiamuhe Formation, Fengcheng Formation, Xiazijie Formation, Lower Urho Formation, and Upper Urho Formation), Triassic (Baikouquan Formation, Kelamayi Formation, and Baijiantan Formation), Jurassic (Badaowan Formation, Sangonghe Formation, Xishanyao Formation, and Toutunhe Formation) and Cretaceous (Turpan Formation) deposits [31] (Figure 2). The Baikouquan Formation was deposited in the Triassic which unconformably overlies the Permian Formation (Figure 1(b)). It was deposited during the depression period of the tectonic evolution. During the whole burial process, the Baikouquan Formation existed in a warm, humid, fresh-brackish water, weakly oxidizing environment [39] and mainly consists of fan delta conglomerates, coarse sandstones, and some interbedded mudstones [38]. The Baikouquan Formation has a large accumulation of oil within multiple zones, but the conglomerate reservoir is tight and strongly heterogeneous (Kuang et al. 2005). Reservoir quality is considered the most important control on hydrocarbon accumulation in this area [40].

3. Samples and Methods

The conglomerate, sandstones, and clays analysed in this study are from the Upper Triassic Baikouquan Formation of the Xinjiang oil field, which is located in the northwestern margin of the Junggar Basin. Detailed core observation and logging analysis were conducted on 13 wells. We collected 283 samples from the 13 wells that consist of many types of lithology, lithofacies, and sedimentary facies. Of these 13 wells, three were selected for detailed sampling (Ma18, Aihu

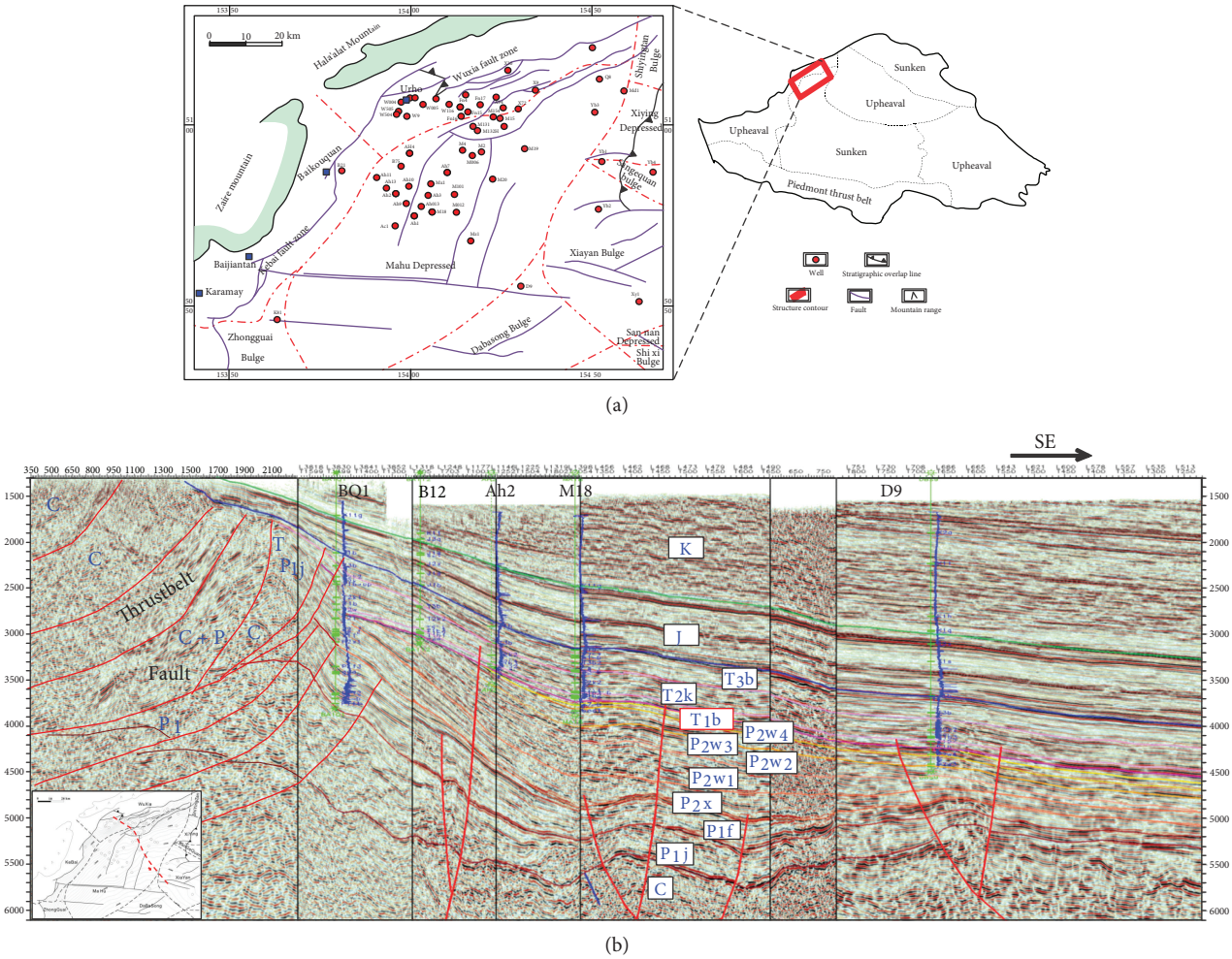


FIGURE 1: (a) Geological map of the western slope of the Mahu Sag in the northwestern Junggar Basin and (b) the south-east cross section showing the different tectonic structural zones and distribution of faults (seismic data are derived from the Research Institute of Exploration and Development, Xinjiang Oilfield Company).

1, and Ma003 wells), from which 97, 53, and 32 samples, respectively, were taken.

The rock composition data of 475 thin section samples (283 cast thin sections and 192 fluorescent thin sections), 8529 reservoir porosity and permeability data points, 622 grading analysis data points, 100 grain shape data points, and 275 mercury injection capillary pressure testing data points and logging data from 13 wells were obtained from the Research Institute of Petroleum Exploration & Development of the Xinjiang Oilfield Company, PetroChina.

More than 300 polished thin sections and 210 blue or red epoxy resin-impregnated thin sections were prepared for the analysis of rock composition, diagenesis, and visual pore characteristics. Because the grain size of the conglomerate is large, we made the thin sections 6 cm in diameter. The thin sections were partly stained with Alizarin Red S and K-ferricyanide for carbonate mineral identification. Point counting was performed on 30 thin sections, where at least 250 points were counted, with a deviation of approximately 6% [41]. A total of 65 reservoir conglomerate samples, 26 sandstone samples, and 3 interbedded mudstone samples were analysed for whole rock and clay fraction mineralogy

using X-ray diffraction (the material that was larger than 2 mm was removed). For the contents of the carbonate cements, quartz cements, primary pores, and feldspar dissolution pores, 15 or 30 micrographs of 86 blue or red epoxy resin-impregnated thin sections were taken using a Zeiss Axioscope A1 APOL digital transmission microscope (for the coarse-grained conglomerates, 15 micrographs were taken; for the sandstones, 30 micrographs were taken). Then, the cements and pores in each micrograph were identified under the microscope and sketched on a computer using the CorelDraw software, and the total cement and pore contents in the 86 micrographs were obtained using the Image-Pro Plus software. Finally, the percentages of the cements and pores were calculated by taking the average of all values from the 15 or 30 micrographs. Cathode luminescence (CL) analyses were performed using an Olympus microscope equipped with a CL8200-MKS CL instrument. Twelve representative samples were viewed by a scanning electron microscope (SEM), and the major elements were analysed by using energy spectrum microanalysis. The SEM was equipped with an energy-dispersive X-ray spectrometer (EDX) using Quanta 450 FEG.

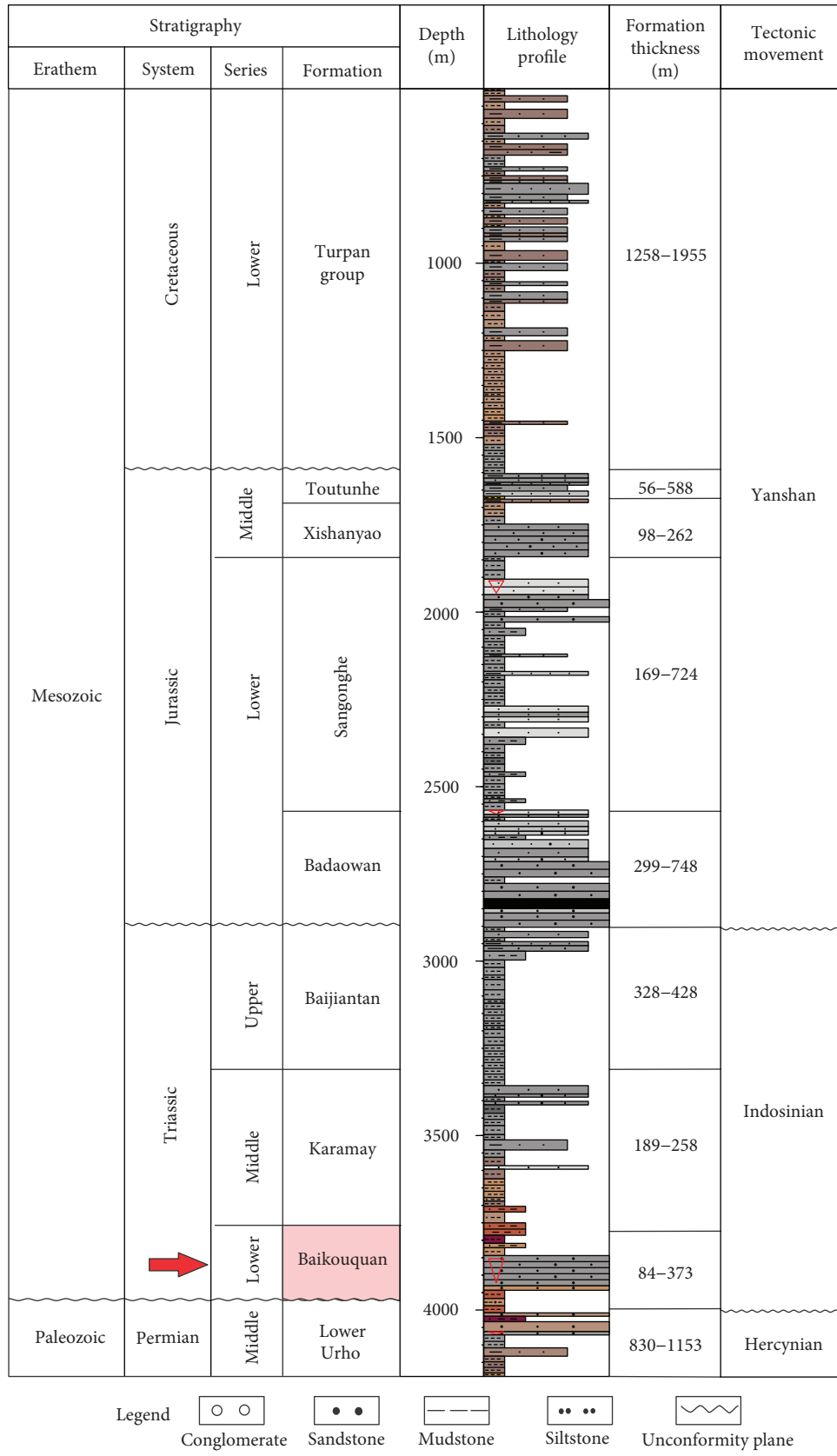


FIGURE 2: Lithostratigraphic columnar section of the western slope of the Mahu Sag in the northwestern Junggar Basin.

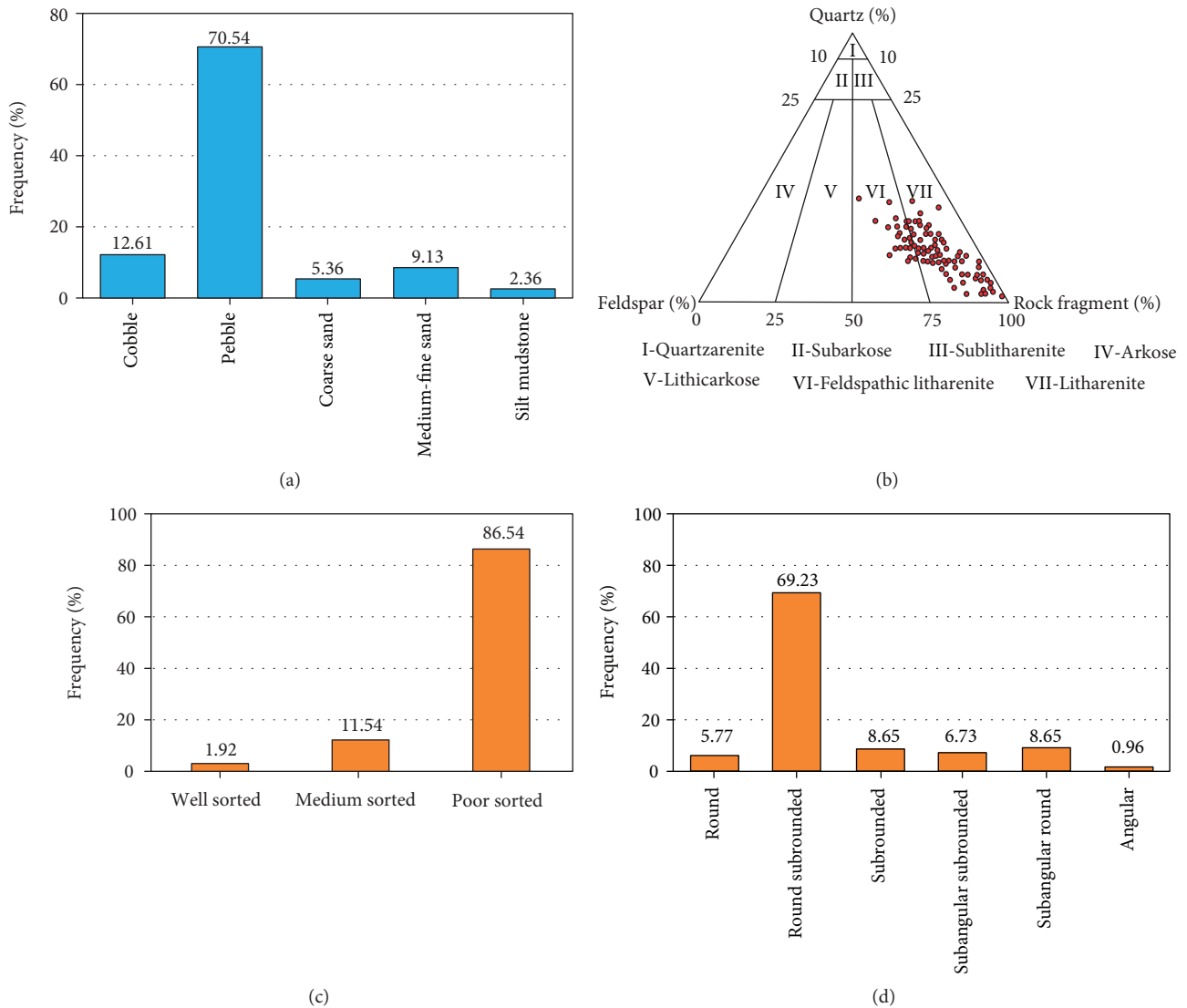


FIGURE 3: Lithological characteristics of the Baikouquan Formation. (a) Distribution characteristics of different types of lithology; (b) rock classification of the Baikouquan Formation; (c) sorting; (d) roundness. I: quartzarenite; II: subarkose; III: sublitharenite; IV: arkose; V: lithic arkose; VI: feldspathic litharenite; VII: litharenite.

To accurately analyse the mineral content of the sample and to quantify the percentage of the material around the mineral, 13 representative samples were cut into $0.5 \times 0.5 \times 0.3$ cm samples and their surfaces were polished. Using FEI Quanta 450 SEM, each sample was scanned continuously for 5×5 grid; then, the 25 fields were stitched into a complete image. Combined with QUEMSCAN analysis software, the mineral composition, pore size, and element data, as well as the composition of the material around the minerals, were determined.

4. Results

4.1. Detrital Composition of the Reservoir. The petrographic investigation of the Baikouquan conglomerate reservoir shows that the detrital components are mainly composed of conglomerates in which gravel accounts for 83.15% (boulders account for 1.21%, cobbles account for 11.4%, and pebbles

account for 70.54%), sandstone accounts for 14.49% (5.36% coarse-grained sandstone and 9.13% medium- to fine-grained sandstone), and siltstone and mudstone account for 2.36% (Figure 3(a)). The XRD results show that the detrital components of the Baikouquan Formation comprise quartz (4.2–62.4%, average of 44.15%), feldspars (2.2–43.8%, average of 22.88%), and rock fragments (22.34–92.36%, average of 40.82%), indicating that the sandstones are mostly litharenite and feldspathic litharenites (Figure 3(b)). The grain size ranges from boulder to mudstone and is poorly sorted (86.54%) (Figure 3(c)). The grain shape is mainly rounded-subrounded (69.23%) (Figure 3(d)), which reflects a short distance to the sediment source.

4.2. Lithofacies. The Baikouquan Formation in Mahu Sag is a set of coarse-grained fan delta deposits and is mainly composed of conglomerate with complex lithology and high content of mud. A large number of studies have been done on

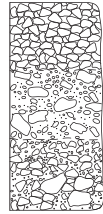

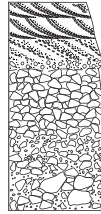


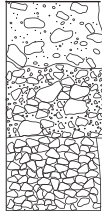








Depositional environment	Fan delta plain				Fan delta front		
	Gravity current	Gravity/traction current	Traction current	Traction current	Traction current	Gravity current	Traction current
Lithofacies facies							
Typical photos	 (A)	 (B)	 (C)	 (D)	 (E)	 (F)	 (G)

FIGURE 4: Different lithofacies characteristics of the Baikouquan Formation.

lithofacies [42, 43], and different classification of lithofacies has been made for different research purposes. Based on the formation mechanism, depositional environment, particle support type, cementation type, particle size, and colour, the sediment was divided into seven lithofacies (Figure 4) that represent the typical sedimentary characteristics in the study area: medium-grained to coarse-grained poorly sorted conglomerates that are mainly sand-gravel supported with angular grains and were deposited by gravity currents in the fan delta plain (Figure 4(a)); fine-grained to coarse-grained poorly sorted conglomerates that are mainly sandstone supported with angular grains and were deposited mainly by gravity and a little of traction currents in the channel with a temporary water flow (Figure 4(b)); coarse-grained sandstone to medium-grained conglomerates that were mainly deposited in the braided channel (Figure 4(c)); mudstone to medium-grained sandstones that were mainly deposited in the braided intrachannel (Figure 4(d)); fine-grained to coarse-grained moderately sorted sandstones, with generally subangular to subrounded grains and few clays, which were mainly deposited in the subaqueous channel of fan delta front (Figure 4(e)); fine-grained sandstone to coarse-grained conglomerates that are mainly multi-particle-supported conglomerates and were mainly deposited in debris flows (Figure 4(f)); and mudstone to siltstones that were mainly deposited in the subaqueous intrachannel (Figure 4(g)).

In the lithofacies (Figure 4(e)) with higher hydrodynamic of deposition and lower mud content, the porosity is larger and the connectivity is better, the pore size is generally larger than 100 microns, and the initial porosity and permeability are better than those of other lithofacies. In the diagenetic stage, it is easy to become an open diagenetic

system due to the good fluidity of fluid; the lithofacies formed in the sedimentary environment with mainly gravity flow (Figures 4(a), 4(b), 4(c), and 4(f)) showed no obvious orientation and disorderly distribution of particles. With the high content of mud, poor separation, and grinding roundness, the dissolution pores of the reservoir are poorly developed and the pore size is generally less than 100 microns. The original physical property is poor. Because of the difficult migration of the fluid, with the dissolution and deposition of particles, a relatively closed diagenetic system is gradually formed.

4.3. Porosity and Permeability. A statistical analysis was performed on 1334 samples from the study area, resulting in a reservoir porosity distribution of 1.9%–16.8% (average of 8.54%); however, the porosity (Figure 5(a)) and permeability (Figure 5(b)) values of the P10 curves (where 10% of the reservoirs have higher values than these) show that some high values exist mainly in the coarse-grained sandstone and the granule stone. The P50 (median) curves show that some higher porosity and permeability intervals exist at 3840–3860 m and 3880–3930 m. The air permeability distribution of the reservoir is from 0.014 mD to 98.1 mD (average of 7.54 mD), and the main distribution range is 0.2 mD–1.0 mD. The percentages of the reservoir with air permeability values of less than 1 mD and 1–10 mD and greater than 10 mD are 44.19%, 37.06%, and 18.75%, respectively. The reservoir properties in the Baikouquan Formation are quite poor, and the heterogeneity of the reservoir is very high.

4.4. Pore Characteristics. Thin section and SEM observations revealed that the conglomerate reservoir pore types mainly consist of intraparticle dissolution pores (Figures 6(a), 6(d),

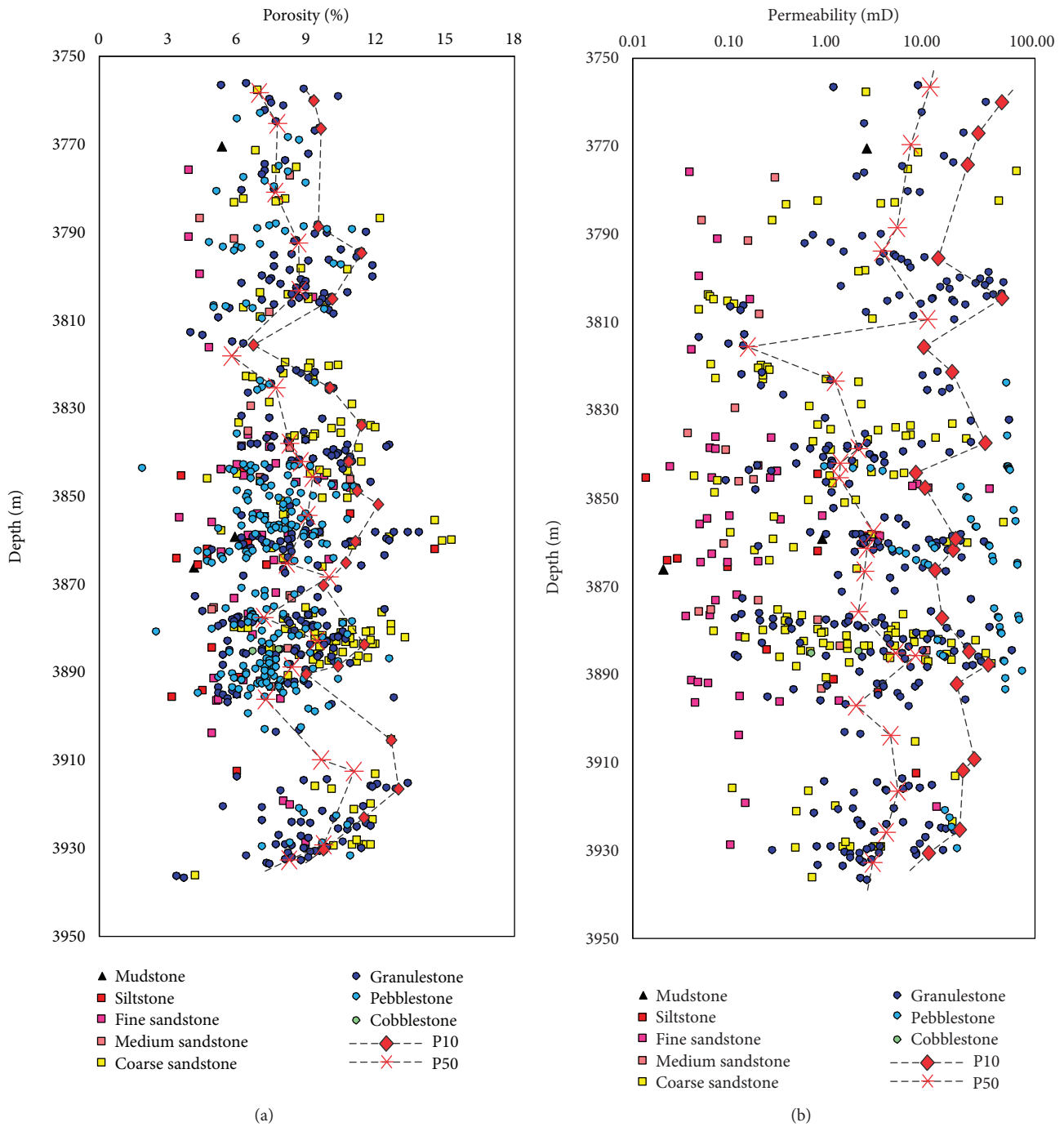


FIGURE 5: Relationship between physical property and depth in the Baikouquan Formation; (a) porosity; (b) permeability.

and 6(e)) and interparticle dissolution pores (Figures 6(a), 6(b), and 6(d)), with some mud shrinkage pores (Figure 6(f)). The interparticle dissolution pores (pore size > 100 μm) were mainly formed by alkali feldspar and acidic rock debris, and only a small amount was formed by calcite cement (Figure 6(c)). The intraparticle dissolution pores (pore size < 100 μm) were mostly produced by orthoclase dissolution. Residual interparticle pores are mainly present in the coarse-grained sandstones and granulestones, and they have better connectivity than the secondary pores. The

proportion of intraparticle dissolution pores increases with increasing depth (Figure 7).

4.5. *Feldspar Dissolution, Authigenic Clay Minerals, and Quartz Cement.* The main diagenetic processes that control the reservoir evolution in the study area are compaction, dissolution, and cementation [44]. The paragenetic sequence includes compaction, early carbonate cementation, chlorite film, illite-smectite mixed-layer clays, feldspar dissolution, precipitation of kaolinite and quartz, montmorillonite

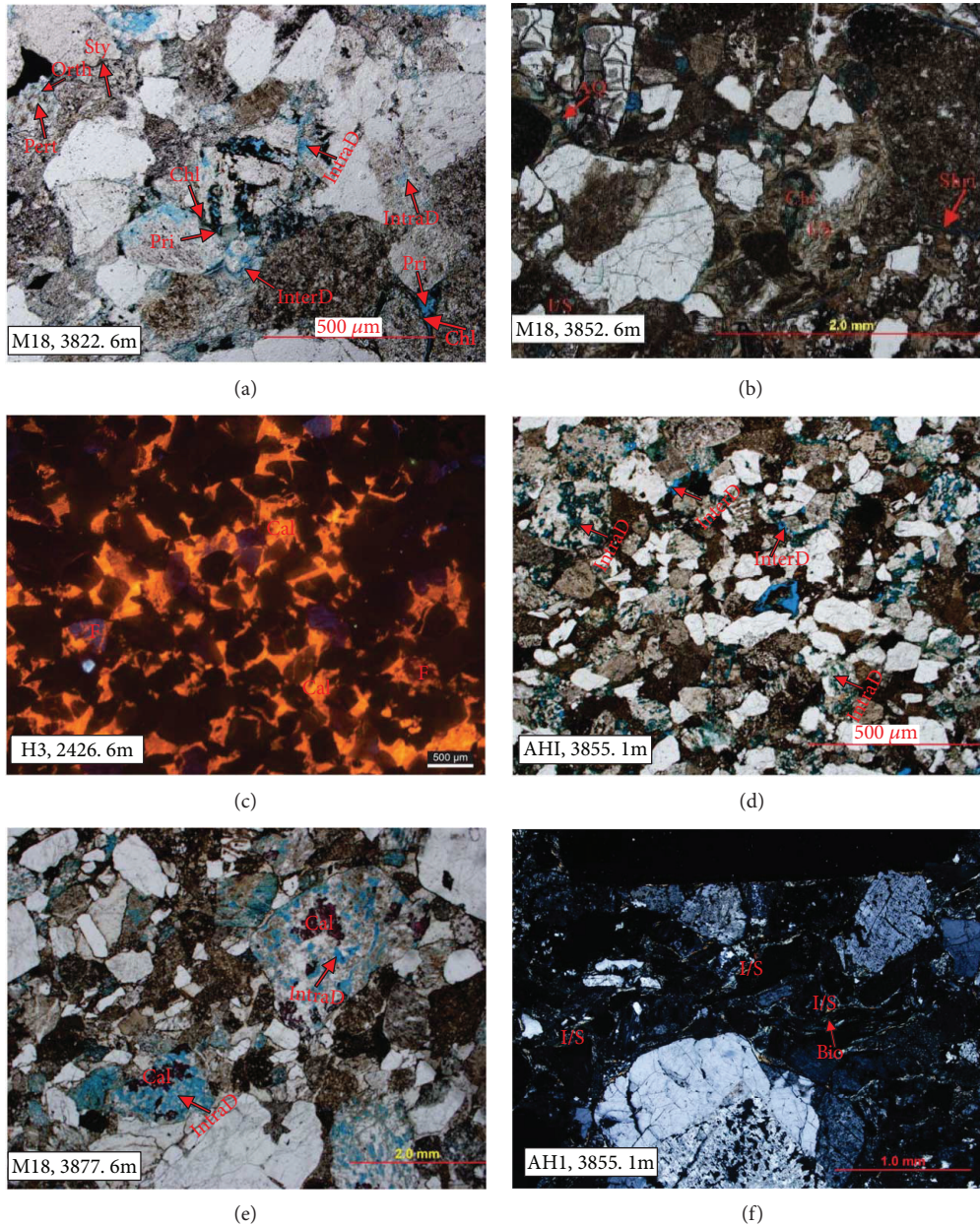


FIGURE 6: Thin section images of the Baikouquan Formation. (a) Plane-polarized light (PPL) images showing orthoclase dissolution with well-developed chlorite and well-preserved original pores; (b) PPL images showing that the intergranular pores are filled with illite in some reservoirs, and only a small amount of the pore is preserved; (c) cathodoluminescence images showing two phases of calcium cement filling the pores, and a small amount of the calcite is dissolved; (d): PPL images showing the developed dissolution pores in the tuffaceous rocks; (e) PPL images showing that calcite cementation is developed in the dissolution pores of the feldspars; and (f) cross-polarized images showing the illite-smectite mixed-layer clay filling pores in some reservoirs. Chl: chlorite film; Sty: stylolite; Pri: primary pore; Pert: perthite; Orth: orthoclase; I/S: illite-smectite mixed-layer clays; Shri: shrinkage; AQ: authigenic quartz; Cal: calcite cement; F: Feldspar; InterD: interparticle dissolution pores; IntraD: intraparticle dissolution pores; Tuff: tuffaceous; Diss: dissolution pores; K: kaolinite; I: illite.

illitization, and weak carbonate cementation [45]. In the study area, the microfracture is less developed which mainly formed at the edge of the gravel and the pore formed by grain dissolution is the main storage space in the reservoir. Feldspar dissolution pores account for the highest percentage of all the secondary pores [30]. The authigenic minerals mainly consist of carbonate cement (Figures 6(c) and

8(b)), kaolinite (Figures 8(a), 8(b), 9(b), 9(d), and 9(e)), chlorite (Figures 6(a), 8(a), 8(b), 9(a), 9(b), and 9(e)), illite (Figures 6(b), 6(f), 8(a), 8(b), 9(a), and 9(e)), illite-smectite mixed-layer clays (Figures 6(b) and 6(f)), and minor quartz cement (Figures 9(c) and 9(e)).

Feldspar grains that have a honeycomb-like texture in porous conglomerate reservoirs usually contain significant

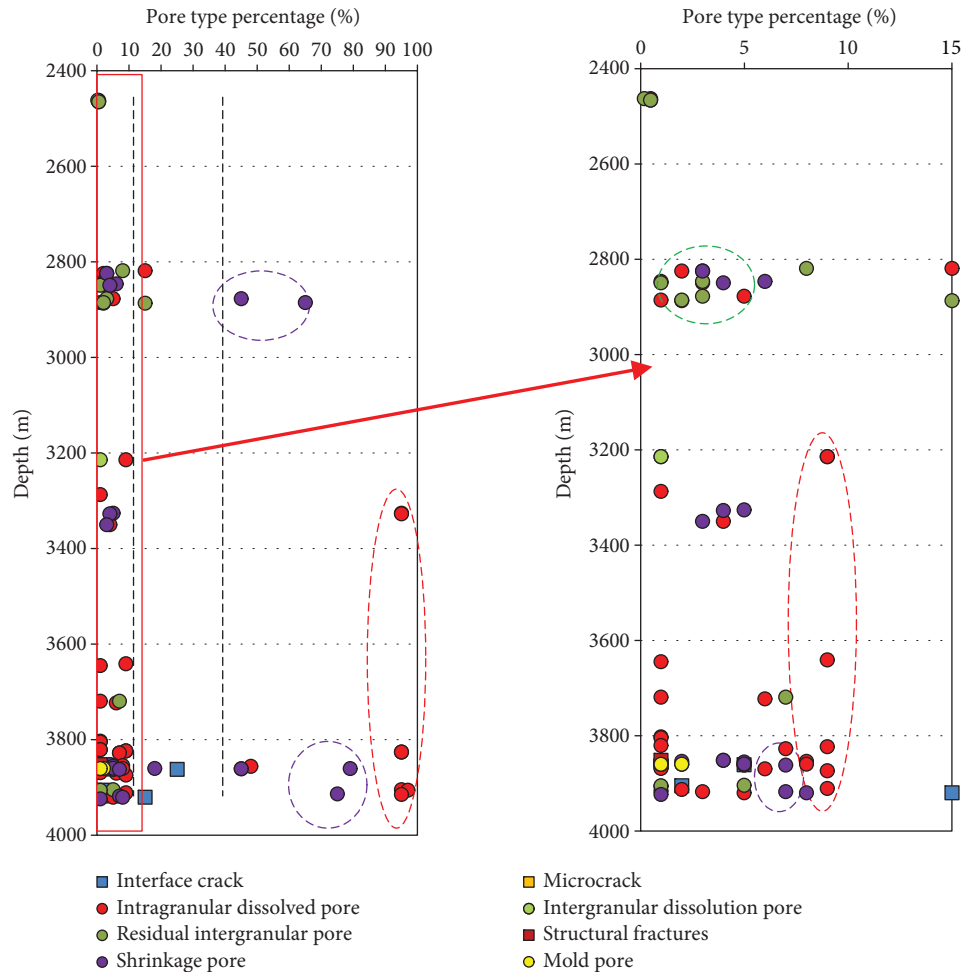


FIGURE 7: The relationship between the contents of pore types and depth.

dissolution pores (Figures 6(a), 8(a), 8(b), 9(a), 9(d), and 9(f)); these grains also display selective dissolution, where orthoclase is dissolved (Figures 8(b), 9(a), and 9(d)) but albite remains stable (Figure 8(a)) [30]. The quantitative porosity analysis of the thin sections shows that the porosity formed by feldspar dissolution can reach up to 6% and feldspar dissolution increases with increasing depth (Figure 10(a)). Quartz cements mainly occur in the form of quartz overgrowths (Figures 9(c) and 9(e)), with thicknesses ranging from $2\ \mu\text{m}$ to $15\ \mu\text{m}$ and a low content (less than 0.1%).

The XRD data and mineral analysis show that illite-smectite mixed-layer clays (average content is 16.61%) dominate the authigenic clays in the different reservoir samples, with minor chlorite (average content is 5.43%), illite (average content is 3.76%), and kaolinite (average content is 2.33%). The SEM analysis revealed that kaolinite mainly occurs as vermicular aggregates and anhedral-pseudohexagonal plates (Figures 8(a), 9(b), 9(d), and 9(e)) filling the primary pores, illite-smectite mixed-layer mainly occurs in reticular form in the primary pores (Figures 6(b), 6(f), and 8(b)), chlorite mainly occurs around the particles (Figures 6(a) and 8(b)), and a few of the chlorite grains also fill the feldspar pores

(Figure 8(a)). Some samples have a high content of illite-smectite mixed-layer clays of up to 78%, and the relative amount of kaolinite is less than 30%. The chlorite distribution is highly heterogeneous, with a maximum content of 64%.

According to XRD analysis, the residual amount of the feldspar in the study area is inversely proportional to the illite-smectite mixed-layer (Figure 10(b)) and is directly proportional to the kaolinite content (Figure 10(c)). With the continuous dissolution of the feldspar, the amount of residual feldspar decreases and a large number of kaolinite is formed in the early diagenetic stage. When the middle diagenetic stage is entered, the kaolinite gradually becomes into smectite and illite in an alkaline diagenetic environment. The pores and authigenic clay minerals formed by dissolution have a very important effect on the quality of reservoirs.

5. Discussion

5.1. Diagenetic Environment. Data from 74 pore water samples from conglomerate reservoirs show that 52.7% of these samples are characterized by CaCl_2 water, 43.2% are

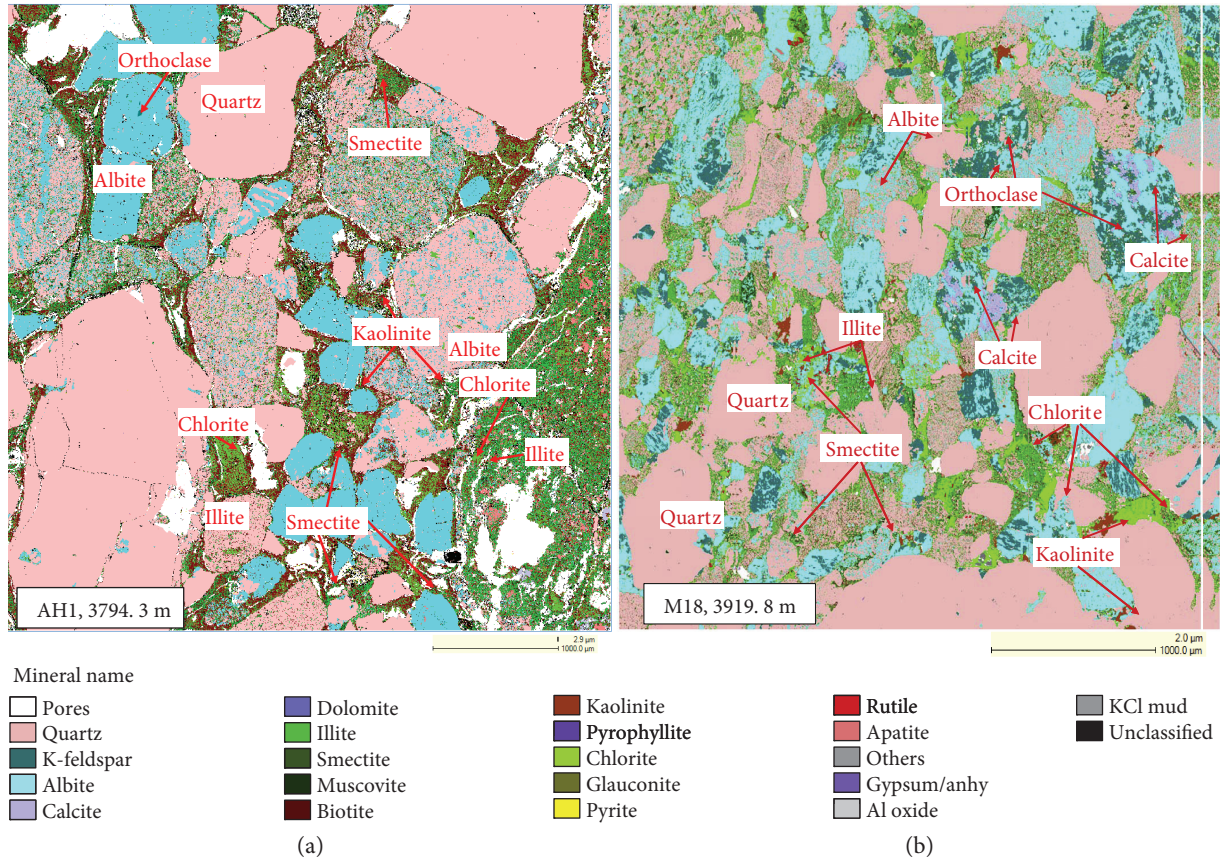
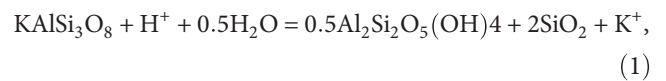


FIGURE 8: Mineral composition analysis of the Baikouquan Formation.

characterized by NaHCO_3 water, and 4.1% are characterized by MgCl_2 water. The salinity ranges from 2774.11 mg/L to 15,093.1 mg/L, which suggests that the pore water may come from different origins [46]. The subaqueous distributary channel (Figure 4(e)) mainly contains pebbles and coarse-grained sandstone which have lower salinity values than others and also has primary high porosity and permeability. The diagenetic environment in this sedimentary microfacies is relatively open (sample salinities are all lower than 7650 mg/L), the flow rate of the pore fluids is high, and the feldspar dissolution by-products are easily transported and rarely precipitated in situ (Figures 6(a), 6(d), and 6(e)). The sedimentary microfacies dominated by gravity flow (Figures 4(a), 4(b), 4(c), and 4(f)) with higher salinity value has a relatively closed system of diagenesis, and the acid dissolution strength of feldspar is low (Figures 6(b) and 6(f)). The data show that the salinity of the samples near the fault is relatively low (all lower than 6000 mg/L) and the fault can provide an effective channel for fluid migration, which highly impacts the feldspar dissolution. In addition, the organic acids generated by the source rocks of the Fengcheng Formation migrate along faults to reservoirs, which has an important effect on the feldspar dissolution [30].

5.2. Mineral Reactions and Mass Transfer. Feldspar dissolution in the study area mainly occurred in the mesodiagenetic

stage [45]. The XRD results show that the albite content is higher (Figure 6(i)) (2.1%–35%) than the orthoclase content (0–4%). This result shows the selective dissolution of feldspar and indicates that orthoclase dissolution plays an important role in improving the physical properties of the reservoir [30]. Orthoclase dissolution increases with increasing depth. According to the statistical QUEMSCAN analysis, the minerals around the pores are mainly quartz (21.48%), albite (15.52), orthoclase (2.73%), chlorite (9.65%), and black mica (16.24%) (Figure 11(a)). The pores are mainly associated with feldspar dissolution. The minerals around the K-feldspar are mainly albite (35.48%), illite (28.24%), and quartz (14.82%) (Figure 11(b)). With continuous K-feldspar dissolution, the concentrations of by-products in the pore waters, such as those of Al^{3+} and SiO_2 (aq), exceed those needed for the saturation of kaolinite and quartz, as shown by the following equation [2, 13]:



where KAlSi_3O_8 is K-feldspar, $\text{Al}_2\text{Si}_2\text{O}_5(\text{OH})_4$ is kaolinite, and SiO_2 is quartz.

The edges of the kaolinite mineral associations (Figure 11(c)) are mainly chlorite (30.97%) and illite (28.98%), indicating that part of the kaolinite converts to

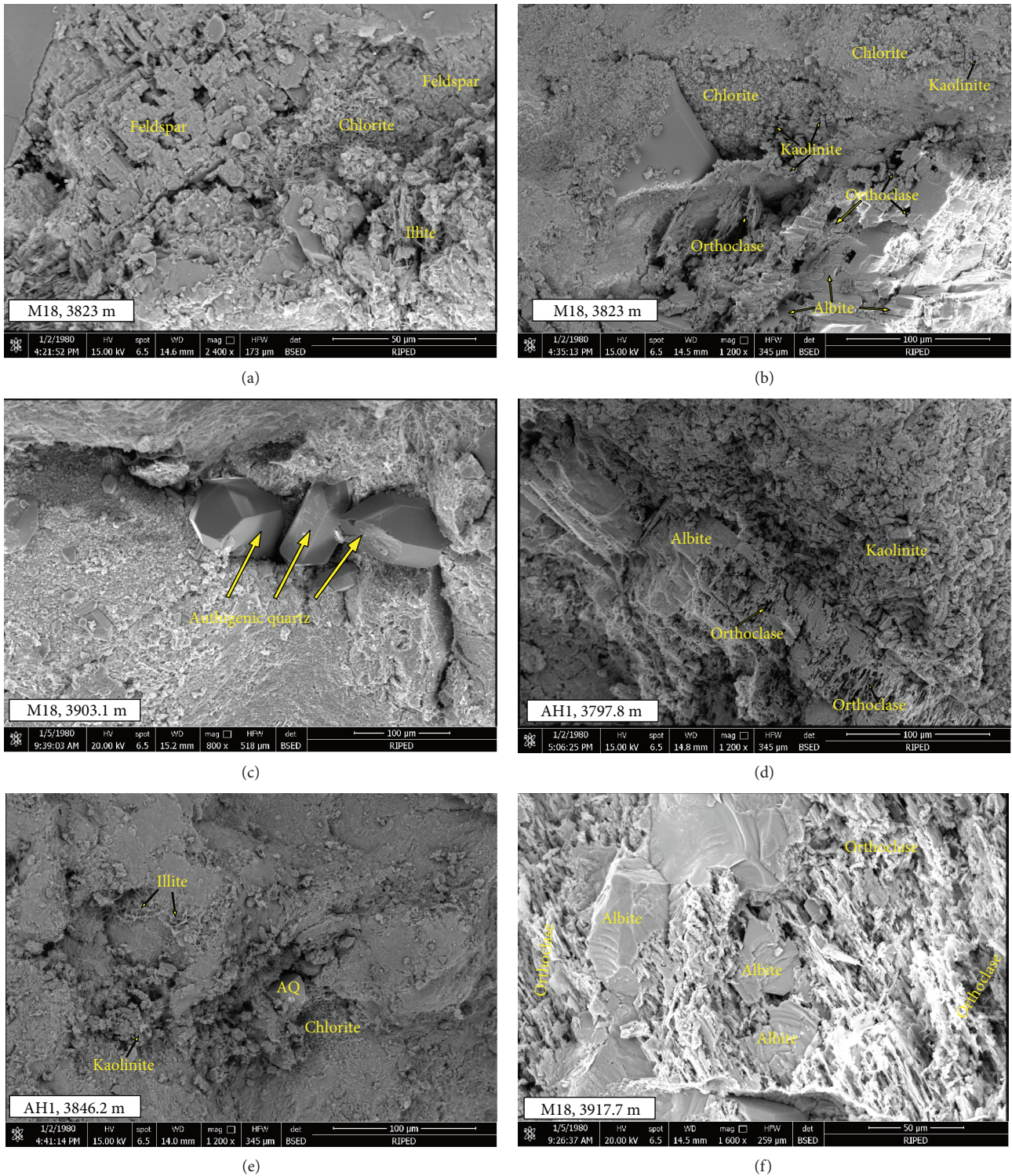
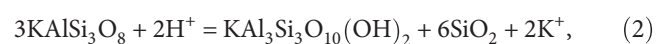


FIGURE 9: Scanning electron microscope images of the Baikouquan Formation. (a) Leached feldspars, chlorite, and illite; (b) kaolinite and chlorite in primary pores and feldspars; (c) quartz crystals; (d) leached feldspars and kaolinite; (e) clay minerals and quartz crystals; and (f) leached feldspars.

illite and chlorite in alkaline pore water. In the process of K-feldspar dissolution, alkaline ions such as potassium and sodium are constantly generated, the diagenetic system gradually becomes closed, the pore fluid gradually becomes alkaline, and when the temperature reaches 70~100°C, the

illitization of feldspars and kaolinite can be expressed as follows [18, 47–49]:



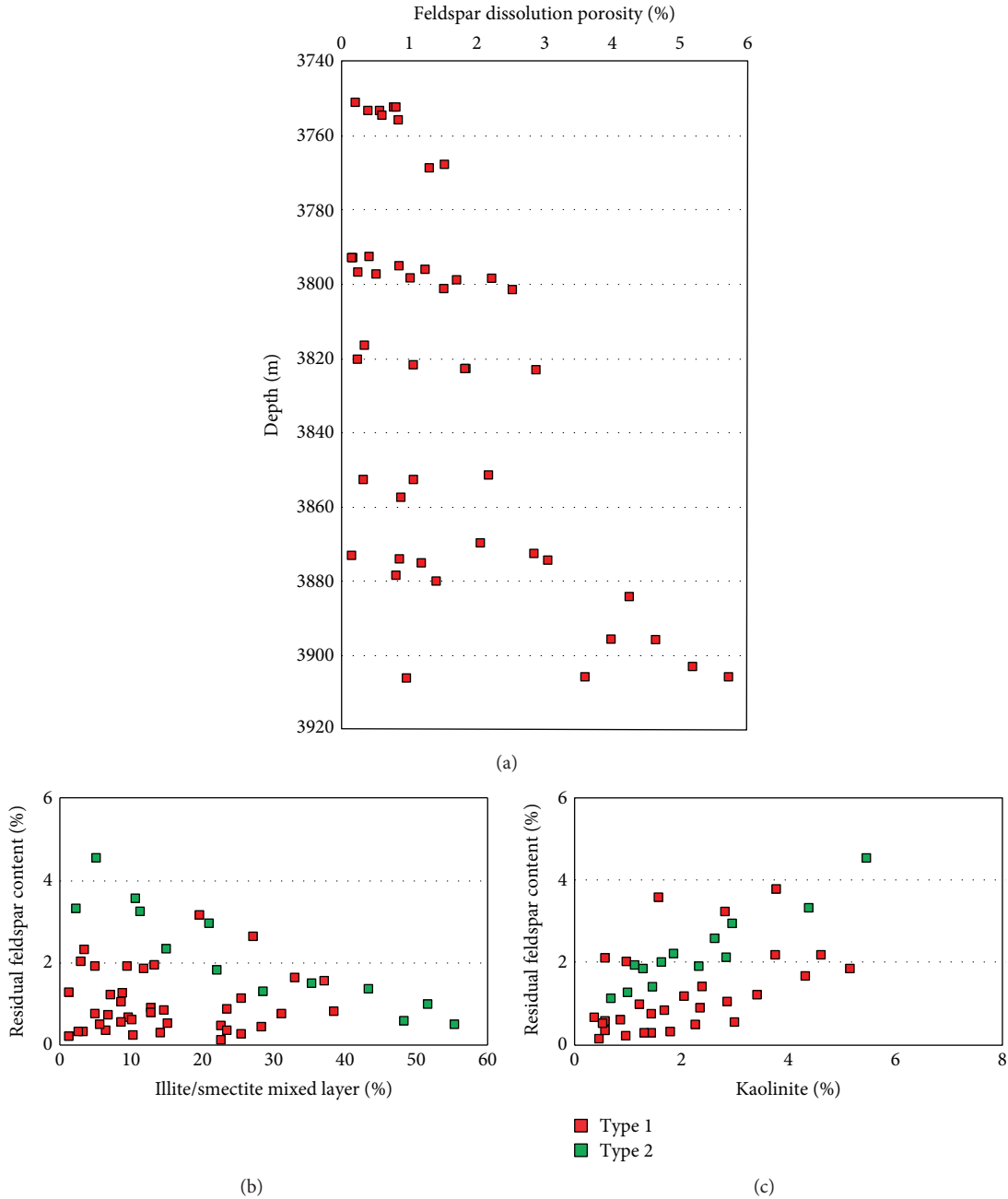
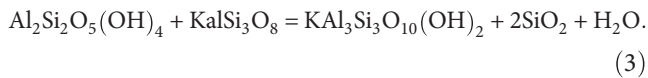
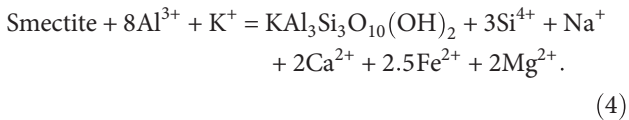


FIGURE 10: (a) Relationship between the feldspar dissolution and depth; (b) the content of illite-smectite mixed-layer clays and (c) kaolinite; type 1 includes lithofacies of A, B, C, and F in the classification of lithofacies in the study area. Type 2 includes lithofacies of C, E, and G in the classification of lithofacies in the study area.

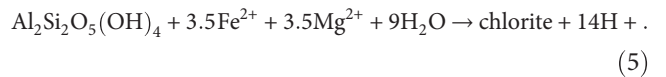
where $\text{KAl}_3\text{Si}_3\text{O}_{10}(\text{OH})_2$ is illite.



Another process that forms illite is montmorillonite illitization, and this process can be expressed as [50]



The minerals on the edge of chlorite are mainly (Figure 11(d)) quartz (27.61%), biotite (22.29%), illite (14.21%), and kaolinite (7.16%). The iron ion released by biotite is the material basis for the transformation of kaolinite into chlorite. When the diagenetic environment changes into a semiclosed system [51] (pH = 9~10) with high amounts of iron and magnesium ions and an appropriate temperature (>90°C) [49], chlorite formation can be described as [52]



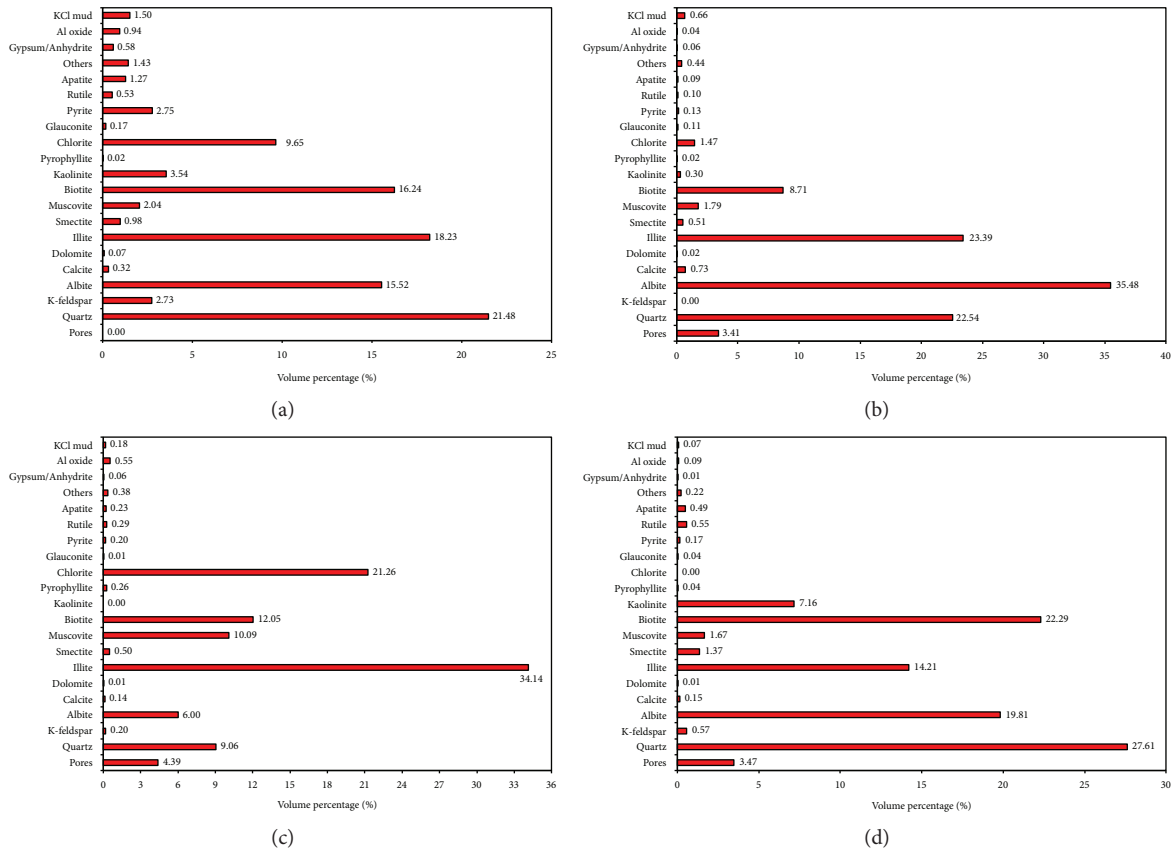


FIGURE 11: The compositions of paragenetic marginal minerals; (a) pores; (b) K-feldspar; (c) kaolinite, and (d) chlorite.

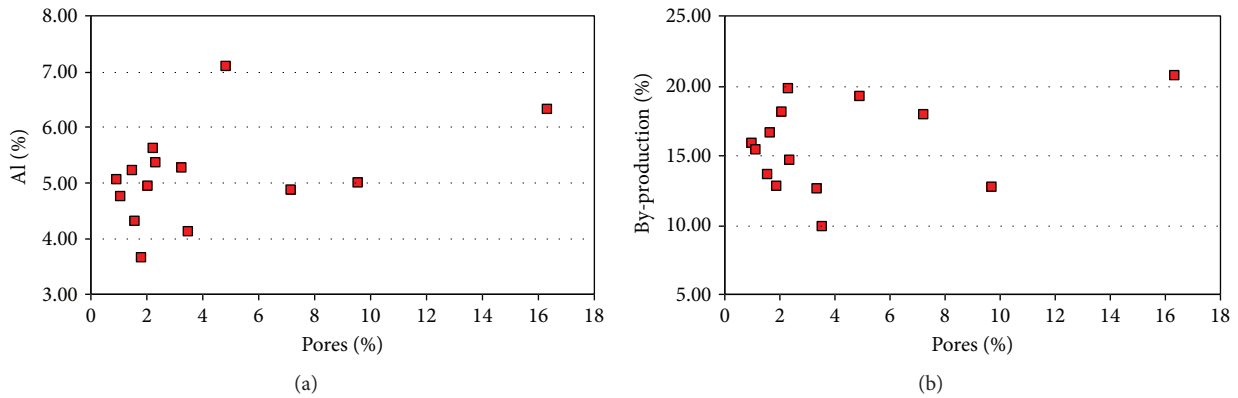


FIGURE 12: (a) The relationship between the dissolution pores and the aluminium ion and (b) by-product contents.

The feldspar porosity (thin section data) can reach up to 7.12%, but the whole feldspar dissolution by-product is less than 2%; however, in some samples, the by-products can be more than 6%. Based on the formula, feldspar dissolution can provide the large amounts of Al^{3+} and SiO_2 needed for clay mineral and authigenic quartz precipitation [15]. However, the QUEMSCAN analysis shows no positive relationships between the feldspar dissolution pores and the aluminium ion (Figure 12(a)) and dissolution by-products (Figure 12(b)). Thus, we concluded that most of the Al^{3+} and $SiO_2(aq)$ released by feldspar dissolution was moved to

a distant area. In a relatively open diagenetic environment, such as the subaqueous distributary channel of a fan delta front (Figure 4(e)), the dissolution by-products are not precipitated in situ [18].



The average detrital quartz content in the Baikouquan reservoirs is 44.15%, and the abundant surface area is available for quartz cementation; however, the authigenic quartz content is less than 1%. The fluid inclusion data show that

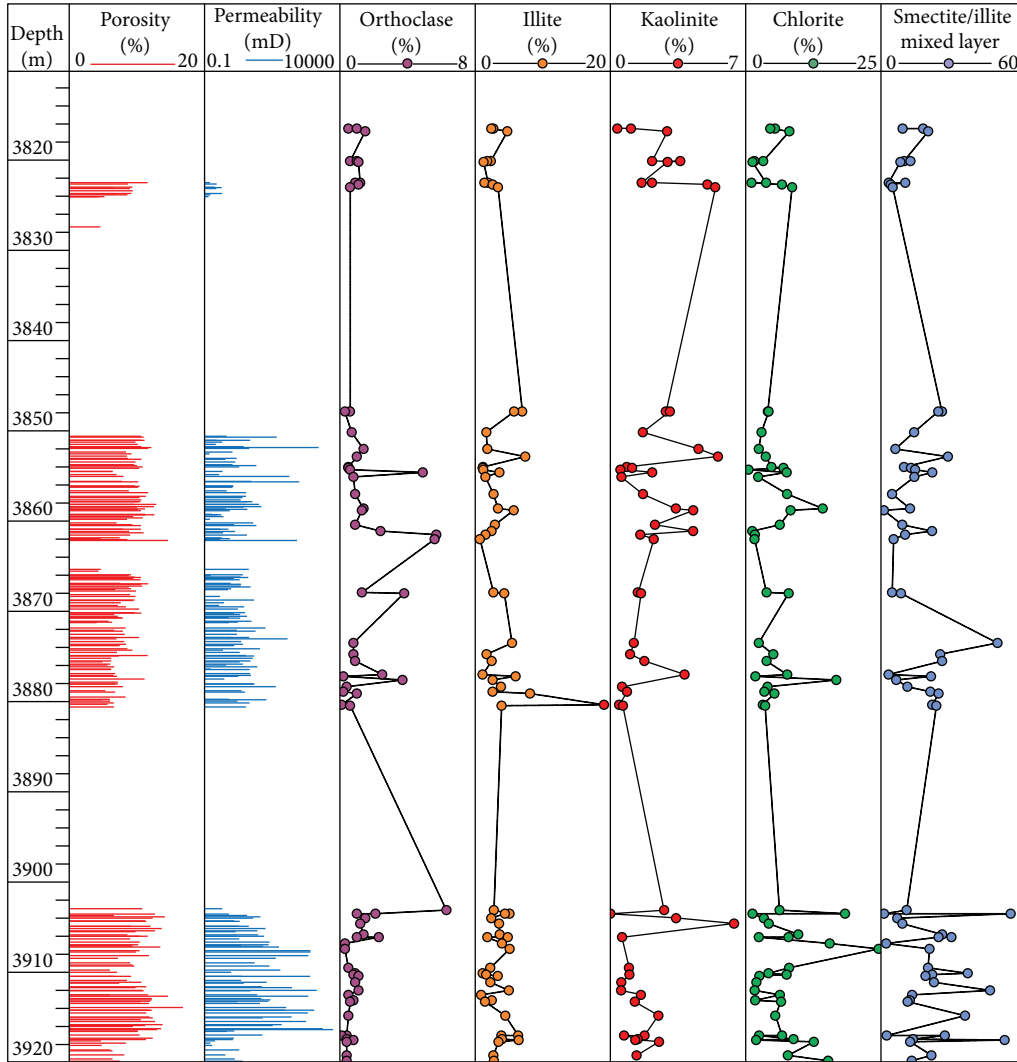


FIGURE 13: Relationship between the physical properties and clay minerals of the M18 well.

[53] the authigenic quartz precipitated in two phases with temperatures of 70°C–90°C and 100°C–120°C. The illite, smectite, and illite-smectite mixed-layer clay contents are high, and the kaolinite content is relatively low (Figure 13). Smectite consumes many potassium ions when it transforms to illite [54].

5.3. The Impact of Feldspar Dissolution on the Physical Properties of the Reservoir. The K-residual feldspar content is inversely proportional to the porosity (Figures 13 and 14(a)), which indicates that the porosity of the study area is mainly derived from K-feldspar dissolution. The strength of K-feldspar dissolution increases with increasing depth (Figure 10(a)). This is related to the acid flue formed by the hydrocarbon source rocks of the Fengcheng Formation. As the acid moves up through the fault, the dissolution decreases. With increasing K-feldspar dissolution, potassium ions are continuously released, which promotes the transformation of illite-smectite mixed-layer clays to illite, and the illite-smectite mixed-layer clay contents decrease

(Figure 10(b)). The kaolinite content significantly increases with the continuous dissolution of K-feldspar (Figure 10(c)).

Observations of thin sections indicate that K-feldspar dissolution in the distributary channel (Figure 4(e)) is more abundant (Figures 6(a), 6(d), and 6(e)) than that in the other sedimentary environments dominated by gravity flow (Figures 6(b) and 6(f)). The lithology of the distributary channel is mainly coarse-grained sandstone, fine-grained conglomerate, and sandy conglomerate. Due to the strong hydrodynamic power of the underwater distributary channel, the mud content is low and the sorting characteristics are good. There is enough space and effective fluid flow conditions to form secondary pores and by-products made by dissolution. The dissolution of feldspar is strong, but the contents of by-products, such as illite and chlorite, are sometimes lower than those (Figures 14(c) and 14(d)) in the braided channel (Figures 4(a) and 4(b)) and the debris flow channel (Figure 4(e)). This indicates that the diagenesis systems in such sedimentary microfacies are more open, the pore water flow velocity is higher, and the dissolution by-products are

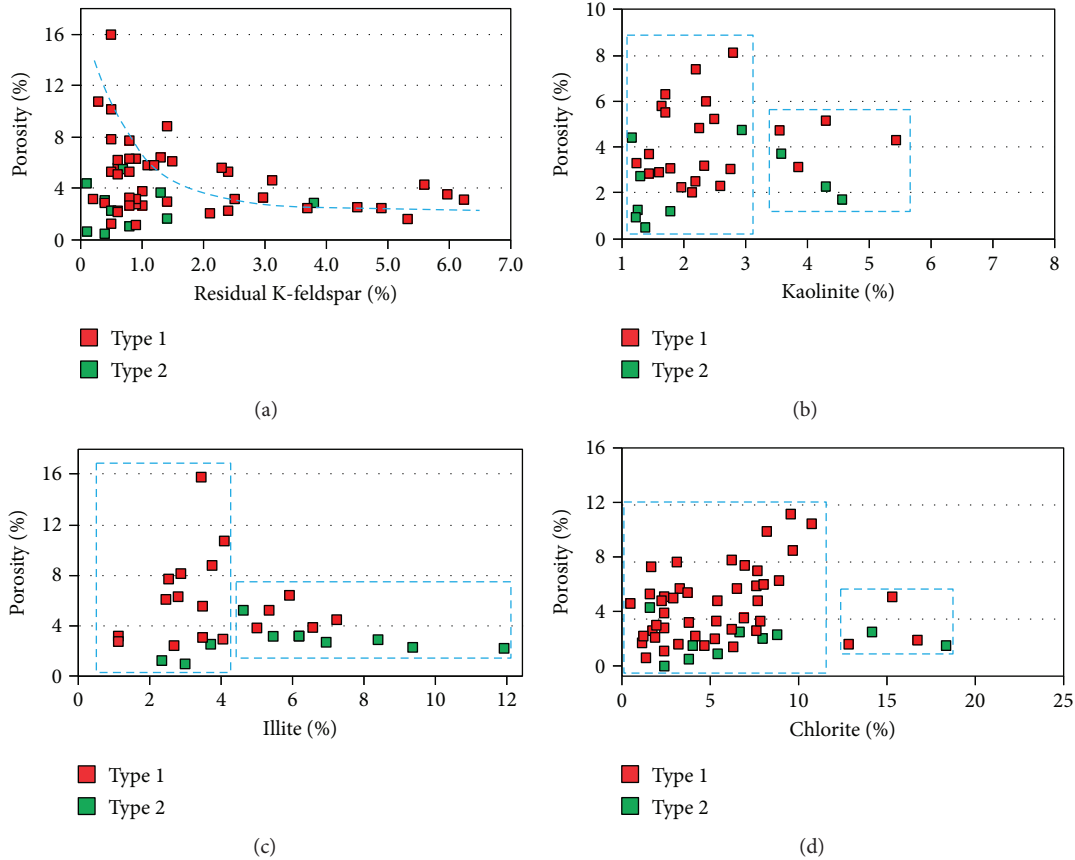


FIGURE 14: The relationship between porosity and K-feldspar (a), kaolinite (b), illite (c), and chlorite (d); type 1 includes lithofacies of A, B, C, and F in the classification of lithofacies in the study area. Type 2 includes lithofacies of C, E, and G in the classification of lithofacies in the study area.

easily transported, which is beneficial to the increase in porosity and permeability.

In sedimentary microfacies dominated by gravity flow, the intensity of K-feldspar dissolution is weak (less than 1.5%) (Figures 6(b) and 6(f)) and the correlation between the amount of feldspar dissolution and its by-products is good. This shows that the feldspar dissolution products have not been transported at a greater distance but are precipitated at or near the dissolution site, which reflects a relatively closed diagenesis system. Feldspar dissolution in closed systems cannot effectively improve the reservoir properties because the material redistribution is carried out only in the local area [29].

The thin section and XRD data indicate that when the kaolinite content is less than 3%, it is positively correlated with porosity (Figure 14(b)). The intercrystalline pores of kaolinite are favourable for porosity. In a sedimentary environment dominated by gravity flow, the kaolinite content can reach to 4.2%. However, when the kaolinite content is greater than 3%, the porosity is significantly reduced (Figure 14(b)), which indicates that kaolinite occupies a large volume of pores. The average illite content of the study area reservoir is 4.23%, which occurs in reticular and filamentous form and fills the pores, or it occurs as a membrane that wraps around the edges of particles (Figures 9(a) and 9(e)).

When the illite content is less than 4%, illite contributes only slightly to the increase in porosity (Figure 14(c)). When the content is greater than 4%, the porosity substantially decreases. Illite can reduce the permeability of the reservoir and affect the reservoir quality [55, 56]. The chlorite film in the study area was formed after the authigenic quartz but before the late calcite cementation (Figure 6(a)), when the reservoir was in its early diagenetic stage B to middle diagenetic stage A. The chlorite content in the subaqueous distributary channel (Figure 4(e)) is high (Figure 6(a)). In a reservoir with high chlorite film content, the contents of illite-smectite mixed-layer clays, illite, and calcite cement are low and the compaction is weak. When the chlorite content is less than 12%, the porosity increases with the increase in chlorite content. When the chlorite content is higher than 12%, the porosity significantly decreases (Figure 14(d)). Because of the precipitation of the chlorite film, the formation of authigenic quartz is inhibited and the compaction, pressure dissolution of quartz, and formation of carbonate cementation decrease, which all have positive impacts on pore preservation [57].

5.4. Feldspar Dissolution and By-Product Distribution Models. Feldspar dissolution is the most important type of dissolution in the Baikouquan Formation of the study area.

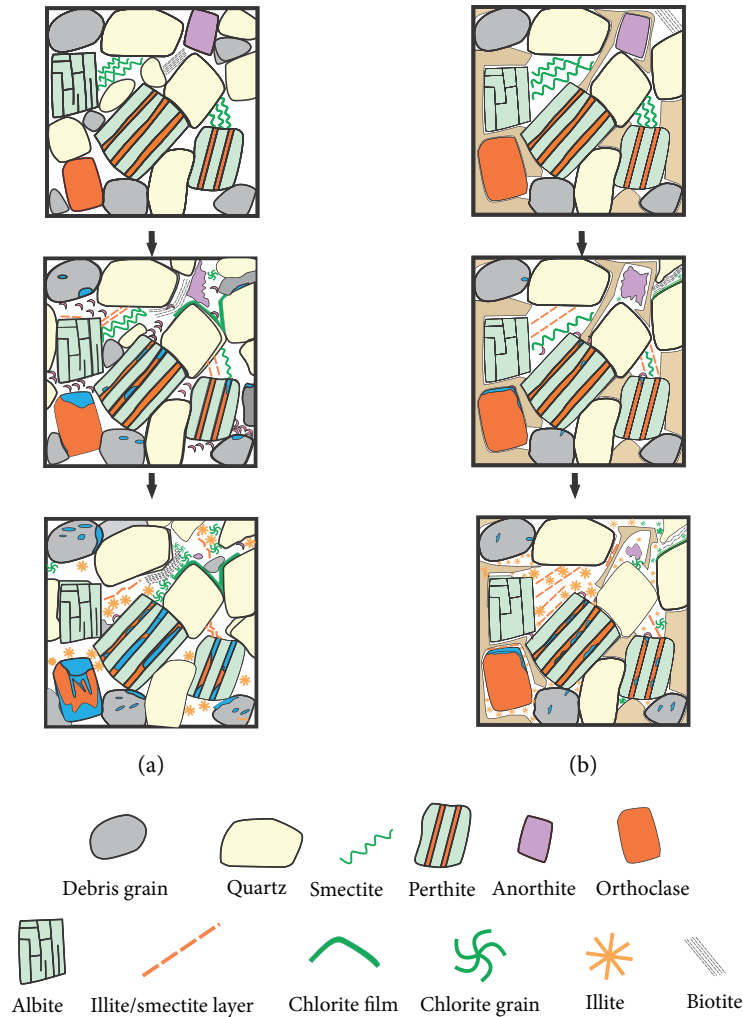


FIGURE 15: Feldspar dissolution and by-product distribution models; (a) relatively open diagenetic system and (b) relatively closed diagenetic system.

On the basis of the analysis presented above, we can establish the feldspar dissolution and by-product distribution models in different diagenetic systems, which is important to determine the heterogeneity of the reservoir.

Eogenesis took place in the Early Triassic to Early Jurassic at diagenesis temperatures of $<85^{\circ}\text{C}$ [58], and the organic acids at that time were mainly derived from mudstones in the Fengcheng Formation [30]. These fluids flowed through permeable layers and dissolved unstable anorthites [5], which also provided Ca^{2+} for the early-stage low-MnO calcite [59] (Figure 6(c)). Thin section identification and QUEMSCAN analysis indicate that no anorthites exist in these samples. With increasing burial depth, mesogenesis began in the Cretaceous at temperatures ranging from 85°C to 120°C [60]. K-feldspar began to dissolve and formed kaolinite. A large amount of the potassium ions was consumed in the illitization process of smectite, so the two reaction processes promoted each other. At this stage, a large amount of potassium feldspar was dissolved and a large amount of illite/smectite layer clay and kaolinite was formed. Under these diagenetic conditions, Na-feldspar remained stable

[61]. The biotite content in the study area is high, which provided Fe^{2+} and Mg^{2+} for the transformation of kaolinite and illite to chlorite.

In relatively open diagenetic systems (Figure 15(a)), such as the underwater distributary channel of the fan delta (Figure 4(e)), the original properties are good, the pore water flows rapidly, and the organic acids from the Fengcheng Formation are easily transported to the reservoir. Because of the relatively open diagenetic system, the by-products formed by K-feldspar dissolution are not deposited in situ (Figure 6(a)) but are carried out by pore water. Therefore, K-feldspar dissolution plays an important role in improving the physical properties of reservoirs in sedimentary environments that are dominated by tractive currents. However, in relatively closed systems (Figures 4(a), 4(c), and 4(f)), the amount of feldspar dissolution is smaller than that in open diagenetic systems (Figure 15(b)). In relatively closed diagenetic systems dominated by gravity flow, the original physical properties are poor and the mud content is high. On the one hand, the acidic fluid needed for dissolution is difficult to transport though a reservoir with poor permeability so the acidic fluid

content required for dissolution is low. On the other hand, the by-products produced by dissolution, such as illite, kaolinite, and chlorite, are difficult to transport in the low-velocity water flow. The concentration of ions in the pore water is saturated so quickly that it is difficult to further dissolve the feldspar. The by-products are basically deposited in situ, for example, chlorite mainly precipitates near illite and biotite. In this diagenetic system, the feldspar dissolution is only redistributed and the physical properties are not significantly increased.

6. Conclusions

- (1) The content of feldspar is high in the conglomerate reservoir of the Baikouquan Formation. Feldspar dissolution, mainly K-feldspar dissolution, is the most important diagenetic process in the study area. When the buried depth is 3840–3860 m and 3880–3930 m, the absolute content of secondary pores of feldspar is high and the maximum can reach 6%. With the dissolution of feldspar, the dissolution products of authigenic clay minerals and siliceous cements are precipitated in pores, which have great influence on reservoir quality.
- (2) The strength of feldspar dissolution increases with depth but varies in different sedimentary environments. In the subaqueous distributary channel of the subaqueous distributary channel with mainly coarse-grained sandstone and fine-grained conglomerate, the original reservoir properties are good, the mud content is low with good sorting, and there is a relatively large amount of feldspar dissolution. In the lithofacies dominated by gravity flow, the dissolution strength of feldspar is low.
- (3) In the subaqueous distributary channel, the content of rigid particles, such as quartz and feldspar, is high and has better sorting and higher original physical properties. In such open diagenetic systems, the velocity of the pore flow is fast and the by-products of the dissolution are easily transported with the fluid and then precipitated in a relatively closed diagenetic system with high mud content and poor original reservoir properties. The strength of dissolution is high, but the by-products of dissolution are relatively less. In the lithofacies dominated by gravity flow, the original physical property is poor and is later easier to become a closed diagenetic system. In this diagenetic system, the acid fluid is difficult to enter the reservoir with poor permeability and the by-products are difficult to be transported. It is also a place where minerals are easily precipitated. In this closed diagenetic system, the dissolution of feldspar has no significant effect on physical properties but only in a smaller range of material redistribution.
- (4) The by-products of dissolution are mainly authigenic clay minerals and authigenic quartz. The amount of authigenic quartz in the study area is relatively low,

which has few effects on the physical properties of the reservoir. The clay minerals in different diagenetic environments and diagenetic stages have different effects on the reservoir. When the kaolinite content is less than 3%, the illite content is less than 4%, and the chlorite content is less than 12%, the clay minerals have a positive effect on the porosity. The clay minerals can reduce porosity and block the throat when they are larger than these values.

Data Availability

The data used to support the findings of this study are available from the corresponding author upon request.

Conflicts of Interest

The authors declare that they have no conflicts of interest.

Acknowledgments

This work is financially supported by the China National Science and Technology Major Projects (Grant no. 2017ZX05001) and the PetroChina Science and Technology Major Projects (Grant no. 2016B-0304).

References

- [1] S. J. Huang, W. H. Wu, J. Liu, L. C. Shen, and C. G. Huang, "Generation of secondary porosity by meteoric water during time of subaerial exposure: an example from Yanchang Formation sandstone of Triassic of Ordos Basin," *Earth Science-Journal of China University of Geosciences*, vol. 4, pp. 419–424, 2003.
- [2] M. R. Giles and R. B. De Boer, "Origin and significance of redistributional secondary porosity," *Marine and Petroleum Geology*, vol. 7, no. 4, pp. 378–397, 1990.
- [3] R. K. Stoessell and E. D. Pittman, "Secondary porosity revisited: the chemistry of feldspar dissolution by carboxylic acids and anions," *The American Association of Petroleum Geologists Bulletin*, vol. 74, pp. 1795–1805, 1990.
- [4] G. Thyne, B. P. Boudreau, M. Ramm, and R. E. Midtbø, "Simulation of potassium feldspar dissolution and illitization in the Statfjord Formation, North Sea," *AAPG Bulletin*, vol. 85, pp. 621–635, 2001.
- [5] J. Bevan and D. Savage, "The effect of organic acids on the dissolution of K-feldspar under conditions relevant to burial diagenesis," *Mineralogical Magazine*, vol. 53, no. 372, pp. 415–425, 1989.
- [6] R. C. Surdam, S. W. Boese, and L. J. Crossey, "The chemistry of secondary porosity," *AAPG Memoir*, vol. 37, pp. 127–149, 1984.
- [7] R. C. Surdam, L. J. Crossey, E. S. Hagen, and S. P. Heasler, "Organic-inorganic and sandstone diagenesis," *AAPG Bulletin*, vol. 73, pp. 1–23, 1989.
- [8] J. S. Seewald, "Organic-inorganic interactions in petroleum-producing sedimentary basins," *Nature*, vol. 426, no. 6964, pp. 327–333, 2003.
- [9] D. Emery, K. J. Myers, and R. Young, "Ancient subaerial exposure and freshwater leaching in sandstones," *Geology*, vol. 18, no. 12, pp. 1178–1181, 1990.

- [10] M. J. Hayes and J. R. Boles, "Volumetric relations between dissolved plagioclase and kaolinite in sandstones: implications for aluminum mass transfer in the San Joaquin Basin, California," *Society for Sedimentary Geology*, vol. 47, pp. 111–123, 1992.
- [11] J. H. S. Macquaker, K. G. Taylor, M. Keller, and D. Polya, "Compositional controls on early diagenetic pathways in fine-grained sedimentary rocks: implications for predicting unconventional reservoir attributes of mudstones," *AAPG Bulletin*, vol. 98, no. 3, pp. 587–603, 2014.
- [12] S. A. Welch and W. J. Ullman, "Feldspar dissolution in acidic and organic solutions: compositional and pH dependence of dissolution rate," *Geochimica et Cosmochimica Acta*, vol. 60, no. 16, pp. 2939–2948, 1996.
- [13] K. Bjørlykke and J. Jahren, "Open or closed geochemical systems during diagenesis in sedimentary basins: constraints on mass transfer during diagenesis and the prediction of porosity in sandstone and carbonate reservoirs," *AAPG Bulletin*, vol. 96, no. 12, pp. 2193–2214, 2012.
- [14] I. Parsons, P. Thompson, M. R. Lee, and N. Cayzer, "Alkali feldspar microtextures as provenance indicators in siliciclastic rocks and their role in feldspar dissolution during transport and diagenesis," *Journal of Sedimentary Research*, vol. 75, no. 5, pp. 921–942, 2005.
- [15] G. Yuan, Y. Cao, J. Gluyas et al., "Feldspar dissolution, authigenic clays, and quartz cements in open and closed sandstone geochemical systems during diagenesis: typical examples from two sags in Bohai Bay Basin, East China," *AAPG Bulletin*, vol. 99, no. 11, pp. 2121–2154, 2015.
- [16] M. Wilkinson, K. L. Milliken, and R. S. Haszeldine, "Systematic destruction of K-feldspar in deeply buried rift and passive margin sandstones," *Journal of the Geological Society*, vol. 158, no. 4, pp. 675–683, 2001.
- [17] W. E. Seyfried, D. R. Janecky, and M. E. Berndt, "Rocking autoclaves for hydrothermal experiments II: the flexible reaction cell system," in *Hydrothermal Experimental Techniques*, H. L. Barnes and G. C. Ulmer, Eds., pp. 216–240, Wiley Interscience, 1987.
- [18] Q. Fu, P. Lu, H. Konishi et al., "Coupled alkali-feldspar dissolution and secondary mineral precipitation in batch systems: 1. New experiments at 200°C and 300 bars," *Chemical Geology*, vol. 258, no. 3–4, pp. 125–135, 2009.
- [19] E. F. McBride, "Quartz cement in sandstones: a review," *Earth-Science Reviews*, vol. 26, no. 1–3, pp. 69–112, 1989.
- [20] J. E. Cook, L. B. Goodwin, and D. F. Boutt, "Systematic diagenetic changes in the grain-scale morphology and permeability of a quartz-cemented quartz arenite," *AAPG Bulletin*, vol. 95, no. 6, pp. 1067–1088, 2011.
- [21] K. E. Higgs, H. Zwingmann, A. G. Reyes, and R. H. Funnell, "Diagenesis, porosity evolution, and petroleum emplacement in tight gas reservoirs, Taranaki Basin, New Zealand," *Journal of Sedimentary Research*, vol. 77, no. 12, pp. 1003–1025, 2007.
- [22] A. Hurst and H. P. Nadeau, "Clay microporosity in reservoir sandstones: an application of quantitative electron microscopy in petrophysical evaluation," *AAPG Bulletin*, vol. 79, pp. 563–573, 1995.
- [23] R. E. Grim, "Crystal structures of clay minerals and their X-ray identification," *Earth Science Reviews*, vol. 18, no. 1, pp. 84–85, 1982.
- [24] J. S. Jahren and P. Aagaard, "Compositional variations in diagenetic chlorites and illites, and relationships with formation-water chemistry," *Clay Minerals*, vol. 24, no. 2, pp. 157–170, 1989.
- [25] M. D. V. Schmidt, "Role of secondary porosity in sandstone diagenesis," *AAPG Bulletin*, vol. 61, pp. 1390–1391, 1977.
- [26] S. Zhou, "A study of the secondary pore space in the cretaceous reservoir in the west slope in Songliao Basin," *Petroleum Exploration and Development*, vol. 5, pp. 16–21, 1989.
- [27] Y. Chen, C. J. Wang, X. F. Sun, M. Wang, Y. Han, and S. Y. Yan, "Progress on mineral solubility and mechanism of dissolution secondary porosity forming in clastic reservoir," *Bulletin of Mineralogy, Petrology and Geochemistry*, vol. 34, pp. 830–836, 2015.
- [28] G. H. Yuan, Y. C. Cao, K. L. Xi, Y. Z. Wang, X. Y. Li, and T. Yang, "Feldspar dissolution and its impact on physical properties of Paleogene clastic reservoir in the northern slope zone of the Dongying Sag," *Acta Petrolei Sinica*, vol. 34, pp. 853–866, 2013.
- [29] T. R. Taylor, M. R. Giles, L. A. Hathorn et al., "Sandstone diagenesis and reservoir quality prediction: models, myths, and reality," *AAPG Bulletin*, vol. 94, no. 8, pp. 1093–1132, 2010.
- [30] X. Kang, W. X. Hu, J. Cao et al., "Selective dissolution of alkali feldspars and its effect on Lower Triassic sandy conglomerate reservoirs in the Junggar Basin, northwestern China," *Geological Journal*, vol. 53, no. 2, pp. 475–499, 2018.
- [31] Y. Tang, Y. Xu, J. H. Zhai, X. C. Meng, and Z. W. Zou, "Fan-delta group characteristics and Its distribution of the Triassic Baikouquan reservoirs in Mahu Sag of Junggar Basin," *Xinjiang Petroleum Geology*, vol. 35, pp. 628–635, 2014.
- [32] F. G. Sui, "Tectonic evolution and its relationship with hydrocarbon accumulation in the northwest margin of Junggar Basin," *Acta Geologica Sinica*, vol. 89, no. 4, pp. 779–793, 2015.
- [33] Y. J. Zhang, J. Cao, and W. X. Hu, "Timing of petroleum accumulation and the division of reservoir-forming assemblages, Junggar Basin, NW China," *Petroleum Exploration and Development*, vol. 37, pp. 257–262, 2010.
- [34] C. C. Pan, Z. Y. Zhou, S. F. Fan, Q. L. Xie, X. L. Wang, and Y. T. Wang, "Thermal history of Junggar Basin," *Geochimica*, vol. 26, no. 6, pp. 1–7, 1997.
- [35] G. Gao, J. Ren, S. Yang, B. Xiang, and W. Zhang, "Characteristics and origin of solid bitumen in glutenites: a case study from the Baikouquan Formation reservoirs of the Mahu Sag in the Junggar Basin, China," *Energy & Fuels*, vol. 31, no. 12, pp. 13179–13189, 2017.
- [36] L. J. Huang, Y. Tang, Y. B. Chen et al., "The subfacies boundary description of fan delta under the control of sequence stratigraphy of Triassic Baikouquan formation in the Mahu slope area, Junggar Basin," *Natural Gas Geoscience*, vol. 26, pp. 25–32, 2015.
- [37] S. C. Zhang, N. N. Zou, J. A. Shi, Q. S. Chang, X. C. Lu, and B. Chen, "Depositional model of the Triassic Baikouquan Formation in Mabei area of Junggar Basin," *Oil & Gas Geology*, vol. 36, pp. 640–650, 2015.
- [38] X. C. Meng, N. G. Chen, H. M. Wang et al., "Sedimentary characteristics of glutenite and its favourable accumulation facies: a case study from T1b, Mabei slope, Junggar Basin," *Acta Sedimentologica Sinica*, vol. 33, pp. 1235–1246, 2015.
- [39] X. Li, L. Q. Zhang, H. Shi, and Y. D. Zheng, "Sedimentary environment of Lower Triassic Baikouquan Formation in Mahu Sag, Junggar Basin: a case study from Ma 18 well," *Lithologic reservoirs*, vol. 28, pp. 80–85, 2016.

- [40] J. G. Pan, G. D. Wang, Y. Q. Qu et al., "Formation mechanism and characteristic of sandy conglomerate diagenetic trap: a case study of the Triassic Baikouquan Formation in the Mahu Sag, Junggar Basin," *Natural Gas Geoscience*, vol. 26, pp. 41–49, 2015.
- [41] L. Van der Plas and A. C. Tobi, "A chart for judging the reliability of point counting results," *American Journal of Science*, vol. 263, no. 1, pp. 87–90, 1965.
- [42] X. H. Yu, J. H. Zhai, C. P. Tan, L. Zhang, X. L. Li, and Z. P. Gao, "Conglomerate lithofacies and origin models of fan deltas of Baikouquan Formation in Mahu Sag, Junggar Basin," *Xinjiang Petroleum Geology*, vol. 35, no. 6, pp. 619–627, 2014.
- [43] C. M. Zhang, X. L. Wng, R. Zhu, J. H. Zhai, J. Pan, and Z. Y. An, "Litho-facies classification of Baikouquan Formation in Mahu Sag, Junggar Basin," *Xinjiang Petroleum Geology*, vol. 37, no. 5, pp. 606–614, 2016.
- [44] B. Chen, Z. Wang, L. Kang, S. Zhang, and J. Shi, "Diagenesis and pore evolution of Triassic Baikouquan Formation in Mabei region, Junggar Basin," *Journal of Jilin University (Earth Science Edition)*, vol. 46, pp. 23–35, 2016.
- [45] J. Jin, X. Kang, W. X. Hu, B. L. Xiang, J. Wang, and J. Cao, "Diagenesis and its influence on coarse clastic reservoirs in the Baikouquan Formation of western slope of the Mahu Depression, Junggar Basin," *Oil & Gas Geology*, vol. 38, pp. 323–333, 2017.
- [46] K. Bjørlykke and K. Gran, "Salinity variations in North Sea formation waters: implications for large-scale fluid movements," *Marine and Petroleum Geology*, vol. 11, no. 1, pp. 5–9, 1994.
- [47] K. Bjørlykke, "Clay mineral diagenesis in sedimentary basins—a key to the prediction of rock properties, examples from the North Sea Basin," *Clay Minerals*, vol. 33, no. 1, pp. 15–34, 1998.
- [48] B. Lanson, D. Beaufort, G. Berger, A. Bauer, A. Cassagnabère, and A. Meunier, "Authigenic kaolin and illitic minerals during burial diagenesis of sandstones: a review," *Clay Minerals*, vol. 37, no. 1, pp. 1–22, 2002.
- [49] R. K. Zhu, C. N. Zou, N. Zhang et al., "Diagenetic fluids evolution and genetic mechanism of tight sandstone gas reservoirs in Upper Triassic Xujiahe Formation in Sichuan Basin, China," *Science in China Series D: Earth Sciences*, vol. 51, no. 9, pp. 1340–1353, 2008.
- [50] J. Hower, E. V. Eslinger, M. E. Hower, and E. A. Perry, "Mechanism of burial metamorphism of argillaceous sediment: 1. Mineralogical and chemical evidence," *Geological Society of America Bulletin*, vol. 87, no. 5, pp. 725–737, 1976.
- [51] H. R. Yuan, Z. Nie, J. Y. Liu, and M. Wang, "Paleogene sedimentary characteristics and their paleoclimatic implications in the Baise Basin, Guangxi," *Acta Geologica Sinica*, vol. 8, pp. 1692–1697, 2007.
- [52] Z. Liu, X. F. Tan, J. Wang et al., "Formation mechanism and alteration of clay minerals in clastic rocks—take the Kongdian Fm. of Paleogene in Jiyang depression for example," *Advances in Geosciences*, vol. 5, no. 6, pp. 467–479, 2015.
- [53] G. Liu, Z. Chen, X. Wang et al., "Migration and accumulation of crude oils from Permian lacustrine source rocks to Triassic reservoirs in the Mahu Depression of Junggar Basin, NW China: constraints from pyrrolic nitrogen compounds and fluid inclusion analysis," *Organic Geochemistry*, vol. 101, pp. 82–98, 2016.
- [54] H. A. Jung, "Transmission and analytical electron microscopy of the smectite-to-illite transition 1," *Clays and Clay Minerals*, vol. 34, no. 2, pp. 165–179, 1986.
- [55] M. J. Pearson and J. S. Small, "Illite-smectite diagenesis and palaeotemperatures in Northern North Sea quaternary to Mesozoic shale sequences," *Clay Minerals*, vol. 23, no. 2, pp. 109–132, 1988.
- [56] W. R. Xie, W. Yang, X. Y. Zhao et al., "Influences of chlorite on reservoir physical properties of the Xujiahe formation in the central part of Sichuan Basin," *Petroleum Exploration & Development*, vol. 37, pp. 674–679, 2010.
- [57] J. D. Grigsby, "Origin and growth mechanism of authigenic chlorite in sandstones of the lower Vicksburg Formation, South Texas," *Journal of Sedimentary Research*, vol. 71, no. 1, pp. 27–36, 2001.
- [58] J. Cao, Y. Zhang, W. Hu et al., "The Permian hybrid petroleum system in the northwest margin of the Junggar Basin, Northwest China," *Marine and Petroleum Geology*, vol. 22, no. 3, pp. 331–349, 2005.
- [59] C. V. Jeans, J. G. Mitchell, M. Scherer, and M. J. Fisher, "Origin of the Permo-Triassic clay mica assemblage," *Clay Minerals*, vol. 29, no. 04, pp. 575–589, 1994.
- [60] N. S. Qiu, X. L. Wang, H. B. Yang, and Y. Xiang, "The characteristics of temperature distribution in the Junggar Basin," *Chinese Journal of Geology*, vol. 36, pp. 350–358, 2001.
- [61] P. Aagaard, P. K. Egeberg, G. C. Saigal, S. Morad, and K. Bjørlykke, "Diagenetic albitization of detrital K-feldspars in Jurassic, Lower Cretaceous and tertiary clastic reservoir rocks from offshore Norway; II, Formation water chemistry and kinetic considerations," *Journal of Sedimentary Research*, vol. 60, no. 4, pp. 575–581, 1990.

Research Article

Effects of Initial Porosity and Water Pressure on Seepage-Erosion Properties of Water Inrush in Completely Weathered Granite

Jinquan Liu,^{1,2} Weizhong Chen,³ Taogen Liu,⁴ Jianxin Yu,⁵ Jingliang Dong ²,
and Wen Nie ¹

¹Quanzhou Institute of Equipment Manufacturing, Haixi Institutes, Chinese Academy of Sciences, Quanzhou, Fujian 362000, China

²School of Civil Engineering and Architecture, East China Jiaotong University, Nanchang, Jiangxi 330013, China

³State Key Laboratory of Geomechanics and Geotechnical Engineering, Institute of Rock and Soil Mechanics, Chinese Academy of Sciences, Wuhan, Hubei 430071, China

⁴College of Civil Engineering & Architecture, Nanchang Institute of Technology, Nanchang, Jiangxi 330013, China

⁵School of Civil Engineering, Henan Polytechnic University, Jiaozuo, Henan 454000, China

Correspondence should be addressed to Jingliang Dong; 429146390@qq.com and Wen Nie; wen.nie@fjirsm.ac.cn

Received 16 March 2018; Accepted 22 April 2018; Published 16 August 2018

Academic Editor: Tommaso Caloiero

Copyright © 2018 Jinquan Liu et al. This is an open access article distributed under the Creative Commons Attribution License, which permits unrestricted use, distribution, and reproduction in any medium, provided the original work is properly cited.

In order to investigate the water inrush mechanism in completely weathered granite, a large-scale triaxial testing system is designed and manufactured, which can induce the mass transfer and monitor the flow properties. Using this system, the effects of water pressure and initial porosity on the mass transfer and flow properties were determined, and the relative critical conditions for water inrush were proposed. The results indicate that (1) the particle transfer could cause an increase in porosity, permeability, and water inflow, which is the essential reason for water inrush in completely weathered granite. (2) Due to the effect of particle transfer, the flow properties may change from a Darcy to a non-Darcy flow, which is a key signal for water inrush. (3) With the increase of water pressure, the mass transfer, permeability, and water inflow increased gradually, and a critical value ($p = 0.6$ MPa) that caused the water inrush was obtained. Furthermore, with the decrease of initial porosity, the mass transfer and flow properties were suppressed rapidly, and a critical porosity (0.23) to anti-inrush was observed. The results obtained can provide an important reference for understanding the mechanism, forecasting the risk, and taking the effective control measures for water inrush.

1. Introduction

In recent years, a large number of tunnels have been constructed in unfavorable geology such as completely weathered granite, karst, and fault [1–4], causing various challenges to the geotechnical engineers, for example, collapse [5], land subsidence [6], groundwater inflow [7, 8], and total environmental hazards [9]. The completely weathered granite, one of the typical unfavorable geologies, is widely distributed in subtropical, tropical, and humid temperature zones [10–12]. This material has the properties of weak water stability, low strength, and strong disintegration [13]. Under the effect of water, this material erodes rapidly and becomes weak and soil-like as observed in recent field investigations ([1]; [14, 15]). Therefore, tunnel construction

in this condition often faces a great risk of water and mud inrush [2, 8, 16], which has become a difficult issue for the tunnel engineers.

In order to analyze and forecast the water inrush, many scholars proposed various simplified methods, such as water inrush coefficient [17, 18], underlying belt theory [19], and key strata model [20]. However, these methods oversimplify the geological conditions and cannot accurately predict the probability of water inrush. Considering the flow properties, some scholars proposed the flow stress coupling models which the flow equation adopted a Darcy or modified Darcy's equation [21–23] and many other analytical and semianalytical solution to predict the water inflow and water inrush ([7, 18, 24]); however, these models do not consider the erosion property and nonlinear flow, which cannot reflect

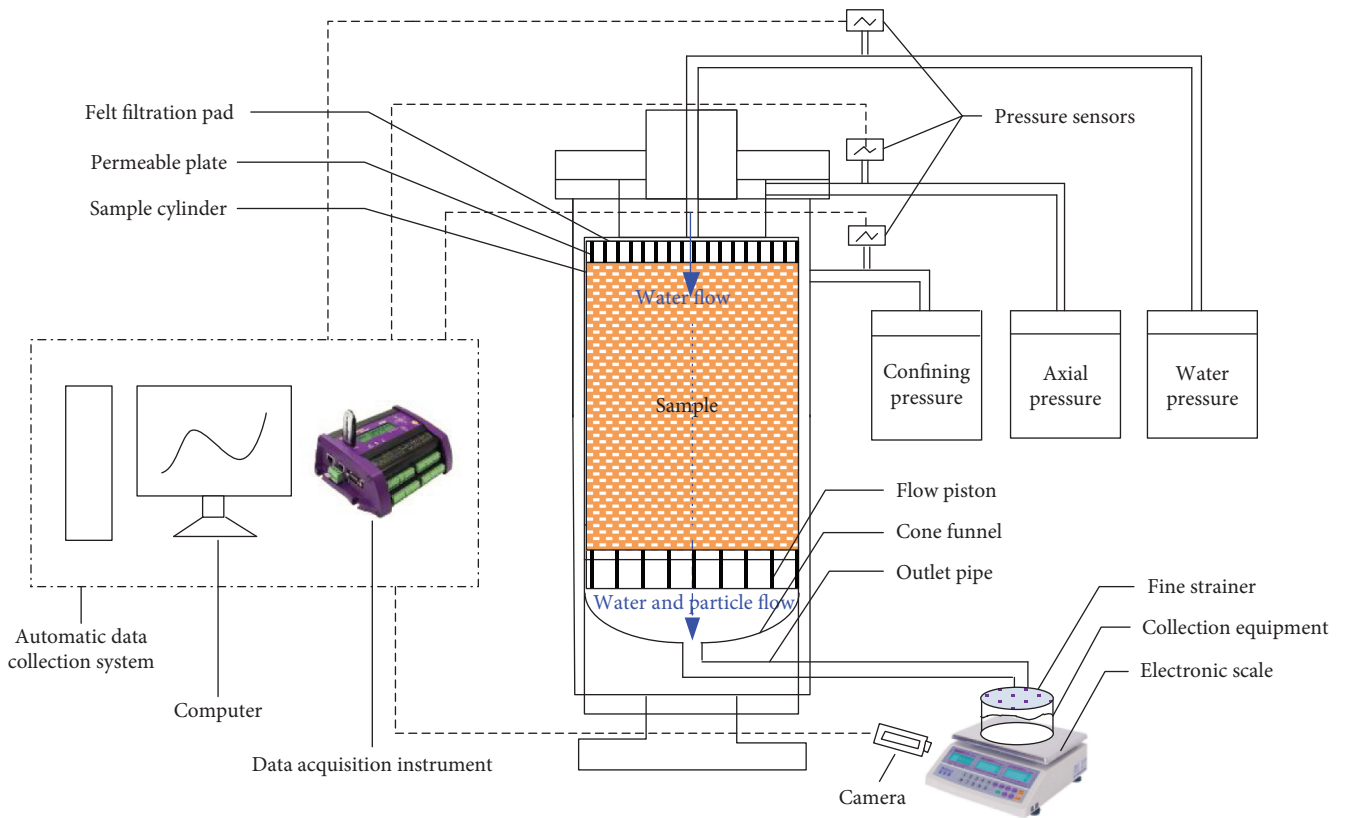


FIGURE 1: Large-scale triaxial testing system.

the mechanism of water inrush in completely weathered granite. Furthermore, many research results showed that lithology, water pressure, and pore structure are the key factors causing water inrush [25–27]. For example, [25] analyzed the water inrush of 12 coal seam floors and found that water inrush is more prone to occur with water pressure increasing. Walsh [28] and Wang et al. [29] studied the permeability under different water pressures and confining pressures. Moreover, many researches showed that the critical conditions existed for water inrush, such as water pressure and excavation thickness [4, 30].

In view of this, the objectives of this study are to investigate the mass transfer and nonlinear seepage properties of completely weathered granite and to quantify the impacts of water pressure and initial porosity on the water inrush evolution. To do this, we designed a new testing system that can simulate the properties of particle transfer and stress conditions, investigated the seepage-erosion properties under different water pressures and initial porosities, and finally proposed the critical relative conditions for water inrush.

2. Experimental System and Procedure

2.1. Testing System. As shown in Figure 1, a self-designed large-scale triaxial testing system is made up of four parties: a pressure control system, a particle transfer permeability testing system, an automatic data collection equipment, and a water and mud collection equipment. Figure 1 illustrates the system connections and principle.

The pressure control system is used to provide a constant stability axial pressure, confining pressure, and water pressure by three independent but the same structure pressure systems, composed of a hydraulic cylinder, gas pump, relief valve, and water pump. In the test, after using the water pump to fill the hydraulic cylinder with water, the gas pump is employed to provide a constant speed water inflow into the permeability system.

The most important part of this system is the particle transfer permeability testing system, which is mainly composed of a sample cylinder, permeable plate, flow piston, and cone funnel. A sample cylinder, with a maximum diameter and height of 100 mm and 300 mm, respectively, is used to place the test sample. The permeable plate design containing numerous “uniform and dense” holes can ensure that the water flows evenly, and the felt filtration pad can prevent the pores of the permeable plate from being blocked by the sample particles. The uniform “13-mm-diameter hole” flow piston will cause some particles from being flown away; the remaining particles pass through the cone funnel and can be collected by an outlet pipe and collection equipment.

The automatic data collection equipment includes pressure sensors, a camera for monitoring the flow rate, a computer, and a data acquisition instrument, which are used to collect the test pressures and flow rate (water flow velocity and particle transfer rate). The water and mud collection equipment includes a fine strainer and a collection container, which are used to filter and collect the particles and water.

TABLE 1: Physical and mechanical parameters of completely weathered granite.

Natural density/g cm ⁻³	Natural moisture/%	Porosity	Permeability coefficient/cm s ⁻¹	Cohesion c_{uu} /kPa	Internal friction angle $\Phi_{uu}/^\circ$
1.9	17	0.36	4.05×10^{-4}	60.2	1.9

TABLE 2: Test scheme.

Number	Water pressure (MPa)	Initial porosity	Total mass m_t (g)	Weight to each particle size (g)				
				$m_{(0-0.25 \text{ mm})}$	$m_{(0.25-2 \text{ mm})}$	$m_{(2-3 \text{ mm})}$	$m_{(3-5 \text{ mm})}$	$m_{(5-10 \text{ mm})}$
1	0.2	0.36	3233	628.5	885.1	569.6	430.9	718.8
2	0.4			628.5	885.1	569.6	430.9	718.8
3	0.6			628.5	885.1	569.6	430.9	718.8
4	0.6	0.23	3890	756.2	1064.9	685.3	518.4	864.8
5		0.30	3536	687.5	968.1	623.0	471.3	786.1
6		0.36	3233	628.5	885.1	569.6	430.9	718.8

2.2. Testing Design and Procedure

2.2.1. Testing Sample and Design. The samples used in the test were selected from approximately -100 strata in a typical weathered granite tunnel engineering, in Junchang tunnel in Guangxi Province of China [16]. Tests by the X-ray diffraction analysis showed that the sample minerals are quartz, illite, and kaolinite with a mass proportion of 75.2%, 19.3%, and 5.5%, respectively. Table 1 presents the basic physical and mechanical parameters of completely weathered granite.

According to practical engineering, the axial pressure, confining pressure, and water pressure tests were 2 MPa, 1 MPa, and 0.6 MPa, respectively. In the test, the coarse particles (>10 mm) were screened out, and the soil particles are classified into the following five groups based on the particle sizes using a screening test sieve machine: 0–0.25 mm, 0.25–2 mm, 2–3 mm, 3–5 mm, and 5–10 mm. The samples used include the above five group particle sizes with the weight designed as shown in Table 2. Furthermore, the designed sample height and diameter were 200 mm and 100 mm, respectively.

2.2.2. Testing Method and Procedure. The samples are required to be completely saturated by water before each experiment. The testing fluid is water with density = 1000 kg/m³ and kinetic viscosity = 1.01×10^{-3} Pa·s at the standard state. To obtain stable readings, measurements of the pressure and flow rate are performed after the axial pressure and confining pressure are maintained at a fixed level.

The test steps are as follows:

- (1) Fill the sample: first, weigh the sample. Place and compact the sample into the sample cylinder as layers and then install the permeable plate and assemble the test system.
- (2) Saturate the sample: saturate the sample with a water injection using the water pressure control system and then measure the initial permeability.

- (3) Apply the axial and confining load: apply the axial and confining load to the sample gradually, reach the desired values, and then keep the loads steady until the test is completed.

- (4) Apply the water pressure to the sample and collect the test data: first, apply the desired water pressure to the sample gradually and start the penetration test. Then immediately monitor the test data (pressure and flow velocity) and collect the eroded particles and water flow every 30 s.

Figure 2 illustrates the entire experimental procedure. The criteria for the test termination are that the particles are not eroded away and the flow water is clear.

2.3. Test Parameter Measurement and Calculation Principle. During water flow in a completely weathered granite, the particles will be washed away because of the effect of water pressure, which will cause an increase in the porosity and permeability and thus induce an increase in the water inflow. Moreover, the flow properties may change from a Darcy flow to a non-Darcy flow, with a consistent increase in particle loss. Therefore, based on the mass transfer, the porosity, permeability, water inflow evolution rate with time, a non-Darcy flow, and water inrush can be determined.

2.3.1. Mass of Particle Transfer. In the tests, particles are collected every 30 s (Δt), and the particle mass transferred in each Δt is $\Delta m_1, \Delta m_2, \dots, \Delta m_m$.

The total particle mass transfer for $t_i = \Delta t_1 + \Delta t_2 + \dots + \Delta t_i = i\Delta t$ ($i = 1, 2, \dots, m$) is m_m .

$$m_i = \Delta m_1 + \Delta m_2 + \dots + \Delta m_i \quad (i = 1, 2, \dots, m). \quad (1)$$

2.3.2. Porosity Evolution. The sample porosity will increase with the particle transfer. Porosity φ_i in time (t_{i-1}, t_i) is

$$\varphi_i = \varphi_0 + \frac{1}{\pi a^2 h_i \rho_s} (\Delta m_1 + \Delta m_2 + \dots + \Delta m_i) \quad (i = 1, 2, \dots, m), \quad (2)$$

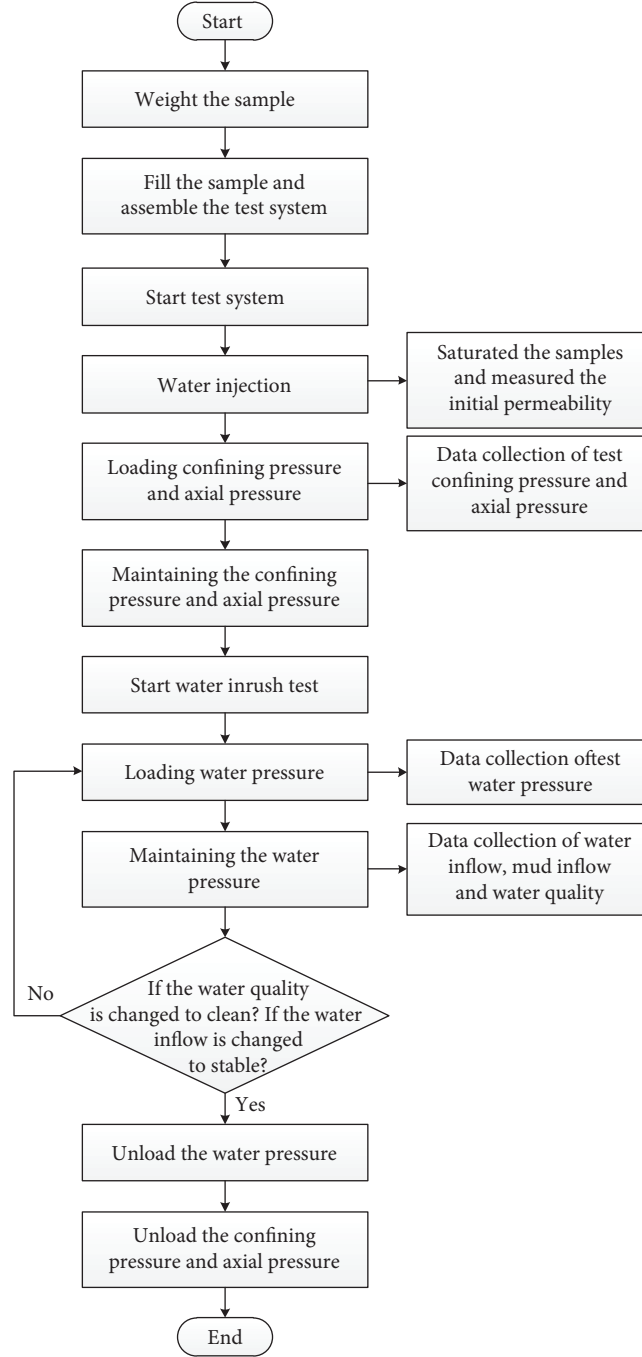


FIGURE 2: Experimental procedure of completely weathered granite.

where a is the sample radius; ρ_s is the mass density of the grain. h_i is the real-time sample height, which is calculated according to the mass transfer. To calculate the real-time height, it is assumed that the mass transfer is approximately from the bottom sample particles, leading to a change in the sample height. The expression of h_i is as follows:

$$h_i = h_0 - \frac{1}{\pi a^2 \rho_s} (\Delta m_1 + \Delta m_2 + \dots + \Delta m_i) \quad (i = 1, 2, \dots, m). \quad (3)$$

2.3.3. Permeability Evolution and Non-Darcy Approach.

Under the effect of particle transfer, the sample permeability will increase and may cause the flow pattern to change from a Darcy to a non-Darcy flow. For a completely weathered granite, the Reynolds number (Re) is defined as follows:

$$Re = \frac{\rho_f v d_p}{\mu \phi}, \quad (4)$$

where ρ_f is the water density, v is the average water flow velocity, d_p is a grain diameter greater than that of 10% of

TABLE 3: Mass transfer amounts with time to each sample (g) (partial results).

Number	Water pressure (MPa)	Initial porosity	Time (min)											
			0	5	10	20	30	40	50	60	90	120		
1	0.2	0.36	0	8.8	17.4	30.8	45.0	54.8						
2	0.4		0	20.0	34.9	66.5	85.0	92.3	116.1	145.7				
3	0.6		0	8.4	25.5	76.7	129.2	205.7	276.9	287.9	345.6			
4	0.6	0.23	0	13.0	22.5	39.1	67.9	86.7	99.4	101.7	113.2	120.3		
5		0.30	0	38.3	62.9	88.1	116.8	137.3	149.0	164.4	240.2	259.9		
6		0.36	0	8.4	25.5	76.7	129.2	205.7	276.9	287.9	345.6			

the particles by weight, and μ is the kinetic viscosity of the water.

Various studies have shown that the critical Reynolds number for a flow between a Darcy and a non-Darcy flow is 10, and that for different porous media, this limit is slightly different [31, 32].

When $Re \leq 10$, the flow satisfies Darcy's law as follows:

$$v = -\frac{k}{\mu}(\nabla p + \rho_f g \nabla z), \quad (5)$$

where k is the sample absolute permeability, ∇p is the pore pressure gradient, g is the gravitational acceleration, and z is the vertical axis passing through the center of the sample and its direction is upward.

Compared with the water pressure, gravity can be ignored owing to the relatively small sample size, and Darcy's law for a one-dimensional axial flow can be simplified as follows:

$$v = -\frac{k}{\mu} \nabla p, \quad (6)$$

where v is calculated by water inflow Q .

$$v = \frac{Q}{\pi a^2}. \quad (7)$$

In the test, the upstream end of the sample was connected to the water pressure system, which could automatically record the change in the pore pressure over time. The inlet boundary at pore pressure p_1 was assumed to have a steady value of p as tested and designed, whereas the outlet boundary was exposed to the atmosphere, causing pore pressure p_2 to be zero. Assuming that the water pressure is uniformly distributed, the pressure gradient can be simplified as follows:

$$\nabla p = \frac{\partial p}{\partial z} = -\frac{p_2 - p_1}{h_i} = -\frac{p}{h_i}. \quad (8)$$

Therefore, combining (5), (6), (7), and (8), permeability k_i at moment t_i can be obtained for the Darcy flow.

$$k_i = \frac{Q\mu h_i}{\pi a^2 p} \quad (i = 1, 2, \dots, m). \quad (9)$$

When $Re > 10$, the flow rate will increase rapidly and the flow process will enter the non-Darcy stage. The Forchheimer equation [33] as given below, considering

the inertia force of the fluid flow, is more suitable for depicting the non-Darcy flow.

$$-\frac{\partial p}{\partial z} = \frac{\mu}{k} v + \rho_f \beta v^2, \quad (10)$$

where β is the coefficient of the non-Darcy flow.

Considering the permeability to be continuously changing in the evolution process, to obtain the time evolution of permeability, permeability k_i at moment t_i was approximately calculated by the average permeability value at time $(t_i - t_{i+1})$. Therefore, the permeability for the non-Darcy flow can be obtained by a second-order polynomial method.

$$k_i = \frac{\mu v_i v_{i+1} (v_{i+1} - v_i)}{(v_{i+1}^2 h_i - v_i^2 h_{i+1}) p} h_i h_{i+1} \quad (i = 1, 2, \dots, m), \quad (11)$$

where v_i is the flow velocity at moment t_i .

2.4. Fluidized Grain Concentration. Fluidized grain concentration c refers to the concentration of grains dissolved in the fluid and is defined as follows:

$$c = \frac{\Delta m_i}{\rho_f \Delta Q_i + \Delta m_i} \quad (i = 1, 2, \dots, m), \quad (12)$$

where ΔQ_m is the water inflow in time Δt .

3. Test Results and Discussion

In order to investigate the impact of water pressure and porosity on seepage-erosion properties of completely weathered granite and to propose the respective critical conditions for water inrush, a series of tests consider the last factors as water pressure and initial porosity were conducted, and the mass transfer, porosity, water inflow, permeability, and the flow pattern through the tests were also monitored. Specifically, first, the tests under different water pressures were conducted to investigate the critical water pressure for water inrush, and then the variable initial porosity based on the critical water pressure was conducted to investigate the critical porosity.

The transferred particles are collected for every 30 seconds; according to (1), the mass transfer for t_i ($i = 1, 2, \dots, n$) can be obtained as shown in Table 3. Meanwhile, according to (2), the porosity to time t_i can be calculated as shown in Table 4. By data collection of water inflow and combining (4), (9), and (11), the Reynolds number,

TABLE 4: Porosity with time to each sample (partial results).

Number	Water pressure (MPa)	Initial porosity	Time (min)										
			0	5	10	20	30	40	50	60	90	120	
1	0.2	0.36	0.36	0.36	0.36	0.37	0.37	0.37					
2	0.4		0.36	0.36	0.37	0.38	0.38	0.38	0.39	0.39			
3	0.6		0.36	0.36	0.37	0.38	0.39	0.41	0.43	0.43	0.44		
4	0.6	0.23	0.23	0.23	0.24	0.24	0.25	0.25	0.25	0.25	0.26	0.26	0.26
5		0.30	0.30	0.31	0.32	0.32	0.33	0.33	0.34	0.34	0.36	0.36	0.36
6		0.36	0.36	0.36	0.37	0.38	0.39	0.41	0.43	0.43	0.44		

TABLE 5: Reynolds number with time to each sample (partial results).

Number	Water pressure (MPa)	Initial porosity	Time (min)										
			0	5	10	20	30	40	50	60	90	120	
1	0.2	0.36	0	0.07	0.11	0.07	0.07	0.10					
2	0.4		0	1.70	2.44	2.32	2.34	2.42	3.50	3.94			
3	0.6		0	0.74	2.11	6.84	8.65	12.16	13.00	10.38	11.81		
4	0.6	0.23	0	0.21	0.12	0.13	0.15	0.14	0.16	0.16	0.16	0.16	0.16
5		0.30	0	1.97	1.36	1.20	1.75	2.51	2.50	2.98	1.54	1.87	
6		0.36	0	0.74	2.11	6.84	8.65	12.16	13.00	10.38	11.81		

TABLE 6: Permeability with time to each sample (unit: $e - 12 \text{ m}^2$) (partial results).

Number	Water pressure (MPa)	Initial porosity	Time (min)										
			0	5	10	20	30	40	50	60	90	120	
1	0.2	0.36	0.5	4.1	5.5	6.2	6.4	6.2					
2	0.4		0.5	3.4	4.4	4.5	4.7	4.3	6.5	7.5			
3	0.6		0.5	1.0	1.8	8.4	12.1	14.9	14.6	14.1	15.6		
4	0.6	0.23	0.3	4.6	3.1	2.5	3.3	3.3	3.9	4.0	4.1	5.2	
5		0.30	0.4	2.4	1.8	1.3	1.7	2.7	2.8	3.5	2.0	2.0	
6		0.36	0.5	1.0	1.8	8.4	12.1	14.9	14.6	14.1	15.6		

permeability can be obtained, as shown in Tables 5 and 6. All of the data are drawn in Figures 3–13.

3.1. Effect of Water Pressure on Seepage-Erosion Properties

3.1.1. Mass Transfer Properties under Different Water Pressures. According to the field investigation, large variations of water pressure exist in the weathered zone of Junchang tunnel, which range from 0.2 to 1.5 MPa. Therefore, tests of different water pressures but the same porosity (0.36) were carried out to study the critical water pressure for water inrush, and the designed water pressures were increased from 0.2 MPa to critical value by every 0.2 MPa.

As shown in Figure 3, the weight of particle transfer m increases with time passes and meets maximum finally. For $p = 0.2$ MPa, the maximum mass transfer is 54.84 g, reaching 1.7% of the total mass, and the average mass rate (curve slope) is 1.37 g/min. When $p = 0.4$ MPa, the mass transfer and average mass rate increase to 190.42 g and 2.5 g/min, respectively. With the pressure increases to 0.6 MPa, the mass

transfer and average mass rate significantly increase to 354.22 g and 5.37 g/min, respectively. This is mainly because of higher water pressure has higher water seepage ability. The mass transfer is lower than 5% of sample total mass when $p \leq 0.4$ MPa; however, when $p = 0.6$ MPa, the mass transfer reaches the 11% of the total mass, indicating that a large amount of particles has been eroded.

Figure 4 shows the porosity increases with water pressure; the final porosity for $p = 0.2, 0.4,$ and 0.6 MPa is 0.37, 0.40, and 0.44, a 2.8%, 11.1%, and 22.2% increase of initial porosity, respectively. It can be obtained that the evolution of porosity is consistent with the mass transfer.

Furthermore, the fluidized grain concentration, which can reflect the effect of the mass generation and water seepage process, can be divided into two stages, namely, increased at first and decreased at last, as shown in Figure 5. At the first stage, owing to the high content of fine particles and low permeability, numerous particles will be generated and cannot be transferred, resulting in an increase in fluidized grain concentration. In contrast, the concentration will

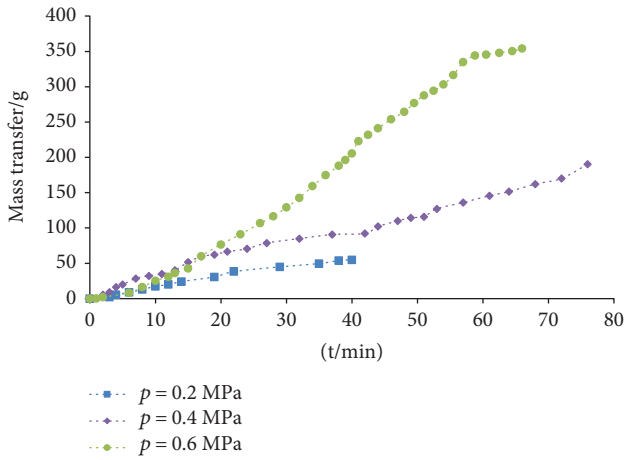


FIGURE 3: Mass transfer for different water pressures.

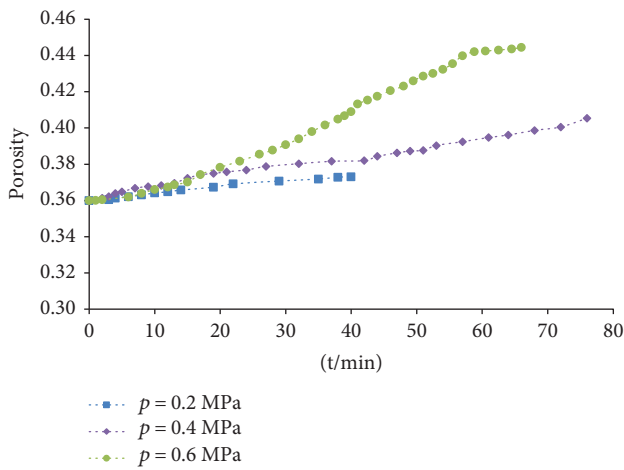


FIGURE 4: Time evolution of porosity for different water pressures.

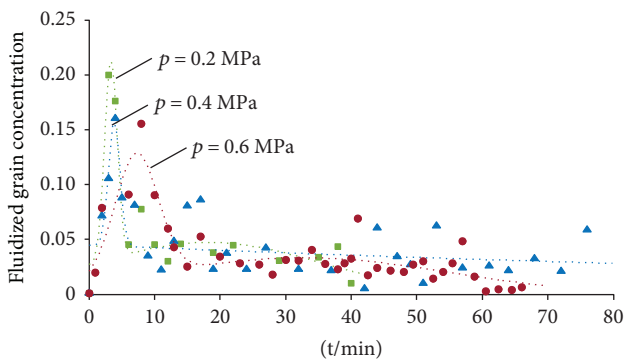


FIGURE 5: Time evolution of fluidize grain concentration for different water pressures.

decrease with the increase in seepage ability along with the decrease in mass generation in the second stage. From Figure 5, the peak value of concentration decreases with the increase in water pressure, and this is mainly because of the higher water pressure has higher water seepage ability,

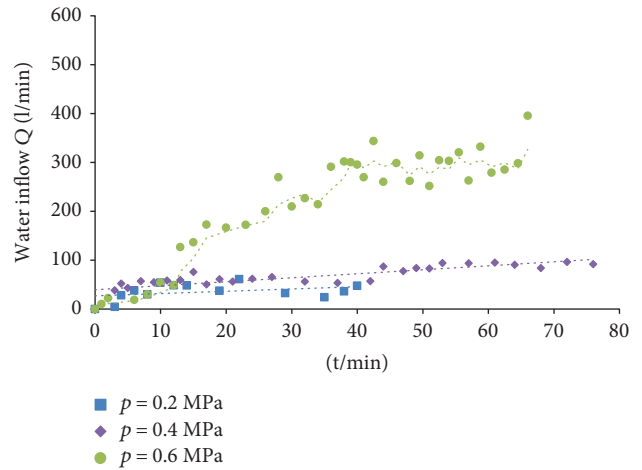


FIGURE 6: Time evolution of water inflow for different water pressures.

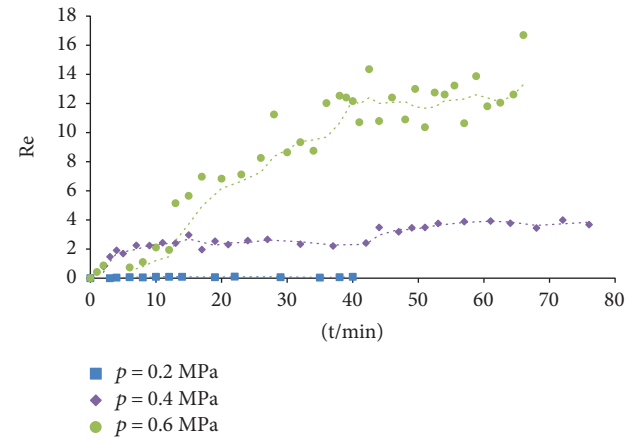


FIGURE 7: Time evolution of Reynolds number for different water pressures.

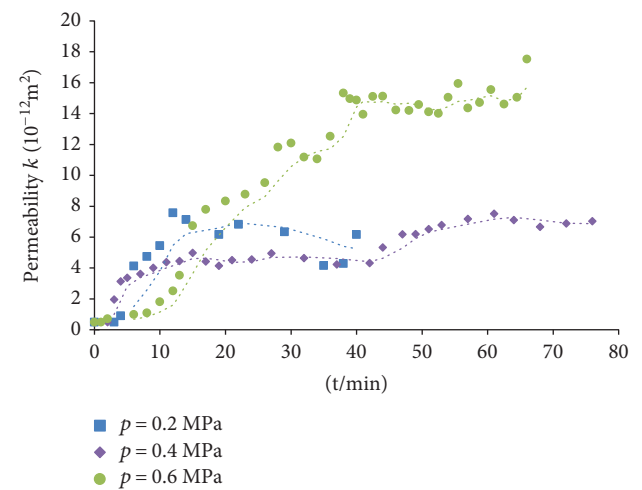


FIGURE 8: Time evolution of permeability for different water pressures.

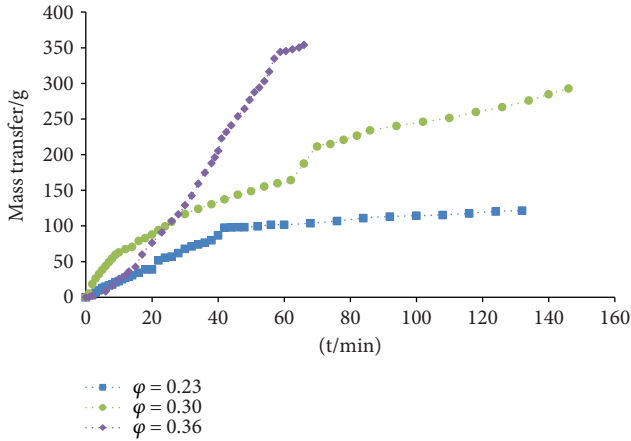


FIGURE 9: Time evolution of mass transfer for different initial porosities.

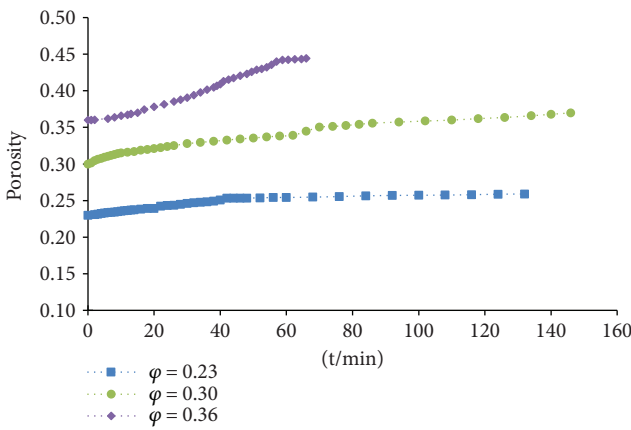


FIGURE 10: Time evolution of porosity for different initial porosities.

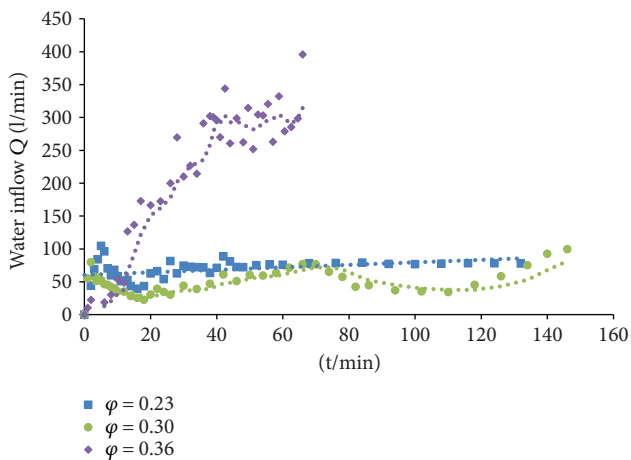


FIGURE 11: Time evolution of water inflow for different initial porosities.

resulting in the particle transfer that is faster than mass generation, which indicates that a water inrush channel is easier to form.

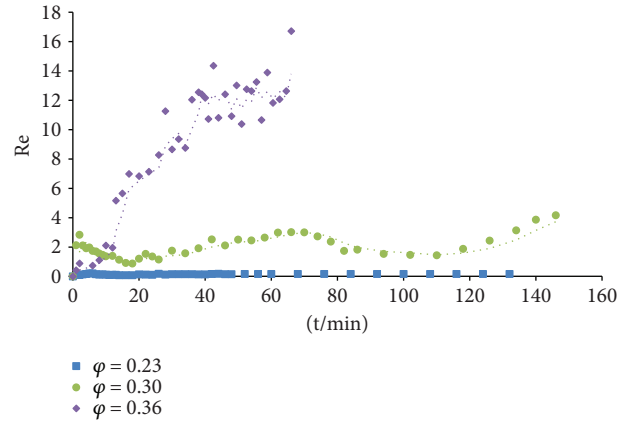


FIGURE 12: Time evolution of Reynolds number for different initial porosities.

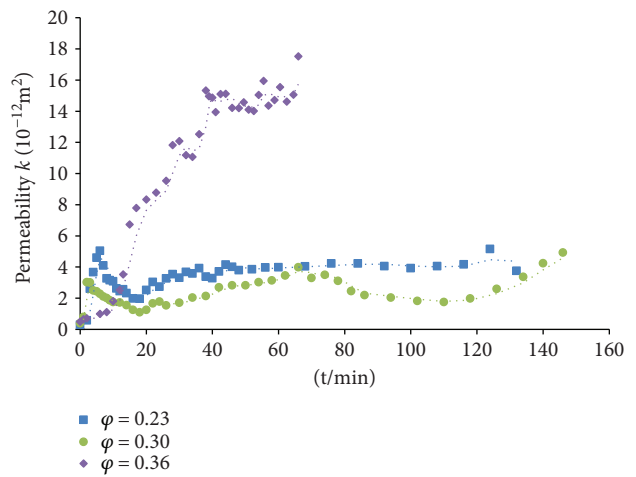


FIGURE 13: Time evolution of permeability for different initial porosities.

Therefore, it is reasonable to conclude that the particle transfer is the key factor determining the porosity and flow properties such as permeability and flow pattern, as discussed in the following sections. In addition, when $p \geq 0.6$ MPa, the mass transfer and porosity increase rapidly in a short time, indicating that the risk of water inrush is more serious.

3.1.2. Seepage Properties under Different Water Pressures.

Water inflow, the key factor in evaluating the risk of water inrush, is shown in Figure 6. The water inflow increases with the increasing water pressure; the increase for $p \leq 0.4$ MPa is linear and smaller, and the maximum value is 91.89 ml/min. In comparison, the water inflow when $p = 0.6$ MPa is as high as 395.84 ml/min, larger by over 4.3 times that when $p \leq 0.4$ MPa. This indicates that there exists a critical water pressure (0.6 MPa) to induce the significant increase of water inflow.

By collecting water inflow data and using (4), the time evolution of the Reynolds number (Re) to variable water pressure can be obtained, which is shown in Figure 7. As stated by various scholars, for a flow between a Darcy and a

non-Darcy, the critical Reynolds number is 10 [31, 32]. Therefore, it can be observed from the figure that in the entire time, Re is linearly evolving, and the maximum Re is 3.67, which is much less than 10 when $p < 0.6$ MPa, indicating that the flow is a Darcy flow. However, when $p = 0.6$ MPa, Re increases rapidly, exceeding 10 in 28 min, and a maximum Re of 16.7 is attained, indicating that the flow pattern has changed from a Darcy to a non-Darcy flow after 28 min of evolution (see Table 7).

By collecting water inflow data, combining (9) and (11), and considering the flow pattern, the time evolution of permeability k with variable water pressure can be obtained, as displayed in Figure 8.

Permeability increases with time, and concurrently, a higher water pressure corresponds to a higher ultimate permeability and permeability increase amplitude, as is evident from Table 8, for example, ultimate permeability and permeability increase amplitude for 0.2 MPa are $6.1e-12 \text{ m}^2$ and 12.2, respectively, and that for 0.6 MPa are $1.8e-11 \text{ m}^2$ and 36, respectively. Meanwhile, the increase in permeability for $p < 0.6$ MPa is relative smaller, while when pressure increases to 0.6 MPa, the permeability increases rapidly and nonlinearly.

It can be observed that the variable of seepage behaviors such as water inflow, Reynolds number, and permeability increased more slowly and that growth is very smaller under low water pressure ($p < 0.6$ MPa), and the flow is a Darcy linear flow. With the increase of water pressure ($p \geq 0.6$ MPa), the evolution of seepage behaviors increased rapidly, and the flow pattern has changed from a Darcy to a non-Darcy flow, which means that the water inrush risk increases seriously.

Therefore, it is reasonable to conclude that the particle transfer is the key factor determining the porosity, permeability, and water inrush. In addition, when $p \geq 0.6$ MPa, the mass transfer and porosity, water inflow, and permeability increase rapidly in a short time, indicating that the risk of water inrush is more serious, and it means that the critical pressure of water inrush is 0.6 MPa.

3.2. Effect of Initial Porosity on Seepage-Erosion Properties.

Based on the above test analysis, a critical water pressure (0.6 MPa) of water inrush was obtained for completely weathered granite with initial porosity of 0.36. Meanwhile, in practical engineering, the pore filling or backfilling is one of the measures to prevent the water inrush. In order to analyze the effect of initial porosity on seepage-erosion properties, and to provide the proposed value for water inrush prevention. Tests are carried out with different initial porosities but with the same water pressure (0.6 MPa); the designed porosities were decreased from 0.36 to critical value by approximately every 16% of initial porosity (0.36), namely, 0.36, 0.3, and 0.23 critical values.

3.2.1. Mass Transfer Properties under Different Initial Porosities.

As shown in Figure 9, the mass transfer decreases with the decrease of initial porosity. For $\varphi = 0.36$, the maximum mass transfer is 354.22 g, reaching 11% of the total mass, When φ decreases from 0.36 to 0.3, the maximum mass

TABLE 7: Results of Reynolds number for different water pressures.

p/MPa	Max (Re)	Time for critical Re/min	Flow pattern
0.2	0.10	—	Darcy
0.4	3.67	—	Darcy
0.6	16.70	28	Darcy, non-Darcy

TABLE 8: Results of permeability for different water pressures.

p/MPa	Initial permeability k_0 (m^2)	Ultimate permeability k_f (m^2)	Total time t (min)	Permeability increase amplitude k_f/k_0
0.2	$5.0e-13$	$6.1e-12$	40	12.2
0.4	$5.0e-13$	$7.1e-12$	76	14.2
0.6	$5.0e-13$	$1.8e-11$	66	36

TABLE 9: Results of porosity for different initial porosities.

Initial porosity (φ_0)	Final porosity (φ_m)	Total time t (min)	Porosity increase amplitude $(\varphi_m - \varphi_0)/\varphi_0$	Porosity increase rate $(\varphi_m - \varphi_0)/t$
0.23	0.25	132	8.7%	0.015%
0.30	0.37	146	23.3%	0.048%
0.36	0.44	66	28.8%	0.121%

transfer decreases from 17.3% to 292.78 g, but still reaching 8.3% of the total mass; moreover, when φ decreases to 0.23, the maximum mass transfer decreases from 65.7% to 121.4 g, only reaching 3.1% of the total mass. This indicates that the decrease of initial porosity is an effect measure to restrain the mass transfer and water inrush risk, especially when the porosity decreases over 30% of the undisturbed soil.

With the decrease of initial porosity, the porosity increase amplitude and rate of final porosity decrease, and the total evolution time extends in general, as shown in Figure 10 and Table 9. For example, the evolution time, the porosity increase amplitude, and increase rate for 0.36 are 66 min, 28.8%, and 0.12%/min, respectively, in comparison, while when $\varphi = 0.23$, the evolution time extends to 132 min, twice longer than that in $\varphi = 0.36$, and the porosity increase amplitude and increase rate are 8.7% and 0.015%/min, respectively, a 70% and 87.5% decrease of that in $\varphi = 0.36$, respectively. This is mainly because that the sample with lower porosity has a higher compactness, a lower permeability, and a smaller flow channels.

3.2.2. Seepage Properties under Different Initial Porosities.

As displayed in Figure 11, water inflow decreases with the decrease of initial porosity, for example, water inflow for $\varphi = 0.36$ is 395.84 ml/min, and the evolution curve is non-linear, while when $\varphi \leq 0.3$, the evolution curve is kept stable and almost unchanged; the final water inflow is less than 100 ml/min, an over 60% decrease of that in $\varphi = 0.36$,

TABLE 10: Results of permeability for different initial porosities.

Initial porosity (φ_0)	Initial permeability k_0 (m^2)	Ultimate permeability k_f (m^2)	Permeability increase amplitude k_f/k_0
0.23	$3.1e-13$	$3.7e-12$	12
0.30	$3.9e-13$	$4.9e-12$	13
0.36	$5.0e-13$	$1.8e-11$	36

indicating that the water inflow decreases rapidly when the initial porosity decreases to 0.3, especially it decreases 30% to 0.23.

Figure 12 shows the time evolution of the Reynolds number (Re) to variable initial porosity. It can be observed from the figure that Re increases rapidly and nonlinearly, exceeding the critical Reynolds number in 28 min when $\varphi = 0.36$, indicating that the flow is a non-Darcy flow. However, with the initial porosity decrease, the maximum Re decreases to 4.17; particularly for 0.23, the maximum Re is only 0.165, which is much less than 10, and in the entire time, Re is linearly evolving, indicating that the flow has changed from a non-Darcy to a Darcy flow.

Figure 13 shows the time evolution of permeability k with variable initial porosity. Permeability increases with time, and concurrently, a lower initial porosity corresponds to a lower ultimate permeability and permeability increase amplitude, as is evident from Table 10, for example, the ultimate permeability and permeability increase amplitude for $\varphi = 0.36$ are $1.8e-11 \text{ m}^2$ and 36, respectively; however, for $\varphi = 0.23$, the ultimate permeability is $3.7e-12 \text{ m}^2$, an 80% decrease of that in $\varphi = 0.36$, and the permeability increase amplitude is 12, a 67% decrease of that in $\varphi = 0.36$. This indicates that the permeability evolution can be effectively restrained when the initial porosity decreases to 0.3 below, particularly for $\varphi = 0.23$.

Based on the above analysis of the mass transfer, porosity, and flow properties under different initial porosities, it is reasonable to conclude that the pore filling or backfilling is an effective measure to ameliorate the anti-inrush properties for completely weathered granite. In addition, when the porosity decreases 30% of initial porosity to 0.23, the ultimate mass transfer, water inflow, and permeability decrease 65.7%, 60%, and 80%, respectively, indicating that the risk of water inrush was reduced significantly, and it means that the critical porosity of anti-inrush in completely weathered granite is 0.23.

4. Conclusions

A self-designed apparatus was developed to investigate the evolution features of water inrush in completely weathered granite, and a series of tests were carried out to study the effects of water pressure and porosity on seepage-erosion properties. The main findings were as follows:

- (1) The particle transfer could cause an increase in the porosity, permeability, and water inflow and eventually induce a water inrush disaster. Meanwhile, the

flow pattern may be changed with the mass transfer; at the beginning, the flow is a Darcy flow; however, with the continuous particle transfer, the flow may be transferred into a nonlinear flow, leading a rapidly increase of permeability and water inflow, which is a significant signal for water inrush.

- (2) A series of tests were designed to investigate the effects of the water pressure on water inrush evolution, and a critical value ($p = 0.6 \text{ MPa}$) that caused the water inrush was obtained. In particular, when the water pressure increased to the critical value, the values of water inflow and permeability reached 395.8 ml/min and $1.8e-11 \text{ m}^2$, respectively, both thrice larger than that at a lower water pressure ($p \leq 0.4 \text{ MPa}$), and the flow changed from a Darcy flow to a significant nonlinear flow.
- (3) Based on the tests under different water pressures, tests with variable porosities were carried out to study the initial porosity on the water inrush evolution, and a critical value ($\varphi = 0.23$) to control the water inrush was observed. In particular, when the initial porosity decreases to the critical value, the values of water inflow and permeability both decrease 80% of that in undisturbed stratum ($\varphi = 0.36$), and the flow pattern has changed from a nonlinear flow to a Darcy flow, indicating that the water inrush risk has been restrained and the pore filling or backfilling technology is an effective measure to prevent water inrush.

Data Availability

The data used to support the findings of this study are available from the corresponding author upon request.

Conflicts of Interest

The authors declare that they have no conflicts of interest.

Acknowledgments

This work was supported by the China National Basic Research Program, the “973 Program” (no. 2013CB036006), and the China National Natural Science Foundation (nos. 51509246 and 51708220). These financial supports are gratefully acknowledged.

References

- [1] Q. L. Cui, H. N. Wu, S. L. Shen, Z. Y. Yin, and S. Horpibulsuk, “Protection of neighbour buildings due to construction of shield tunnel in mixed ground with sand over weathered granite,” *Environment and Earth Science*, vol. 75, no. 6, p. 458, 2016.
- [2] J. Liu, W. Chen, D. Yang, J. Yuan, X. Li, and Q. Zhang, “Nonlinear seepage-erosion coupled water inrush model for completely weathered granite,” *Marine Georesources & Geotechnology*, vol. 36, no. 4, pp. 484–493, 2017.
- [3] B. Yao, Z. Chen, J. Wei, T. Bai, and S. Liu, “Predicting erosion-induced water inrush of karst collapse pillars using inverse

- velocity theory," *Geofluids*, vol. 2018, Article ID 2090584, 18 pages, 2018.
- [4] K. Zhang, B. Zhang, J. Liu, D. Ma, and H. Bai, "Experiment on seepage property and sand inrush criterion for granular rock mass," *Geofluids*, vol. 2017, Article ID 9352618, 10 pages, 2017.
 - [5] D. L. Zhang, Q. Fang, and H. C. Lou, "Grouting techniques for the unfavorable geological conditions of Xiang'an subsea tunnel in China," *Journal of Rock Mechanics and Geotechnical Engineering*, vol. 6, no. 5, pp. 438–446, 2014.
 - [6] S. L. Shen and Y. S. Xu, "Numerical evaluation of land subsidence induced by groundwater pumping in Shanghai," *Canadian Geotechnical Journal*, vol. 48, no. 9, pp. 1378–1392, 2011.
 - [7] S. L. Shen, Y. X. Wu, and A. Misra, "Calculation of head difference at two sides of a cut-off barrier during excavation dewatering," *Computers and Geotechnics*, vol. 91, pp. 192–202, 2017.
 - [8] Y. Zhao, P. Li, and S. Tian, "Prevention and treatment technologies of railway tunnel water inrush and mud gushing in China," *Journal of Rock Mechanics and Geotechnical Engineering*, vol. 5, no. 6, pp. 468–477, 2013.
 - [9] H. M. Lyu, W. J. Sun, S. L. Shen, and A. Arulrajah, "Flood risk assessment in metro systems of mega-cities using a GIS-based modeling approach," *Science of the Total Environment*, vol. 626, pp. 1012–1025, 2018.
 - [10] F. Arıkan, R. Ulusay, and N. Aydın, "Characterization of weathered acidic volcanic rocks and a weathering classification based on a rating system," *Bulletin of Engineering Geology and the Environment*, vol. 66, no. 4, pp. 415–430, 2007.
 - [11] T. I. Gamon, "A comparison of existing schemes for the engineering description and classification of weathered rocks in Hong Kong," *Bulletin of the International Association of Engineering Geology*, vol. 28, no. 1, pp. 225–232, 1983.
 - [12] T. Y. Irfan, "Mineralogy, fabric properties and classification of weathered granites in Hong Kong," *Quarterly Journal of Engineering Geology and Hydrogeology*, vol. 29, no. 1, pp. 5–35, 1996.
 - [13] S. Ceryan, S. Tudes, and N. Ceryan, "A new quantitative weathering classification for igneous rocks," *Environmental Geology*, vol. 55, no. 6, pp. 1319–1336, 2008.
 - [14] J. N. Shirlaw, "Pressurised TBM tunnelling in mixed face conditions resulting from tropical weathering of igneous rock," *Tunnelling and Underground Space Technology*, vol. 57, pp. 225–240, 2016.
 - [15] J. N. Shirlaw, S. R. Hencher, and J. Zhao, "Design and construction issues for excavation and tunnelling in some tropically weathered rocks and soils," in *International Society for Rock Mechanics International Symposium*, Melbourne, Australia, 2000.
 - [16] J. Liu, W. Chen, J. Yuan, C. Li, Q. Zhang, and X. Li, "Groundwater control and curtain grouting for tunnel construction in completely weathered granite," *Bulletin of Engineering Geology and the Environment*, vol. 77, no. 2, pp. 515–531, 2018.
 - [17] W. J. Guo and Y. X. Liu, "The concept of water in-rush coefficient and its application," *Journal of Hebei Coal*, vol. 2, pp. 56–60, 1989.
 - [18] Y. X. Wu, J. S. Shen, W. C. Cheng, and T. Hino, "Semi-analytical solution to pumping test data with barrier, wellbore storage, and partial penetration effects," *Engineering Geology*, vol. 226, pp. 44–51, 2017.
 - [19] L. J. Li, *Study of Water In-Rush Mechanism*, Ph.D. Thesis, China University of Mining and Geology, Xuzhou, Peoples's Republic of China, 1996.
 - [20] D. Ma, "Boundary integral computation of elastic water resisting key strata under the condition of discontinuous load," *Computer Modeling in Engineering and Sciences*, vol. 83, pp. 561–574, 2012.
 - [21] J. A. Wang and H. D. Park, "Coal mining above a confined aquifer," *International Journal of Rock Mechanics and Mining Sciences*, vol. 40, no. 4, pp. 537–551, 2003.
 - [22] T. Yang, C. Tang, and H. Liu, "Numerical model of the instability-failure process of the coal-bed floor due to confined water inrush," *Journal of Geomechanics*, vol. 9, pp. 281–288, 2003.
 - [23] T. H. Yang, J. Liu, W. C. Zhu, D. Elsworth, L. G. Tham, and C. A. Tang, "A coupled flow-stress-damage model for groundwater outbursts from an underlying aquifer into mining excavations," *International Journal of Rock Mechanics and Mining Sciences*, vol. 44, no. 1, pp. 87–97, 2007.
 - [24] X. X. Liu, S. L. Shen, Y. S. Xu, and Z. Y. Yin, "Analytical approach for time-dependent groundwater inflow into shield tunnel face in confined aquifer," *International Journal for Numerical and Analytical Methods in Geomechanics*, vol. 42, no. 4, pp. 655–673, 2018.
 - [25] H. Liu, T. H. Yang, Q. L. Yu, S. K. Chen, and C. H. Wei, "Numerical analysis on the process of water inrush from the floor of seam 12 in Fangezhuang coal mine," *Coal Geology & Exploration*, vol. 38, no. 3, pp. 27–31, 2010.
 - [26] D. Ma, X. X. Miao, Z. Q. Chen, and X. B. Mao, "Experimental investigation of seepage properties of fractured rocks under different confining pressures," *Rock Mechanics and Rock Engineering*, vol. 46, no. 5, pp. 1135–1144, 2013.
 - [27] Z. P. Meng, B. B. Zhang, X. T. Xie, Z. W. Shen, F. J. He, and Z. D. Pan, "Evaluation of water inrush risk of seam floor based on lithology-structure," *Coal Geology & Exploration*, vol. 39, no. 5, pp. 35–40, 2011.
 - [28] J. B. Walsh, "Effect of pore pressure and confining pressure on fracture permeability," *International Journal of Rock Mechanics and Mining Sciences & Geomechanics Abstracts*, vol. 18, no. 5, pp. 429–435, 1981.
 - [29] L. Wang, Z. Chen, H. Kong, and H. Shen, "Effects of pore pressure on permeability of sandstone during bending deformation," *International Journal of Rock Mechanics and Mining Sciences*, vol. 70, pp. 26–32, 2014.
 - [30] F. Geng and J. H. Saleh, "Challenging the emerging narrative: critical examination of coalmining safety in China, and recommendations for tackling mining hazards," *Safety Science*, vol. 75, pp. 36–48, 2015.
 - [31] P. Erhard, D. Etling, U. Muller, U. Riedel, K. R. Sreenivasan, and J. Warnatz, *Prandtl-Essentials of Fluid Mechanics*, Springer Science & Business Media, New York, NY, USA, 3rd edition, 2009.
 - [32] X. Y. Kong, *Advanced Mechanics of Fluids in Porous Media*, Press of University of Science and Technology of China, Hefei, China, 2nd edition, 2010.
 - [33] P. Forchheimer, "Wasserbewegung durch boden," *Zeitschrift des Vereins Deutscher Ingenieure*, vol. 45, pp. 1782–1788, 1901.

Research Article

Study on the Law of Membrane Efficiency of Unsaturated Shale and Its Application

Long Chang ^{1,2} Hongkui Ge ^{1,2,3} Yinghao Shen ^{1,2} Zehui Huang^{1,2} and Qian Zhang^{1,2}

¹State Key Laboratory of Petroleum Resources and Prospecting, China University of Petroleum, Beijing 102249, China

²Unconventional Natural Gas Institute, China University of Petroleum, Beijing 102249, China

³China University of Petroleum-Beijing, Karamay 834000, China

Correspondence should be addressed to Hongkui Ge; gehongkui@163.com

Received 14 March 2018; Revised 25 May 2018; Accepted 4 July 2018; Published 25 July 2018

Academic Editor: Carmine Apollaro

Copyright © 2018 Long Chang et al. This is an open access article distributed under the Creative Commons Attribution License, which permits unrestricted use, distribution, and reproduction in any medium, provided the original work is properly cited.

The microscopic interaction mechanism between working fluids and shale reservoirs is the key basic issue for the efficient development of shale gas. The initial water saturation of clay-rich shale is low, and the water absorption through strong chemical osmosis is an important factor for the wellbore instability of the drilling fluid filtration loss and the low flowback rate of hydraulic fracturing. Membrane efficiency is a key parameter in evaluating the mechanical-chemical coupling of shale-fluid interaction. Because microcracks develop in reservoir shale, pressure transfer experiments are no longer capable of obtaining membrane efficiency value. In this paper, the characteristics of shale water saturation are considered. The model calculating membrane efficiency is obtained, and the shale membrane efficiency of the reservoir studied, based on the triple-layer model of clay mineral-water interface electrochemistry. Membrane efficiency of unsaturated shale depends on the excess charge density of the surface of the solid in different water saturations. The analysis of factors influencing shale membrane efficiency in unsaturated reservoirs shows that the shale membrane efficiency decreases with the increase of water saturation under unsaturated conditions. The partition coefficient of counterion in the Stern layer, cation exchange capacity, and solute concentration in pore fluid will affect the membrane efficiency of unsaturated shale. The membrane efficiency of the reservoir section shale in Fuling area is calculated and analyzed, and the water-absorbing capacity by chemical osmosis of the reservoir interval shale is evaluated based on the membrane efficiency model of unsaturated shale.

1. Introduction

Horizontal wells with long horizontal sections and staged fracturing technology are the key technologies for the successful development of shale gas. The engineering practice of shale gas drilling and production has found that phenomena such as drilling fluid filtration loss promote instable propagation of microcracks in boreholes within surrounding rock. Low backflow rates of hydraulic fracturing are widespread [1, 2]. Compared with conventional oil and gas reservoirs, shale has low initial water saturation but large potential for water absorption. The dynamic force of shale reservoir imbibition working fluid mainly includes two aspects: (1) the development of micronanopores with strong capillary force and (2) strong mechanical-chemical coupling and

interaction between working fluid and shale reservoirs due to high clay mineral content [3–5].

Chemical osmosis is a kind of infiltration driven by chemical gradients. Shale with semipermeable membrane properties is present in the concentration gradient, which will produce corresponding chemical osmotic pressure. The chemical osmotic problem in clay-rich shale is relevant to geophysics, environmental science, civil engineering, petroleum industry, and so forth.

Membrane efficiency is a key parameter in the study of mechanical-chemical coupling in the interaction between shale and fluid. Membrane efficiency represents the ability to restrain solute migration but allows solvent migration of a semipermeable membrane, defined as the ratio of hydraulic pressure caused by chemical osmosis to ideal osmotic pressure

when balanced on both ends of a semipermeable membrane [6]. Shale is usually a nonideal semipermeable membrane, whose efficiency is between 0 and 1. The value can be obtained by a pressure transfer experiment under different chemical potential (Cretaceous clay [7]; Wakkanai mudstones [8]; Ghom shale [9]).

A great deal of research has been carried out by related scholars on the microscopic mechanism of chemical osmosis and the experiment of coupling effects, and several theoretical models of membrane efficiency have been proposed [10]. According to the irreversible thermodynamic coupling flow theory, Katchalsky and Curran [11] considered that, under static conditions, thermodynamic force on the semipermeable membrane is in balance with the sum of mechanical friction forces produced by various components of solution in the membrane. Marine and Fritz [12, 13] further developed the model and calculated the rules of the membrane efficiency of four types of clay minerals: montmorillonite, chlorite, illite, and kaolinite, varying with porosity in solutions with different concentrations of NaCl. This model predicted that shale membrane efficiency would be higher at low porosity and high cation exchange capacities.

Based on the Gouy-Chapman diffuse double layer theory (DDL), Kemper and Rollins [14], Letey et al. [15], and Kemper and Quirk [16] superimposed ion exclusion factors in the water membrane thickness of clay particles. The theory proposes a theoretical model of membrane efficiency. It shows that the membrane efficiency under the action of the monovalent cation solution is higher than that of the divalent cation solution, and the membrane efficiency under the action of the divalent anion solution is higher than that of the monovalent anion solution. Based on this theory, Bresler [17] further found that membrane efficiency is related to the water membrane thickness and solution concentration of the clay particles, and that membrane efficiency decreases with the increase of the product of the water membrane thickness and the square root of the solution concentration. Bader [18] summarized the model and produced a calculation formula. By using the Bresler membrane efficiency model, the membrane efficiency of Pierre Shale [19, 20], Ponza bentonite and Bisaccia clay [21], Boom clay [22], and Callovo-Oxfordian clay [23] was studied.

Neither Marine and Fritz's model nor Kemper and Bresler's model, can directly characterize the influence of water saturation on the membrane efficiency of unsaturated porous media. Aiming at the electrokinetic problem of clay-rich porous media, Leroy and Revil [24] proposed a triple-layer model (TLM) that describes the electrochemical properties of clay minerals. By using this model, the charged triple-layer structure of Stern and diffuse layers in clay-water interfaces was analyzed: the calculated results of ζ potential and low-frequency (few kHz) surface conductivity show that the structure has good applicability to the 1:1 type (kaolinite) and 2:1 type (montmorillonite) of clay minerals. Using the triple-layer theory, Revil et al. [25] and Gonçalves et al. [26] studied the multifield coupling flow regularity of clay-rich porous media fluid. The computational model of membrane efficiency was obtained and applied in aspects such as ion diffusion of Callovo-Oxfordian argillite,

fluid migration, and electrokinetic coupling. Concerning water saturation, the model is also applicable to unsaturated porous rocks [27, 28].

Based on the triple-layer model of clay-water interfaces established by Leroy and Revil [24], a computational model of unsaturated shale membrane efficiency is established in this paper by using the coupling constitutive equations of heterogeneous porous media. Taking water saturation into account, the change law of the membrane efficiency of clay-rich porous media is analyzed by numerical calculation. Finally, the theory is applied to predict the membrane efficiency of reservoir shale in Fuling area. The distribution law of the membrane efficiency under initial water-saturated condition is obtained, and the water-absorbing capacity by chemical osmosis of per unit pore of the shale in the reservoir section is evaluated.

2. Electrochemical Properties of a Clay-Water Interface

The semipermeable membrane property of shale can be attributed to the charged structure on the surface of clay mineral. Clay platelets are close to each other in low aperture shale, and electrical fields overlap while charged ions are blocked in this channel. At this moment, the channel will act as a semipermeable membrane effectively (Figure 1(a)). However, if the two clay platelets are far apart, and their electrical fields do not overlap (Figure 1(b)), then ions can pass through the channel freely. The clay particle act as a nonideal semipermeable membrane [29, 30].

The surface of a shale clay mineral has negative charge, attracts the counterions (cations) in the liquid phase in the shale pore, and repels the electrostatic of the same sign ion. At low water saturations, the counterions are packed in a smaller volume and therefore the effective excess charge density of the pore water is relatively high. At high water saturations, the excess charge density of the pore water is relatively low, such as illustrated in Figure 2. Membrane efficiency of unsaturated shale depends on the excess charge density of the surface of the solid in different water saturations.

A triple layer structure with the opposite sign and equal amount of charge appears on both sides of the solid-liquid interface. As shown in Figure 3, the layers of the clay mineral-water interface are as follows: the inner Helmholtz layer (IHP), the outer Helmholtz layer (OHP), and the diffuse layer. The IHP and OHP form the Stern layer, which firmly adheres to the solid surface. In the event of an electrokinetic phenomenon, the Stern layer moves with the solid particles and causes relative sliding within the diffuse layer. The interface between the Stern layer and the diffuse layer is called the shear plane. The potential difference between the shear plane and the solution body is called ζ potential. The magnitude of ζ potential reflects the degree of charge within the solid particles.

The porous shale is saturated by two immiscible phases, with one wetting phase for the solid phase and one nonwetting phase. The pore water comprises the water molecules,

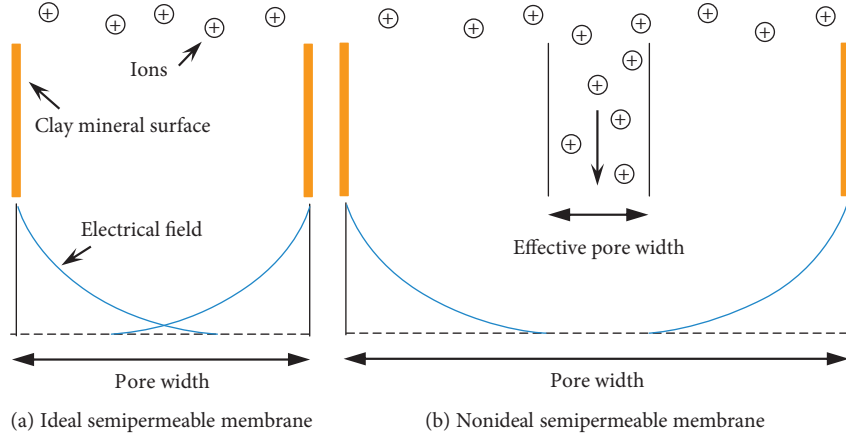


FIGURE 1: Clay as semipermeable membrane.

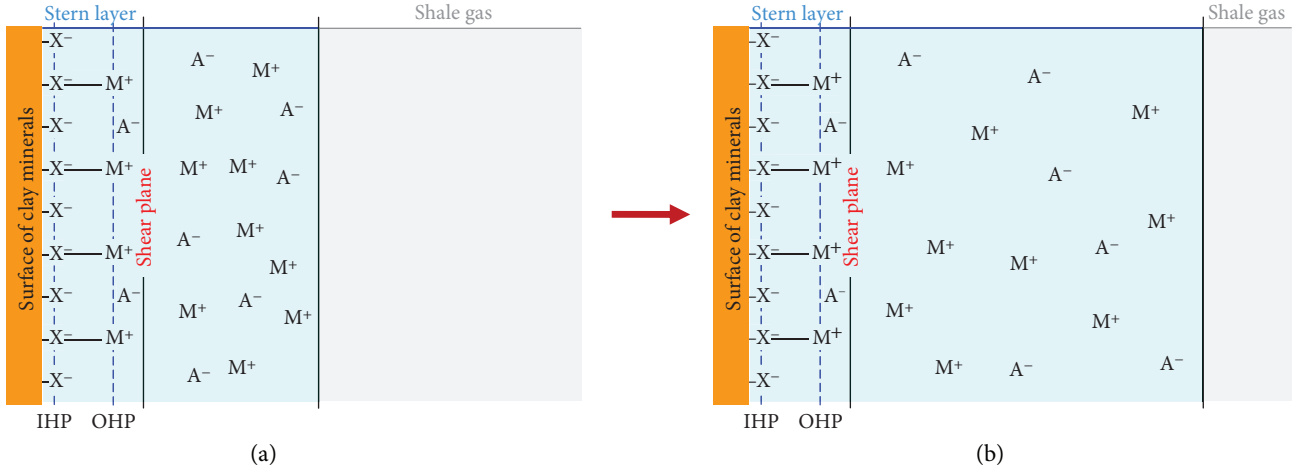


FIGURE 2: Sketch of the excess charge density of the pore water in different water saturations.

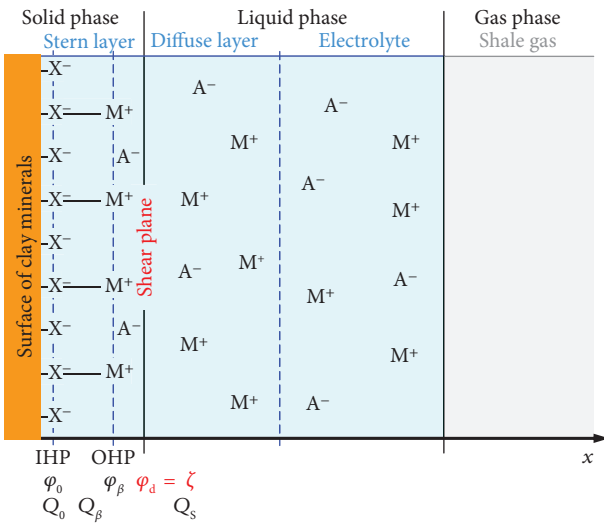


FIGURE 3: Sketch of triple-layer model of the clay-water interface.

plus solute species and the nonwetting phase is shale gas. In the reference state, the water saturation is defined by

$$s_w = \frac{\theta}{\phi}, \quad (1)$$

where θ is the water content (volume fraction); ϕ is connected porosity.

We denote by S_{sw} the contact area between the shale solid phase and the wetting phase and by S_{nw} the contact area between the nonwetting phase and the wetting phase. Q_0 represents the charge density of the surface minerals; Q_β represents the charge density of the Stern layer; finally, Q_s represents the charge density of the diffuse layer [26].

$$Q_s = Q_0 + Q_\beta. \quad (2)$$

Ignoring the gas/water interface charge, the porous shale electrical balance equation is

$$\bar{Q}_V^0 + \frac{S_{sw}}{V_w} Q_s = 0, \quad (3)$$

where V_w is the volume of pore water in the representative elementary volume (REV), m^3 ; \bar{Q}_V^0 is the volume charge density of the pore space in fully saturated rock, C/m^3 . Under unsaturated conditions, when the water saturation is s_w , the effective charge density \bar{Q}_V is

$$\bar{Q}_V = \frac{\bar{Q}_V^0}{s_w}. \quad (4)$$

Under saturated conditions, the total charge density of counterion per unit pore volume Q_V^0 (C/m^3) is

$$Q_V^0 = \rho_g \frac{1-\phi}{\phi} \text{CEC}, \quad (5)$$

where ρ_g is the grain density of shale, kg/m^3 ; CEC is cation exchange capacity, meq/g.

The volume charge density of counterion in rock pore space is

$$\bar{Q}_V^0 = (1 - f_Q) Q_V^0, \quad (6)$$

where f_Q is the distribution coefficient and represents the distribution ratio of counterion in the Stern layer.

$$f_Q = \frac{\sum_{i=1}^Q z_i \Gamma_{X_i, M}^0}{\sum_{i=1}^Q z_i \Gamma_{X_i, M}^0 + \sum_{i=1}^Q z_i \Gamma_{X_i, M}^S}, \quad (7)$$

where $\Gamma_{X_i, M}^0$ and $\Gamma_{X_i, M}^S$ are, respectively, the surface position densities of counterion absorbed in the Stern layer and diffuse layer; Q is the type number of counterion in the electrolyte, z is the valence.

3. Membrane Efficiency of Unsaturation Porous Media

In isothermal conditions, the macroscopic flux of the salt, J_s , the macroscopic current density, J_c , and the Darcy velocity, J_f , are all cross-coupled macroscopic fluxes. These fluxes are all dependent on thermodynamic forces, taken here as the gradients of the thermodynamics potentials. They are the chemical potential of the salt, μ_f , the electrical potential, ψ , and the effective pore fluid pressure, \bar{p} [25].

$$\begin{bmatrix} 2J_s - (\bar{C}_+ + \bar{C}_-)J_f \\ J_c - \bar{Q}_V J_f \\ J_f \end{bmatrix} = - \begin{bmatrix} \frac{\sigma_e}{e^2} & \frac{1}{e}(\sigma_e^+ - \sigma_e^-) & 0 \\ \frac{1}{e}(\sigma_e^+ - \sigma_e^-) & \sigma_e & 0 \\ \frac{k}{\eta_f}(\bar{C}_+ + \bar{C}_-) & \frac{k}{\eta_f}\bar{Q}_V & \frac{k}{\eta_f} \end{bmatrix} \cdot \begin{bmatrix} \nabla \mu_f \\ \nabla \psi \\ \nabla \bar{p} \end{bmatrix}. \quad (8)$$

The chemical potential gradient and osmotic pressure gradient are, respectively,

$$\nabla \mu_f = k_B T \nabla \ln C_f, \quad (9)$$

$$\nabla \pi = 2k_B T \nabla C_f. \quad (10)$$

There is a relationship between the chemical potential gradient and osmotic pressure gradient:

$$\nabla \mu_f = \nabla \frac{\pi}{2} C_f. \quad (11)$$

By coupling the flow constitutive equation, the influence of flow potential on total current density is neglected:

$$J_c = -\frac{1}{e}(\sigma_e^+ - \sigma_e^-) \nabla \mu_f - \sigma_e \nabla \psi. \quad (12)$$

Additionally,

$$T_e^+ = \frac{\sigma_e^+}{\sigma_e} = 1 - T_e^-. \quad (13)$$

T_e^+ is the Hittorf number of the cation:

$$T_e^+ = \frac{\beta_+ (\sqrt{1+R^2} + R)}{\beta_+ (\sqrt{1+R^2} + R) + \beta_- (\sqrt{1+R^2} - R)}, \quad (14)$$

where β_{\pm} are the mobilities of anion and cation in water, $m^2/s \cdot V$.

There is

$$\nabla \psi|_{J_c=0} = \frac{1}{e} (1 - 2T_e^+) \nabla \mu_f = \frac{1}{e} (1 - 2T_e^+) \nabla \frac{\pi}{2} C_f. \quad (15)$$

By

$$\begin{aligned} \bar{p} &= p - \pi, \\ \bar{C}_+ + \bar{C}_- &= 2C_f \sqrt{1+R^2}, \\ R &= \frac{\bar{Q}_V}{2eC_f}. \end{aligned} \quad (16)$$

Additionally, the Darcy velocity in constitutive equation is

$$J_f = -\frac{k}{\eta_f} [(\bar{C}_+ + \bar{C}_-) \nabla \mu_f + \bar{Q}_V \nabla \psi + \nabla \bar{p}], \quad (17)$$

and becomes

$$J_f = -\frac{k}{\eta_f} \left[\sqrt{1+R^2} \nabla \pi + R(1 - 2T_e^+) \nabla \pi + \nabla p - \nabla \pi \right]. \quad (18)$$

TABLE 1: Analysis parameters of membrane efficiency.

Parameters	Value	Units
e	1.6×10^{-19}	C
β_+	5.19×10^{-8}	$\text{m}^2 \cdot \text{s}^{-1} \cdot \text{V}^{-1}$
β_-	7.91×10^{-8}	$\text{m}^2 \cdot \text{s}^{-1} \cdot \text{V}^{-1}$
ρ_g	2655	$\text{kg} \cdot \text{m}^{-3}$
ϕ	4.2	%
f_Q	0.94	—
CEC	0.07	$\text{meq} \cdot \text{g}^{-1}$
C_f	0.10	$\text{mol} \cdot \text{L}^{-1}$

Note: The mobilities of ions in water is 298 K NaCl aqueous solution.

According to the definition of membrane efficiency of chemical osmosis,

$$\begin{aligned} \mathbf{J}_f &= -\frac{k}{\eta_f} [\nabla p - \sigma \nabla \pi], \\ \sigma &\equiv \left(\frac{\Delta p}{\Delta \pi} \right)_{J_f=0}. \end{aligned} \quad (19)$$

Contrasting (18), the membrane efficiency expression of unsaturated porous media can be obtained as follows:

$$\sigma = 1 - \sqrt{1 + R^2} - R(1 - 2T_c^+). \quad (20)$$

4. Sensitivity Study

The physical and chemical parameters related to the shale of organic-rich reservoirs are substituted into the above formula, and the variables are controlled appropriately. Then, the change laws of the counterion partition coefficients of the Stern layer, as well as the cation exchange capacity and the shale membrane efficiency under the influence of the solute concentration in pore fluid, are obtained under unsaturated conditions. The relevant data used in the calculation are shown in Table 1.

4.1. Partition Coefficient of Counterion in the Stern Layer. By (10), the partition coefficient f_Q is defined as the surface concentration of counterions in the Stern layer, divided by the total surface concentration of counterions in both the diffuse layer and the Stern layer. By using the triple-layer model, Leroy and Revil [31] calculated and obtained that the pure clay mineral kaolinite f_Q is 0.98, illite f_Q is 0.90, and smectite f_Q is 0.85. Revil [32] analyzed the electrical double-layer structure of argillaceous sandstone and obtained that f_Q is from 0.89 to 0.99. With high solute concentration in pore fluid, the charged layer is compressed, and the specific gravity of the counterion in the Stern layer is larger. The value of f_Q ranges from 0.90 to 0.98 for sensitivity analysis of the parameter in this paper.

The calculated results of membrane efficiency varying with water saturation under different partition coefficients are shown in Figure 4(a). The membrane efficiency decreases

with the increase of water saturation when the partition coefficients are different. The partition coefficient of counterion in Stern layer approaches 1, and the membrane efficiency approaches 0 when under full-saturated conditions. At this time, shale cannot act as a semipermeable membrane. The membrane efficiency decreases at different rates while water saturation increases. When the water saturation increases to 60%, the reduction of membrane efficiency decreases. The larger the partition coefficient is, the larger the reduction of membrane efficiency is. As shown in Figure 4(b), for shale with different water saturation, the membrane efficiency decreases with the increase of partition coefficient; if the partition coefficient is greater than 0.96, the reduction of shale membrane efficiency, varying with the increase of partition coefficient, is larger with different levels of water saturation.

4.2. Cation Exchange Capacity (CEC). The CEC represents the capacity of a porous material to exchange cations between the mineral surface and the solution in pore fluid. According to the clay mineral content and composition of reservoir shale, sensitivity analysis of cation exchange capacities in the range of 0.03–0.13 meq/g was carried out, with the curve of membrane efficiency varying with water saturation under different CECs and the curve of membrane efficiency varying with CEC under different water saturation. The results are shown, respectively, in Figure 5.

With a different cation exchange capacity, the trend of membrane efficiency decreasing with the increase of water saturation is different. The membrane efficiency of low CEC shale further decreases with the increase of water content, and the membrane efficiency is lower under saturated conditions. Too low of a cation exchange capacity will render the shale ineffective as a semipermeable membrane, and higher cation exchange capacity of the shale corresponds with higher membrane efficiency under full saturated conditions. This conclusion is consistent with the research results of Marine and Fritz [12]. Under different water-saturation conditions, the membrane efficiency will increase with the increase of CEC and will change from rapid increase to a gentle increase. Shale membrane efficiency is higher with low water saturation and high cation exchange capacity.

4.3. Solute Concentration in Pore Fluid. Fluid salinity is high in marine sedimentary shale formations. The study of the effect of solute concentration in pore fluid on shale membrane efficiency under unsaturated conditions is conducted in the range of 0.02~0.27 mol/L. As shown in Figure 6, the membrane efficiency decreases with the increase of water saturation under different solute concentrations in pore fluid. Under full saturated conditions, the solute concentration in pore fluid of shale acting as a semipermeable membrane grows higher as membrane efficiency grows lower. This conclusion agrees with the research of Bresler [17] and Bader [18] in their study of membrane efficiency and solution concentration. Under unsaturated conditions, shale membrane efficiency also decreases with the increase of solute concentration in pore fluid. As solute concentration increases, the reduction rate of membrane efficiency is initially quick but later becomes slow. It eventually tends to gentle decline.

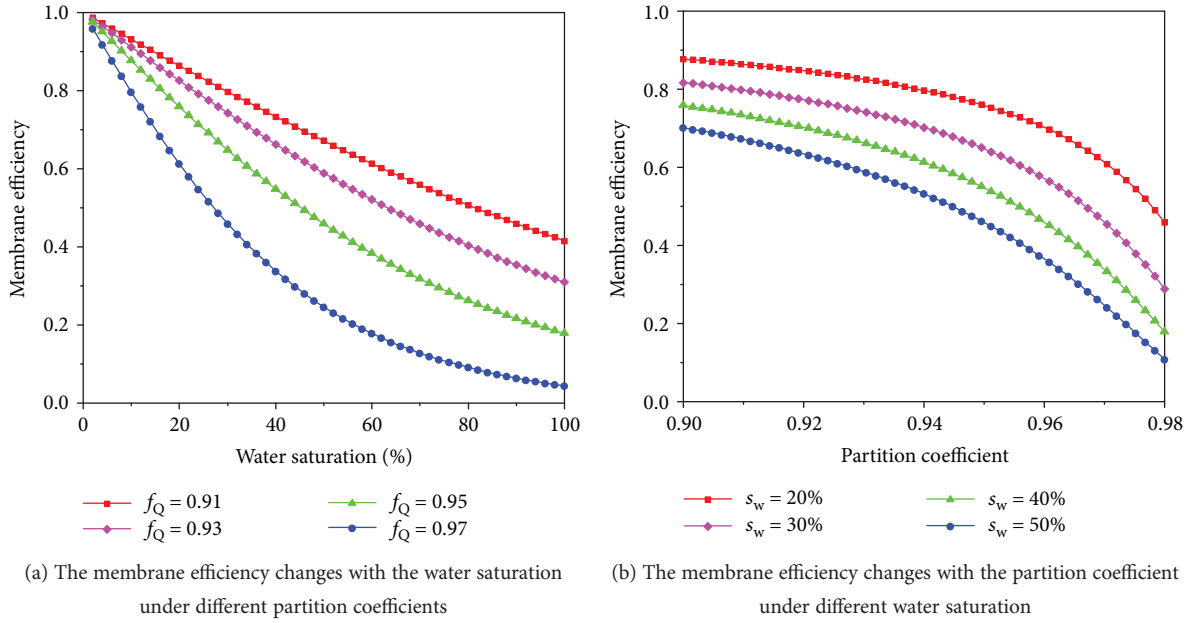


FIGURE 4: Effect of partition coefficient on membrane efficiency under unsaturated conditions.

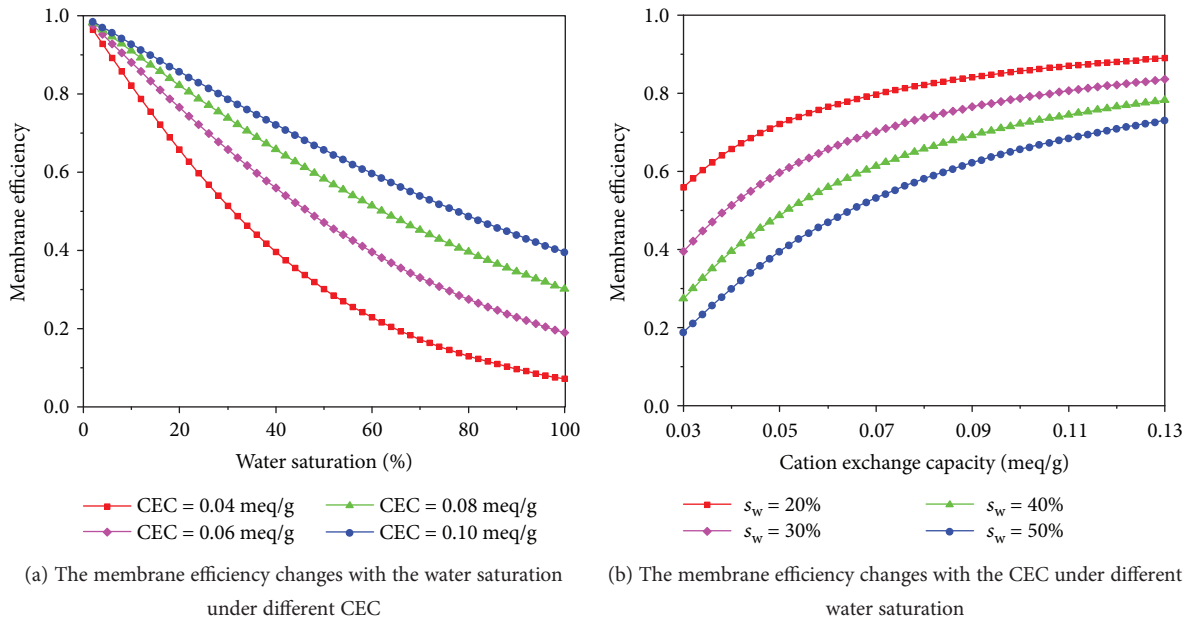


FIGURE 5: Effect of cation exchange capacity on membrane efficiency under unsaturated conditions.

5. Application

Membrane efficiency of Fuling shale was analyzed by using the abovementioned unsaturated porous membrane efficiency model, which in consequence evaluated the water-absorbing capacity by chemical osmosis of the shale.

5.1. The Cation Exchange Capacity of Reservoir Shale. Through experiments with five reservoir shale samples in the Fuling area, the cation exchange capacity of shale was

determined to be 0.058~0.094 meq/g, and the value of specific surface area is between 16 and 28 m²/g. The experimental results is close to the research of Fuling shale obtained by Lin et al. [33]. In contrast with the cation exchange capacity of different single clay minerals and argillaceous sandstone [34], the cation exchange capacity of Fuling shale is low, as shown in Figure 7.

The experimental results of rock core, whole-rock mineral content in the reservoir interval, show that the content of clay minerals is 17.5%~59% with an average of 38.26%, which

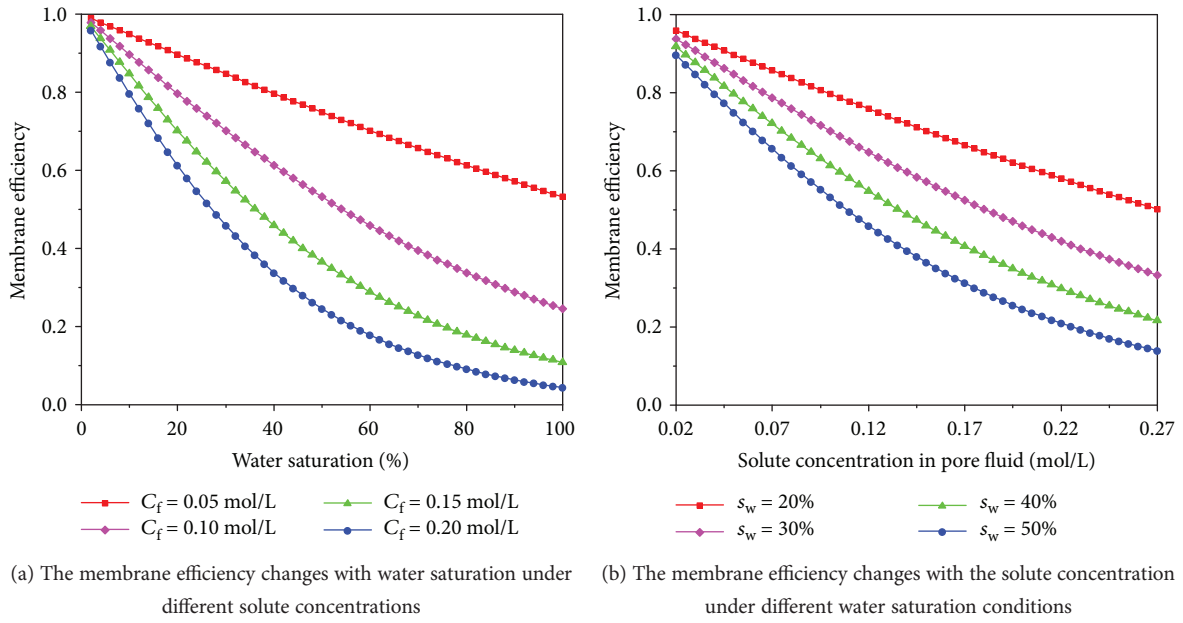


FIGURE 6: Effect of solute concentration in pore fluid on membrane efficiency under unsaturated conditions.

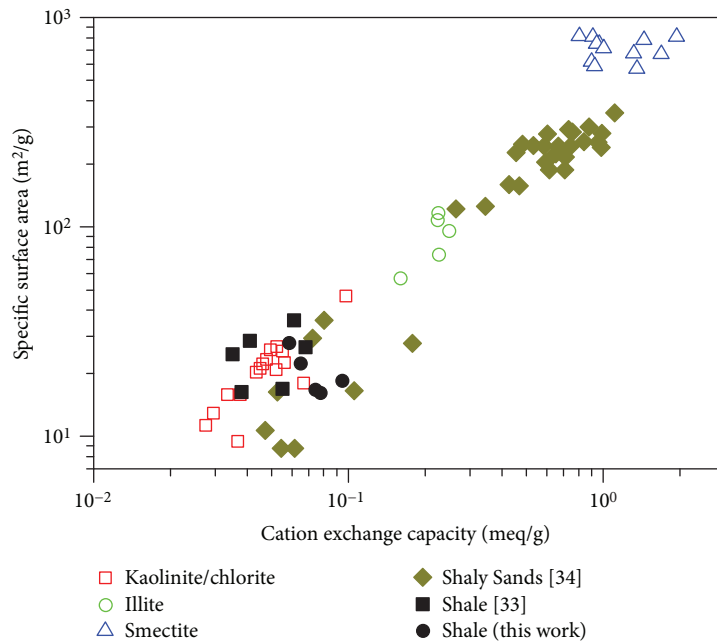


FIGURE 7: Relationship between specific surface area and cation exchange capacity.

shows an upward trend from bottom to top. The clay minerals mainly include mixed layer minerals of illite/smectite and illite, followed by chlorite (Figure 8). The ratio of illite/smectite in mixed-layer minerals is 10%. The low cation exchange capacity of the major clay minerals is responsible for the low cation exchange capacity of the Fuling shale.

Aiming at the reservoir shale containing multicomponent clay minerals in the whole well, its cation exchange capacity is determined by the clay mineral content of each

component and the cation exchange capacity of a single mineral [35].

$$CEC = \chi_I CEC_I + \chi_C CEC_C + \chi_S CEC_S, \quad (21)$$

where χ_i and CEC_i are, respectively, the mass fraction of the clay mineral component i and the cation exchange capacity, the subscripts I, C, and S, respectively, represent illite, chlorite, and smectite.

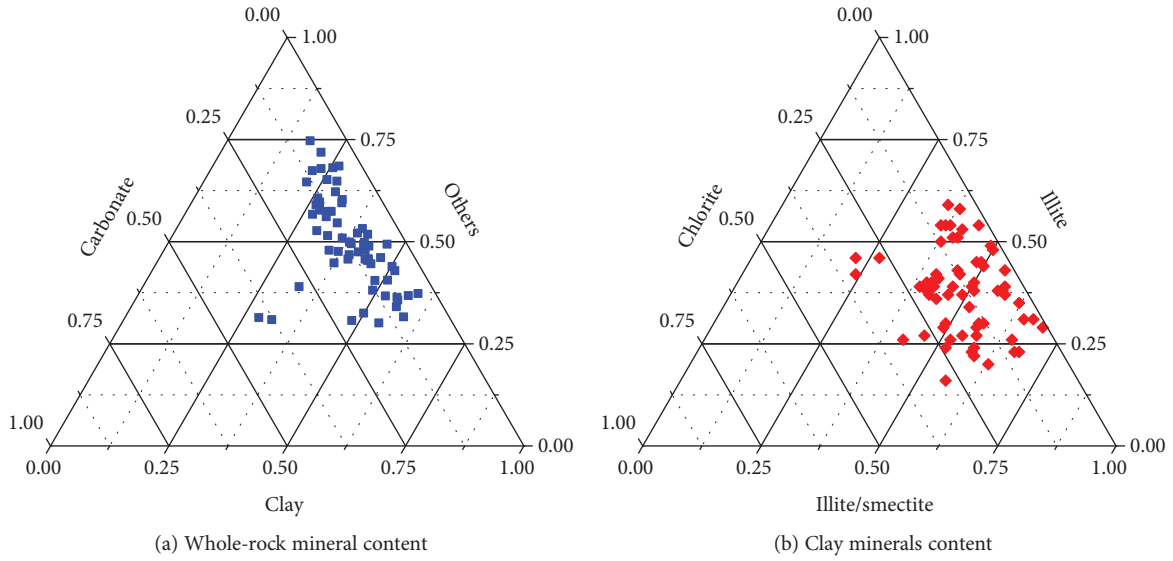


FIGURE 8: The characteristics of reservoir shale mineral composition.

TABLE 2: Cation exchange capacity of different clay minerals.

Clay minerals	CEC (meq/g)	Reference value (meq/g)
Smectite	1.00	0.80~1.50
Illite	0.25	0.10~0.40
Chlorite	0.15	0.10~0.40

According to the reference range for the cation exchange capacity of each clay mineral, the shale clay mineral content and measured shale cation exchange capacity were fitted to determine the CEC calculated values of the three clay minerals, as shown in Table 2.

In Figure 9, the distribution results of clay mineral content show reservoir interval shale and CEC varying with depth. As the depth of the well increases, the total amount of clay minerals decreases. The contents of three types of clay minerals thus decrease in turn. The shale cation exchange capacity is mainly in the range of 0.06~0.12 meq/g, decreasing with the increase of well depth.

5.2. The Membrane Efficiency of Reservoir Shale. Parameters such as reservoir interval core porosity and initial water saturation are used as they are substituted into the shale membrane efficiency model. Additionally, the vertical distribution of shale membrane efficiency under the original formation condition is calculated and obtained, which is used to characterize the water-absorbing capacity by chemical osmosis.

The calculating parameters and results regarding reservoir shale are shown in Figure 9. Shale grain density ranges from 2581 to 2790 kg/m³, decreasing with the increase of well depth. The porosity of reservoir shale is mainly in the range of 3%~5%; the minimum value is 1.95%, and the maximum value is 5.27%. The overall trend is as follows: the shale porosity increases as well depth decreases. Initial water

saturation of cores is measured in the range of 20%~60%, which is highly correlated with shale clay mineral content and decreases with the increase of well depth. Solute concentration in shale pore fluid is equivalent to 0.2 mol/L NaCl solution. The calculated initial water-saturated membrane efficiency of shale is mainly in the range of 0.4~0.6. The minimum is 0.38; the maximum is 0.73; and the average is 0.48. Although reservoir interval shale grain density, porosity, initial water saturation, and cation exchange capacity each correlate with depth by their own law, the initial water-saturated membrane efficiency of shale does not change significantly with depth under the comprehensive influence.

With water saturation at 100%, the membrane efficiency of reservoir shale under full water-saturated conditions is calculated, with results being shown in Figure 9. The membrane efficiency of shale under full water-saturated conditions is mainly in the range of 0.05~0.25; the minimum is 0.02, and the maximum is 0.31. As the calculating values of water saturation are the same (100%), the membrane efficiency of shale shows a good correlation law with well depth, and the membrane efficiency of shale decreases with the increase of well depth.

5.3. Water-Absorbing Capacity by Chemical Osmosis of Reservoir. The reservoir shale has high membrane efficiency at initial water saturation. Water absorption increases water saturation, causing membrane efficiency to decrease. According to calculation results in Section 5.2, initial water saturation and membrane efficiency of a reservoir interval core under saturated conditions both change regularly as the well depth changes. To characterize the chemical osmotic kinetics of unit pore volume in the process of water absorption, its membrane efficiency is calculated on a range from initial water saturation s_{wi} to a full water saturated condition. Formula (22) is used to integrate membrane efficiency within the scope of the water adoption saturation and to

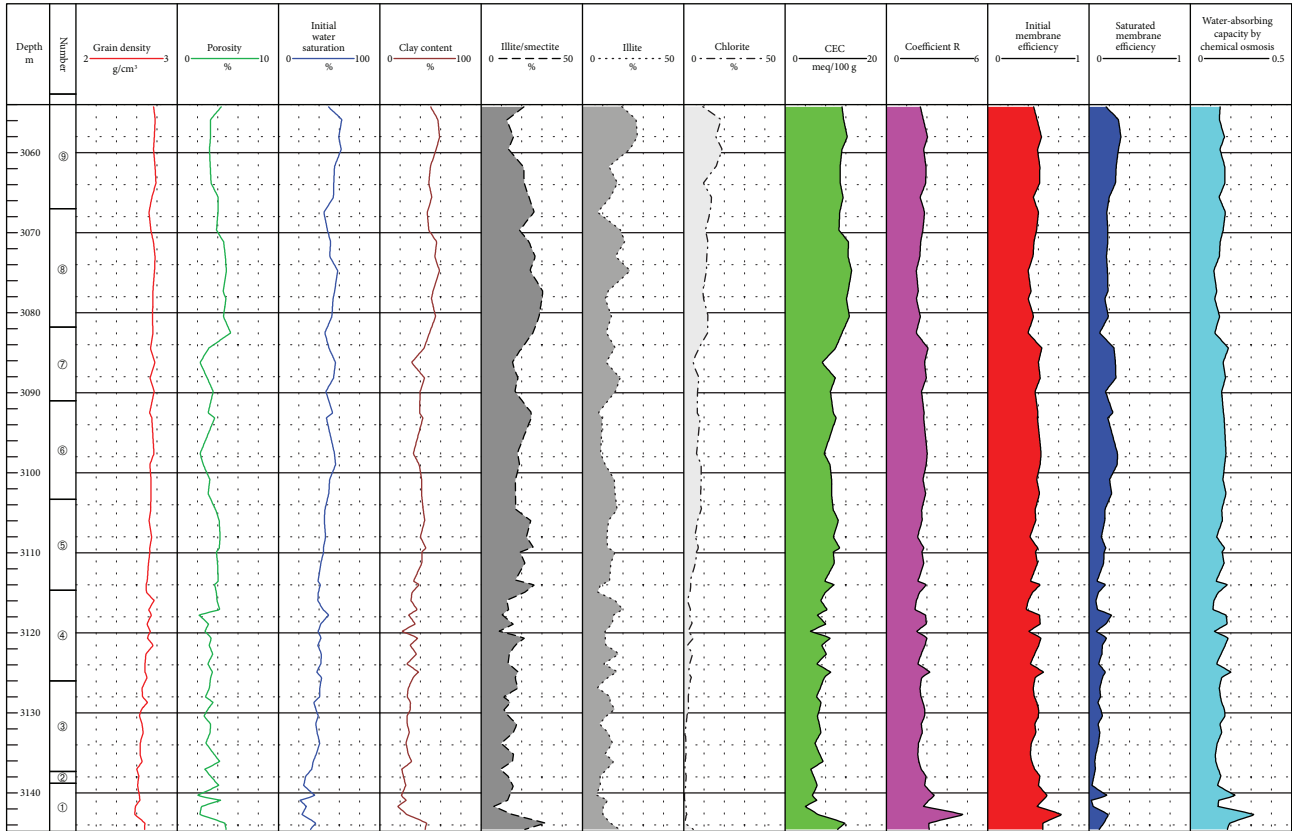


FIGURE 9: Vertical variation within the water-absorbing capacity by chemical osmosis of reservoir interval shale.

characterize water-absorbing capacity by chemical osmosis per unit pore shale.

$$J = \int_{s_{wi}}^{100\%} \sigma ds_w \quad (22)$$

Figure 10 calculates the membrane efficiency of some layers of the reservoir shale by using the average of various physical property parameters. The initial water saturation of each layer shale increases with the number of layers, and the corresponding initial water-saturated membrane efficiency is close. Membrane efficiency decreases with the increase of water saturation, and the membrane efficiency of shale water adoption under saturated conditions increases with the number of layers. However, the integral interval decreases as it moves from initial water saturation to a full water saturated condition, leaving no obvious difference between the integral values of membrane efficiency of water absorption interval.

Longitudinal changes within the water-absorbing capacity by chemical osmosis of reservoir interval shale are shown in Figure 9, and the average value of each layer is shown in Table 3. The water-absorbing capacity by chemical osmosis per unit pore of shale is mainly within the range of 0.14~0.17, the overall difference between the layers being not large. The minimum average value is found in the ⑧ layer, whereas the average value of ① layer is the largest. Under the condition that there is not much difference in water-absorbing capacity by chemical osmosis per unit pore

of reservoir shale, the water absorption capacity of each layer of shale depends more on its porosity.

6. Conclusion

- (1) Based on the electrochemistry theory of a clay mineral-water interface, a computational model of the shale membrane efficiency considered water saturation is obtained by using the constitutive equation of multiphase porous media coupling and parameter transformation.
- (2) Under unsaturated conditions, the membrane efficiency of shale will decrease with the increase of saturation of water. At high partition coefficient of counterion in the Stern layer, high cation exchange capacity, and low solute concentration in pore fluid, the membrane efficiency of shale is relatively high.
- (3) The clay minerals within reservoir shale in Fuling area have a low cation exchange capacity, and the cation exchange capacity of reservoir shale is mainly in the range of 0.06~0.12 meq/g, which decreases with the increase of well depth.
- (4) Calculations of membrane efficiency of Fuling shale show that it is mainly in the range of 0.4~0.6 under initial water saturated conditions, and a change trend at each layer is not obvious when observed at different depths. With the increase of water

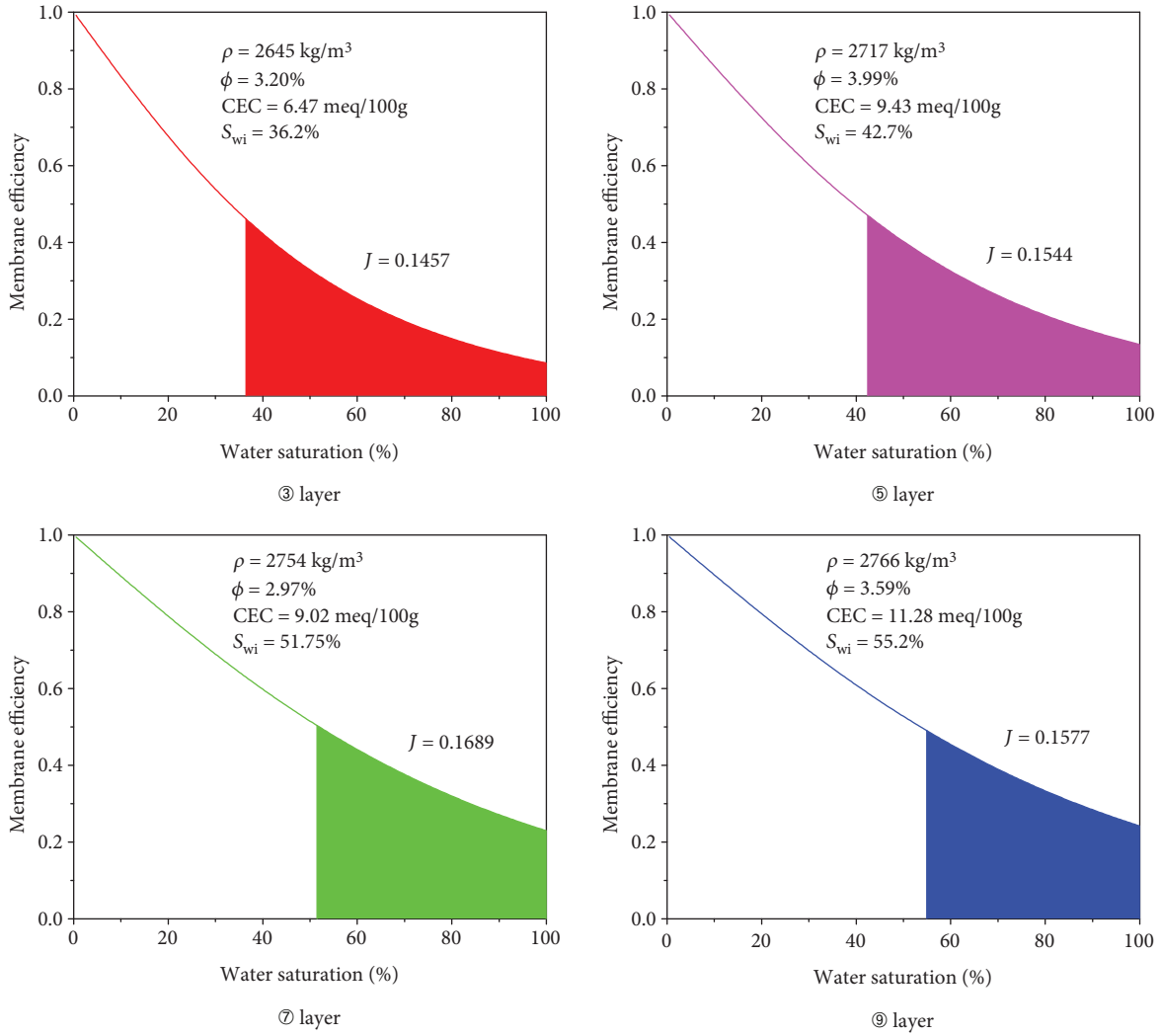


FIGURE 10: The change in membrane efficiency of reservoir shale throughout the process of water adoption.

TABLE 3: Water-absorbing capacity by chemical osmosis of reservoir shale.

Layer	Grain density kg/m ³	Porosity %	Initial water saturation %	Clay content %	CEC meq/100 g	Initial membrane efficiency	Saturated membrane efficiency	Water-absorbing capacity by chemical osmosis
⑨	2766	3.59	55.20	52.26	11.28	0.4881	0.2414	0.1577
⑧	2762	4.66	52.01	53.10	12.15	0.4314	0.1687	0.1351
⑦	2754	2.97	51.75	39.70	9.02	0.5018	0.2296	0.1689
⑥	2742	3.09	51.14	39.83	9.14	0.4934	0.2170	0.1654
⑤	2717	3.99	42.70	39.56	9.43	0.4679	0.1335	0.1544
④	2712	3.26	41.55	31.82	7.41	0.4661	0.1239	0.1527
③	2645	3.20	36.20	27.29	6.47	0.4647	0.0858	0.1457
②	2618	3.02	30.37	23.40	5.85	0.5139	0.0731	0.1615
①	2631	3.69	27.85	32.20	7.75	0.5766	0.0922	0.1954

saturation, the membrane efficiency of shale under full water-saturated conditions is mainly in the range of 0.05~0.25, and it decreases with the increase of well depth.

(5) The membrane efficiency of shale should be integrated from the initial water saturation to full water-saturated conditions, and characterize the water-absorbing capacity by chemical osmosis per unit pore of shale.

The calculated results show that there is no obvious difference in water-absorbing capacity by chemical osmosis per unit pore between each layer at different depths of reservoir interval shale in Fuling area.

Nomenclature

C_f :	Concentration of the solute ($\text{mol}\cdot\text{L}^{-1}$)
CEC:	Cation exchange capacity ($\text{C}\cdot\text{kg}^{-1}$)
e :	Elementary charge (C)
f_Q :	Fraction of charge located in the Stern layer
J_c :	Macroscopic current density ($\text{A}\cdot\text{m}^{-2}$)
J_f :	Darcy velocity ($\text{m}\cdot\text{s}^{-1}$)
J_s :	Macroscopic flux of the salt ($\text{mol}\cdot\text{m}^{-2}\cdot\text{s}^{-1}$)
k :	Intrinsic permeability of the shale (m^2)
k_B :	Boltzmann constant ($\text{J}\cdot\text{K}^{-1}$)
K_s :	Distribution coefficient of the solute in the membrane
p :	Intrinsic pore fluid pressure (Pa)
\bar{p} :	Effective pore fluid pressure (Pa)
Q_0 :	Charge density of the surface minerals ($\text{C}\cdot\text{m}^{-2}$)
Q_S :	Charge density of the diffuse layer ($\text{C}\cdot\text{m}^{-2}$)
Q_β :	Charge density of the Stern layer ($\text{C}\cdot\text{m}^{-2}$)
\bar{Q}_V :	Effective charge per unit pore volume of the shale ($\text{C}\cdot\text{m}^{-3}$)
Q_V^0 :	Total charge density ($\text{C}\cdot\text{m}^{-3}$)
\bar{Q}_V^0 :	Pore charge density of the water-saturated shale ($\text{C}\cdot\text{m}^{-3}$)
R :	Electrical conductivity dimensionless number
s_w :	Water saturation
S_{nw} :	Surface area of the interface between shale gas and water (m^2)
S_{sw} :	Surface area of the interface between shale and water (m^2)
T :	Temperature (K)
T_e^+ :	Macroscopic Hittorf numbers
V_m :	Volume of the pore water in the representative elementary volume (m^3)
β_{\pm} :	Mobilities of the cation and anion in water ($\text{m}^2\cdot\text{s}^{-1}\cdot\text{V}^{-1}$)
ρ_g :	Bulk density of the grains ($\text{kg}\cdot\text{m}^{-3}$)
θ :	Water content
ϕ :	Porosity of the shale
μ_f :	Chemical potential of the salt (J)
ψ :	Electrical potential (V)
π :	Osmotic pressure (Pa)
σ :	Membrane efficiency
σ_e :	Electrical conductivity of the shale ($\text{S}\cdot\text{m}^{-1}$)
σ_e^\pm :	Contribution of ions to the total DC-electric conductivity ($\text{S}\cdot\text{m}^{-1}$).

Data Availability

The data used to support the findings of this study are available from the corresponding author upon request.

Conflicts of Interest

The authors declare that they have no conflicts of interest.

Acknowledgments

This research was supported by the National Natural Science Foundation of China (Major Program 51490652), Research Foundation of China University of Petroleum-Beijing at Karamay (RCYJ2016B-01-001), and National Science and Technology Major Project (2017ZX05039-004). The authors also would like to thank Sinopec Chongqing Fuling Shale Gas Exploration and Development Co. Ltd., who kindly provided the in-site shale samples for the experimental tests.

References

- [1] R. Rezaee, *Fundamentals of Gas Shale Reservoirs*, John Wiley & Sons, 2015.
- [2] M. A. Sayed, G. A. Al-Muntasheri, and F. Liang, "Development of shale reservoirs: knowledge gained from developments in North America," *Journal of Petroleum Science and Engineering*, vol. 157, pp. 164–186, 2017.
- [3] H. Singh, "A critical review of water uptake by shales," *Journal of Natural Gas Science and Engineering*, vol. 34, pp. 751–766, 2016.
- [4] J. Wang and S. S. Rahman, "Investigation of water leakoff considering the component variation and gas entrapment in shale during hydraulic-fracturing stimulation," *SPE Reservoir Evaluation & Engineering*, vol. 19, no. 3, pp. 511–519, 2016.
- [5] Z. Zhou, H. Abass, X. Li, D. Beringer, and W. Frank, "Mechanisms of imbibition during hydraulic fracturing in shale formations," *Journal of Petroleum Science and Engineering*, vol. 141, pp. 125–132, 2016.
- [6] A. J. Staverman, "Non-equilibrium thermodynamics of membrane processes," *Transactions of the Faraday Society*, vol. 48, pp. 176–185, 1952.
- [7] B. D. Cey, S. L. Barbour, and M. J. Hendry, "Osmotic flow through a Cretaceous clay in southern Saskatchewan, Canada," *Canadian Geotechnical Journal*, vol. 38, no. 5, pp. 1025–1033, 2001.
- [8] M. Takeda, T. Hiratsuka, M. Manaka, S. Finsterle, and K. Ito, "Experimental examination of the relationships among chemico-osmotic, hydraulic, and diffusion parameters of Wakkanai mudstones," *Journal of Geophysical Research: Solid Earth*, vol. 119, no. 5, pp. 4178–4201, 2014.
- [9] I. R. Kivi, M. J. Ameri, and A. Ghassemi, "Experimental and numerical study of membrane properties and pore pressure transmission of Ghom shale," *Measurement*, vol. 91, pp. 93–100, 2016.
- [10] I. Medved and R. Černý, "Osmosis in porous media: a review of recent studies," *Microporous and Mesoporous Materials*, vol. 170, pp. 299–317, 2013.
- [11] A. Katchalsky and P. F. Curran, *Nonequilibrium Thermodynamics in Biophysics*, Harvard University Press, Cambridge, MA, USA, 1965.
- [12] I. W. Marine and S. J. Fritz, "Osmotic model to explain anomalous hydraulic heads," *Water Resources Research*, vol. 17, no. 1, pp. 73–82, 1981.
- [13] S. J. Fritz and I. W. Marine, "Experimental support for a predictive osmotic model of clay membranes," *Geochimica et Cosmochimica Acta*, vol. 47, no. 8, pp. 1515–1522, 1983.
- [14] W. D. Kemper and J. B. Rollins, "Osmotic efficiency coefficients across compacted clays," *Soil Science Society of America Journal*, vol. 30, no. 5, pp. 529–534, 1966.

- [15] J. Letey, W. D. Kemper, and L. Noonan, "The effect of osmotic pressure gradients on water movement in unsaturated soil," *Soil Science Society of America Journal*, vol. 33, no. 1, pp. 15–18, 1969.
- [16] W. D. Kemper and J. P. Quirk, "Ion mobilities and electric charge of external clay surfaces inferred from potential differences and osmotic flow," *Soil Science Society of America Journal*, vol. 36, no. 3, pp. 426–433, 1972.
- [17] E. Bresler, "Anion exclusion and coupling effects in nonsteady transport through unsaturated soils: I. Theory," *Soil Science Society of America Journal*, vol. 37, no. 5, pp. 663–669, 1973.
- [18] S. Bader, *Osmosis in Groundwater: Chemical and Electrical Extensions to Darcy's law [Ph.D. thesis]*, TU Delft, Delft University of Technology, 2005.
- [19] C. E. Neuzil, "Osmotic generation of 'anomalous' fluid pressures in geological environments," *Nature*, vol. 403, no. 6766, pp. 182–184, 2000.
- [20] A. M. Garavito, H. Kooi, and C. E. Neuzil, "Numerical modeling of a long-term in situ chemical osmosis experiment in the Pierre Shale, South Dakota," *Advances in Water Resources*, vol. 29, no. 3, pp. 481–492, 2006.
- [21] B. Loret, A. Gajo, and F. M. F. Simões, "A note on the dissipation due to generalized diffusion with electro-chemo-mechanical couplings in heteroionic clays," *European Journal of Mechanics - A/Solids*, vol. 23, no. 5, pp. 763–782, 2004.
- [22] A. M. Garavito, P. De Cannière, and H. Kooi, "In situ chemical osmosis experiment in the boom clay at the Mol underground research laboratory," *Physics and Chemistry of the Earth, Parts A/B/C*, vol. 32, no. 1–7, pp. 421–433, 2007.
- [23] S. Baechler, J. Croisé, and S. Altmann, "Modelling coupled chemico-osmotic and advective–diffusive transport of nitrate salts in the Callovo-Oxfordian clay," *Advances in Water Resources*, vol. 49, pp. 76–85, 2012.
- [24] P. Leroy and A. Revil, "A triple-layer model of the surface electrochemical properties of clay minerals," *Journal of Colloid and Interface Science*, vol. 270, no. 2, pp. 371–380, 2004.
- [25] A. Revil, P. Leroy, and K. Titov, "Characterization of transport properties of argillaceous sediments: application to the Callovo-Oxfordian argillite," *Journal of Geophysical Research*, vol. 110, no. B6, 2005.
- [26] J. Gonçalves, P. Rousseau-Gueutin, and A. Revil, "Introducing interacting diffuse layers in TLM calculations: a reappraisal of the influence of the pore size on the swelling pressure and the osmotic efficiency of compacted bentonites," *Journal of Colloid and Interface Science*, vol. 316, no. 1, pp. 92–99, 2007.
- [27] D. Jougnot, A. Revil, N. Lu, and A. Wayllace, "Transport properties of the Callovo-Oxfordian clay rock under partially saturated conditions," *Water Resources Research*, vol. 46, no. 8, 2010.
- [28] A. Revil, "Transport of water and ions in partially water-saturated porous media. Part 1. Constitutive equations," *Advances in Water Resources*, vol. 103, pp. 119–138, 2017.
- [29] A. Meunier, *Clays*, Springer Science & Business Media, 2005.
- [30] A. H. D. Cheng, *Poroelasticity*, Springer, Cham, Switzerland, 2016.
- [31] P. Leroy and A. Revil, "A mechanistic model for the spectral induced polarization of clay materials," *Journal of Geophysical Research*, vol. 114, no. B10, 2009.
- [32] A. Revil, "Spectral induced polarization of shaly sands: influence of the electrical double layer," *Water Resources Research*, vol. 48, no. 2, 2012.
- [33] Y. X. Lin, S. Y. Gao, and Y. J. Zeng, "Study of shale microfracture propagation based on tomographic technique," *Scientia Sinica Physica, Mechanica & Astronomica*, vol. 47, no. 11, article 114606, 2017.
- [34] W. F. Woodruff and A. Revil, "CEC-normalized clay-water sorption isotherm," *Water Resources Research*, vol. 47, no. 11, 2011.
- [35] A. Rabaute, A. Revil, and E. Brosse, "In situ mineralogy and permeability logs from downhole measurements: application to a case study in chlorite-coated sandstones," *Journal of Geophysical Research: Solid Earth*, vol. 108, no. B9, 2003.

Research Article

Study of the Corrosion Characteristics of Tunnel Fissures in a Karst Area in Southwest China

Yanjie Zhao,¹ Fugang Wang ,¹ Cangsong Li,² Yuqing Cao,¹ and Hailong Tian¹

¹Key Laboratory of Groundwater Resources and Environment Ministry of Education, Jilin University, Changchun 130021, China

²China Railway Southwest Research Institute Co. Ltd., Chengdu, Sichuan 611731, China

Correspondence should be addressed to Fugang Wang; wangfugang@jlu.edu.cn

Received 24 February 2018; Revised 23 May 2018; Accepted 24 June 2018; Published 24 July 2018

Academic Editor: Luigi Borrelli

Copyright © 2018 Yanjie Zhao et al. This is an open access article distributed under the Creative Commons Attribution License, which permits unrestricted use, distribution, and reproduction in any medium, provided the original work is properly cited.

The development of the fissures in soluble rock of karst areas directly affects the construction and operation safety of tunnel engineering. It is thus of theoretical and practical significance to study the characteristics of its corrosion and its influencing factors. Taking the Wulong tunnel as the research object, the numerical model of the study area was established to quantitatively analyze the corrosion range, corrosion ratio, and changes in the permeability and porosity of the fissures in soluble rock of karst areas of the tunnel over the past 100 years, and the simulation results were verified by field experiments. The results show that the main controlling factor of the fissure corrosion of the tunnel in the karst area is the flow rate. The corrosion range and corrosion ratio of the fissures of the tunnels in the karst area increased with temperature because the reaction rate constant increased with temperature, causing the reactions' equilibrium to move towards the direction of the solution. The larger the initial permeability and the larger the porosity of the fissures, the faster the fissures corrode. In the same time period, the fissures with high permeability and large porosity will lead to the permeability and porosity being more enhanced, thus causing the corrosion of the fissures to exhibit secondary enhancement effects. The opening of the dead-end pores greatly enhanced the permeability and slightly increased the porosity, which caused the differential corrosion of fissures in the karst area. The protection of the tunnel should be strengthened, mainly in strong hydrodynamic conditions and in the fracture development zone.

1. Introduction

Carbonate rocks account for 35% of the land area distribution of China [1, 2]. The karst development is very strong in Southwest China, which often led to geohazards and a variety of accidents of engineering construction [3–8]. Due to the distribution of abundant mountains in Southwest China, the ratio of bridges and tunnels relative to roads or railways is mostly over 70%, some up to 90% [2, 9, 10]. The karst caves and subterranean rivers that are broadly distributed in karst regions often lead to accidents during tunnel construction and increase the cost of the tunnels' operation and maintenance [9–11]. The Wulong tunnel is one of the representative tunnel projects in the karst area of Southwest China. According to a preliminary investigation, karst doline, karst caves, and subterranean rivers were found in the tunnel crossing area [2, 9, 10].

Elucidating the corrosion mechanism of carbonate rocks helps us analyze the corrosion development of the fissures in soluble rock of karst areas. Scholars have carried out many studies on the influence factors of karst development through experiments, numerical simulations, and other methods [12–24]. These studies showed that the corrosion of carbonate rocks was influenced by internal factors, such as geological structures and rock compositions, as well as external factors, such as flow rates (rainfall), temperature, and pH.

In terms of the impact of fissures on karst corrosion, scholars have found that faults and fractures play a vital role in karst corrosion [25–27]. They found that in the unidirectional one-dimensional limestone fissures, the corrosion rate of the limestone fissures shows a nonlinear increase with time [16, 28–33]. At the same time, scholars have also studied the characteristics of fissures and pore evolution under two-dimensional [14] and three-dimensional conditions

[17, 34–37]. In addition, by studying the changes in the microstructures of the carbonate rocks that were corroded, it was determined that corrosion is first determined by the lithology and its own structure [38–40].

As for the influence of external environmental factors, such as flow rates, on karst corrosion, which are based on the basic principles of mineral dissolution, scholars obtained the basic differential equation of calcite dissolution rates through experimental research and mathematical statistics [15, 41]; based on the corrosion law and surface corrosion theory of carbonate rocks, it was concluded that the flow rate, surface area, and concentration of major ions obviously affect the dissolution [22, 23, 42–44]. To assess the temperature factor, carbonate rock corrosion experiments between 0°C and 250°C were conducted, using rate equations for the corresponding temperature conditions to discuss the influence of temperature on the dissolution, precipitation, and surface corrosion of carbonate minerals [13, 19, 21, 23, 45–51]. In terms of pH, under natural conditions, the pH change in rain water is mostly caused by changes in the CO₂ content of air [22, 23, 28, 52]. Scholars found that the variation of pCO₂ in the range of 1–50 atm obviously affected the corrosion of carbonate minerals [22, 23], while at pCO₂ values of lower than 0.1 atm, pCO₂ had very little influence on the corrosion of carbonate minerals [28, 52, 53].

For tunnel engineering in a karst area, the geological and hydrogeological natural conditions must be taken into consideration [54]. The systematic study of the corrosion mechanism by numerical simulation and field experiments is of great importance for tunnel operation and maintenance.

In this paper, the Wulong tunnel, a typical tunnel project in Southwest China, was studied. The corrosion range, corrosion ratio, and changes in the porosity and permeability of karst cracks in the tunnel vault within a timeframe of 100 years were analyzed, and the differences in corrosion were discussed.

2. The Background of the Wulong Tunnel Engineering Area

The Wulong tunnel is located in Wulong County of China (Figure 1) with a full length of 9418 m; it stretches along with the Wujiang Canyon and goes through the Wuling Mountains, with a maximum burial depth of approximately 830 m. The middle part of the tunnel passes through 3800 m of soluble rock. Many karst caves and subterranean rivers have been found in the Wulong tunnel engineering area. Therefore, the engineering geological and hydrogeological conditions in the tunnel area are very complicated.

Wulong County is subtropical, with four distinct seasons, rain and heat over the same period, temperatures between –3.5°C and 41.7°C, and annual precipitation of approximately 1000–1200 mm.

Carbonate rocks and clastic rocks are predominant in the Wulong tunnel area. For the lithology of the tunnel from entrance to exit, see Table 1 and Figure 2.

The study site is located within the Maokou limestone formation (P_{1m}), and it is close to the Wujiaping Formation (P_{2w}), which is a set of coal-bearing strata near the contact

zone of insoluble and soluble rock. A large “Tiankeng,” a karst doline (Yangaotuo doline), can be found on the ground above the tunnel (Figures 3 and 4(a)). The karst phenomenon is very developed near the area of the tunnel, and karst caves can be found in nearby strata (Figure 4(b)).

In the study area, groundwater mainly receives rainfall infiltration, and the recharge, runoff, and discharge are controlled by topography, lithology, and faults. Karst groundwater flows to the Wujiang River in the form of subterranean rivers and springs in the tunnel area. The 2[#] and 3[#] subterranean rivers pass through the middle section of the tunnel area, which is the most karst-developed section of the whole tunnel, having karst caves and karst funnels (Figures 2–4). The 2[#] river is located 4496 m from the tunnel entrance (Figure 2). The 3[#] river is located 4643 m from the tunnel entrance. The two subterranean rivers are both nearly orthogonal with the tunnel line. The 2[#] and 3[#] subterranean rivers intruded into the tunnel many times during the tunnel construction, which caused great difficulties in the tunnel engineering construction and maintenance [55].

Karst fractures increase the contact area of water and carbonate rock, which is helpful to promote the corrosion of carbonate rock, and have a certain effect on the stability of tunnel bedrock. Moreover, the tunnel vault is one of the most vulnerable parts of a tunnel, and it is prone to cause tunnel accidents. Therefore, in this study, the most vulnerable area, the tunnel vault fracture zone, which is located under the Yangaotuo karst funnel and above the 2[#] and 3[#] subterranean rivers, was chosen as the key study area (Figures 2 and 3).

3. The Fissure Evolution Model and Simulation Scheme in the Karst Area of the Tunnel

3.1. Conceptual Model of the Fissures in the Karst Area of the Tunnel. According to field investigations, the geological/hydrogeological conditions, length, hydrochemical characteristics, and flow rates of 2[#] and 3[#] subterranean rivers were similar. A conceptual model was established for the study area, the main fissure, and the damage zone, which is above the 2[#] subterranean river (Figure 5). Based on previous investigations about the impact zones of different sizes of faults and fissures [56–61], the widths of the impact zones are generally 5–10 meters. In this study, the length and width of the impact zone of the tunnel fracture zone are all set to 24 meters, and the height of the simulated area was set as 60 meters based on the saturated zone above the vault of the tunnel. In field conditions, groundwater infiltrates from the top fracture zone, flowing through fissures and finally converging into the subterranean rivers. In the model, the upper and lower boundaries of the model were set as constant flow boundaries, and the lateral boundaries were set as no flow boundaries (Figure 5). In the horizontal direction, the length of the long fissures is approximately 80 m and the length of the short fissure is approximately 5 m (Figure 5).

3.2. Numerical Model. The numerical model was constructed based on the conceptual model. The modeling area was divided into 10 layers in the vertical direction, with each layer

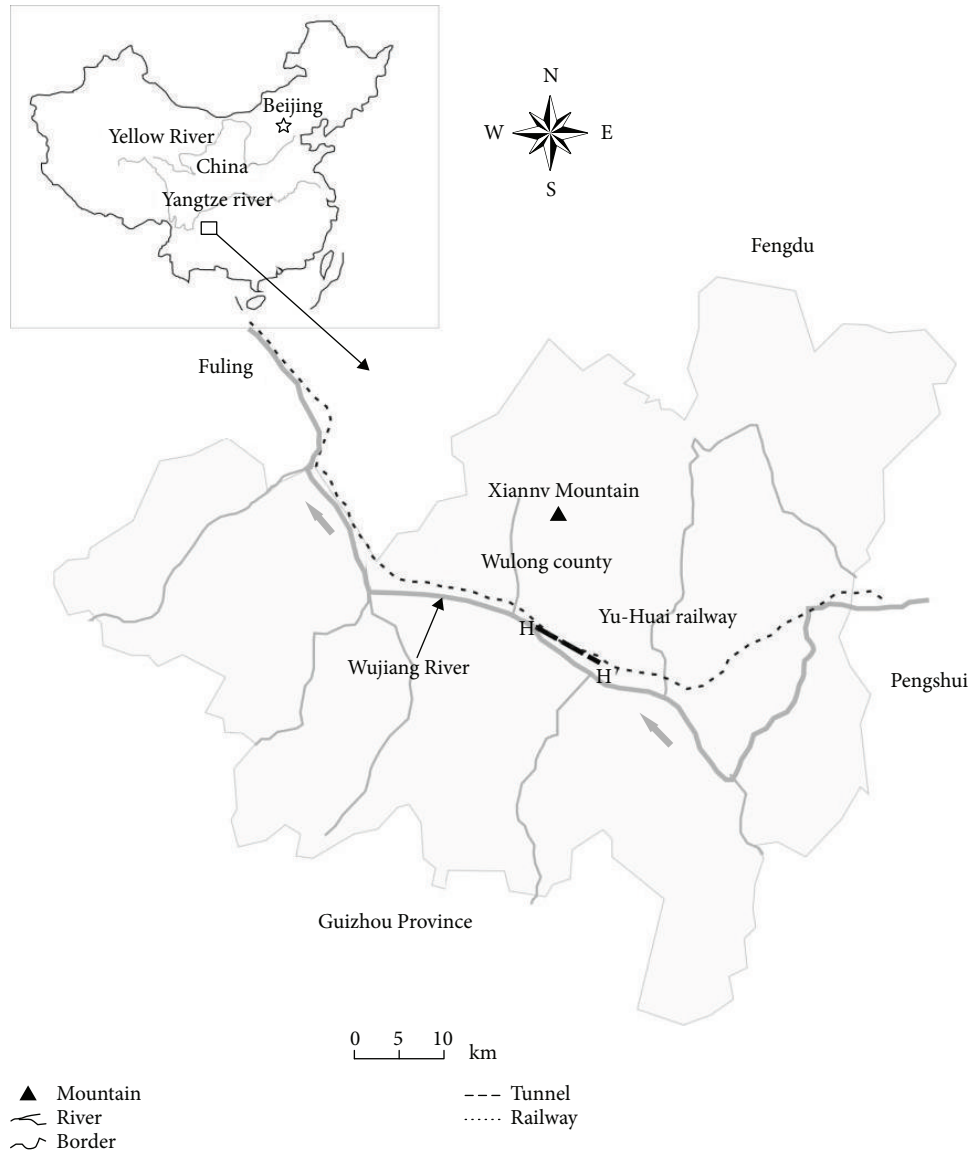


FIGURE 1: The location of the study area and tunnel project.

TABLE 1: Formation lithology of the Wulong tunnel area.

System	Formation		Lithology
Jurassic	Zhenzhuchong	J_{1z}	Dark-brown shale and mudstone, light-gray sandstone
	Xujiahe	T_{3xj}	Dark-brown shale, light-gray sandstone
Triassic	Leikoupo	T_{2l}	The upper part is dark-brown shale and marlstone. The middle part is dark-brown shale and light-gray sandstone. The lower part is gray limestone
	Jialingjiang	T_{1j}	Gray limestone intercalated with dolomitic limestone
	Feixianguan	T_{1f}	Gray limestone, dark-brown shale
Permian	Changxing	P_{2c}	Dark-gray limestone
	Wujiaping	P_{2w}	Dark-gray limestone
	Maokou	P_{1m}	Gray and dark-gray limestone
	Liangshan	P_{1q+l}	Limestone intercalated with bioclastic limestone
Silurian	Luoreping	S_{1lr}	Gray and dark-gray mudstone

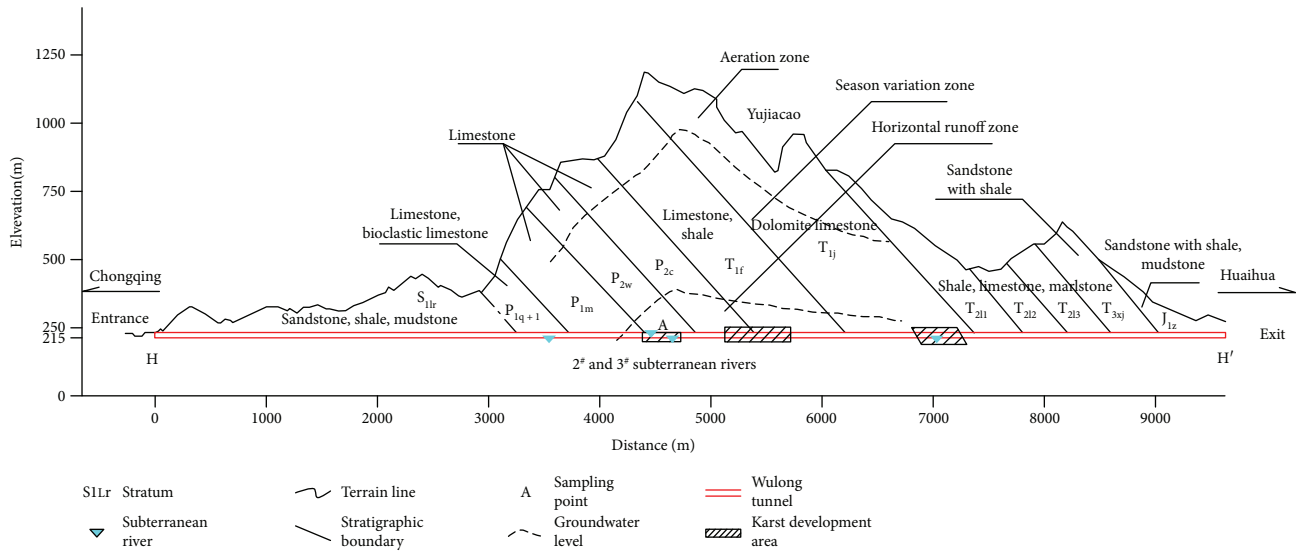


FIGURE 2: Simplified hydrogeological cross section of the Wulong tunnel area.

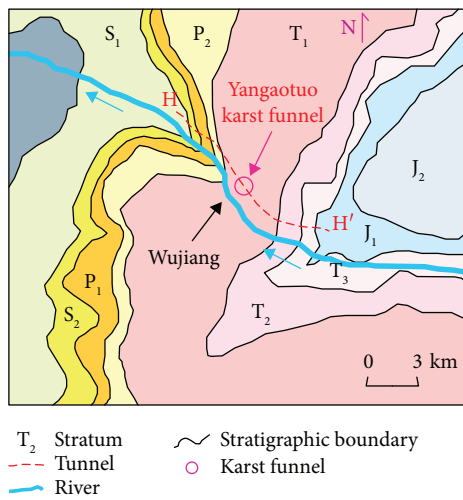


FIGURE 3: Geological map of the Wulong tunnel area.



FIGURE 4: Karst phenomena in the study area ((a) karst doline; (b) karst caves).

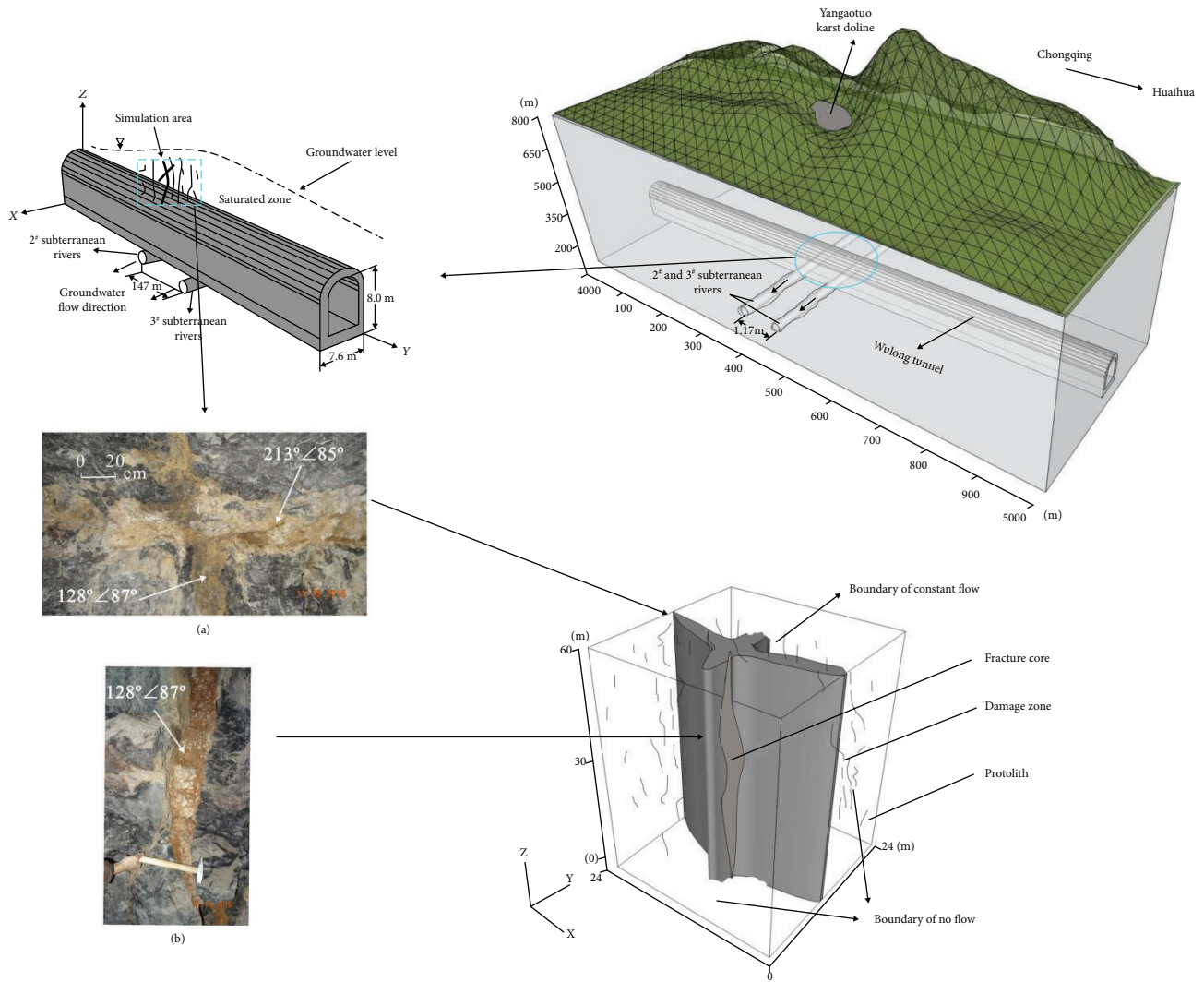


FIGURE 5: Conceptual model of the study area.

being 6 meters high, and the horizontal direction was divided into 6 columns, with each column being 4 meters wide; overall, the numerical model area was divided into 360 grids (Figure 6). The central part of the model is the fracture core zone; moving outward from this zone are the damage zone and protolith zone successively. In addition, the permeability and porosity decrease from the central part of the fracture zone to both sides outward (Figure 6).

3.3. Model Parameters and Simulation Scheme. According to previous research data [9, 10], the permeability of the karst fracture zone in the simulation area is between $1.8 \times 10^{-11} \text{ m}^2$ and $1.3 \times 10^{-10} \text{ m}^2$. The average permeability of $7.4 \times 10^{-11} \text{ m}^2$ was taken as the permeability of the fracture core zone. To study the impacts of porosity and permeability on corrosion, a high-permeability condition of $7.4 \times 10^{-10} \text{ m}^2$ and a low-permeability condition of $7.4 \times 10^{-12} \text{ m}^2$ were additionally assigned to the fracture core zone in our study based on its range of empirical values. The permeability of the protolith is approximately $1 \times 10^{-17} \text{ m}^2 \sim 2.8 \times 10^{-13} \text{ m}^2$ according to the measured data of the porosity and

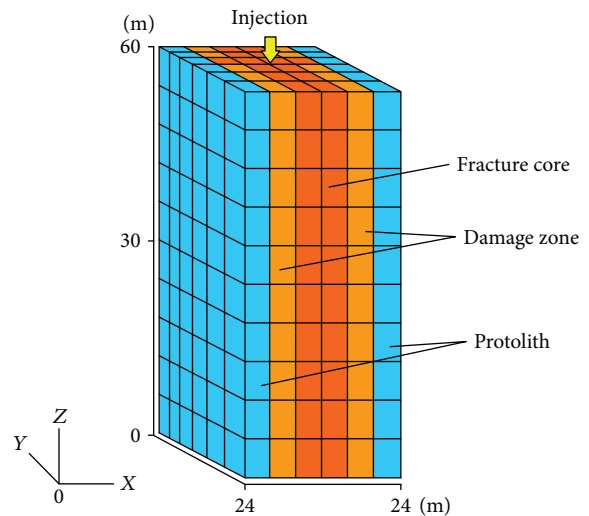


FIGURE 6: Numerical model.

TABLE 2: Model parameters.

Category	Density (kg/m ³)	Porosity	Water pressure (Pa)	Permeability (m ²)
Protolith	2680	7%	$1 \times 10^5 \sim 6 \times 10^5$	1.5×10^{-14}
Fracture core	2000~2280	20%~35%		$7.9 \sim 790 \times 10^{-12}$

TABLE 3: Karst ratio of the Wulong tunnel.

The starting position of each section from the tunnel inlet (m)	The length of the section (m)	Karst ratio
0~3396	3396	0.2
3396~3892	496	0.4
3892~5276	1384	0.5
5276~7276	2000	0.3
7276~9418	2142	0.2

permeability of the carbonatite (protolith) [62–64]. Therefore, in our model, the permeability of the protolith was set as $1.5 \times 10^{-14} \text{ m}^2$. Because the damage zone is distributed around the fracture core zone, the permeability in the model gradually decreases from the fracture core zone outward to the protolith zone.

According to the tunnel investigation department and at the same time the reference of the empirical value in Southwest China, the porosity of the protolith is approximately 7% and the porosity of the fracture core zone is approximately 20% to 35%. In the model, the porosity of the fracture core zone was set as 35%, 29%, and 20%, and the corresponding permeability values were set as $7.4 \times 10^{-10} \text{ m}^2$, $7.4 \times 10^{-11} \text{ m}^2$, and $7.4 \times 10^{-12} \text{ m}^2$, respectively. The porosity and permeability of the protolith were set as 7% and $1.5 \times 10^{-14} \text{ m}^2$, respectively. The mineral composition and density of the protolith were determined by the measured data of calcite (95%), illite (2%), and montmorillonite (3%). The chemical composition of groundwater was determined by water sample analysis, and its pH is 7.3. The water pressure range of the simulation area was assigned according to the field conditions (Table 1). The atmosphere temperature in the study area is between -3.5°C and $\sim 41.7^\circ\text{C}$, and the temperature of the groundwater is between 10°C and 25°C . The temperatures of the injection water were set as 10°C , 15°C , 20°C , 25°C , 30°C , and 35°C in our model. The model parameters are shown in Table 2. The karst ratios of different tunnel sections (Table 3) were obtained from analyzing the number of the fissures in soluble rock of karst areas and the karstification level [9, 10].

The simulation area is in the middle section of the tunnel (3892 m~5276 m), where the karst development is the strongest. Because the karst development depends on water-rock action, the flow rates directly influence the development of karst. According to the field investigation of the tunnel, based on the water balance principle [9, 10, 65], the annual rainfall infiltration amount of the whole tunnel area was calculated. The water quantity of the whole tunnel area was then allocated to the different sections of the tunnel using the karst

TABLE 4: Simulation scenarios.

Scenario code	Permeability (m ²)	Porosity	Temperature (°C)	Flow rates (kg/s)		
				a	b	c
Case 1			10			
Case 2			15			
Case 3	7.4×10^{-10}	35%	20	1.9	2.9	3.9
Case 4			25			
Case 5			30			
Case 6			35			
Case 7			10			
Case 8			15			
Case 9	7.4×10^{-11}	29%	20	1.9	2.9	3.9
Case 10			25			
Case 11			30			
Case 12			35			
Case 13			10			
Case 14			15			
Case 15	7.4×10^{-12}	20%	20	1.9	2.9	3.9
Case 16			25			
Case 17			30			
Case 18			35			

ratios in Table 3; thus, the runoff distribution coefficient k_i was obtained. k_i can be calculated by

$$k_i = \frac{r_i \times l_i}{\sum_{i=1}^n r_i \times l_i}, \quad (1)$$

where r_i is the karst ratio and l_i is the length of the tunnel section.

From the data in Table 3, the flow rates of different tunnel sections were calculated by (2). The flow rate of the simulated area in the model (Q_z) was finally obtained by (3):

$$Q_i = k_i \times Q, \quad (2)$$

$$Q_z = k_z \times Q_i, \quad (3)$$

where Q is the precipitation infiltration in the whole tunnel area and k_z is the ratio of the simulation area size to the length of the most karst-developed parts of the tunnel.

According to the field conditions, the simulation time length was set as 100 years in consideration of the service period of the tunnel. The injection flow rates were based on the rainfall of the dry year, the normal flow year, and the wet year, that is, 800 mm, 1100 mm, and 1500 mm in Wulong, respectively. Using (1), (2), and (3), the injection

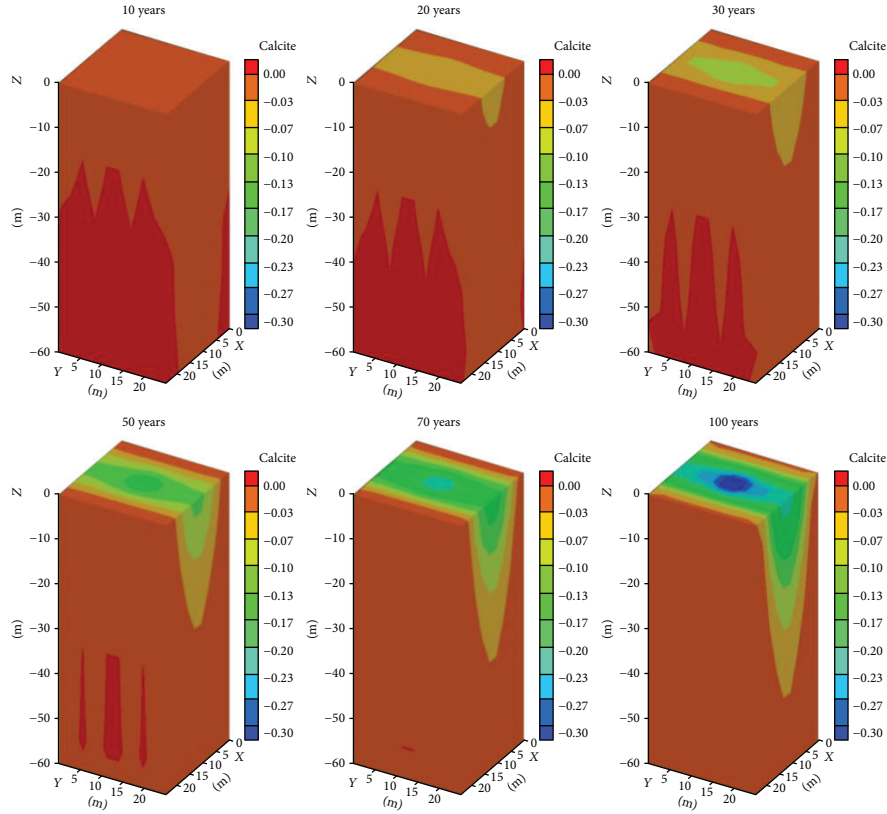


FIGURE 7: The corrosion range of the fissure under medium hydrodynamic conditions-medium permeability—10°C.

flow rates of the weak hydrodynamic condition (a), the middle hydrodynamic condition (b), and the strong hydrodynamic condition (c) were calculated to be 1.9 kg/s, 2.9 kg/s, and 3.9 kg/s, respectively. There were 54 different conditions considered to evaluate the evolution of fissure corrosion (Table 4).

The simulation software used in this study was TOUGH-REACT, which is widely used in the numerical simulation of water-rock interactions [66, 67].

4. Results and Discussion

4.1. Corrosion Range under Different Conditions. The conditions of medium hydrodynamics and medium permeability were taken as examples (case 7(b)~case 12(b)) with which the corrosion process of fissures under different temperatures was analyzed (Figures 7–9). By comparing Figure 7 with Figure 9, during the same corrosion time, the corrosion range of 35°C was larger than that of 10°C. After 100 years of corrosion, the horizontal and vertical corrosion ranges of 35°C were 1.2 times and 1.3 times higher than those of 10°C, respectively.

The condition of medium hydrodynamics and the temperature of 20°C were taken as examples (case 3(b), case 9(b), and case 15(b)) with which the corrosion process of tunnel fractures under different porosity and permeability conditions was analyzed (Figures 10–12). By comparing Figure 10 with Figure 12, during the same corrosion time, the corrosion range of high-porosity and high-permeability

conditions was larger than that of low-porosity and low-permeability conditions. After 100 years of corrosion, the horizontal and vertical corrosion ranges of high-porosity and high-permeability conditions were 1.4 times and 1.6 times higher than those of low-porosity and low-permeability conditions, respectively.

The conditions of 20°C and medium permeability were taken as examples (case 9(a), case 9(b), and case 9(c)) with which the corrosion process of the tunnel fissure under different flow rates was analyzed (Figures 13–15). By comparing Figure 13 with Figure 15, during the same corrosion time, the corrosion range of the strong hydrodynamic condition was larger than that of the weak hydrodynamic condition. After 100 years of corrosion, the corrosion ranges of the strong hydrodynamic condition were 1.8 times and 2.2 times higher than those of the weak hydrodynamic condition, respectively.

4.2. Corrosion Ratios under Different Conditions. Taking the high-porosity/permeability (case 1~case 6) and low-porosity/permeability conditions (case 13~case 18) as examples, we analyzed the corrosion ratios of the tunnel fissure under different flow rates and temperatures (Figures 16(a) and 17(b)). From Figures 16(a) and 17(b), we can see that the corrosion ratio increased with the time of corrosion. During the same corrosion time, the higher the temperature, the greater the corrosion ratio. After 100 years of corrosion, the corrosion ratio (strong hydrodynamic condition and high porosity and permeability) of 35°C (0.4032%) was 1.2 times higher than that of 10°C (0.3369%).

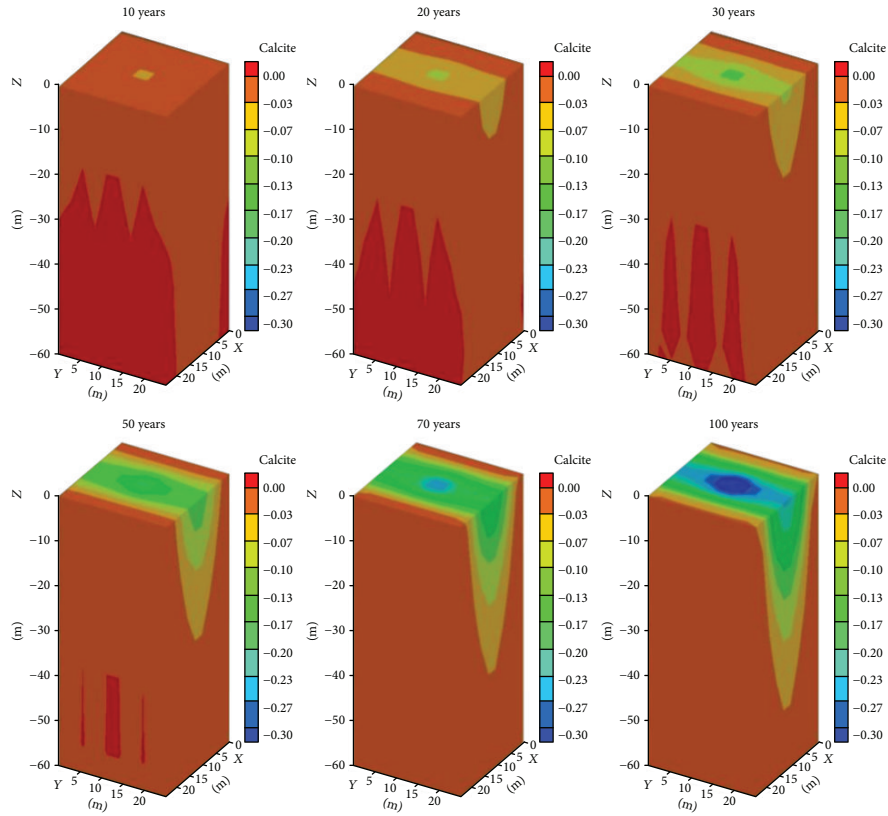


FIGURE 8: The corrosion range of the fissure under medium hydrodynamic conditions-medium permeability—20°C.

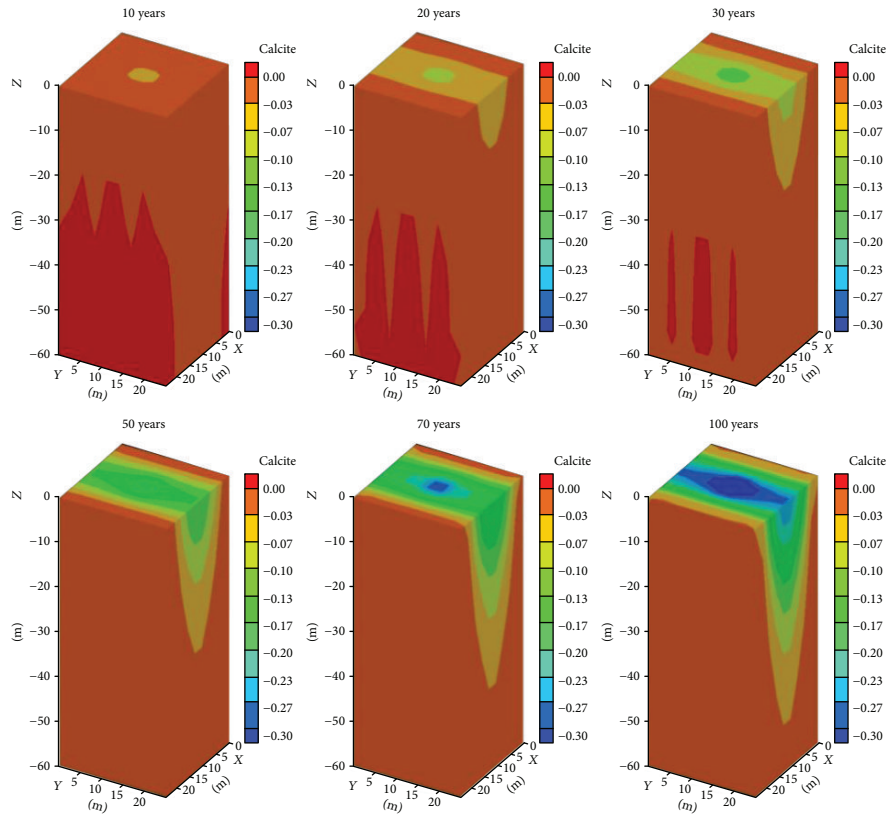


FIGURE 9: The corrosion range of the fissure under medium hydrodynamic conditions-medium permeability—35°C.

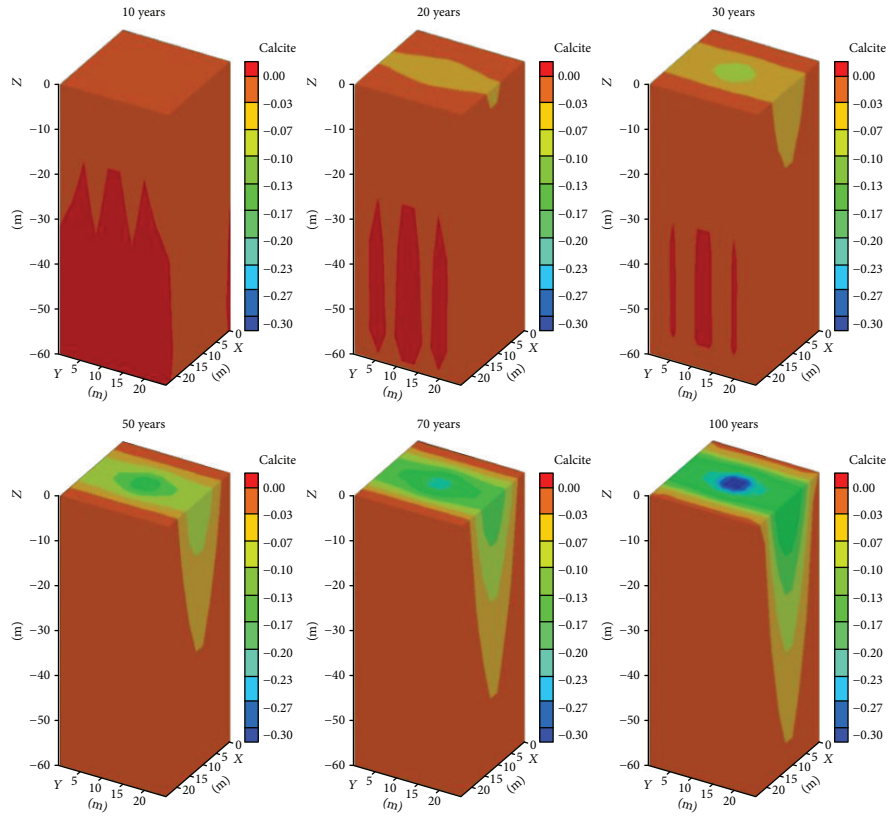


FIGURE 10: The corrosion range of the fissure under medium hydrodynamic conditions-low permeability—20°C.

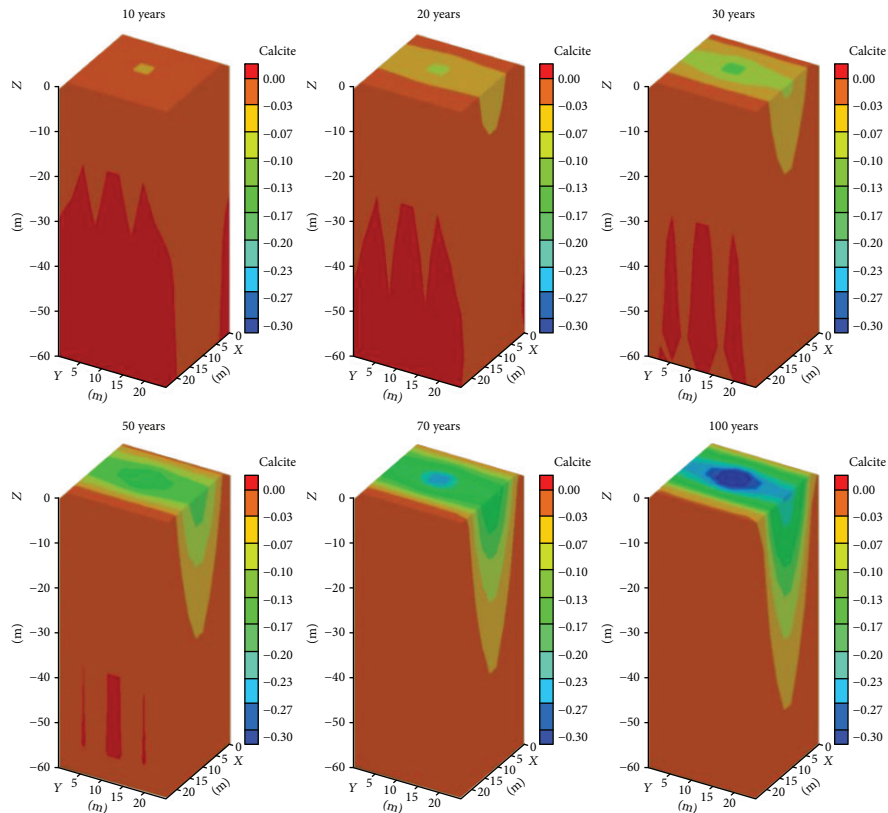


FIGURE 11: The corrosion range of the fissure under medium hydrodynamic conditions-medium permeability—20°C.

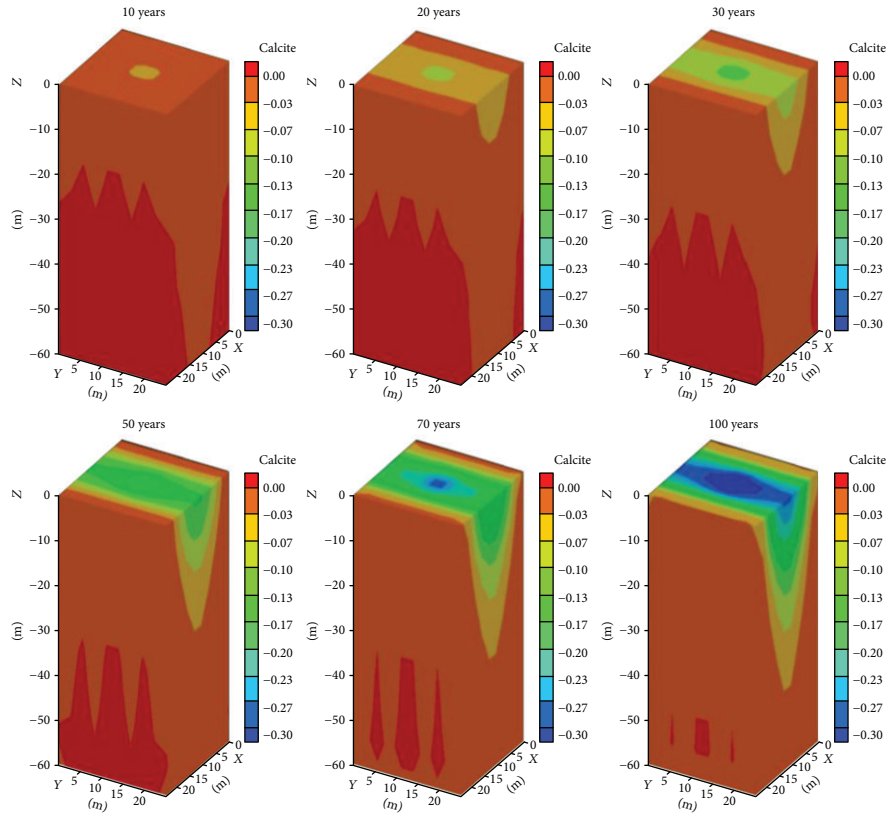


FIGURE 12: The corrosion range of the fissure under medium hydrodynamic conditions-high permeability—20°C.

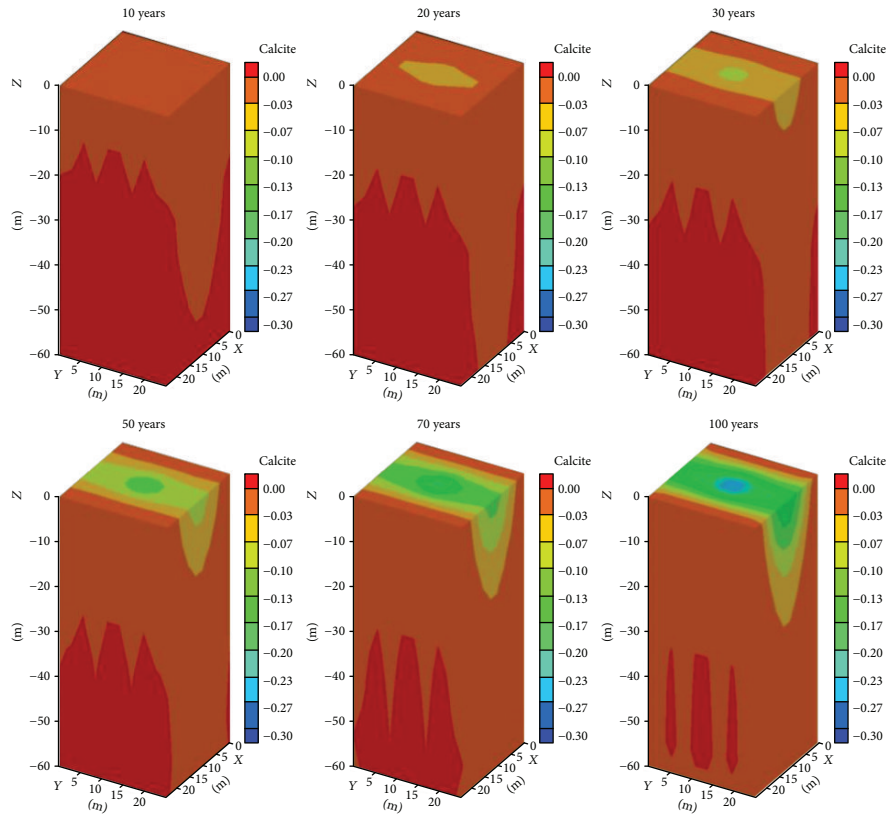


FIGURE 13: The corrosion range of the fissure under weak hydrodynamic conditions-medium permeability—20°C.

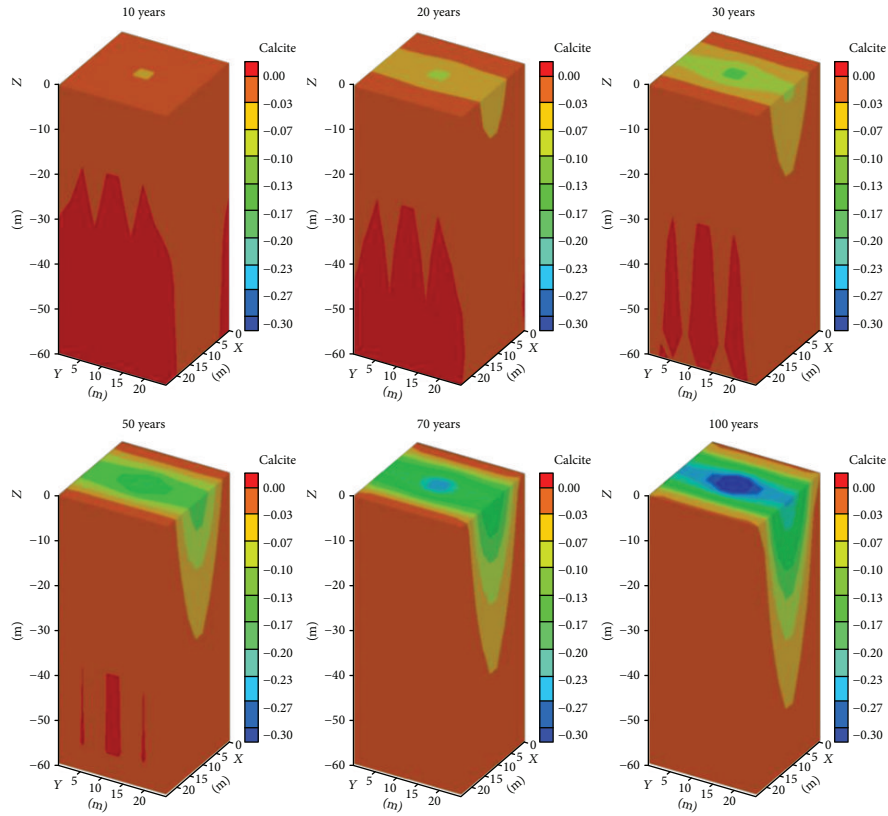


FIGURE 14: The corrosion range of the fissure under medium hydrodynamic conditions-medium permeability—20°C.

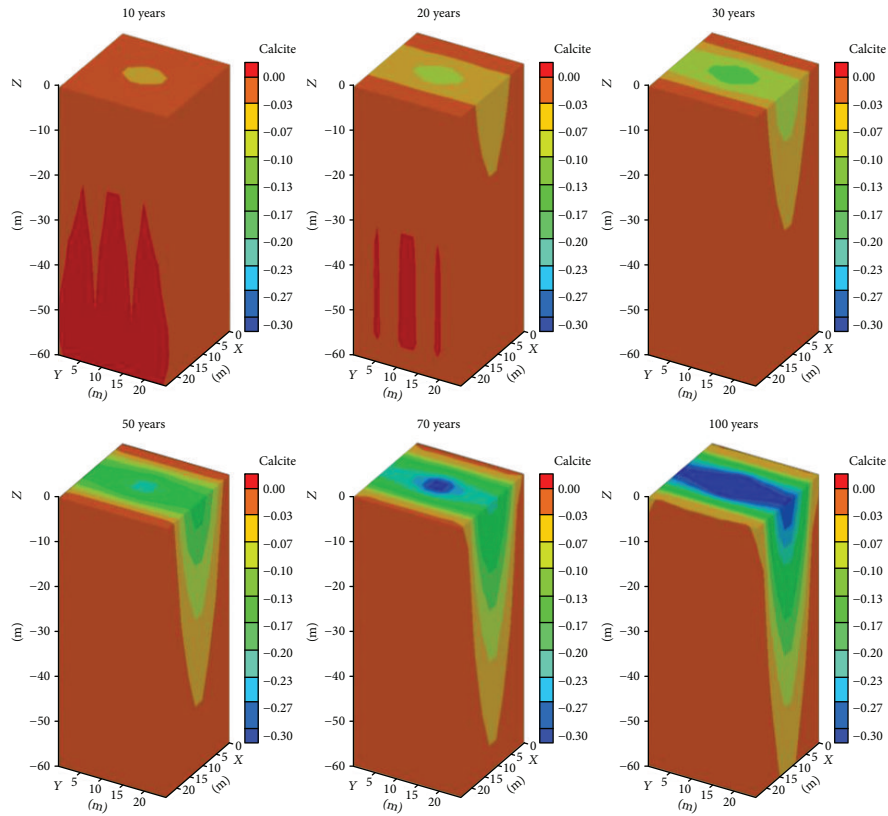


FIGURE 15: The corrosion range of the fissure under strong hydrodynamic conditions-medium permeability—20°C.

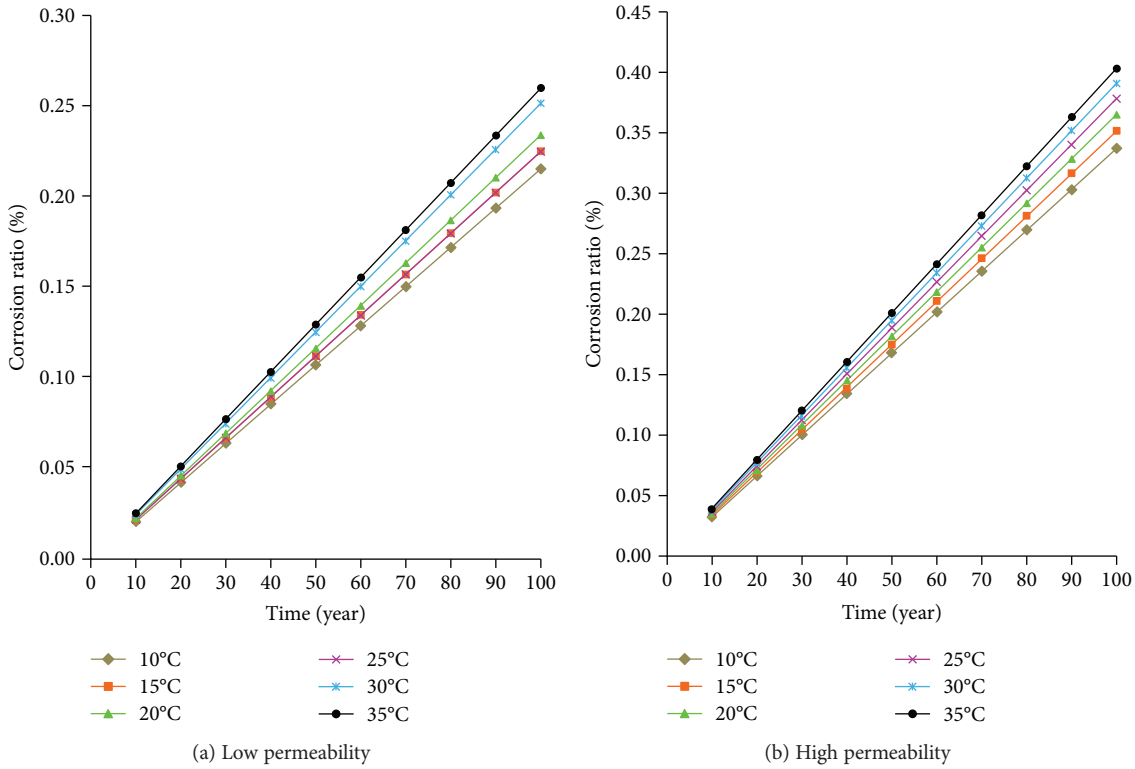


FIGURE 16: The corrosion ratio of the fissure under strong hydrodynamic conditions over time.

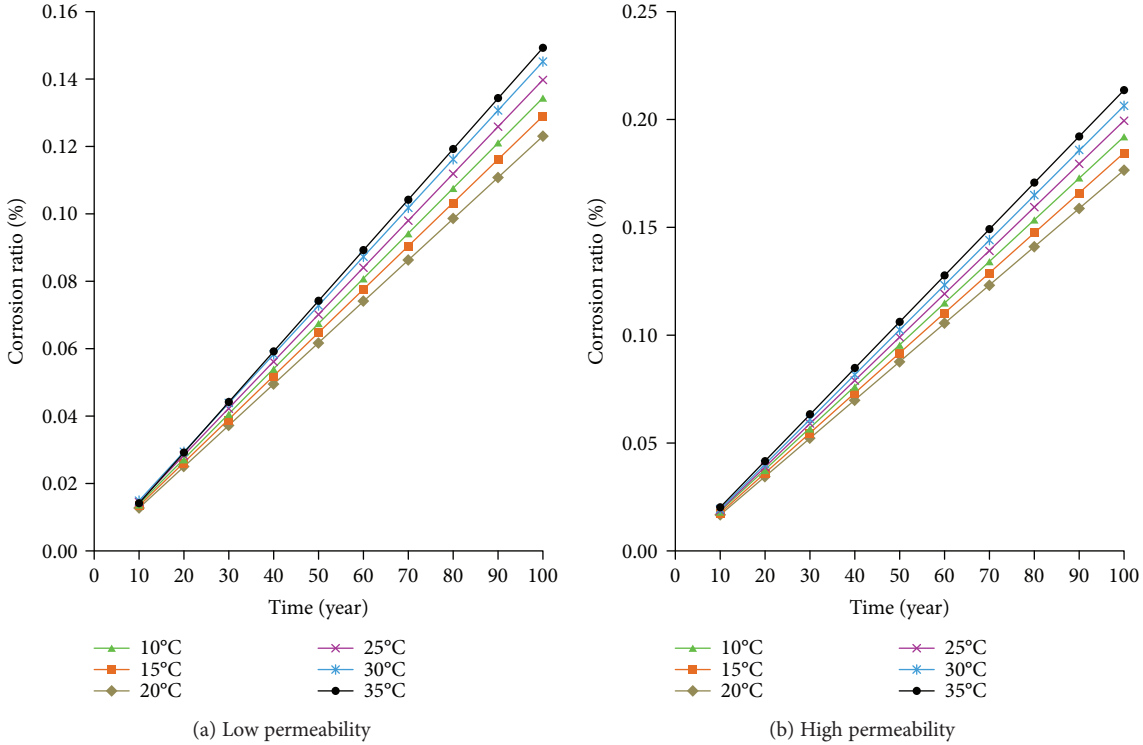


FIGURE 17: The corrosion ratio of the fissure under weak hydrodynamic conditions over time.

The comparisons of Figure 16(a) with Figure 16(b) and Figure 17(a) with Figure 17(b), during the same corrosion time, reveal that the corrosion ratio of the tunnel fissure

under the high-permeability condition ($7.4 \times 10^{-10} \text{ m}^2$) was greater than that under the low-permeability condition ($7.4 \times 10^{-12} \text{ m}^2$). After 100 years of corrosion, the corrosion

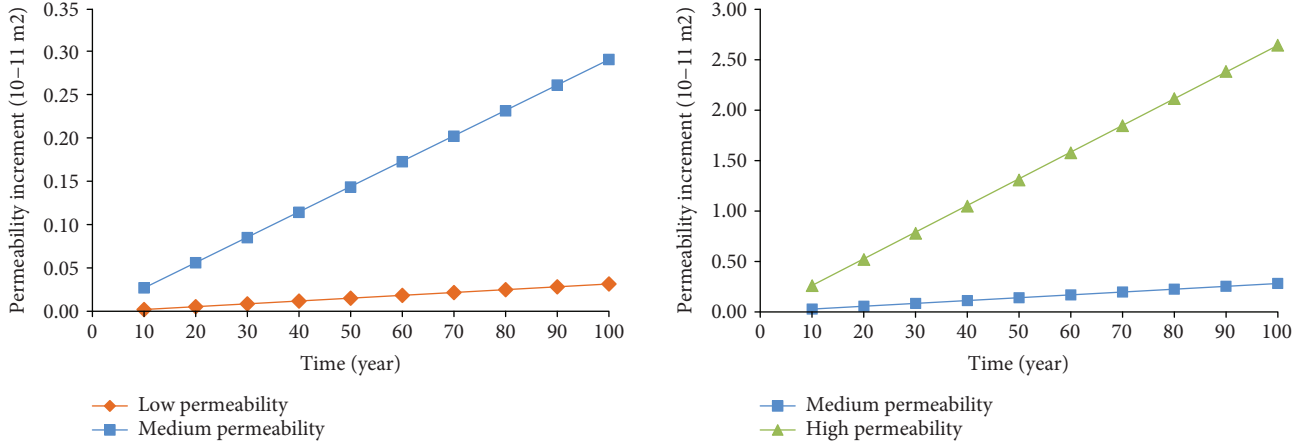


FIGURE 18: The rate of increase of permeability over time.

ratio (strong hydrodynamic condition, 35°C, and high porosity and permeability) (0.4032%) was 1.6 times higher than that of low porosity and permeability (0.2599%).

The comparison of Figure 16(a) with Figure 17(a) and Figure 16(b) with Figure 17(b), during the same corrosion time, reveals that under strong hydrodynamic conditions, the corrosion ratio was greater than that under the weak hydrodynamic condition. After 100 years of corrosion, the maximum corrosion ratio (0.4032%) under the strong hydrodynamic conditions (high porosity and permeability, 35°C) was 2.1 times than that under the weak hydrodynamic condition (0.1908%).

4.3. Evolution of Porosity and Permeability in the Fissure Zone. The structure of the fissures in soluble rock of karst areas is the foundation of the corrosion. The porosity and permeability conditions in fissure zones are the main factors affecting the development of karst. Through the analysis of the effects of different temperatures and flow rates on corrosion, it was found that the most significant corrosion occurred at the temperature of 35°C and strong hydrodynamic conditions. Therefore, we selected 35°C and strong hydrodynamic conditions as an example with which the variation of the porosity and permeability of the fissure zone within 100 years was discussed.

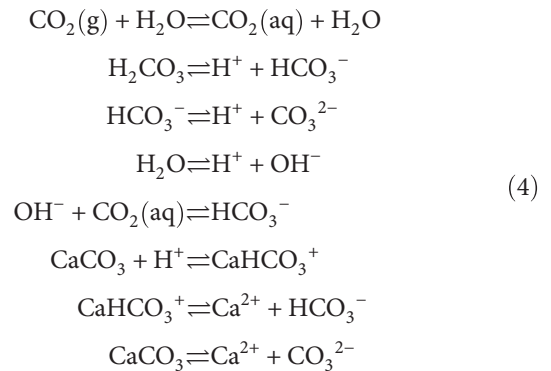
According to the simulation results of 10–100 years of corrosion, the porosity and permeability changes in the fracture core zone of the karst development area were obtained. The relation curves of the increase of permeability with time are shown in Figure 18. As shown in Figure 18, the rate of change of permeability also increased with time. Permeability increased much faster under the condition of high permeability than under the condition of low permeability. After 100 years of corrosion, the permeability increased from $7.40 \times 10^{-12} \text{ m}^2$ to $7.73 \times 10^{-12} \text{ m}^2$; the maximum increase of permeability was $0.33 \times 10^{-12} \text{ m}^2$ under the low-permeability condition. Meanwhile, under the high-permeability condition, the permeability increased from $740.00 \times 10^{-12} \text{ m}^2$ to $767.5 \times 10^{-12} \text{ m}^2$ and the maximum increase of permeability was $27.5 \times 10^{-12} \text{ m}^2$. It was

83.3 times higher than that under the low-permeability condition.

As shown in Figure 19, under the conditions of different porosities, the porosity increased with the corrosion time (linear relationship). Under the condition of high porosity, porosity increased much faster than that under the low-porosity condition. After 100 years of corrosion, the porosity of the low-porosity condition increased from 0.200 to 0.203, while under the high-porosity condition, the porosity increased from 0.350 to 0.354. The maximum increase of porosity under the high-porosity condition was 2 times higher than that under the low-porosity condition.

The reasons for the changes in the corrosion range, porosity, and permeability of the fissure zone are discussed as follows:

The lithology of the study area is carbonate rocks comprising 95% calcite; the corrosion of carbonate rocks was mainly caused by calcite corrosion, and the chemical reaction equations are as follows:



Because calcite corrosion’s chemical balance will be affected by temperature, in the range of simulated temperatures (10°C~35°C), the reaction rate constant increased with temperature, causing the reaction’s equilibrium to move towards the direction of the solution. These results have the same corrosion trend as those obtained by Pokrovsky et al. [23] and Huang [68]. They used an experimental method to

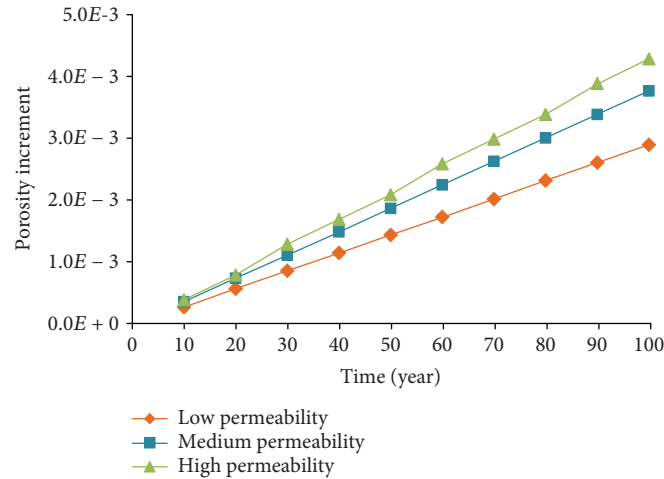


FIGURE 19: The increase of porosity over time.

explore corrosion under neutral conditions and different temperatures ($0.5^{\circ}\text{C}\sim 40^{\circ}\text{C}$).

According to (4), during the corrosion of calcite, Ca^{2+} was the main product of the chemical reaction. Under weak hydrodynamic conditions, the flow through the fissures was less and the travel time of water through the fissures was longer. Therefore, the concentration of dissolved Ca^{2+} was higher in the water, and when the water flow reached the lower part of the fissure, the concentration of Ca^{2+} in the water was close to saturation. Therefore, corrosion mainly occurred in the upper part of the fissure under the weak hydrodynamic condition, and the corrosion ratio was relatively small. In contrast, in the strong hydrodynamic conditions, the flow rate through the fissures was faster and the travel time of water through the fissures was shorter than that under the weak hydrodynamic condition. Therefore, the concentration of dissolved Ca^{2+} was lower in water under the strong hydrodynamic condition, and when the water seepage reached the lower part of the fracture, the concentration of Ca^{2+} was lower. The resulting corrosion of the fissures was more obvious than that of those in the weak hydrodynamic condition, and the corrosion range runs through the whole fissure with a higher corrosion ratio. In addition, due to the increased flow rate, the mechanical failure of the rock is enhanced, which makes the surface of the rock broken. The rock powder on the broken surface of the rock was carried away by the water, thus increasing the corrosion ratio and corrosion range.

Under the conditions of high porosity and permeability, the porosity and permeability increased faster than those under the low-porosity and low-permeability condition. After 100 years of corrosion, the permeability change under the high-permeability condition was 83.3 times higher than that under the low-permeability condition, while the change of porosity under the high-permeability condition was only 2 times higher than that under the low-permeability condition. It can be speculated that with continuing corrosion, more and more dead-end pores became effective pores. Due to the transformation of dead-end pores into effective pores, the connectivity between pores was significantly enhanced



FIGURE 20: The site of the field experiment.

and the increase of fissure permeability became significantly larger, while the porosity increased only slightly. Therefore, the degree of change in permeability was much greater than that in porosity in the same period.

According to the simulation results, the larger the porosity and permeability were, the more significant the increases in porosity and permeability were, which led to the enhancement of corrosion in the high-porosity and high-permeability zones and enhancement the differential corrosion of karst.

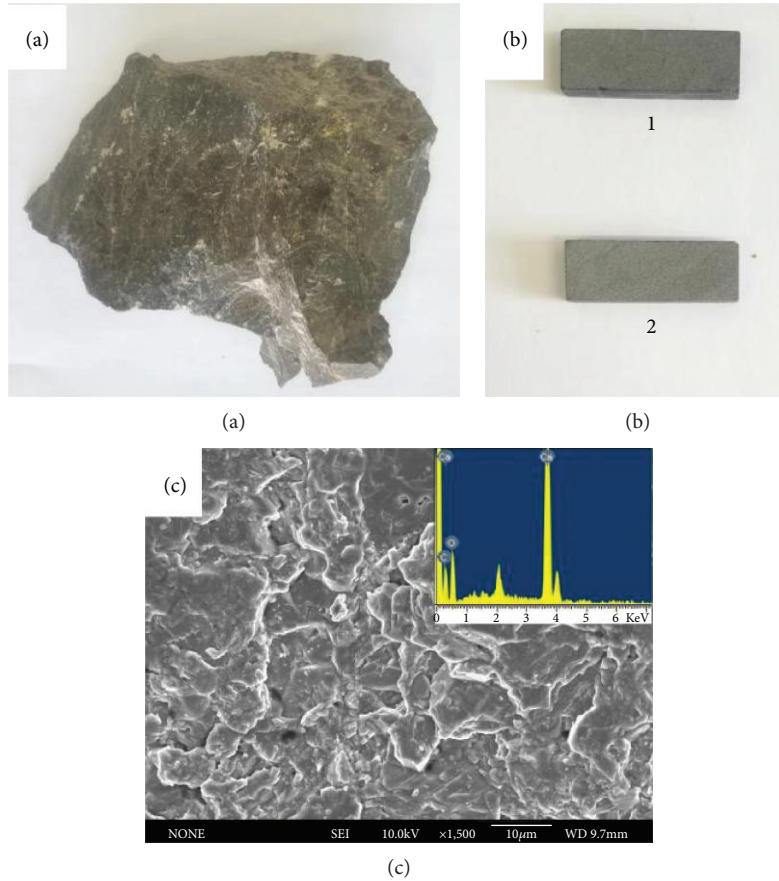


FIGURE 21: Rock samples. (a) Original experimental samples, (b) rock samples after being cut, and (c) SEM photograph (×1500).

5. Comparison of the Field Corrosion Experiment Results to the Numerical Simulation Results

To further explore the corrosion characteristics of rock samples at the tunnel’s key karst development parts and verify the reliability of the simulation results, a field corrosion experiment was carried out. The field experimental site was a gully in the Wulong tunnel construction area, which is in the key development parts of the tunnel karst area. The width of the gully is approximately 2.5 meters (Figure 20), and the lithology of the underlayer stratum is thick-layer limestone. The gully is covered with clay, gravel, and plants. The burial depth of groundwater was small.

The experimental rock samples were made of the limestone of the Changxing Formation, with a size of 30 mm × 10 mm × 10 mm (Figure 21(b)). The rock samples were placed into a plastic box with holes that allowed groundwater to flow through it. The plastic box was buried underground below the groundwater level (Figures 20 and 22).

After one year of corrosion, the box was taken out and the degrees of corrosion of the rock samples (Figure 20) were measured. Because the corrosion of rock samples depends on the surface area of the water-rock



FIGURE 22: The process of the field experiment.

interaction, we used (5) to calculate the surface corrosion ratio R ($g/(m^2 \cdot a)$).

$$R = \frac{m}{s \cdot t}, \tag{5}$$

where $R = m/st$ is the corrosion ratio of the unit area ($g/(m^2 \cdot a)$); s is the surface area of the water-rock interaction (m^2); t is the corrosion time (a).

For numerical simulation, according to Figures 16(a) and 17(b), the corrosion ratio showed a linear variation with time. The corrosion ratio (after one year of corrosion) was obtained by linear interpolation; then, the surface corrosion

TABLE 5: The surface corrosion ratios of the field experiment and numerical simulation.

Corrosion condition		Before corrosion (g)	Corrosion amount (g)	Surface corrosion ratio (g/(m ² ·a))
Field experiment	Field experiment (1)	8.5940	0.0033	2.3571
	Field experiment (2)	8.4638	0.0037	2.6429
Numerical simulation	Strong hydrodynamic condition-high permeability (20°C)	8.0870×10^4	2.8604	9.9319
	Strong hydrodynamic condition-medium permeability (20°C)	8.2598×10^4	2.5292	8.7818
	Strong hydrodynamic condition-low permeability (20°C)	8.4326×10^4	1.9142	6.6466
	Medium hydrodynamic condition-high permeability (20°C)	8.0870×10^4	2.2369	7.7669
	Medium hydrodynamic condition-medium permeability (20°C)	8.2598×10^4	2.0014	6.9492
	Medium hydrodynamic condition-low permeability (20°C)	8.4326×10^4	1.5440	5.3612
	Weak hydrodynamic condition-high permeability (20°C)	8.0870×10^4	1.4678	5.0965
	Weak hydrodynamic condition-medium permeability (20°C)	8.2598×10^4	1.3356	4.6376
	Weak hydrodynamic condition-low permeability (20°C)	8.4326×10^4	1.0667	3.7039

ratio (g/(m²·a)) was calculated with (5). The surface corrosion ratios of rock samples per unit area in the field experiment and numerical simulation are listed in Table 5.

From Table 5, we can see that the surface corrosion ratio of rock samples in the field experiments was less than that in the numerical simulation. The surface corrosion ratio of the weak hydrodynamic condition (numerical simulation) was close to that of the field experiments. Analyzing the hydrogeological conditions of the field experiment and the setting of hydrogeological conditions in numerical simulation, the water flow in the numerical simulation was mainly in the fracture core and the flow rates were faster than those in the field experiments. Thus, in the strong hydrodynamic condition and medium hydrodynamic condition, the surface corrosion ratios obtained in the simulation were higher than those obtained in the field experiment. However, overall, the differences in the corrosion ratio between the numerical simulation and field experiment were on the same order of magnitude. Therefore, the results of the numerical simulation model were reliable, and the model can be used to predict the corrosion evolution of the fissures in soluble rock of the tunnel in the future.

6. Conclusion

In this study, the numerical simulation model of the fissures in soluble rock of karst areas of the Wulong tunnel was established, and the corrosion characteristics of the fissures were evaluated. The conclusions were as follows:

(1) The development of the fissures in soluble rock of karst areas of the tunnel was mostly affected by the flow rates. After 100 years of corrosion, under

the influence of temperature and porosity and permeability, the maximum corrosion range and corrosion ratio were only 1.2 times~1.6 times higher than the minimum values, respectively. In contrast, the corrosion range of the strong hydrodynamic condition was approximately 1.8 times~2.2 times higher than that of the weak hydrodynamic condition, and the corrosion ratio of the strong hydrodynamic condition was 2.1 times higher than that of the weak hydrodynamic condition.

- (2) In the temperature range of 10°C~35°C, the corrosion range and the corrosion ratio were proportional to the temperature because the reaction rate constant increased with temperature, causing the reactions' equilibria to move towards the direction of the solution. After 100 years of corrosion, the corrosion ranges of 35°C were 1.2 times~1.3 times higher than those of 10°C, and the corrosion ratio of 35°C was 1.2 times higher than that of 10°C.
- (3) The porosity and permeability of the fissure zone enhanced the corrosion of the fissure and enhanced the differential corrosion of karst. The higher the porosity and permeability were, the more significant the enhancement effects on the porosity and permeability were. Many of the dead-end pores became effective pores, which greatly increased the permeability, but the slightly increased porosity also accelerated the corrosion damage of the tunnel.
- (4) The simulation results were verified by the field experiment, and the simulation model can be used

to quantitatively predict the corrosion evolution of a fissure zone within the acceptable range of error.

Data Availability

The data used to support the findings of this study are available from the corresponding author upon request.

Conflicts of Interest

The authors declare no conflict of interest.

Acknowledgments

This work was supported by the Graduate Innovation Fund of Jilin University (no. 2017148), the National Natural Science Foundation of China (no. 41372334), and the China National Science and Technology Major Project (no. 2016ZX05016-005).

References



- [1] D. T. Li and Y. Luo, "Measurement of carbonate rocks distribution area in China," *Carsologica Sinica*, vol. 2, pp. 147–150, 1983.
- [2] C. S. Li, J. F. Ding, and Y. K. Liao, *Geochemical Dynamics and Fractal Features of Karst Tunnel*, The Science Publishing Company, Beijing, China, 2017.
- [3] F. Gutierrez, "Hazards associated with karst," in *Geomorphological Hazards and Disaster Prevention*, I. Alcantara-Ayala and A. S. Goudie, Eds., pp. 161–176, Cambridge University Press, Cambridge, UK, 2010.
- [4] F. Gutierrez, M. Parise, J. De Waele, and H. Jourde, "A review on natural and human-induced geohazards and impacts in karst," *Earth Science Reviews*, vol. 138, pp. 61–88, 2014.
- [5] M. Parise and J. Gunn, Eds., *Natural and Anthropogenic Hazards in Karst Areas: Recognition, Analysis and Mitigation*, Geological Society Special Publication 279, London, UK, 2007.
- [6] M. Parise, D. Closson, F. Gutierrez, and Z. Stevanovic, "Anticipating and managing engineering problems in the complex karst environment," *Environmental Earth Sciences*, vol. 74, no. 12, pp. 7823–7835, 2015.
- [7] X. Q. Qin, M. Q. Zhu, and Z. C. Jiang, "A review on recent advances in rocky desertification in Southwest China karst region," *Carsologica Sinica*, vol. 25, pp. 234–238, 2006.
- [8] Y. Wang, *The Karst Water Accumulation Law in the Faulted Basin*, Science and Technology Press, Kunming, China, 2003.
- [9] C. S. Li, B. Gao, and Z. R. Mei, *Karst and Groundwater Advance Prediction Techniques*, Southwest Jiaotong University Press, Chengdu, China, 2013.
- [10] S. C. Li, Z. Q. Zhou, L. P. Li, Z. H. Xu, Q. Q. Zhang, and S. S. Shi, "Risk assessment of water inrush in karst tunnels based on attribute synthetic evaluation system," *Tunnelling and Underground Space Technology*, vol. 38, pp. 50–58, 2013.
- [11] A. C. Waltham and P. G. Fookes, "Engineering classification of karst ground conditions," *Quarterly Journal of Engineering Geology and Hydrogeology*, vol. 36, no. 2, pp. 101–118, 2003.
- [12] R. S. Arvidson, C. Fischer, and A. Luttge, "Calcite dissolution kinetics," *Aquatic Geochemistry*, vol. 21, no. 5, pp. 415–422, 2015.
- [13] D. Buhmann and W. Dreybrodt, "Calcite dissolution kinetics in the system $\text{H}_2\text{O}-\text{CO}_2-\text{CaCO}_3$ with participation of foreign ions," *Chemical Geology*, vol. 64, no. 1–2, pp. 89–102, 1987.
- [14] W. Dreybrodt, F. Gabrovšek, and D. Romanov, *Processes of Speleogenesis: A Modeling Approach*, Karst Research Institute, ZRC SAZU, Postojna, Slovenia, 2005.
- [15] L. Eisenlohr, K. Meteva, F. Gabrovšek, and W. Dreybrodt, "The inhibiting action of intrinsic impurities in natural calcium carbonate minerals to their dissolution kinetics in aqueous $\text{H}_2\text{O}-\text{CO}_2$ solutions," *Geochimica et Cosmochimica Acta*, vol. 63, no. 7–8, pp. 989–1001, 1999.
- [16] F. Gabrovšek and M. Ž. Huzjan, *Evolution of Early Karst Aquifers: From Simple Principles to Complex Models*, Založba ZRC, Ljubljana, Slovenia, 2000.
- [17] T. Hiller, D. Romanov, G. Kaufmann, J. Epting, and P. Huggenberger, "Karstification beneath the Birs weir in Basel/Switzerland: a 3D modeling approach," *Journal of Hydrology*, vol. 448–449, pp. 181–194, 2012.
- [18] A. A. Jeschke and W. Dreybrodt, "Pitfalls in the determination of empirical dissolution rate equations of minerals from experimental data and a way out: an iterative procedure to find valid rate equations, applied to Ca-carbonates and -sulphates," *Chemical Geology*, vol. 192, no. 3–4, pp. 183–194, 2002.
- [19] A. C. Lasaga, *Kinetic Theory in the Earth Sciences*, Princeton University Press, Princeton, NJ, USA, 2014.
- [20] J. W. Morse and R. A. Berner, "Dissolution kinetics of calcium carbonate in sea water; I, A kinetic origin for the lysocline," *American Journal of Science*, vol. 272, no. 9, pp. 840–851, 1972.
- [21] L. N. Plummer and E. Busenberg, "The solubilities of calcite, aragonite and vaterite in $\text{CO}_2-\text{H}_2\text{O}$ solutions between 0 and 90°C, and an evaluation of the aqueous model for the system $\text{CaCO}_3-\text{CO}_2-\text{H}_2\text{O}$," *Geochimica et Cosmochimica Acta*, vol. 46, no. 6, pp. 1011–1040, 1982.
- [22] O. S. Pokrovsky, S. V. Golubev, and J. Schott, "Dissolution kinetics of calcite, dolomite and magnesite at 25°C and 0 to 50 atm $p\text{CO}_2$," *Chemical Geology*, vol. 217, no. 3–4, pp. 239–255, 2005.
- [23] O. S. Pokrovsky, S. V. Golubev, J. Schott, and A. Castillo, "Calcite, dolomite and magnesite dissolution kinetics in aqueous solutions at acid to circumneutral pH, 25 to 150°C and 1 to 55 atm $p\text{CO}_2$: new constraints on CO_2 sequestration in sedimentary basins," *Chemical Geology*, vol. 265, no. 1–2, pp. 20–32, 2009.
- [24] Y. J. Zhao, F. G. Wang, C. S. Li, F. S. Wu, and Y. Q. Cao, "Carbonate karst erosion experiment research of Guizhou Huangguoshu tunnel," *Coal Technology*, vol. 35, no. 7, pp. 310–312, 2016.
- [25] H. Cai, Z. Chen, and H. Zhou, "Impact analysis of fracture on the karst development and groundwater flow of Wulong cave," *Safety & Environmental Engineering*, vol. 22, no. 2, pp. 1–6, 2015.
- [26] G. Kaufmann, "Modelling karst aquifer evolution in fractured, porous rocks," *Journal of Hydrology*, vol. 543, Part B, pp. 796–807, 2016.
- [27] J. Siemers and W. Dreybrodt, "Early development of karst aquifers on percolation networks of fractures in limestone," *Water Resources Research*, vol. 34, no. 3, pp. 409–419, 1998.
- [28] W. Dreybrodt, "Principles of early development of karst conduits under natural and man-made conditions revealed by mathematical analysis of numerical models," *Water Resources Research*, vol. 32, no. 9, pp. 2923–2935, 1996.

- [29] W. Dreybrodt, *Processes in Karst Systems: Physics, Chemistry, and Geology*, Springer Series in Physical Environment, Springer, Berlin, Heidelberg, 1988.
- [30] W. Dreybrodt, "The role of dissolution kinetics in the development of karst aquifers in limestone: a model simulation of karst evolution," *Journal of Geology*, vol. 98, no. 5, pp. 639–655, 1990.
- [31] W. Dreybrodt and F. Gabrovšek, "Dynamics of the evolution of a single karst conduit," in *Speleogenesis: Evolution of Karst Aquifers*, A. Klimchouk, D. C. Ford, A. N. Palmer, and W. Dreybrodt, Eds., pp. 184–193, National Speleological Society, Huntsville, AL, USA, 2000.
- [32] R. B. Hanna and H. Rajaram, "Influence of aperture variability on dissolutional growth of fissures in karst formations," *Water Resources Research*, vol. 34, no. 11, pp. 2843–2853, 1998.
- [33] A. N. Palmer, "Origin and morphology of limestone caves," *Geological Society of America Bulletin*, vol. 103, no. 1, pp. 1–21, 1991.
- [34] W. K. Annable, *Numerical analysis of conduit evolution in karstic aquifers*, [Ph.D. thesis], University of Waterloo, Waterloo, ON, Canada, 2003.
- [35] T. Hiller, G. Kaufmann, and D. Romanov, "Karstification beneath dam-sites: from conceptual models to realistic scenarios," *Journal of Hydrology*, vol. 398, no. 3–4, pp. 202–211, 2011.
- [36] G. Kaufmann, "Modelling karst geomorphology on different time scales," *Geomorphology*, vol. 106, no. 1–2, pp. 62–77, 2009.
- [37] G. Kaufmann, D. Romanov, and T. Hiller, "Modeling three-dimensional karst aquifer evolution using different matrix-flow contributions," *Journal of Hydrology*, vol. 388, no. 3–4, pp. 241–250, 2010.
- [38] Q. Liu, Y. R. Lu, F. E. Zhang, J. X. Qi, and S. Zhang, "Qualitative analysis of microcorrosion of limestone induced by temperature and hydrodynamic pressure," *Rock and Soil Mechanics*, vol. 31, no. S2, pp. 149–154, 2010.
- [39] H. D. Yu, D. Yang, D. Wang, and M. Y. Han, "Top-down fabrication of calcite nanoshoot arrays by crystal dissolution," *Advanced Materials*, vol. 22, no. 29, pp. 3181–3184, 2010.
- [40] W. H. Zhu, X. Y. Qu, L. W. Qiu, Y. Chen, F. X. Gong, and S. X. Wu, "Characteristics and erosion mechanism of carbonate in acetic acid and hydrochloride solutions, an example from the Nanpu depression," *Bulletin of Mineralogy, Petrology and Geochemistry*, vol. 34, pp. 619–625, 2015.
- [41] U. Svensson and W. Dreybrodt, "Dissolution kinetics of natural calcite minerals in CO₂-water systems approaching calcite equilibrium," *Chemical Geology*, vol. 100, no. 1–2, pp. 129–145, 1992.
- [42] P. Cubillas, S. Köhler, M. Prieto, C. Causserand, and E. H. Oelkers, "How do mineral coatings affect dissolution rates? An experimental study of coupled CaCO₃ dissolution—CdCO₃ precipitation," *Geochimica et Cosmochimica Acta*, vol. 69, no. 23, pp. 5459–5476, 2005.
- [43] D. W. Finneran and J. W. Morse, "Calcite dissolution kinetics in saline waters," *Chemical Geology*, vol. 268, no. 1–2, pp. 137–146, 2009.
- [44] C. Fischer, I. Kurganskaya, T. Schäfer, and A. Lüttge, "Variability of crystal surface reactivity: what do we know?," *Applied Geochemistry*, vol. 43, pp. 132–157, 2014.
- [45] E. Busenberg and L. Niel Plummer, "Kinetic and thermodynamic factors controlling the distribution of SO₃²⁻ and Na⁺ in calcites and selected aragonites," *Geochimica et Cosmochimica Acta*, vol. 49, no. 3, pp. 713–725, 1985.
- [46] D. K. Gledhill and J. W. Morse, "Calcite dissolution kinetics in Na–Ca–Mg–Cl brines," *Geochimica et Cosmochimica Acta*, vol. 70, no. 23, pp. 5802–5813, 2006.
- [47] Q. Gong, J. Deng, Q. Wang, L. Yang, and M. She, "Experimental determination of calcite dissolution rates and equilibrium concentrations in deionized water approaching calcite equilibrium," *Journal of Earth Science*, vol. 21, no. 4, pp. 402–411, 2010.
- [48] A. C. Lasaga and A. Lüttge, "Mineralogical approaches to fundamental crystal dissolution kinetics," *American Mineralogist*, vol. 89, no. 4, pp. 527–540, 2004.
- [49] A. Lüttge, "Crystal dissolution kinetics and Gibbs free energy," *Journal of Electron Spectroscopy and Related Phenomena*, vol. 150, no. 2–3, pp. 248–259, 2006.
- [50] Q. Gong, J. Deng, Q. Wang, L. Yang, and M. She, "Calcite dissolution in deionized water from 50°C to 250°C at 10 MPa: rate equation and reaction order," *Acta Geologica Sinica - English Edition*, vol. 82, no. 5, pp. 994–1001, 2008.
- [51] R. Shiraki and S. L. Brantley, "Kinetics of near-equilibrium calcite precipitation at 100°C: an evaluation of elementary reaction-based and affinity-based rate laws," *Geochimica et Cosmochimica Acta*, vol. 59, no. 8, pp. 1457–1471, 1995.
- [52] K. Adamczyk, M. Premont-Schwarz, D. Pines, E. Pines, and E. T. J. Nibbering, "Real-time observation of carbonic acid formation in aqueous solution," *Science*, vol. 326, no. 5960, pp. 1690–1694, 2009.
- [53] J. Xu, C. Fan, and H. H. Teng, "Calcite dissolution kinetics in view of Gibbs free energy, dislocation density, and pCO₂," *Chemical Geology*, vol. 322–323, pp. 11–18, 2012.
- [54] W. Zhou and B. F. Beck, "Engineering issues on karst," in *Karst Management*, P. E. Beynen, Ed., pp. 9–45, Springer, Dordrecht, Netherlands, 2011.
- [55] X. H. Zhang and Q. W. Liu, "Analysis of the features of water outbursts from underground rivers and the countermeasures in Wulong tunnel," *Modern Tunnelling Technology*, vol. 42, pp. 59–64, 2005.
- [56] A. Amann Hildenbrand, J. P. Dietrichs, and B. M. Krooss, "Effective gas permeability of tight gas sandstones as a function of capillary pressure – a non-steady-state approach," *Geofluids*, vol. 16, no. 3, 383 pages, 2016.
- [57] J. Angelier, F. Bergerat, O. Dauteuil, and T. Villemin, "Effective tension-shear relationships in extensional fissure swarms, axial rift zone of Northeastern Iceland," *Journal of Structural Geology*, vol. 19, no. 5, pp. 673–685, 1997.
- [58] D. R. Faulkner, C. A. L. Jackson, R. J. Lunn et al., "A review of recent developments concerning the structure, mechanics and fluid flow properties of fault zones," *Journal of Structural Geology*, vol. 32, no. 11, pp. 1557–1575, 2010.
- [59] A. Giwelli, C. Delle Piane, L. Esteban et al., "Laboratory observations of fault transmissibility alteration in carbonate rock during direct shearing," *Geofluids*, vol. 16, no. 4, 672 pages, 2016.
- [60] M. Johri, E. M. Dunham, M. D. Zoback, and Z. Fang, "Predicting fault damage zones by modeling dynamic rupture propagation and comparison with field observations," *Journal of Geophysical Research: Solid Earth*, vol. 119, no. 2, pp. 1251–1272, 2014.

- [61] L. Micarelli, A. Benedicto, and C. A. J. Wibberley, "Structural evolution and permeability of normal fault zones in highly porous carbonate rocks," *Journal of Structural Geology*, vol. 28, no. 7, pp. 1214–1227, 2006.
- [62] J. He, Y. Kang, D. Liu, M. Lei, and Z. Shu, "The stress sensitivity research on porous and fractured porous carbonate reservoirs," *Drilling & Production Technology*, vol. 28, no. 2, pp. 84–86, 2005.
- [63] D. Q. Li, Y. L. Kang, and L. J. You, "Experimental study on permeability stress sensitivity of carbonate rocks," *Natural Gas Geoscience*, vol. 202, no. 3, pp. 12–22, 2014.
- [64] Y. Wan, J. Zan, and H. Tao, "Study on pore structure of carbonate reservoir," *Oil-Gas Field Surface Engineering*, vol. 27, no. 12, pp. 13–14, 2008.
- [65] D. Zhu and Q. Li, "Predication of outflow in tunnel based on experimental permeating coefficient of precipitation," *Journal of Railway Engineering Society*, vol. 1, pp. 100–102, 1995.
- [66] T. Xu, E. Sonnenthal, N. Spycher, and K. Pruess, "TOUGH-REACT—a simulation program for non-isothermal multi-phase reactive geochemical transport in variably saturated geologic media: applications to geothermal injectivity and CO₂ geological sequestration," *Computers & Geosciences*, vol. 32, no. 2, pp. 145–165, 2006.
- [67] L. Yang, T. Xu, M. Wei, G. Feng, F. Wang, and K. Wang, "Dissolution of arkose in dilute acetic acid solution under conditions relevant to burial diagenesis," *Applied Geochemistry*, vol. 54, pp. 65–73, 2015.
- [68] S. Y. Huang, "The corrosion of carbonates and environment temperature," *Carsologica Sinica*, vol. 4, pp. 287–296, 1987.

Research Article

Groundwater-Mixing Mechanism in a Multiaquifer System Based on Isotopic Tracing Theory: A Case Study in a Coal Mine District, China

Pinghua Huang ^{1,2} and Xinyi Wang ^{1,2}

¹School of Resources and Environment Engineering, Henan Polytechnic University, Jiaozuo 454000, China

²Collaborative Innovation Center of Coalbed Methane and Shale Gas for Central Plains Economic Region, Henan Province, Jiaozuo 454000, China

Correspondence should be addressed to Pinghua Huang; hph2001@hpu.edu.cn and Xinyi Wang; wangxy@hpu.edu.cn

Received 3 January 2018; Revised 27 April 2018; Accepted 4 June 2018; Published 9 July 2018

Academic Editor: Carmine Apollaro

Copyright © 2018 Pinghua Huang and Xinyi Wang. This is an open access article distributed under the Creative Commons Attribution License, which permits unrestricted use, distribution, and reproduction in any medium, provided the original work is properly cited.

Water inrush of mixed groundwater is the primary threat against safe production in coal mines. To study the mixing mechanism of a multiaquifer groundwater system, groundwater samples were collected from different strata in a typical North China-type coalfield (Chaochuan Coal Mine) and were then tested using environmental isotopes (^{18}O , ^2H , ^3H , ^{13}C , and ^{14}C) and hydrochemical ions (Ca^{2+} , Mg^{2+} , Na^+ , K^+ , HCO_3^- , SO_4^{2-} , and Cl^-) as tracer agents. Results demonstrate that HCO_3^- and Cl^- exhibit a linear relationship with the mixing ratio, whereas Na^+ , Ca^{2+} , and SO_4^{2-} show certain degrees of curvature. This condition indicates that groundwater mixing involves major chemical actions. The $\delta\text{D}-\delta^{18}\text{O}$ plot reveals that karst water and groundwater from Quaternary and sandstone aquifers are mainly mixtures of local rainfall, evaporated groundwater, and “palaeo-groundwater.” The $^3\text{H} < 0.5$ TU and ^{14}C content in the groundwater sample number 27 is 13.6 pmc, which suggests that this groundwater sample is the last rainfall recharge in the ice stage. Palaeo-groundwater in a sandstone aquifer accounts for more than 60%, and that in the Cambrian limestone aquifer is lower than 20%. Groundwater from the Quaternary aquifer is supplied by “modern” rainfall. The $\delta^{13}\text{C}$ of groundwater from a sandstone aquifer decreases with the increase in $\text{CO}_3^{2-} + \text{HCO}_3^-$, and this condition reflects that organic matters exhibit biological degradation reaction. However, $\delta^{13}\text{C}$ increases with the rise in $\text{CO}_3^{2-} + \text{HCO}_3^-$ in the Cambrian limestone groundwater, and this condition indicates that organic matters produce methane due to methanogens.

1. Introduction

Limestones are generally hidden directly below the Quaternary system of unconsolidated sediments in North China-type coalfields. Thus, they may cause vertical hydraulic connections between karst water and shallow groundwater. The gradual longitudinal advancement in coal exploitation has made hydrogeological conditions in mines increasingly complicated. Long-term water filling after exploitation may also destroy the original groundwater circulation in aquifers and intensify the mixing effect. Groundwater inrush occurs frequently, which prevents exploitation of abundant explored coal resources. Therefore, studying the

groundwater-mixing process in coalfields during exploitation is extremely important.

Isotope geochemistry presents unique advantages in studying groundwater movement and has developed rapidly. It can extract useful information of water circulation and is free from restrictions of water content [1–19]. For example, stable water isotopes (^{18}O , ^2H , and ^3H) can be used as conservative natural tracer agents in a hydrological environment and provide a new perspective for groundwater circulation. They not only can trace the movement mode and process of groundwater but also can disclose the inner link profile of unsaturated water with surface and ground water. Apart from stable isotopes such as H and O, T and ^{14}C are also

two important and powerful radioactive tracers [19]. They can be used to recognize modern and submodern rainfall recharges. They have been proven to be very useful in estimating recharging characteristics [20], correcting groundwater model [15], and examining regional groundwater movement [10]. T is used to estimate the mixing ratio of modern and submodern water in shallow aquifers and investigate the mixing process of groundwater [6]. Water movement rate and retention time can also be explored by recognizing the ^3H peak value [16, 17]. Tenalem et al. studied the correlation between surface water and groundwater in the Awash River Basin by using environmental isotopes and water chemistry method and examined the flowing mode of groundwater by considering the local geological background. The isotope method has been widely used to analyze sources of groundwater, altitude of supply regions, and relative proportions of different supply sources [21]. Lima et al. explored environmental isotope features and groundwater sources in an aquifer in the Recife Coastal Plain in Brazil [22]. The isotope analysis results showed that groundwater includes three parts, namely, latest recharged groundwater, old evaporated groundwater, and saline water. Vengosh et al. investigated groundwater sources of a sandstone aquifer in Nubia, Israel [23]. The unique isotopic features and deuterium excess value demonstrate that groundwater has various supply sources. Murad examined the variation process of groundwater hydrogen and oxygen isotopes between the Oman Gulf and the Arabian Gulf [24]. He concluded that rainfall is the main supply source of groundwater, water vapor of rainfall comes from the Mediterranean, and rainfall evaporates before recharging to groundwater.

This study aims to evaluate the mixing characteristics of various types of groundwater and to determine the sources of groundwater and its mixing mechanism in the main water inrush aquifers under an environment where the degree of coal mining is becoming increasingly serious. This study also aims to provide a theoretical conclusion and lay a foundation for judging the source of water inrush.

2. Hydrogeological Conditions

The Chaochuan Coalfield lies between the North Asian and South Asian belts in the east section of the latitudinal structure in the Qinling Mountains. The coalfield is an arc unclinal structure, with the arc top orienting to the south. The east wing formation extends toward the northeast and leans to the northwest, with a dip angle of approximately 20° . The west wing formation extends toward the northwest and leans to the northeast. The dip angle of strata is generally larger than 70° , accompanied with local upright or inverted strata. Complicated structures are also present in the region. The study region is mainly developed with a northwest-trend fault and a northeast-trend fault, which constitute the mine plot or boundaries of the coalfield. Faults control and influence the hydrogeological conditions in the study area in different degrees. An arc normal fault is developed at the north boundary in the study area. The fault is higher than 1000 m. A karst-fractured aquifer is buried deeply below the Quaternary strata in the north of the fault,

thereby forming water-blocking boundaries. A fault is present in the east boundary and also blocks water. Cambrian limestone is exposed in the southwest and south regions as belts and acts as the karst water recharge area (Figure 1). The groundwater usually flows from west to east and from south to north. In the study area, groundwater is generally discharged from the mine wells to the surface. Cambrian karst, Permian sandstone, and Quaternary aquifers are main aquifers in the study area. The Cambrian karst aquifer is developed with karst and has the strongest water among others. It is also the main water inrush aquifer at the coal seam floor because of its high hydraulic pressure and abundant recharge sources.

The Quaternary aquifer is of the Quaternary age and is composed of sands and gravels with a general thickness of 20–55 m, and it generates water inflows of 15–50 m^3/h . The coal-bearing sandstone aquifer comprises sandstone, siltstone, and shale layers with permeability (K) of 0.0178–0.0594 m/d. This aquifer is in turn underlain by a Cambrian karst aquifer, which is the most important aquifer in the area. The latter aquifer has a thickness of approximately 250 m and is mainly composed of dolomitic, gray, and dark-gray limestones with permeability (K) of 0.137–14.3 m/d. This aquifer has well-developed karst features.

The study area belongs to a semiarid continental monsoon climate region. The annual average precipitation is 668.1 mm. Uneven rainfall distribution is observed among four seasons. Most precipitation occurs in July, August, and September and accounts for 50%–60% of annual precipitation. The evaporation is three times of precipitation, and the annual average evaporation is 1834 mm. The annual average air temperature is 14.2°C (1957–2002). The Chaochuan River, which is the primary river in the study area, flows from southwest to northwest. River flow is controlled by atmospheric rainfall. The Chaochuan Reservoir is constructed in the middle stream of the Chaochuan River. The control basin area is 21 km^2 , and the effective reservoir capacity is 1,500,000 m^3 . The Chaochuan Reservoir is built in the limestone-exposed region. The surrounding areas are highly developed with surface and underground karsts. A large karst cave is present (Figure 1(a)), and Cambrian limestone is hidden directly below the Quaternary unconsolidated sediments (Figure 1(b)). The karst water can exhibit vertical hydraulic correlation with groundwater in a Quaternary aquifer.

3. Materials and Methods

3.1. Sample Collection and Testing. The 37 groups of water samples collected from the study area in August 2016 and October 2016 mainly include surface water and groundwater (Figure 1). Cambrian limestone groundwater samples were collected by stratification sampling at leakage points under the shaft, mixed groundwater samples were collected using the drilling method, and groundwater samples in the Quaternary aquifer were collected from a motor-pumped well for civil use. Electrical conductivity, pH, and TDS field measurement of water samples were performed during sampling. Water samples were collected with 550 mL clean plastic

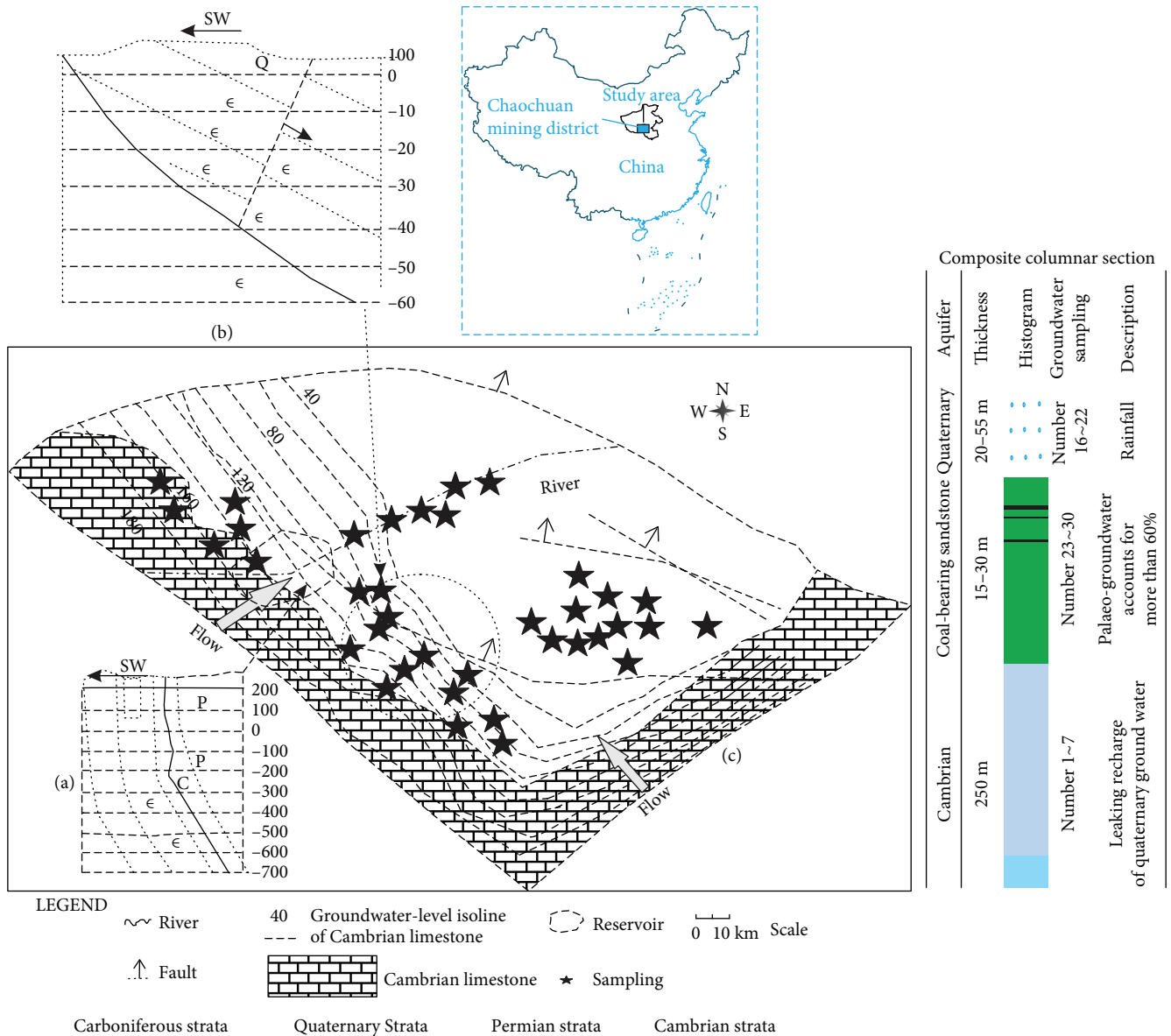


FIGURE 1: Hydrogeological map of the Chaochuan coal mining district in China. C: Carboniferous strata; Q: Quaternary strata; P: Permian strata; ε: Cambrian strata.

bottles to test isotopes and aqueous chemical ions. Samples were passed through 0.45 μm precleaned membrane filters and were kept refrigerated at approximately 4°C before analyses. Relevant parameters of all water samples were analyzed, including TDS, pH, Ca²⁺, Mg²⁺, Na⁺, K⁺, HCO₃⁻, SO₄²⁻, Cl⁻, δ¹⁸O, δ²H, δ³H, and δ¹³C. Table 1 shows the mean of analysis results. The hydrogen isotope test of water samples used the Zn reaction method, and the oxygen isotope test used the O-CO₂ balance method. MAT253 isotope mass spectrometer was applied. Test results are expressed in ‰ in accordance with VSMOW standards. The test accuracies are expressed as ±0.2‰ and ±0.1‰. Radioactive tritium and ¹⁴C content were tested with the low-background liquid scintillation counter Tri-Carb 3170 TR/SL. Anion (SO₄²⁻, Cl⁻) compositions of water samples were tested using the Dionex UltiMate 3000

with a relative error of 0.1%. HCO₃⁻ and CO₃²⁻ were tested by double indicator neutralization titration. The method was titrated by acid distribution and indicated by different indicators. The concentration of HCO₃⁻ and CO₃²⁻ was calculated from the dosage of H₂SO₄ standard solution. The cation (Ca²⁺, Mg²⁺, Na⁺, and K⁺) concentration of water samples was measured using the Hitachi Z-5000 atomic absorption spectrophotometer.

3.2. Descriptive Statistics Analysis. The standard deviation of TDS, Na⁺, Ca²⁺, SO₄²⁻, and HCO₃⁻ in water samples is greater than 60, which reflects that the water quality characteristics obviously differ. Meanwhile, the standard deviation of δ¹⁸O, δ²H, and δ¹³C value in water samples is greater than 1‰, which indicates that the sources of groundwater vary (Table 2). Notably, the TDS median of the MIX group is

TABLE 1: Mean of chemical composition of water samples in the study area (mg/L).

Number	Type	K ⁺ (mg/L)	Na ⁺ (mg/L)	Ca ²⁺ (mg/L)	Mg ²⁺ (mg/L)	Cl ⁻ (mg/L)	SO ₄ ²⁻ (mg/L)	HCO ₃ ⁻ (mg/L)	CO ₃ ²⁻ (mg/L)	pH	TDS (mg/L)	δO _{-SMOW} (‰)	δD _{-SMOW} (‰)	H ³ (TU)	¹⁴ C (pmc)	δ ¹³ C- PDB (‰)
1	CLG	1.69	35.09	123.36	34.15	24.26	172.04	376.63	0	7.21	570	-8.2	-67.9	13.31	—	-9.36
2	CLG	2.23	34.55	122.82	33.88	24.08	171.9	376.09	0	7.23	560	-8.1	-66.3	13.31	—	-9.87
3	CLG	2.01	54.04	127.85	35.94	24.15	194.6	425.13	0	7.09	653	-8	-64.5	10.15	—	-9.74
4	CLG	3.12	52.93	126.74	35.38	23.78	194.32	424.02	0	7.2	643	-7.8	-62.5	10.15	—	-9.35
5	CLG	1.01	34.08	120.33	33.14	23.25	169.01	372.59	0	7.05	681	-7.9	-66.2	11.21	—	-12.05
6	CLG	0.58	33.97	121.08	33.3	23.5	170.16	373.77	0	7.06	672	-8.1	-65.1	12.12	—	-9.36
7	CLG	2.35	51.69	120.8	33.59	21.8	187.55	415.73	0	7.03	663	-8	-67.1	10.57	—	-9.16
8	MIX	1.05	110.43	144.84	42.73	31.56	331.08	456.6	0	7.3	899	-8	-65.2	18.31	—	-9.25
9	MIX	3.24	108.24	142.65	41.63	30.83	330.53	454.41	0	7.32	880	-8.2	-66.3	18.31	—	-9.13
10	MIX	1.23	313.82	195.96	93.67	33.28	626.56	987.29	0	6.89	1987	-8.3	-66.5	13.17	—	-9.61
11	MIX	2.12	312.93	195.07	93.22	32.98	626.34	986.4	0	6.81	1748	-8.5	-67.3	13.17	—	-9.78
12	MIX	1.15	107.67	148.75	42.68	31.53	335.57	456.5	0	7.26	818	-7.9	-66.2	17.39	—	-8.45
13	MIX	2.13	106.69	147.77	42.19	31.2	335.33	455.52	0	7.23	886	-7.8	-67.2	17.39	—	-6.72
14	MIX	0.58	75.9	151.72	33.24	28.17	308.15	377.74	0	7.61	765	-8.3	-66.5	13.17	—	-7.89
15	MIX	0.95	75.53	151.35	33.06	28.04	308.05	377.37	0	7.69	775	-8.1	-65.4	13.17	—	-8.12
16	QG	6.12	27.5	182.26	21.24	47.59	221.56	402.71	0	7.02	700	-8	-63.7	15.17	—	-8.02
17	QG	4.32	29.3	184.06	22.14	48.19	222.01	404.51	0	7.12	710	-8.2	-64.5	15.17	—	-5.79
18	QG	1.23	58.65	181.53	28.37	36.81	234.3	480.83	0	6.62	771	-8.2	-68.3	16.29	—	-8.82
19	QG	2.31	57.57	180.45	27.83	36.45	234.03	479.75	0	6.63	782	-8.4	-69.3	16.29	—	-5.92
20	QG	3.12	37.68	160.41	30.52	43.28	200.08	424.02	0	6.93	692	-7.7	-62.8	21.51	—	-4.61
21	QG	2.14	38.66	161.39	31.01	43.61	200.33	425	21.5	9.85	682	-7.6	-63.7	21.51	—	-8.74
22	QG	7.12	10.56	89.07	1.35	10.04	73.95	218.65	0	7.42	303	-7.2	-61.2	15.16	—	-11.35
23	CSG	15.02	300.76	5.14	4.78	51.51	1.22	715.02	15.3	8.1	743	-10	-75.5	3.18	—	-12.83
24	CSG	16.02	304.76	9.42	6.78	52.84	2.22	719.02	15.1	8.15	726	-10.4	-76.5	2.38	16.2	-13.01
25	CSG	17.12	289.68	5.34	4.67	46.91	1.02	718	16.8	8.79	764	-9.5	-74.3	4.76	—	-13.98
26	CSG	16.03	298.67	4.63	3.82	49.04	1.13	716.87	17.4	8.46	772	-10.1	-76.6	2.12	16.8	-13.26
27	CSG	14.15	297.35	7.32	6.53	40.41	2.01	714.86	11.2	8.12	743	-11.1	-85.9	<0.5	13.6	-11.85
28	CSG	13.02	312.52	6.57	5.35	43.74	1.53	713.33	9.6	8.23	754	-10.3	-77.1	3.03	—	-11.25
29	CSG	10.58	311.12	4.68	4.36	36.11	2.13	711.2	8.5	8.15	712	-9.7	-76.2	2.12	—	-10.14
30	CSG	20.89	322.05	6.55	5.54	38.24	2.05	709.15	8.7	8.34	736	-9.6	-73.2	5.52	—	-9.62

TABLE 1: Continued.

Number	Type	K ⁺ (mg/L)	Na ⁺ (mg/L)	Ca ²⁺ (mg/L)	Mg ²⁺ (mg/L)	Cl ⁻ (mg/L)	SO ₄ ²⁻ (mg/L)	HCO ₃ ⁻ (mg/L)	CO ₃ ²⁻ (mg/L)	pH	TDS (mg/L)	δO _{-SMOW} (%)	δD _{-SMOW} (%)	H ³ (TU)	¹⁴ C (pmc)	δ ¹³ C- PDB (‰)
31	sw	3.11	33.42	90.69	20.81	14.92	140	277.59	0	7.78	741	-6.9	-62.6	14.78		-11.21
32	sw	4.02	32.5	89.77	20.35	14.61	139.77	276.67	0	7.35	437	-6.6	-60.6	14.78		-12.05
33	sw	4.53	15.67	78.03	19.12	12.67	94.36	257.86	0	7.77	356	-6.7	-62.1	16.05		-11.36
34	sw	5.21	14.99	77.35	18.78	12.44	94.19	257.18	0	7.72	352	-6.8	-61.6	16.05		-13.24
35	sw	2.13	59.92	114.1	25.67	27.65	200.33	333.48	0	7.76	598	-7.4	-63.1	16.62		-10.25
36	sw	3.14	58.91	113.09	25.16	27.31	200.08	332.47	0	7.67	589	-7.3	-63.9	16.62		-11.58
37	sw	6.23	11.45	89.96	1.12	10.33	74.17	219.54	0	7.47	316	-7	-61.3	15.16		-11.64

CLG: Cambrian groundwater aquifer; QG: Quaternary aquifer groundwater; CSG: coal-bearing sandstone aquifer groundwater; sw: surface water; MIX: represent mixing water.

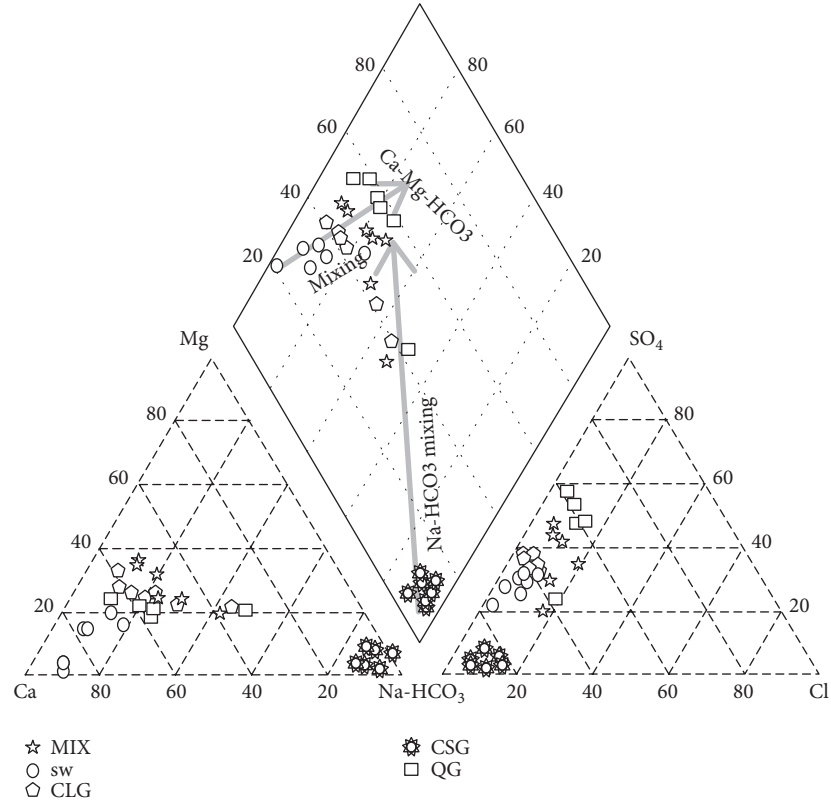


FIGURE 2: Piper trilinear diagram of the water samples. MIX: mixing water; CLG: Cambrian aquifer groundwater; QG: Quaternary aquifer groundwater; sw: surface water; CSG: coal-bearing sandstone aquifer groundwater.

TABLE 2: Chemical composition descriptive statistics of water samples in the study area.

Component	Total sample	Min	Max	Mean	Std. deviation
K ⁺ (mg/L)	37	0.58	20.89	5.48	5.63
Na ⁺ (mg/L)	37	10.56	322.05	119.765	118.02
Ca ²⁺ (mg/L)	37	4.63	195.96	107.64	62.42
Mg ²⁺ (mg/L)	37	1.12	93.67	26.94	20.84
Cl ⁻ (mg/L)	37	10.04	52.84	31.27	12.09
SO ₄ ²⁻ (mg/L)	37	1.02	626.56	183.88	151.96
HCO ₃ ⁻ (mg/L)	37	218.65	987.29	481.71	197.96
CO ₃ ²⁻ (mg/L)	37	0	21.50	3.35	6.36
pH	37	6.62	9.85	7.55	0.65
TDS (mg/L)	37	303.00	1987.0	734.56	314.18
δ ¹⁸ O (‰-SMOW)	37	-11.10	-6.60	-8.26	1.10
δD (‰-SMOW)	37	-85.90	-60.60	-67.41	5.72
H ³ (TU)	36	2.12	21.51	12.75	5.41
¹⁴ C (pmc)	3	13.60	16.80	15.53	1.70
δ ¹³ C-PDB (‰)	37	-13.98	-4.61	-9.95	2.19

significantly higher than that of the others and reflects a pollution characteristic. However, the concentrations of Na⁺, Ca²⁺, and HCO₃⁻ of the CSG group reflect a cation exchange characteristic.

3.3. *Mixing Ratio Analysis.* The H and O stable isotopes of groundwater would not change during their interaction with rocks under low temperature (<60°C). Thus, the mixing ratio could be calculated by a linear mixing ratio calculation model of two or three end members. The model ($n = 3$) is as follows:

$$\begin{aligned}\delta D &= X_1(\delta D)_1 + \dots + (\delta D)_n, \\ \delta^{18}O &= X_1(\delta^{18}O)_1 + \dots + (\delta^{18}O)_n,\end{aligned}\quad (1)$$

$$X_1 + X_2 + \dots + X_n = 1,$$

where δD and $\delta^{18}O$ are the compositions of mixed H and O stable isotopes, respectively, and $(\delta D)_1, \dots, (\delta D)_n$ and $(\delta^{18}O)_1, \dots, (\delta^{18}O)_n$ are the compositions of H and O stable isotopes, respectively, of different end members. X_1, X_2, \dots, X_n denote the mixing ratios of different end members. The groundwater tracing results in the study area show that rainfall-penetrated groundwater and evaporated groundwater (Quaternary groundwater) and “palaeo-groundwater” (coalbed sandstone groundwater) exhibit different H and O stable isotope characteristics. Therefore, the two types of groundwater can be used as a mixing end member directly.

4. Results and Discussion

The two major hydrochemical types of groundwater in the study area are (1) Ca-Mg-HCO₃ and (2) Na-HCO₃. The

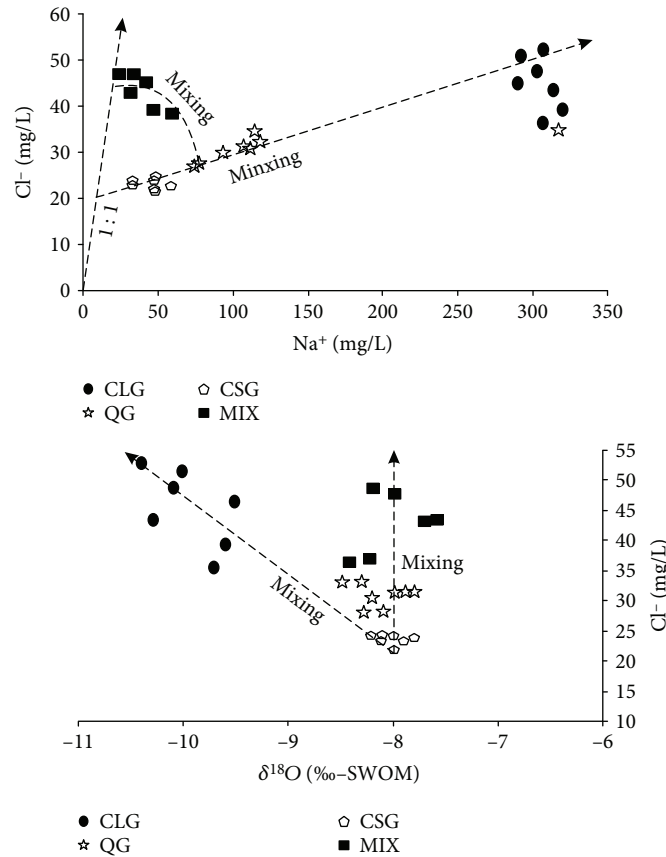


FIGURE 3: Na⁺/Cl⁻ and Cl-δ¹⁸O diagrams of the water samples. MIX: mixing water; CLG: Cambrian aquifer groundwater; QG: Quaternary aquifer groundwater; sw: surface water; CSG: coal-bearing sandstone aquifer groundwater.

main hydrochemical type of sandstone groundwater in the coalbed is Na-HCO₃, and the positive ion concentrations are Na⁺ > Ca²⁺ > Mg²⁺ (Figure 2). The major hydrochemical type of Cambrian limestone groundwater and Quaternary groundwater is Ca-Mg-HCO₃. Ca-Mg-HCO₃ is mainly mixed by Cambrian limestone groundwater and Quaternary groundwater, deviates significantly from the Na⁺/Cl⁻ = 1 : 1 line, and falls on the same fitting line with Cambrian limestone groundwater and mixed drilling groundwater (Figure 3). Cl-δ¹⁸O reveals that an appropriate amount of sandstone groundwater in the coalbed participates in the mixing along the groundwater runoff.

Quaternary groundwater and Cambrian limestone groundwater samples mostly distribute along the evaporation line; this distribution implies that karst water and Quaternary groundwater have the same source in the study area and are mainly recharged by penetration of surface water (Figure 4). However, some Quaternary groundwater, Cambrian limestone groundwater, and coalbed sandstone groundwater samples deviate from the evaporation line greatly, and this deviation indicates remarkable mixing with “palaeo-groundwater.” The ³H value of one coalbed sandstone groundwater sample is smaller than 0.5, which is smaller than the test value of the instrument. The ¹⁴C content is 13.6 pmc, which indicates that this sample may be the last

one recharged by rainfall in the ice stage and can be used as the end member of palaeo-groundwater.

The δD and δ¹⁸O values of Quaternary groundwater and Cambrian limestone groundwater increase with the increase in TDS (Figure 5). TDS is mixed with the original aquifer groundwater along the runoff direction, thereby decreasing the δD and δ¹⁸O values. However, TDS along the runoff direction increases. In coalbed sandstone groundwater, δ¹³C decreases with the increase in CO₃²⁻ + HCO₃⁻ (line 3 in Figure 6). This condition indicates kinetic fractionation of groundwater in biodegradation of organic matters. δ¹³C increases with the increase in CO₃²⁻ + HCO₃⁻ in Cambrian limestone groundwater, and this condition indicates that organic matters produce methane due to methanogens (line 1 in Figure 6). For Quaternary groundwater, δ¹³C decreases with the increase in CO₃²⁻ + HCO₃⁻ (line 2 in Figure 6).

Groundwater samples from different aquifers in the study area are drawn in the δ¹⁸O-δD scatter diagram in accordance with the δ value (δD and δ¹⁸O) (Figure 7). ΔABC is determined in accordance with the distribution features of water sample points. The results of the established linear groundwater-mixing ratio calculation model and groundwater recharge process and tracing qualitatively show that A in ΔABC represents palaeo-groundwater with low proportion, B stands for rainfall-penetrated groundwater free from

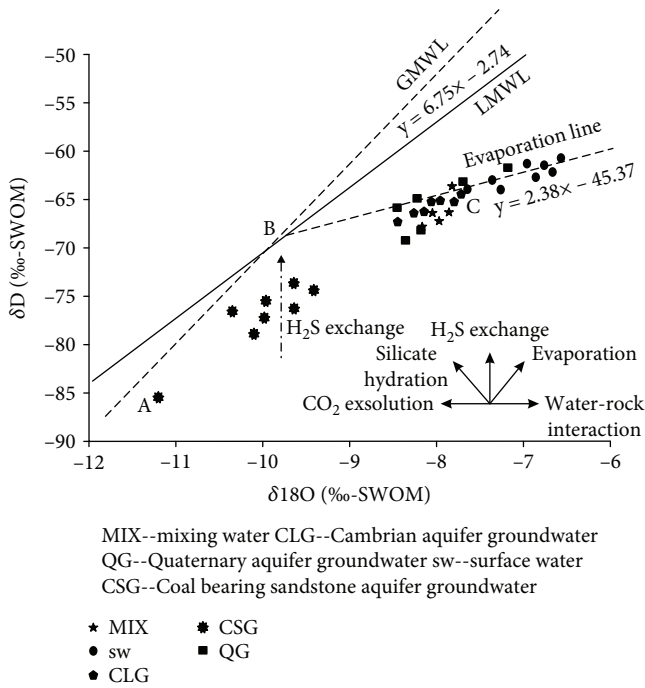


FIGURE 4: δD - $\delta^{18}O$ plot showing the stable isotope composition of water in the study area, which indicates the recharge sources. MIX: mixing water; CLG: Cambrian aquifer groundwater; QG: Quaternary aquifer groundwater; sw: surface water; CSG: coal-bearing sandstone aquifer groundwater.

evaporation, and C is Quaternary groundwater that has experienced surface evaporation and has high δ . The $\delta^{18}O$ - δD scatter diagram of groundwater shows that the Quaternary groundwater and Cambrian limestone groundwater are close to the intersection end of the “BC” and “AC” lines. Penetration water in the aquifer due to evaporation takes the dominant advantages. Coalbed sandstone groundwater is close to the intersection end of the “BA” and “AC” lines, and this condition shows remarkable mixing with palaeo-groundwater.

As shown in Figure 8, HCO_3^- and Cl^- exhibit a linear relationship with the mixing ratio, whereas Na^+ , Ca^{2+} , and SO_4^{2-} show certain degrees of curvature. This condition reflects that HCO_3^- and Cl^- can be used as conservative tracing ions to study the mixing process of groundwater. From the calculation results, coalbed sandstone groundwater is found to account for more than 60%. On the contrary, the deep limestone groundwater accounts for less than 20%, which is close to that of the Quaternary groundwater. This finding demonstrates that deep limestone groundwater mainly comes from the leaking recharge of Quaternary groundwater, which is considered “modern” rainfall recharge.

5. Conclusion

In this study, aquifer groundwater, local rainfall, and surface water samples, which exert important impacts on coal exploitation in a typical coalfield (Chaochuan Coal Mine),

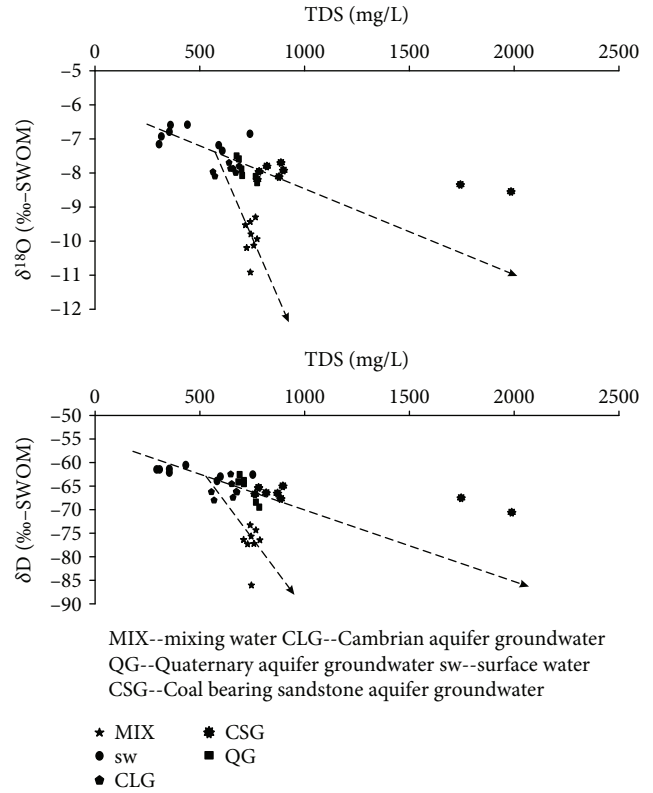


FIGURE 5: δD -TDS and $\delta^{18}O$ -TDS plots showing the increase in oxyhydrogen stable isotope (δ value) of groundwater samples with the change in TDS. MIX: mixing water; CLG: Cambrian aquifer groundwater; QG: Quaternary aquifer groundwater; sw: surface water; CSG: coal-bearing sandstone aquifer groundwater.

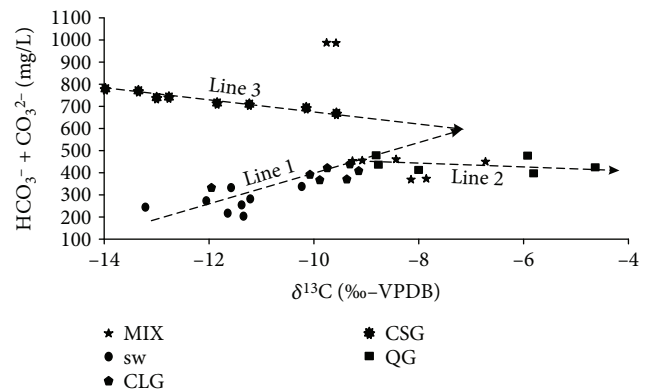


FIGURE 6: $\delta^{13}C$ versus $CO_3^{2-} + HCO_3^-$ diagram of the water samples. MIX: mixing water; CLG: Cambrian aquifer groundwater; QG: Quaternary aquifer groundwater; sw: surface water; CSG: coal-bearing sandstone aquifer groundwater.

were collected at different seasons. The following conclusions were drawn:

- (1) In the study area, long-term water filling after exploitation of aquifer occurs, which may destroy the original groundwater circulation of the aquifer.

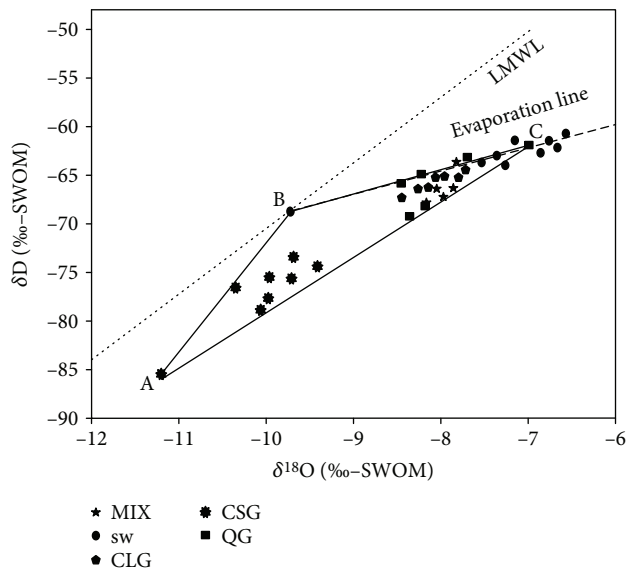


FIGURE 7: $\delta D-\delta^{18}O$ plot showing the mixing process of groundwater. MIX: mixing water; CLG: Cambrian aquifer groundwater; QG: Quaternary aquifer groundwater; sw: surface water; CSG: coal-bearing sandstone aquifer groundwater.

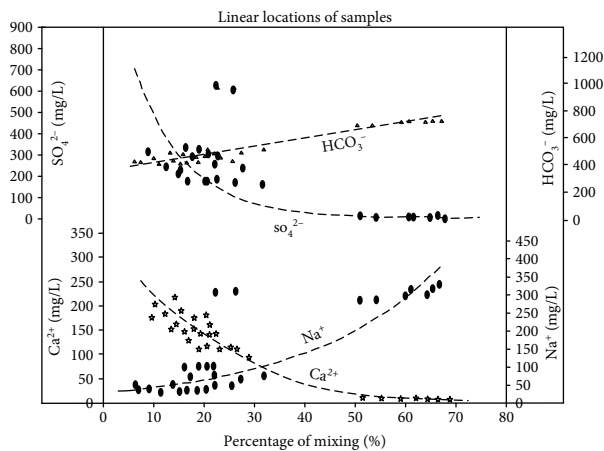


FIGURE 8: Plot of mixing ratio versus Na^+ , Ca^{2+} , HCO_3^- , and SO_4^{2-} showing the use of conservative tracing ions in studying the mixing process of groundwater.

Hydraulic alteration in the recharge area accelerates, and surface water is recharged into the aquifer in the study area.

- (2) In the main recharging aquifer in the study area, rainfall penetration is the main source of Cambrian limestone groundwater in the north limestone outcropped region, and surface water penetration is the main source of Quaternary groundwater. Coalbed sandstone groundwater mainly comes from the mixture of palaeo-groundwater and Quaternary groundwater. Cambrian limestone groundwater, coalbed sandstone groundwater, and Quaternary groundwater present a high potential to be mixed together.

- (3) Water sources during coal mining can be deduced from the quantitative perspective in accordance with the dynamic changes in stable isotope compositions and the variation in the trend of the linear member mixing ratio at an effluent sampling site under the shaft. Specific countermeasures against water inrush accidents should be taken to protect groundwater resources effectively. This model is applicable to water disaster control in North China-type coalfields after proper modifications. The research conclusions can provide important references for water disaster control in other coalfields.

Data Availability

The data used to support the findings of this study are available from the corresponding author upon request.

Conflicts of Interest

The authors declare that they have no conflicts of interest.

Acknowledgments

This work was financially supported by the National Natural Science Foundation of China (Grant 41672240); Henan Province Technical Innovation Guidance Special (Grant 182107000019); Science and Technology Key Research Project of the Education Department of Henan, China (Grants 13A170313 and 14A510022); China Postdoctoral Science Foundation (2017M612395); Innovation Scientists and Technicians Troop Construction Projects of Henan Province (Grant CXTD2016053); Henan Province’s Technological Innovation Team of Colleges and Universities (Grant 15IRTSTHN027); Fundamental Research Funds for the Universities of Henan Province (NSFRF1611); and Scientists and Technicians Projects of Henan Province (Grant 172107000004).

References

- [1] A. Akerman, F. Poitrasson, P. Oliva, S. Audry, J. Prunier, and J. J. Braun, “The isotopic fingerprint of Fe cycling in an equatorial soil–plant–water system: the Nsimi watershed, South Cameroon,” *Chemical Geology*, vol. 385, pp. 104–116, 2014.
- [2] A. Ben Moussa, H. Mzali, K. Zouari, and H. Hezzi, “Hydrochemical and isotopic assessment of groundwater quality in the Quaternary shallow aquifer, Tazoghrane region, north-eastern Tunisia,” *Quaternary International*, vol. 338, pp. 51–58, 2014.
- [3] C. A. Delconte, E. Sacchi, E. Racchetti, M. Bartoli, J. Mas-Pla, and V. Re, “Nitrogen inputs to a river course in a heavily impacted watershed: a combined hydrochemical and isotopic evaluation (Oglio River Basin, N Italy),” *Science of the Total Environment*, vol. 466–467, pp. 924–938, 2014.
- [4] D. Zhang, X. D. Li, Z. Q. Zhao, and C. Q. Liu, “Using dual isotopic data to track the sources and behaviors of dissolved sulfate in the western North China Plain,” *Applied Geochemistry*, vol. 52, pp. 43–56, 2015.

- [5] D. M. Kim, S. T. Yun, M. J. Kwon, B. Mayer, and K. H. Kim, "Assessing redox zones and seawater intrusion in a coastal aquifer in South Korea using hydrogeological, chemical and isotopic approaches," *Chemical Geology*, vol. 390, pp. 119–134, 2014.
- [6] D. M. Han, X. F. Song, M. J. Currell, and M. Tsujimura, "Using chlorofluorocarbons (CFCs) and tritium to improve conceptual model of groundwater flow in the south coast aquifers of Laizhou Bay, China," *Hydrological Processes*, vol. 26, no. 23, pp. 3614–3629, 2012.
- [7] G. Martinelli, A. Chahoud, A. Dadomo, and A. Fava, "Isotopic features of Emilia-Romagna region (North Italy) groundwaters: environmental and climatological implications," *Journal of Hydrology*, vol. 519, pp. 1928–1938, 2014.
- [8] H. el Mejri, A. Ben Moussa, and K. Zouari, "The use of hydrochemical and environmental isotopic tracers to understand the functioning of the aquifer system in the Bou Hafna and Haffouz regions, Central Tunisia," *Quaternary International*, vol. 338, pp. 88–98, 2014.
- [9] I. Matiatos, A. Alexopoulos, and A. Godelitsas, "Multivariate statistical analysis of the hydrogeochemical and isotopic composition of the groundwater resources in northeastern Peloponnesus (Greece)," *Science of the Total Environment*, vol. 476–477, pp. 577–590, 2014.
- [10] J. Sültenfuß, R. Purtschert, and J. F. Führböter, "Age structure and recharge conditions of a coastal aquifer (northern Germany) investigated with ^{39}Ar , ^{14}C , ^3H , He isotopes and Ne," *Hydrogeology Journal*, vol. 19, no. 1, pp. 221–236, 2011.
- [11] L. J. Lambán, J. Jódar, E. Custodio, A. Soler, G. Sapriza, and R. Soto, "Isotopic and hydrogeochemical characterization of high-altitude karst aquifers in complex geological settings: the Ordesa and Monte Perdido National Park (Northern Spain) case study," *Science of the Total Environment*, vol. 506–507, pp. 466–479, 2015.
- [12] J. M. Heikoop, T. M. Johnson, K. H. Birdsell et al., "Isotopic evidence for reduction of anthropogenic hexavalent chromium in Los Alamos National Laboratory groundwater," *Chemical Geology*, vol. 373, pp. 1–9, 2014.
- [13] N. Mohammed, H. Celle-Jeanton, F. Huneau et al., "Isotopic and geochemical identification of main groundwater supply sources to an alluvial aquifer, the Allier River valley (France)," *Journal of Hydrology*, vol. 508, pp. 181–196, 2014.
- [14] T. Hosono, O. Lorphensriand, S.-i. Onodera et al., "Different isotopic evolutionary trends of $\delta^{34}\text{S}$ and $\delta^{18}\text{O}$ compositions of dissolved sulfate in an anaerobic deltaic aquifer system," *Applied Geochemistry*, vol. 46, pp. 30–42, 2014.
- [15] W. Sanford, "Calibration of models using groundwater age," *Hydrogeology Journal*, vol. 19, no. 1, pp. 13–16, 2011.
- [16] J. Chen, X. Liu, C. Wang et al., "Isotopic constraints on the origin of groundwater in the Ordos Basin of northern China," *Environmental Earth Sciences*, vol. 66, no. 2, pp. 505–517, 2012.
- [17] X. Y. Liu, J. S. Chen, X. X. Sun, and Z. G. Su, "Study on soil water movement during rainfall infiltration using stable isotopic tracing method," *Nuclear Science and Techniques*, vol. 22, pp. 251–256, 2011.
- [18] X. Xu, H. Guan, and Z. Deng, "Isotopic composition of throughfall in pine plantation and native eucalyptus forest in South Australia," *Journal of Hydrology*, vol. 514, pp. 150–157, 2014.
- [19] Y. Zhang, S. Ye, and J. Wu, "A modified global model for predicting the tritium distribution in precipitation, 1960–2005," *Hydrological Processes*, vol. 25, no. 15, pp. 2379–2392, 2011.
- [20] C. M. Ordens, A. D. Werner, V. E. A. Post, J. L. Hutson, C. T. Simmons, and B. M. Irvine, "Groundwater recharge to a sedimentary aquifer in the topographically closed Uley South Basin, South Australia," *Hydrogeology Journal*, vol. 20, no. 1, pp. 61–72, 2012.
- [21] T. Ayenew, S. Kebede, and T. Alemyahu, "Environmental isotopes and hydrochemical study applied to surface water and groundwater interaction in the Awash River basin," *Hydrological Processes*, vol. 22, no. 10, pp. 1548–1563, 2008.
- [22] E. S. Lima, S. M. G. Montenegro, and A. A. Montenegro, "Environmental isotopes and the analysis of the origin of groundwater salinity in the Cabo Aquifer in Recife coastal plain, Pernambuco, Brazil," in *Proceedings of the IV South American Symposium on Isotope Geology*, Salvador, BA, Brazil, 2009.
- [23] A. Vengosh, S. Hening, J. Ganor et al., "New isotopic evidence for the origin of groundwater from the Nubian sandstone aquifer in the Negev, Israel," *Applied Geochemistry*, vol. 22, no. 5, pp. 1052–1073, 2007.
- [24] A. Murad, "Evolution of isotopic compositions in groundwater of the area between the Gulf of Oman and the Arabian Gulf," *Chinese Journal of Geochemistry*, vol. 29, no. 2, pp. 152–156, 2010.